THE CORRELATION OF MICROSTRUCTURE WITH THE STRENGTH AND FRACTURE TOUGHNESS OF PEARLITIC STEELS

by

Brian Edward O'Donnelly BSc

A thesis submitted to the University of Strathclyde in fulfilment of the requirements for the award of the degree of Doctor of Philosophy

Department of Metallurgy

University of Strathclyde

December 1984

To my Mother and Father.

LIST OF SYMBOLS

d_α Ferrite grain size.

d_c Composite ferrite grain size.

d_p Pearlite grain size.

k_α Hall-Petch parameter for pure ferrite.

k_p Hall-Petch parameter for a fully pearlitic microstructure.

$\bar{L}_{\alpha I}$ Mean pro-eutectoid ferrite width.

$\bar{L}_\gamma$ Prior-austenite grain size.

N_p Pearlite nodule size.

S_r Mean random pearlite interlamellar spacing.

$\bar{t}_r$ Mean cementite width.

V_α Volume fraction of ferrite.

V_P Volume fraction of pearlite.

σ_α Yield stress for pure ferrite.

σ_c Composite yield (proof) stress.

σ_o Friction stress for ferrite.

σ_P Yield (proof) stress for case of a fully pearlitic microstructure.

$\bar{\lambda}_\alpha$ Mean free ferrite distance.

CONTENTS

ACKNOWLEDGEMENTS

I wish to thank Professor H B Bell of the Department of Metallurgy, University of Strathclyde, for the opportunity of conducting this research project.

I am particularly indebted to my supervisor, Dr. T N Baker for his constant interest, support and advice. Thanks are also due to Dr. R L Reuben for helpful discussions.

I am grateful to my Industrial Supervisor, Dr. R R Preston, for the interest he has shown and I wish to thank the British Steel Corporation for the use of laboratory facilities. Thanks are also due to the technical staff of BSC Sheffield laboratories and in particular to Dr. P Morris, Mr. T Wilkinson and Mr. L J Drewett for their assistance in instrumented-impact and fracture toughness testing.

I wish to acknowledge the Science and Engineering Research Council and British Steel Corporation for financial support.

A special thanks is addressed to Mrs. M Aird and Mrs. M McCann for the typing of this manuscript.

Finally, I wish to express my gratitude to my father for his help and encouragement in the preparation of this thesis.

ABSTRACT

The role of composition, heat treatment and microstructural variables on the hardness, flow stress and fracture toughness has been investigated for a range of C-Mn steels. The study is divided into two parts.

In Part 1, the influence of various ferrite-pearlite microstructures on the hardness and flow stress has been examined with respect to a Hall-Petch analysis. In contrast with previous reports it was found that a Hall-Petch equation can be applied satisfactorily in describing these properties provided care is taken in obtaining the appropriate mean slip distance for a given microstructure.

The mean random interlamellar spacing was found to best quantify the microstructure when account is taken of the ferrite volume fraction, ferrite grain size, prior-austenite grain size and calculated cementite thickness. These parameters have been combined in a simple law of mixtures model to evaluate the mean slip distance in ferrite for a range of pearlite volume fractions between 20 and 100%. By substituting the mean slip distance for the effective ferrite grain size in a Hall-Petch equation both a positive friction stress and a very good correlation was obtained with measured hardness and flow stress data.

In Part 2,the effect of changes in microstructure on the toughness of high carbon pearlitic steels was studied using standard Charpy,instrumented-impact and plane strain fracture toughness tests. Controversy in the literature regarding the influence of pearlite colony and prior-austenite grain boundaries in obstructing cleavage crack propagation has been resolved by close examination of the microstructure and fracture surface. The pearlite nodule size was found to be directly related to the cleavage facet size when pro-eutectoid ferrite is considered in hypo-eutectoid steels. Refining the pearlite nodule size by low austenitising temperatures and accelerated cooling gives improved toughness. Although the pearlite nodule size was shown to primarily determine the ductile-brittle transition temperature, it is suggested that the pearlite spacing may be of more importance as regards fracture toughness.

INTRODUCTION

Medium to high carbon pearlitic steels have been used in the manufacture of rail steel for many years. In the last decade or so,however,marked changes in railroad transformation practice towards higher train speeds and greater axial loads have necessitated considerable interest in the production of high strength rail steels. From an historical viewpoint the most economical method of resisting rising severity of service environment has been to increase the carbon content of the steel with concomitant increase in strength. At the present time however,the microstructure of rail steels is already close to fully pearlitic and additional strengthening due to carbon and manganese content alone, is ineffective. Accordingly emphasis in metallurgical studies is on enhanced strength by means of heat treatment and/or by further additions of alloying element.

Unlike rail head wear and plastic deformation levels which can be monitored periodically to forecast replacement, rail fracture is less easy to anticipate. Failures frequently initiate from small fatigue cracks very difficult to detect when the rail is in service. The occurrence of brittle fracture of complete rail sections and the possibility of derailment and loss of life have made it mandatory that increased strength should be accompanied by no appreciable loss in ductility and fracture toughness. It is

therefore of considerable interest to identify the microstructural conditions which give optimum strength and toughness.

Although many studies have shown that the pearlite interlamellar spacing controls the yield stress more work is needed before the precise nature of this strengthening is understood for ferrite-pearlite as well as fully pearlitic steels. Similarly, those microstructural features governing toughness in both hypo-eutectoid and eutectoid steels have still to be fully discerned.

The present study will examine the role of microstructure on the strength and fracture toughness of medium to high carbon pearlitic steels within the constraints of relatively simple yet commercially practical heat treatment variations. The compositions of the steels chosen are similar to those used in the manufacture of rails.

The study is divided into two parts. In part one the relationship between microstructure hardness and flow stress will be studied in some detail with the aim of obtaining a predictive structure-property model. In part two the resistance to brittle fracture will be investigated, with reference to conventional impact and fracture toughness testing. The findings of both sections should then indicate the heat-treatments and microstructures which give rise to both high strength and toughness.

PART 1

CHAPTER I

THE NUCLEATION,GROWTH AND CRYSTALLOGRAPHY OF PEARLITE

1.1 THE NUCLEATION AND GROWTH OF PEARLITE

In the Fe-C system pearlite is a two phase lamellar product composed of alternate plates of ferrite and cementite (Fe_3C) which results from eutectoidal decomposition of austenite at temperatures below 727^{o}C. Formation is by heterogeneous nucleation,predominantly on austenite grain boundaries,and subsequent growth of both phases outwardly from the boundary of origin into the untransformed austenite.

In general,there is no rigid pattern to the nucleation event and either phase can nucleate first and by so doing promote the nucleation of the second phase in an adjacent site[1]. In hypo-eutectoid steels prior separation of ferrite will normally nucleate cementite whereas in an hyper-eutectoid steel pro-eutectoid cementite will nucleate ferrite[2]. However, as pearlite is a two phase structure growth can only proceed after both phases have nucleated[1,2].

The classic text book explanation of nucleation and growth,due to Hull and Mehl[3] is depicted in Fig. 1.1. The appearance of the first nucleus, assumed by the authors to be cementite, depletes the surrounding austenite of carbon thus favouring the nucleation of a ferrite plate, adjacent to the

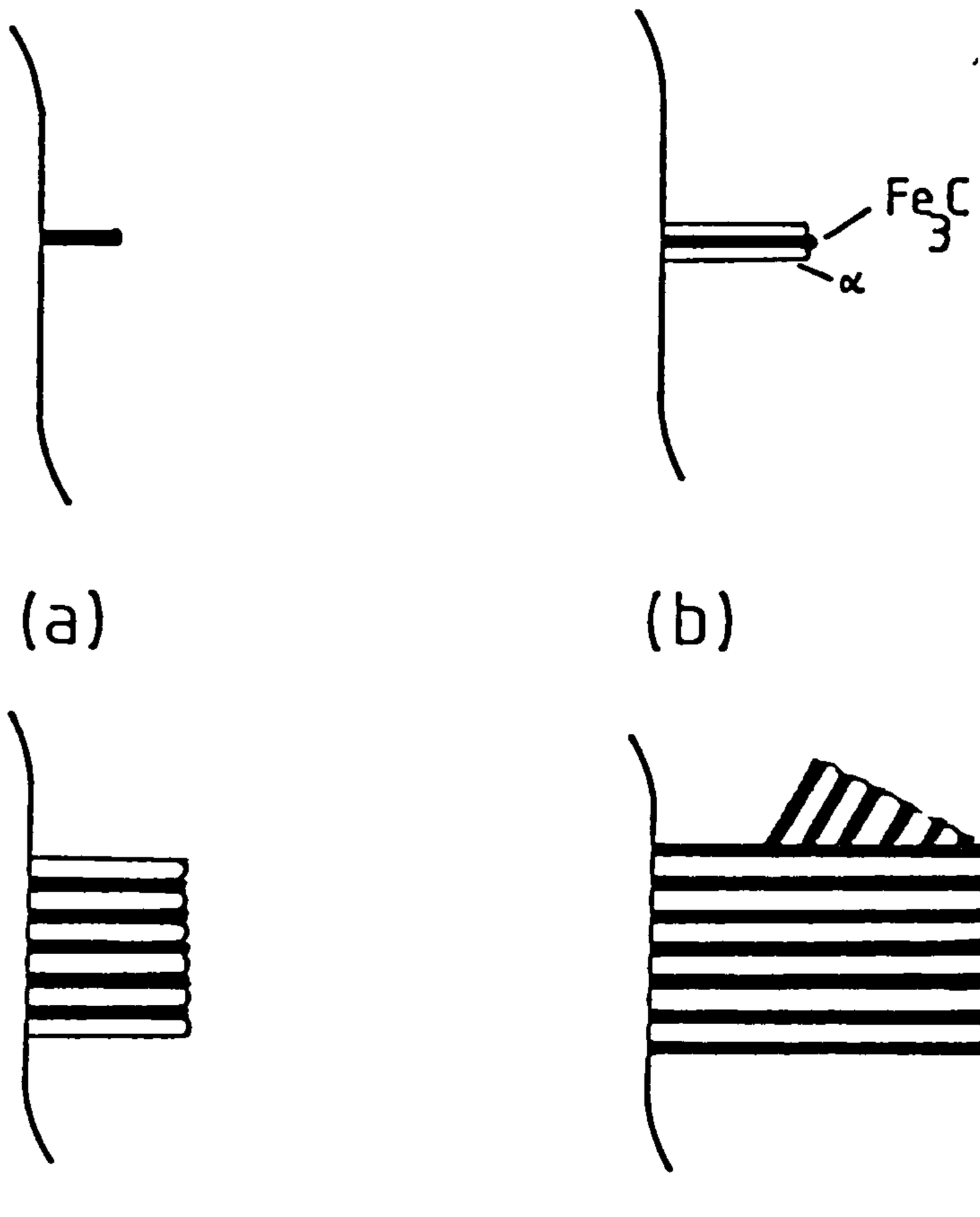

Fig 1.1 Nucleation and growth of pearlite colonies. (After Mehl[8])

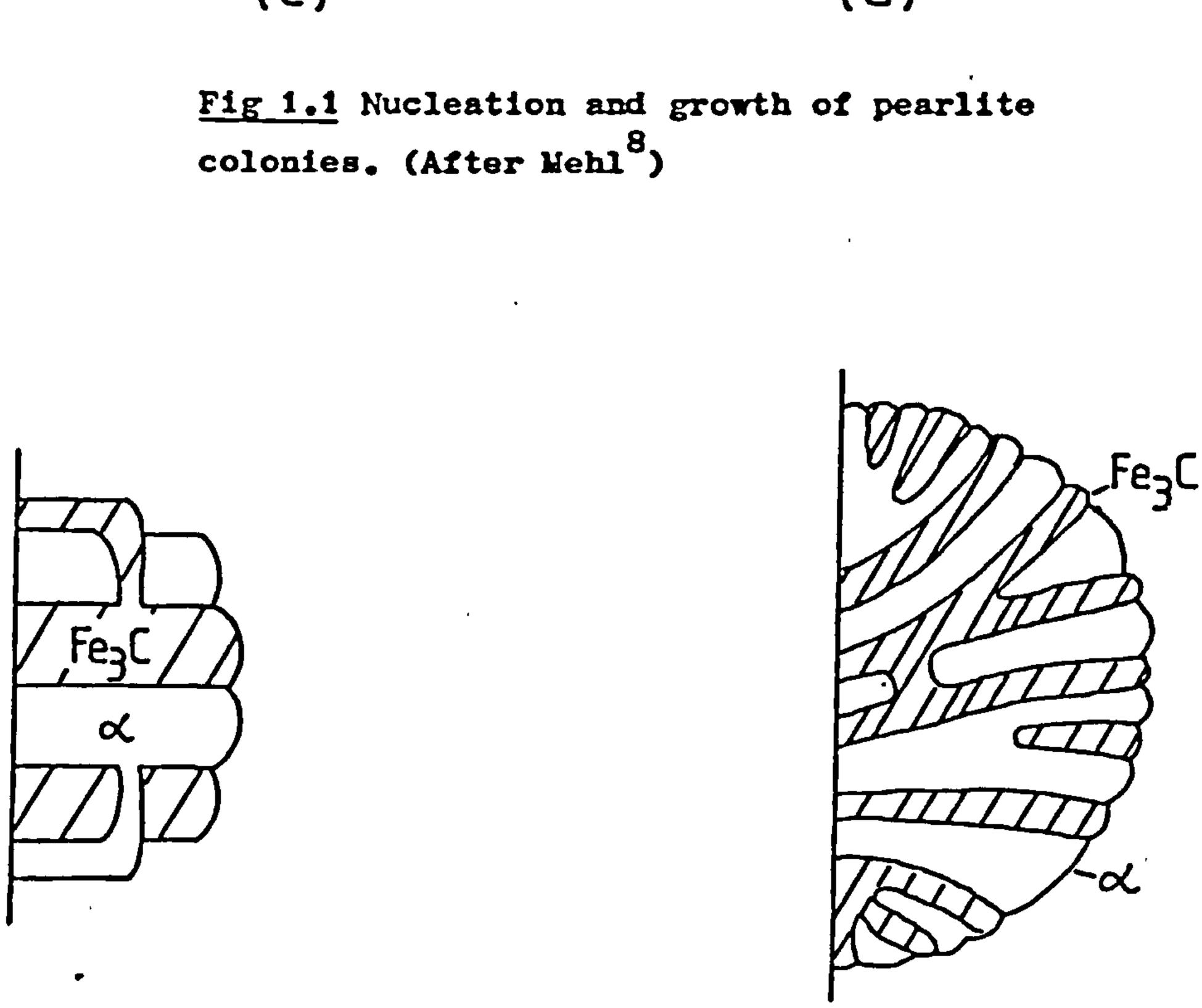

Fig 1.2 Nucleation and growth of pearlite nodules. (After Chadwick[1])

cementite nucleus (Fig.1.1(a) & (b). In turn, the ferrite plate rejects carbon atoms into the surrounding austenite thereby favouring the formation of cementite and so on.

At the same time as the pearlite colony grows sideways by repeated nucleation of both phases, the ferrite and cementite advance edgewise into the austenite since the carbon atoms, rejected ahead of the advancing ferrite, diffuse into the path of the growing cementite (Fig. 1.1(c). Eventually a cementite platelet of different orientation will form and this acts to promote the growth of a new pearlite colony as shown in Fig. 1.1(d).

It is now generally accepted however, from the work of Hillert[2] and others[4] that such a "sideways" repeated nucleation rarely occurs. Instead the ferrite and cementite phases bridge or branch over each other to take advantage of growth in areas depleted or enriched in solute[1] (Fig. 1.2(a). Periodic branching leads to a rapid multiplication of the number of individual lamellae within each growth centre. This "cooperative" growth together with edgewise migration results in a nodular structure as schematically illustrated in Fig. 1.2(b).

Pearlite nodules advance by the radial growth of a number of pearlite colonies, i.e. regions in which the lamellae have usually one direction[5,6] from which the nodule is composed[3,7,8]. Growth continues until the nodule impinges upon other growing nodules nucleated from different sites. In general the rate of transformation depends on the rate of nucleation of pearlite nodules (i.e. the number of nodules formed in unit volume in unit time) and also on the rate of growth of the nodules. The change in these variables with temperature for a eutectoid steel is shown in Fig. 1.3.

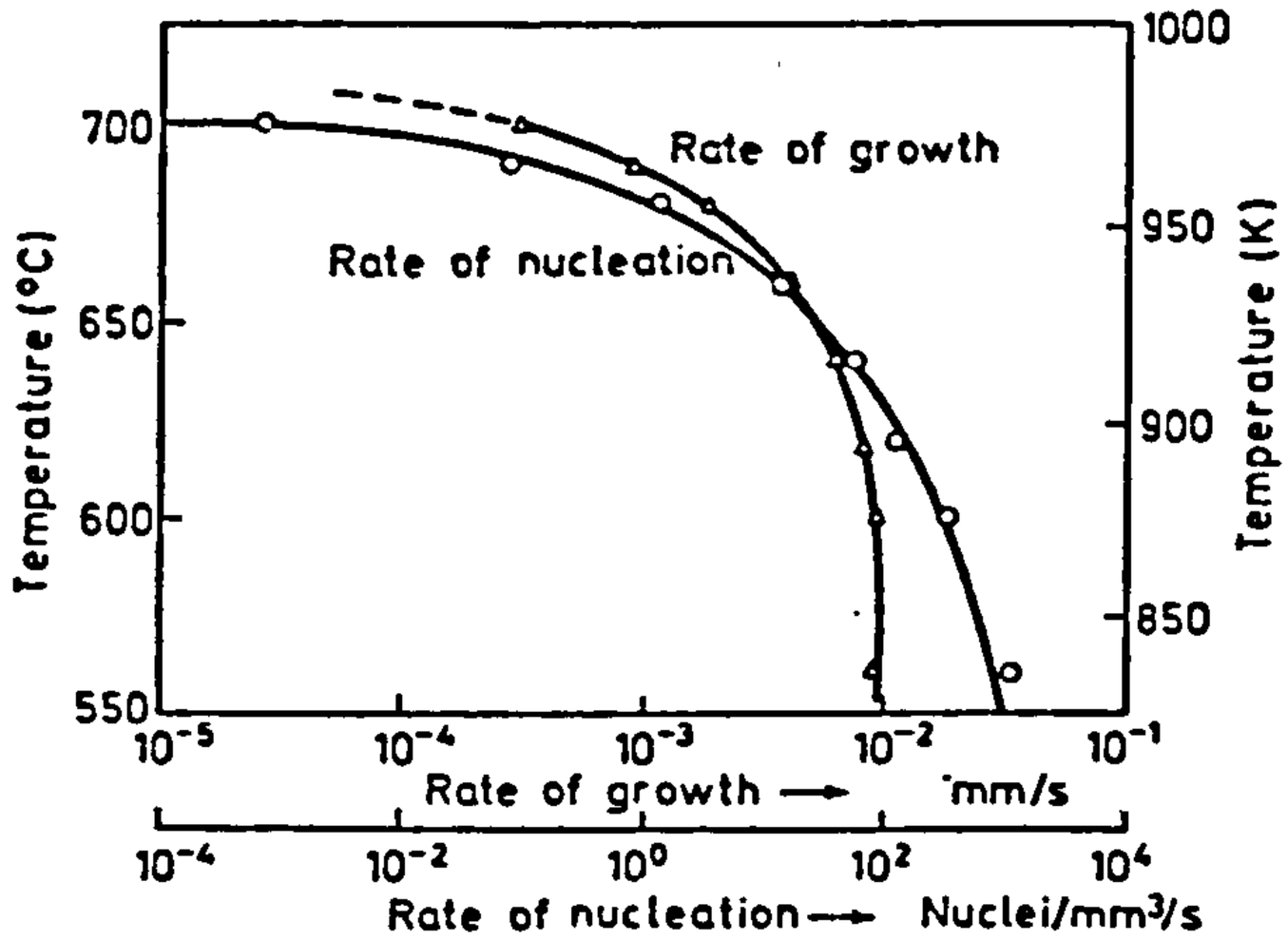

Fig 1.3 The effect of temperature on the rate of nucleation and the rate of growth of pearlite in a eutectoid steel. (After Mehl[8])

The rate of nucleation, as expected, increases with decreasing temperature. However, unlike the rate of growth which is controlled by the diffusion of carbon and is therefore structure insensitive[8,9], nucleation rates are markedly influenced by the structure of the austenite prior to transformation. As nucleation occurs almost exclusively at austenite grain boundaries in homogeneous austenite, the size of the austenite grains will determine the available boundary area at which nucleation can occur. Therefore pearlite formation will commence at lower temperatures for larger grain sizes. Such is the basis of hardenability in steels[9]. In addition, for a constant transformation temperature, less nuclei will form in larger grain sized austenite and this will lead to larger pearlite nodules[8].

Although the rate of growth is governed by the diffusion of carbon, which decreases with temperature, the interlamellar spacing also decreases with temperature, the result being a shorter diffusion path at lower temperatures and thus higher growth rates[9]. The rate of growth is discussed further in Section 1.4.

The extent of development of a pearlite nodule from homogeneous austenite is, therefore, dependent on the prior-austenite grain size and the reaction characteristics, that is the balance between the rate of nucleation and the rate of growth[8]. For example, at high transformation temperatures, at a constant prior-austenite grain size, the rate of nucleation may be very low in comparison to the rate of growth. This will often result in the formation of a small number of pearlite nodules which grow to be of a size larger than the original austenite grains[8].

The ability of pearlite colonies and hence pearlite nodules to grow across a prior-austenite grain boundary has been the source of some debate in the literature. Jolivet[10] had stated as early as 1939, that "the case is never met with where any one colony is not entirely localized in a single grain of austenite and is not arrested in the growth by the boundaries of this grain". Mehl and co-authors[3,7,8] assumed that the orientation of the cementite,"the active nucleus", was directly related to the orientation of the austenite from which it is derived. As the pearlitic ferrite takes its orientation from the cementite, both phases grow into the austenite to which they bear a precise crystallographic orientation. Since the colony cannot have an orientation relationship with more than one austenite grain Mehl et al[3,7,8] predicted that the growth of the pearlite colony must cease at the boundary of the austenite grain in which it is growing. However, the fact that twin boundaries ordinarily have no effect on the growth of pearlite is inconsistent with this view[2]. The controversy regarding the growth of pearlite across austenite twin and grain boundaries is resolved with reference to Smith's hypothesis[11] concerning orientation relationships.

1.1.1 Smith's Hypothesis

Smith[11] suggested that the ferrite component of a pearlite 'unit' formed at a grain boundary would have a definite orientation relationship with one of the grains of austenite,resulting in a semi-coherent interface. As the lattice orientation cannot at the same time be related to the other grain of austenite, an incoherent interface will form on this side. As the mobility of an incoherent interface is high at low degrees of undercooling,

whereas a semi-coherent interface is relatively immobile, growth will occur predominantly by the movement of the incoherent interface. Thus pearlite is nucleated with respect to a given austenite grain to which it bears a precise orientation relationship (the parent grain) but growth occurs into the adjacent grain with which there is no relationship. Hillert[2], emphasising the importance of this incoherent interface, concluded that pearlite can grow within the nucleating austenite grain with any orientation relationship apart from those which lead to coherency. Hillert[2] thus implied that there is no specific orientation relationship between ferrite and cementite. As will be shown later this is not the case.

Smith's hypothesis predicts that when growing pearlite reaches an austenite grain boundary there is only remote possibility that the lattice orientation relationship to this grain allows a degree of coherency to be established. The arrest of pearlite growth at an austenite grain boundary is therefore unlikely. Occasionally a change in lamella direction or disruption of cooperative growth is observed at a grain boundary. This is probably due to the influence of the high energy boundary on the steady state conditions at the pearlite front. This observations may then explain why Jolivet[10] and others[3,7,8] concluded that pearlite colonies were always localized within one grain of austenite.

1.1.1.1 Hypo-eutectoid steels.

Smith's[11] hypothesis may also be used with respect to hypo-eutectoid alloys where separation of ferrite normally precedes the growth of pearlite. Analogous with pearlite growth, a

ferrite nucleus formed at the boundary between two austenite grains will form a semi-coherent interface with the parent grain to which it bears a crystallographic relationship. At low degrees of supersaturation growth will occur by the advance of the incoherent interface into the matrix grain with which no orientation relationship exists (Fig. 1.4(a) and (b). High supersaturation may encourage the propagation of semi-coherent interfaces and result in needle or plate allotriomorphs characteristic of Widmanstätten morphologies[1,2,12] (Fig. 1.4(c)). In certain cases, semi-coherent interfaces can develop on both sides of the boundary (Fig. 1.4(d), even when their orientation deviates appreciably from ideal conditions. In this case, the crystal of ferrite will presumably be highly coherent towards one grain of austenite and yet have some low degree of coherency towards the other[1,2].

Although Hillert[2] indicated the reverse situation to Fig. 1.4(d), where a ferrite crystal at an austenite grain boundary may be incoherent with both grains, such allotriomorphs are not discussed by Aaronson[12] or Chadwick[1]. However, Hillert's[2] observations may be explained as follows.

In the general case many separate nucleation events will occur along any grain boundary, each nucleus being semi-coherent with one grain and incoherent with the other. Incoherency will not occur with the same grain for all nuclei and approximately half the number of nuclei will be incoherent with one grain and half with the other[1,12] (Fig. 1.5). At low degrees of supersaturation, the mobility of the incoherent interfaces will result in a grain boundary filament of ferrite in which the ferrite-austenite interface is totally incoherent (Fig. 1.5). Similarly at high

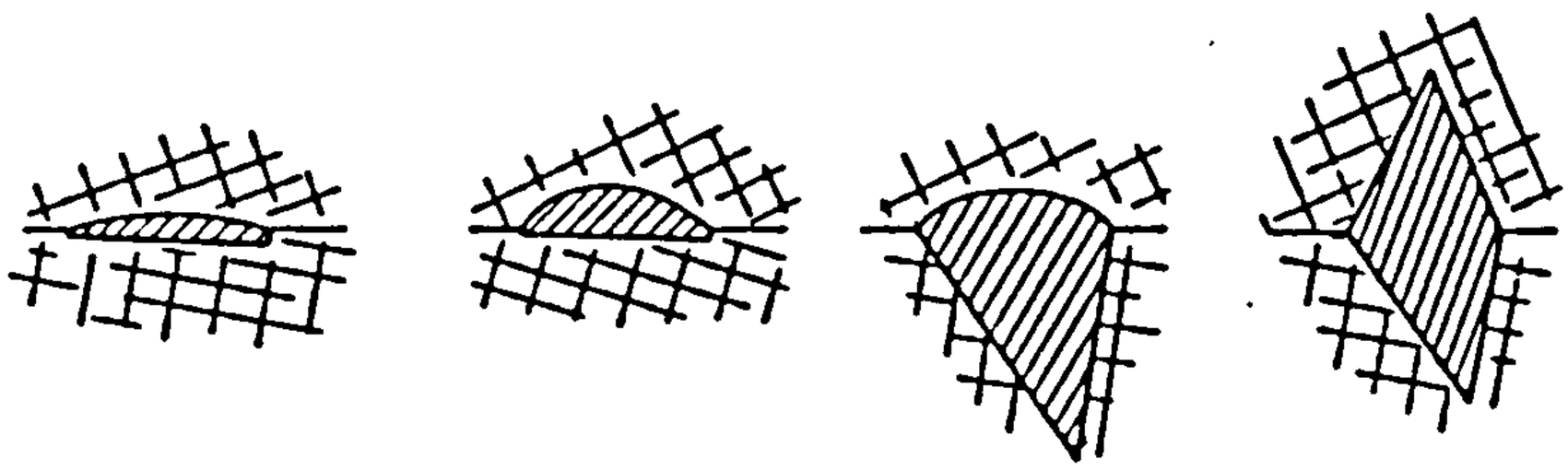

(a) (b) (c) (d)

Nucleation and growth sequence of a precipitate at a grain boundary. (a) the nucleation event generally occurs with the production of one semi-coherent interface and one incoherent interface on opposite sides of the nucleus; (b) growth at low supersaturations favours the propagation of the incoherent interface; (c) growth at high supersaturations leads to the migration of the semi-coherent interface; (d) if certain crystallographic conditions are satisfied, semi-coherent interfaces can develop on both sides of the precipitate

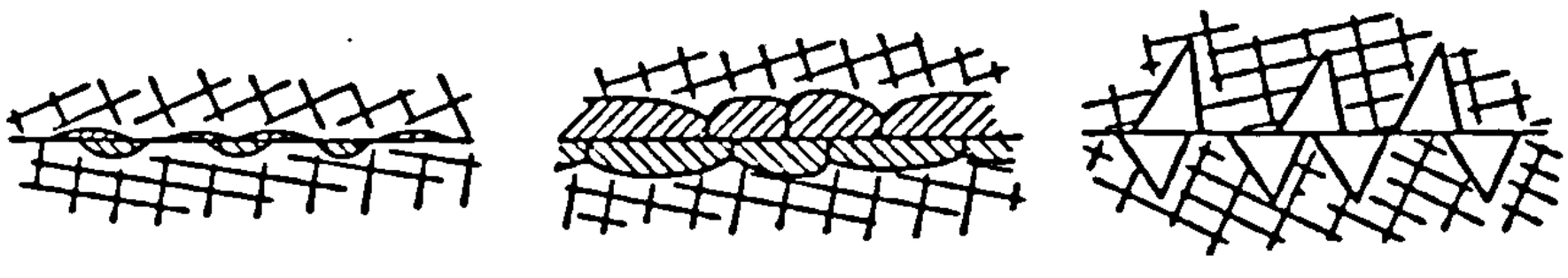

(a) (b) (c)

Nucleation and growth of multiple precipitates at a grain boundary. (a) The semi-coherent and incoherent interfaces of the individual precipitates are arranged randomly along the boundary plane; (b) at low supersaturations the incoherent boundaries overgrow the semi-coherent boundaries, giving rise to a grain boundary network of precipitate; (c) at high supersaturations the semi-coherent interfaces develop

Fig 1.4(top) & 1.5 After Chadwick[1]

supersaturations, the semi-coherent interface may grow and allotriomorphs, as represented by Fig. 1.5(c), will occur. The boundary between allotriomorphs of the type depicted in Fig. 1.5, which have grown in contact with one another, can be difficult to discern by normal optical metallographic techniques. Understandably absorption of ferrite (or cementite[13]) crystals by their neighbours may be apparent from studies of continuous pro-eutectoid grain boundary films. Incoherent growth of two apparently unseparated ferrite crystals into neighbouring grains of austenite may then explain Hillert's[2] observations.

1.2 THE CRYSTALLOGRAPHY OF PEARLITE

Smith's[11] hypothesis has resulted in a number of investigations of the crystallography of pearlite. These studies have determined not only the orientation relationship between ferrite and cementite but also the relationship of each phase with respect to austenite. Such relationships have been studied in some detail by Dippenaar and Honeycombe[4], Ohmori et al[14] and more recently by Samuel[15,16].

Dippenaar and Honeycombe[4] used a 13 wt.%Mn 0.8 wt.%C steel in which retained austenite and pearlite can coexist at room temperature. The authors found two distinct orientation relationships between ferrite (α) and cementite (c) in pearlite colonies. In agreement with earlier studies[17,18,19] these are:

1. The Pitsch-Petch[17,18] relationship where,

$(100)_c$ 2.6° from $[13\bar{1}]_\alpha$

$(010)_c$ 2.6° from $[113]_\alpha$

$(001)_c$ || $(5\bar{2}\bar{1})_\alpha$

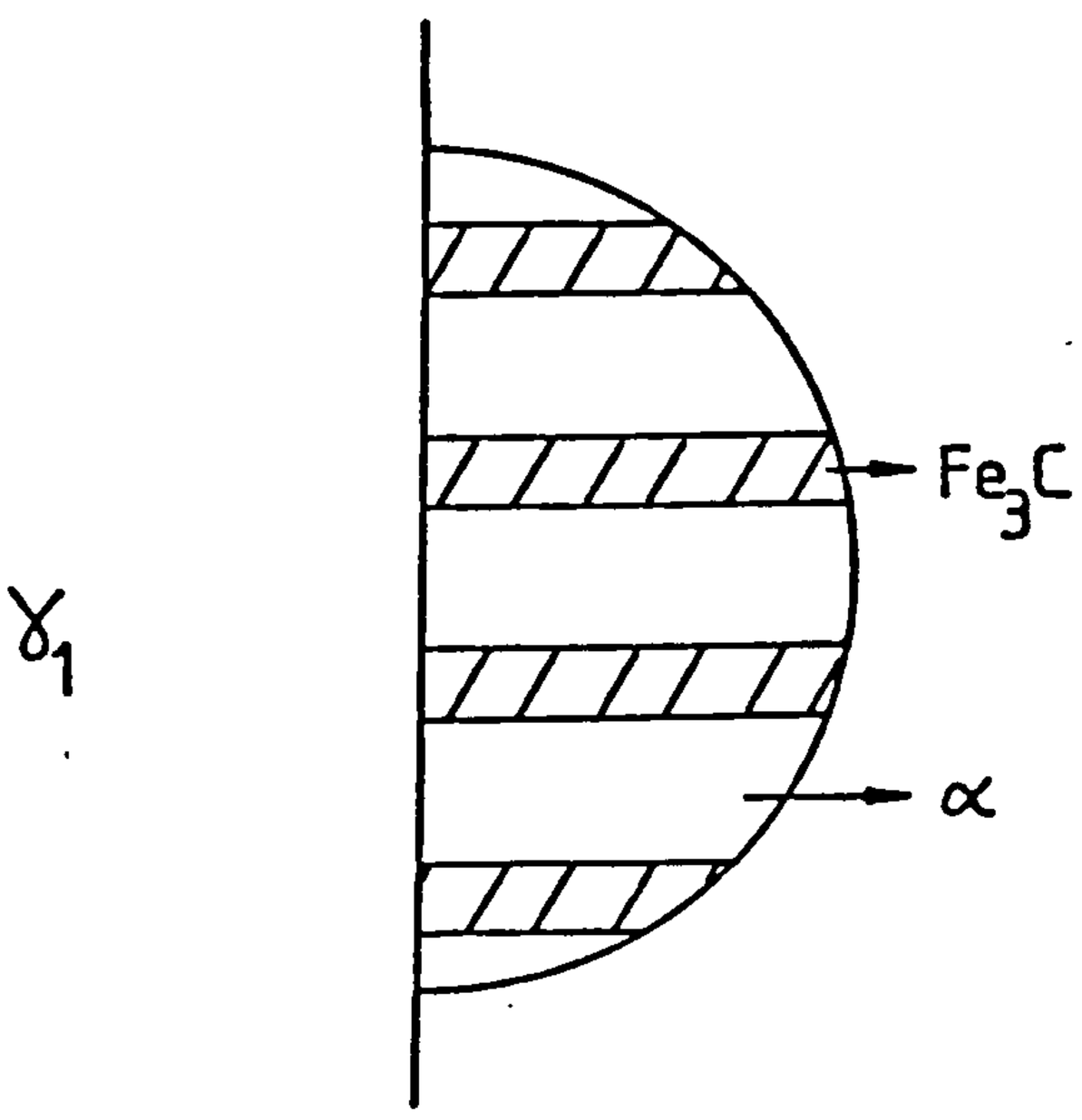

Fig 1.6 Schematic diagram of pearlite formed on an austenite grain boundary and growing hemispherically into one of the austenite grains(γ_2).(After Dippenaar and Honeycombe[4])

and,

2. The Bagaryatski[19] relationship where

$$(100)_c \quad || \quad (0\bar{1}1)_\alpha$$
$$(010)_c \quad || \quad (1\bar{1}\bar{1})_\alpha$$
$$(001)_c \quad || \quad (211)_\alpha$$

Dippenaar and Honeycombe[4] clearly distinguished between two specific crystallographic forms of pearlite in which either one of the above relationships held.

In the case where pearlite grew incoherently from a "clean" pro-eutectoid phase free austenite grain boundary, the ferrite and cementite exhibited the Pitsch-Petch[17,18] relationship. In addition, both the pearlitic cementite and ferrite are related to the adjacent austenite grain γ_1 (Fig. 1.6) into which the colony was not growing, and are unrelated to the grain into which it was growing, i.e. γ_2. The crystallographic orientation of pearlitic ferrite was constant within a given colony and its relationship with γ_1 was close to the classical Kurdjumov-Sachs[20] relationship frequently found between fcc and bcc phases, i.e.

$$\{111\}_\gamma \quad || \quad \{110\}_\alpha$$
$$\langle 110\rangle_\gamma \quad || \quad \langle 111\rangle_\alpha$$

The pearlitic cementite/γ_1 relationship was close to the range of orientations found by Pitsch[17] between austenite and hyper-eutectoid Widmanstätten cementite. The orientation relationship found by Pitsch was within 5^o of:

$$(100)_c \quad || \quad [1\bar{1}1]_\gamma$$
$$(010)_c \quad || \quad [110]_\gamma$$
$$(001)_c \quad || \quad [\bar{1}12]_\gamma$$

These observations are clearly in excellent agreement with Smith's[11] predictions.

On the other hand, the Bagaryatski[19] relationship invariably occurred when pearlite formed from γ_1/γ_2 grain boundaries which exhibited a filament layer of hyper-eutectoid cementite. The pearlitic cementite lamellae were found to be continuous with, and of the same orientation as the grain boundary cementite. The cementite was related to γ_1 by a relationship close to that found by Pitsch[17] for Widmanstätten cementite, as stated above, but was unrelated to γ_2. Surprisingly the orientation of the pearlitic ferrite in this case, although constant within a given colony, was unrelated to both austenite grains γ_1 and γ_2. However, as pointed out by Park[21], such an observation is rather hard to accept in view of the fact that ferrite bears an orientation relationship with cementite which in turn is related to γ_1. In fact Andrews[22] and Samuel[15,16] have shown that the Kurdjumov-Sachs[20] relationship does - hold even in colonies having a Bagaryatski[19] crystallography.

Although not studied by the authors, both the work of Dippenaar and Honeycombe[4] and Samuel[15,16] predict that the Bagaryatski[19] relationship will predominate in pearlite colonies found in the vicinity of pro-eutectoid ferrite. In which case it might be assumed that pro-eutectoid and pearlitic ferrite will be continuous and of the same crystallographic orientation. In support, Hillert[2] and Hultgren and Öhlin[23] have shown that pro-eutectoid and pearlitic ferrite may indeed have the same lattice orientation, provided the pro-eutectoid ferrite is an "active" rather than "informal" nucleus. That is, in cases where pro-eutectoid

ferrite has grown incoherently into a grain of austenite to which it bears no orientation relationship, further growth by the advance of the incoherent interface will result in pearlite in which the ferrite has the same lattice orientation as the pro-eutectoid phase.

1.3 NON-LAMELLAR PEARLITE

The eutectoidal decomposition of austenite does not always result in a lamellar microstructure and the occurrence of non-lamellar pearlite in plain C-Mn[24,25], alloyed pearlitic steels[26,27,28,29] and in non-ferrous systems[1] is well documented. Particularly in steels, the incidence of "degenerate" pearlite appears to be closely related to three factors.

(a) The carbon content of the steel.

(b) The cooling rate or transformation temperature.

(c) The presence of alloying elements especially molybdenum and high manganese contents.

The role of carbon content in the range 0.22 to 0.82 wt.% on the morphology of isothermally transformed pure Fe-C alloys is considered in detail by Cheetham and Ridley[30]. The authors found that the degeneracy of the pearlite increased with decreasing carbon content; with low carbon steels transformed at low temperatures containing discontinuous parallel rows of cementite.

Cheetham and Ridley[30] draw attention to the work of Cooksey et al[31] on lamellar eutectics. Cooksey et al[31] found that a transition from a lamellar to a rod morphology occurred when the volume fraction of the minor phase fell below $\simeq 28\%$, for systems where the interfacial energy was isotropic and at lower

volume fractions for anisotropic systems. As the volume fraction of cementite in a eutectoid steel is ≃12%, the lamellar structure is associated with a marked anisotropy of interfacial energy. In hypo-eutectoid steels, transformed at low temperatures, the suppression of ferrite separation gives rise to dilute pearlite with a lower volume fraction of cementite than a eutectoid alloy. Cheetham and Ridley[30] thus argue that although interfacial energy effects will attempt to stabilize the lamellar structure, the extent to which this can occur will be limited by the volume fraction of cementite, and therefore aligned discontinuous structures result.

The occurrence of non-lamellar cementite in eutectoid steels transformed at low temperatures is considered by Samuel[15,16] and Ohmori et al[14]. These authors postulated that at low temperatures there may be insufficient diffusion of carbon atoms to maintain the continuous formation of the cementite at the austenite-pearlite interface. Employing a similar approach Hillert[2] in an earlier report discussed non-lamellar pearlite from the viewpoint of cooperative growth of ferrite and cementite; regular lamellar pearlite being the result of a high degree of cooperation between the growing phases. If the situation arises where different degrees of coherency are established between the growing pearlite and the matrix austenite, Hillert[2] argues that it may be possible to find the case where the formation of pearlite has not been completely inhibited, but sufficient coherency remains to prevent satisfactory cooperation from developing. Such structures reports Hillert[2], may be regarded as intermediate between pearlite and bainite.

In support of Hillert's prediction, Smith and Fletcher[26] and others[27] have observed disordered "rod like" pearlite structures in molybdenum bearing rail steels and have designated the term transitional pearlite to this non-lamellar microstructure as it more closely resembles pearlite than bainite. Other alloying elements which retard the pearlite transformation include manganese and chromium, and work at British Steel Corporation[32] has observed "transitional pearlite" in rail steels containing chromium.

Very little work appears to have been carried out on the crystallographic relationships in 'degenerate' pearlite. Nevertheless the studies of Samuel[15,16] and Ohmari, Davenport and Honeycombe[4] suggest that the degeneration or spheroidisation of cementite lamellae, as a result of lowering the transformation temperature, has no effect on the lattice relationships. As both the Pitsch[17] and Bagaryatski[19] relationships were observed between ferrite and non-lamellar cementite, Samuel[15,16] concluded that these orientation relationships depend on the nucleation mechanism, with the degeneracy arising from insufficient diffusion of carbon to maintain the growth of cementite lamellae.

1.4 THE RATE OF GROWTH OF PEARLITE

Concurrent with studies of pearlite morphology, much progress has been made in the understanding of pearlite growth kinetics, particularly for isothermal transformations. As comprehensive reviews are already available[33,34] only a brief summary of this work will be given.

The rate of isothermal transformation of pearlite is expressed by the Johnson-Mehl equation[35] in terms of the fraction of product transformed in time t, f(t) where,

$$f(t) = 1 - \exp\left(-\pi/3\ N.G^3.t^4\right) \qquad (1.1)$$

and N and G are respectively the rates of nucleation and growth. Since very high rates of heterogeneous nucleation occur at most temperatures nucleation rates are of little importance in determining the overall reaction rate[9]. G is thus considered as the controlling parameter. The growth rate can be determined from the rate of change of pearlite nodule radius with time[33]. Growth rates in pearlite depend upon the diffusion of carbon to sustain the simultaneous development of both ferrite and cementite. In general the two main diffusion paths considered are;

(a) volume diffusion of carbon ahead of the advancing interface, and

(b) diffusion of carbon along the interface.

1.4.1 Volume Diffusion

Brandt[36] proposed that carbon concentrations will be established in the vicinity of the moving interface, with high carbon concentrations in front of the ferrite and low carbon concentrations in front of the cementite providing the necessary downhill gradient for the diffusion of carbon. These limiting concentrations were obtained by Brandt[36] using the Hultgren[37] extrapolation of equilibrium curves. The difference between these concentrations and the interlamellar spacing defines the concentration gradient. This gradient and the diffusion coefficient together determine how fast carbon is delivered to the growing carbide plate and thus define the rate of growth.

Unfortunately the experimentally determined growth velocities in eutectoid steel by Hull, Colton and Mehl[38], did not agree with the values of Brandt[36] calculated using interlamellar spacing and diffusion coefficient data. However, substantial improvements to the volume diffusion model were made by Zener[39] and Hillert[40].

Zener[39] considered the free energy of the transformation which, he argued, included the driving force for the reaction and the energy required by the creation of ferrite-cementite interfaces. Zener[39] proposed that the system will stabilize at the pearlite spacing for which the growth velocity is a maximum, and both he and Hillert[40] independently arrived at an expression for the growth velocity, V, of the form,

$$V = \frac{D}{a} \frac{A}{S} \left(1 - \frac{S_c}{S}\right) \qquad (1.2)$$

where D is the volume diffusion coefficient for carbon in austenite, a is a geometric factor, A the relative supersaturation and S_c is the theoretical critical interlamellar spacing for which the velocity of the reaction reduced to zero. $(1 - S_c/S)$ is then the fractional reduction in reaction driving force due to the accumulation of surface free energy between lamellar product.

As the pearlite spacing, S, is set by the free energy available in the reaction and more energy is available to be employed in creating ferrite-cementite interfaces at low temperatures of formation, S will decrease with temperature. Thus at the maximum growth rate, when half of the energy of transformation is used up as interfacial energy and the other half as the driving force for the reaction, $S = 2S_c$.

Zener[39] also showed that the pearlite spacing could be related to the undercooling, ΔT through,

$$S = 2 S_c = 4 \frac{\sigma^{\alpha C} T_e}{\Delta H_v \Delta T} \qquad (1.3)$$

where $\sigma^{\alpha C}$ is the surface energy of the ferrite-cementite interface ΔH_v the change in enthalpy between parent and product phases and T_e the eutectoid temperature.

1.4.2 Interfacial Diffusion Model

Quantitative analysis of ferrous and non-ferrous eutectoid reaction rates predicted that the transformation proceeds much too rapidly to satisfy a volume diffusion process[1]. It was therefore concluded[1] that a short circulating path is taken by the diffusing species. The most likely short circuiting path is the interface between the parent and product phase, as envisaged by Turnbull[41] and Cahn[42].

Interfacial diffusion models by Sundquist[43], Shapiro and Kirkaldy[44] and Hillert[40] arrived at similar growth velocity relationships of the form,

$$V = 12K D_B \delta \frac{A}{S^2} \left(1 - \frac{S_c}{S}\right) \qquad (1.4)$$

where K is the boundary segregation coefficient, D_B is the boundary diffusion coefficient and δ is the boundary thickness. The similarity between equations 1.2 and 1.4 is obvious. Since the relative supersaturation, A, is proportional to the undercooling ΔT[39], and, from equation 1.3 ΔT is proportional to 1/S, equations 1.2 and 1.4 may be rearranged to give respectively,

$$VS^2 = K_1 D \qquad (1.5)$$

$$VS^3 = K_2 D_B \qquad (1.6)$$

where K_1 and K_2 are constants.

The applicability of volume and interfacial diffusion models can therefore be checked using pearlite spacing and growth rate measurements, and much work has been published in this area[33, 45-48].

The large number of results for reaction kinetics in eutectoid steels has recently been reviewed by Puls and Kirkaldy[33] and by Marder and Bramfitt[46]. The latter authors have compiled results for both isothermal and continuously cooled Fe-0.8 wt.%C binary eutectoid alloys in the form of a Zener[39], $S/\Delta T$ relationship, as shown in Fig. 1.7. As all the data fitted within a scatter band of slope very close to the Zener[39] theoretical value of -1, for a similar log plot, Marder and Bramfitt[46] concluded that the degree of undercooling determined the interlamellar spacing irrespective of whether the transformation was isothermal or continuous cooling.

Comparison of growth rate data, with interlamellar spacing is given in Fig. 1.8. If D and D_B in equations 1.5 and 1.6 are assumed to be constant, then VS^2 and VS^3 are also constant. As can be seen from Fig. 1.8 these assumptions lead to a remarkable agreement of experimental data with VS^2 = constant, rather than VS^3 = constant. Thus contrary to earlier predictions a volume diffusion rate controlling process would appear to be operative at most reaction temperatures. However, the results of both Puls and Kirkaldy[33] and Marder and Bramfitt[46] inferred that there may be a transition from volume diffusion control at high temperatures to interfacial control at low temperatures.

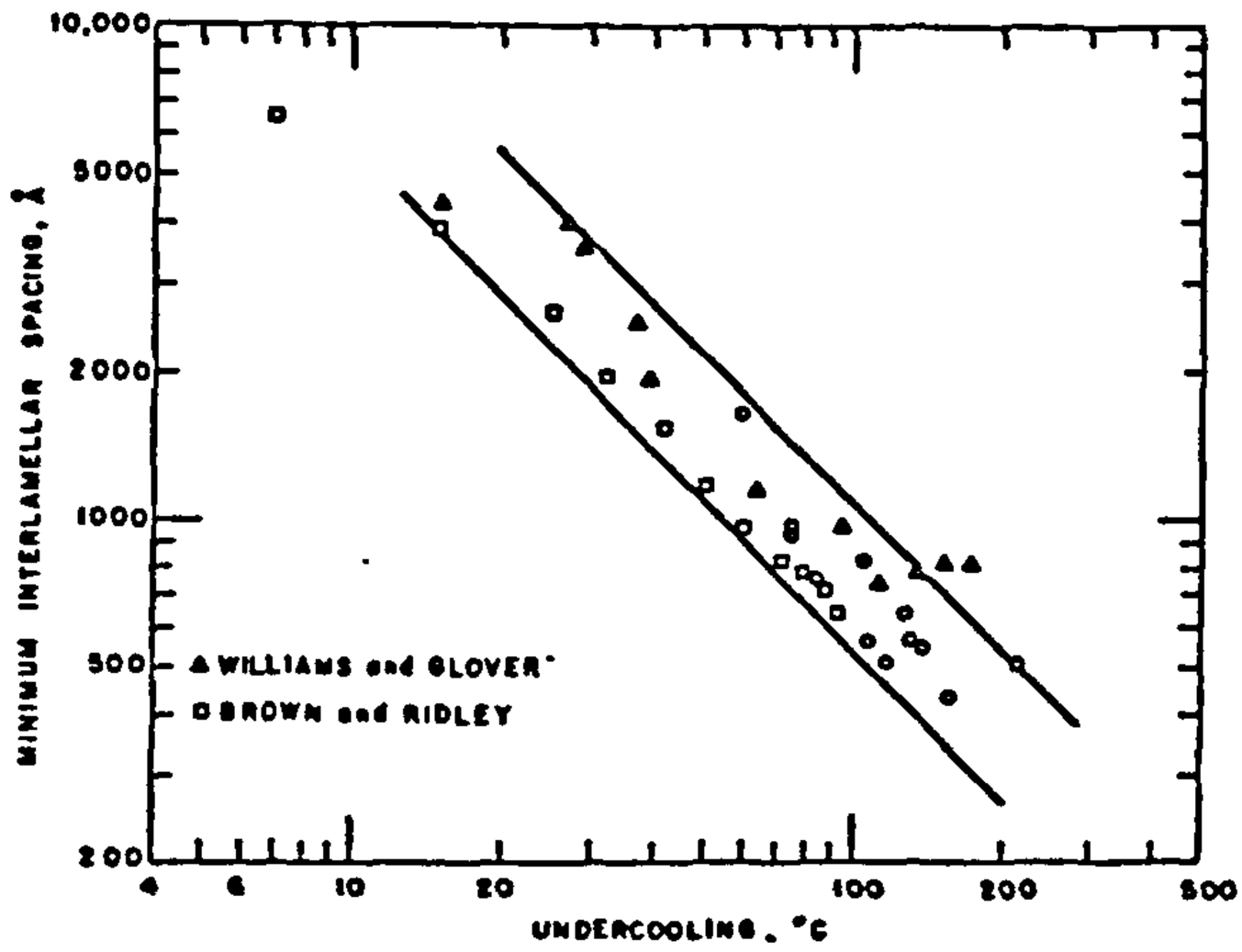

Fig 1.7 The effect of the degree of undercooling on the interlamellar spacing of pearlite in isothermally transformed and continuously cooled eutectoid steels. (After Marder and Bramfitt[46])

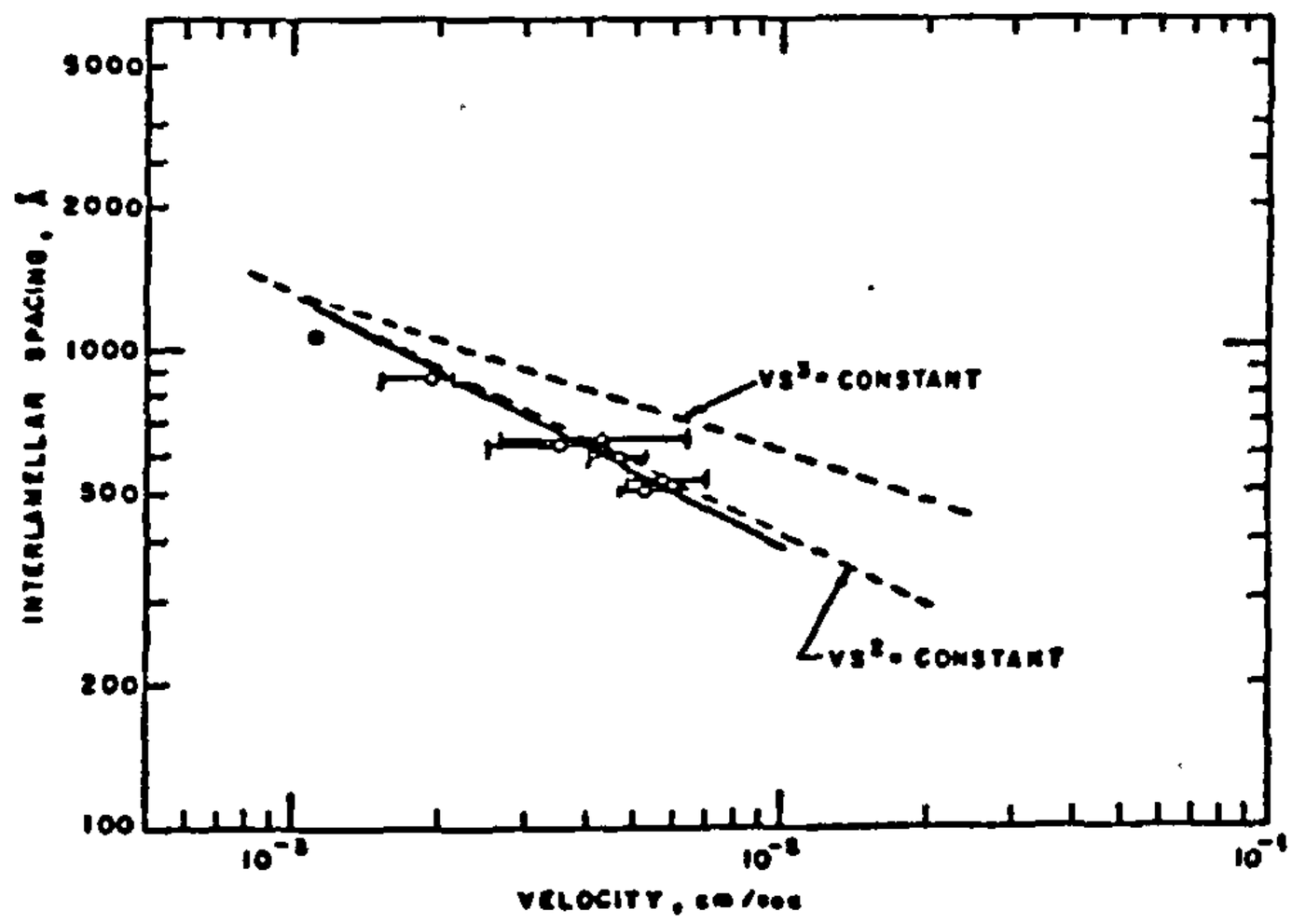

Fig 1.8 The relationship between the growth rate and the interlamellar spacing in a continuously cooled eutectoid steel. (After Marder and Bramfitt[46])

CHAPTER 2

THE YIELD AND FLOW STRESS OF PEARLITIC STEELS

2.1 THE YIELD AND FLOW STRESS OF MILD STEEL

The yield stress of a single phase polycrystal is composed of the yield stress of a constrained single crystal and the strengthening effect of grain boundaries. As the lower yield stress is the stress at which slip can propagate across the gauge length of the specimen, it is reasonable to assume that deformation spreads discontinuously from one grain to the next (Fig.2.1). Physically this means that the concentrated shear stress at the tip of a slip band or dislocation array at the Luder's front in grain A, increases the stress in grain B, until at some critical shear stress, τ_c, at a distance r within grain B, dislocations become unpinned and the grain yields[49].

From dislocation theory[50,51] the shear stress at r is

$$(\tau - \tau_i) \left(\frac{d}{4r}\right)^{\frac{1}{2}} \qquad (2.1)$$

where d, is the length of the slip path which is assumed to be the grain diameter[49], τ is the applied shear stress and τ_i the shear stress opposing the motion of an unlocked dislocation in the slip band.

At the critical value of stress, τ_c, the criterion for yield propagation is therefore:

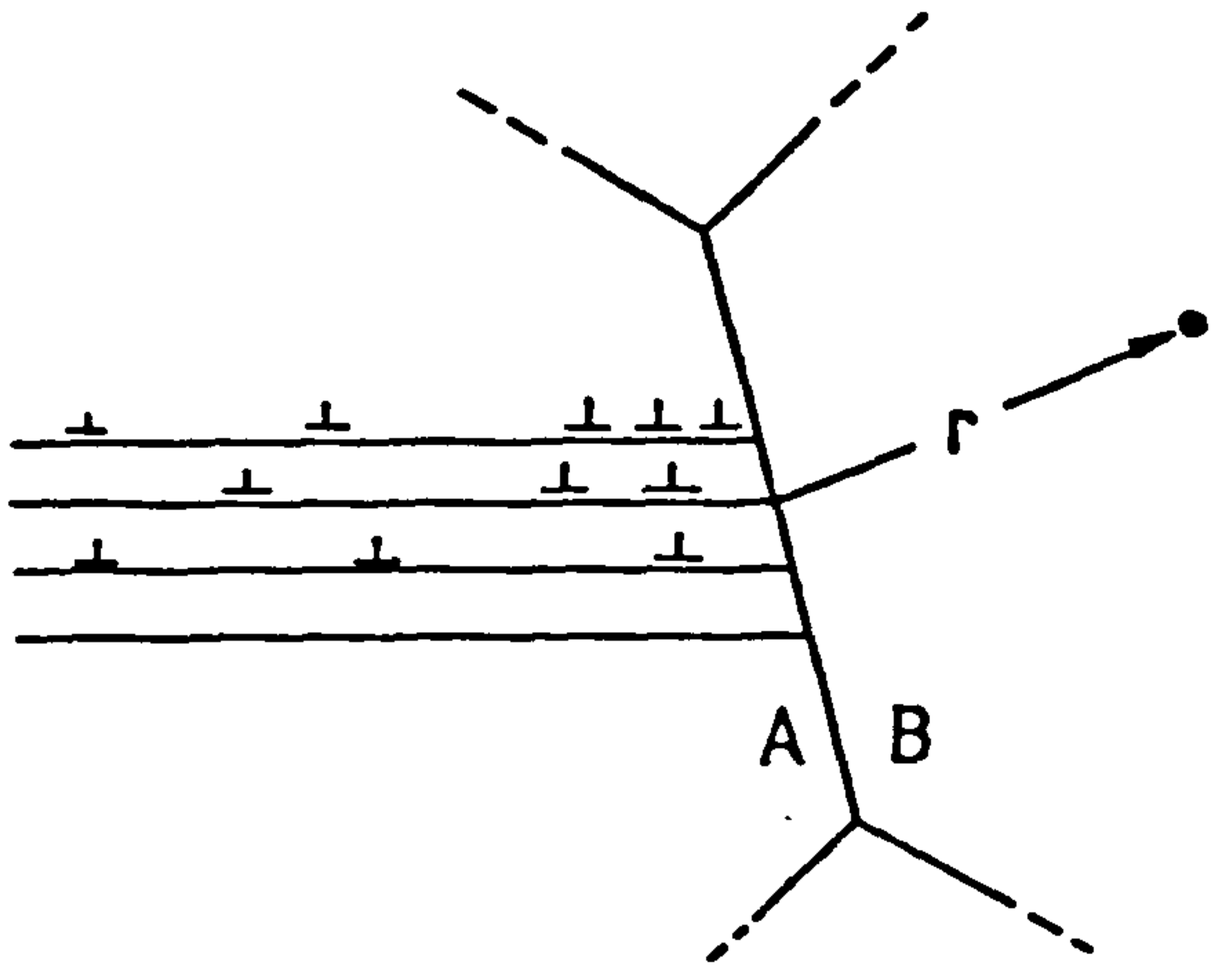

Fig 2.1 Schematic diagram of dislocation pile-ups at a grain boundary.

$$(\tau - \tau_i) \left(\frac{d}{4r}\right)^{\frac{1}{2}} \simeq \tau_c \qquad (2.2)$$

or

$$\tau = \tau_i + 2\tau_c\, r^{\frac{1}{2}}\, d^{-\frac{1}{2}}$$

As all the slip planes and directions are assumed to make an angle of $\simeq 45^o$ with the tensile axis, the lower yield stress $\sigma_L \simeq 2\tau$ and equation 2.2. becomes:

$$\sigma_L = 2\tau_i + 4\tau_c\, r^{\frac{1}{2}}\, d^{-\frac{1}{2}} \qquad (2.3)$$

or

$$\sigma_L = \sigma_o + k_y\, d^{-\frac{1}{2}}$$

σ_o is frequently referred to as the friction stress and is associated with $2\tau_i$. σ_o is therefore a measure of the resistance of the ferrite lattice to the motion of dislocations and as such is affected by factors which cause distortion of the lattice or which will alter the ability of dislocations to glide, e.g. solid solution atoms, precipitates, test temperature and strain rate. Similarly k_y, a constant, approximates to[52] $4\tau_c\, r^{\frac{1}{2}}$. Equation 2.3 was first proposed by Hall[53] and later studied in detail by Petch[54] and fellow workers[55]. It describes the relationship between the lower yield stress and the grain size in polycrystals and is commonly known as the Hall-Petch equation.

As the grain size determines the number of dislocations in a pile-up and hence the stress intensification generated at the grain boundaries, it is clear that yield propagation will occur at lower applied stresses in coarse grain material than in fine. Equation 2.3 therefore explains in a quantitative manner the

previously known advantage of grain refinement raising the lower yield stress in mild steel. From the linear plot of σ_L versus $d^{-\frac{1}{2}}$ both the ordinate intercept, σ_o, and the slope, k_y, may be obtained.

Armstrong et al[55] have extended the above theory to take account of the differing orientation of crystals present in a random polycrystalline aggregate. With reference to the classic work of Taylor[56], the yield criterion of equation 2.1 was shown by Armstrong et al[55] to be given more precisely by,

$$(\tau - \tau_i)\left(\frac{d}{4r}\right)^{\frac{1}{2}} = \frac{m\tau_c}{2} \qquad (2.4)$$

k, in terms of shear stresses, k_s is therefore, $k_s = m\tau_c r^{\frac{1}{2}}$ (2.5)

m, the average Taylor[56] orientation parameter is related to the operative number and relative misorientation of slip planes in the polycrystal. m is obtained from the average m_f for a collection of randomly oriented free crystals, where m_f relates the axial tensile stress σ_s applied to a single crystal to the shear stress τ_s on the most favourably oriented slip planes by $\sigma_s = m_f \tau_s$. The tensile yield stress will then be $m\tau$, the average over the randomly oriented polycrystalline aggregate, i.e.

$$\sigma_L = m\tau_i + m^2\tau_c r^{\frac{1}{2}} d^{-\frac{1}{2}} \qquad (2.6)$$

σ_o and k_y are then associated with $m\tau$ and $m^2\tau_c r^{\frac{1}{2}}$ respectively.

The theory of Armstrong et al[55] does, however, only apply to a randomly oriented polycrystalline aggregate. When there is a preferred orientation the averaging proceedure for m breaks down. Further modification by Wilson and Chapman[57] has therefore

suggested that the tensile yield stress should be expressed in the form:

$$\sigma = m_1 \tau_i + m_1 m_2 \tau_c r^{\frac{1}{2}} d^{-\frac{1}{2}} \qquad (2.7)$$

where m_1 represents the macroscopic effects of slip plane orientation relative to the applied stress axis and m_2 is concerned with the orientation relationship of adjacent grains. m_1 and m_2 will then be different when the polycrystalline aggregate has a preferred orientation but will be the same when the grain orientations are random.

The work of Armstrong et al[55] also investigated the grain size dependence of flow stress at various strain values for common metals and their alloys. They regarded the grain boundary resistance to the formation of a slip band as a general effect and not limited to the lower yield point. In support of this approach their conclusions indicated that, in spite of the development of obstacles within a grain as strain proceeds, the grain boundary resistance to slip remains an important factor in determining the level of flow stress. In addition, dislocation locking continues to determine the limiting grain boundary resistance, even after considerable plastic deformation. This point is illustrated in Fig. 2.2 which shows the relationship between grain diameter and flow stress for mild steel at room temperature.

In general the tensile flow stress, σ_{fl}, at constant strain is related to the grain diameter by a Hall-Petch equation of a similar form to equation 2.3, i.e.

$$\sigma_{fl}(\varepsilon_p) = \sigma_o(\varepsilon_p) + k(\varepsilon_p)\, d^{-\frac{1}{2}} \qquad (2.8)$$

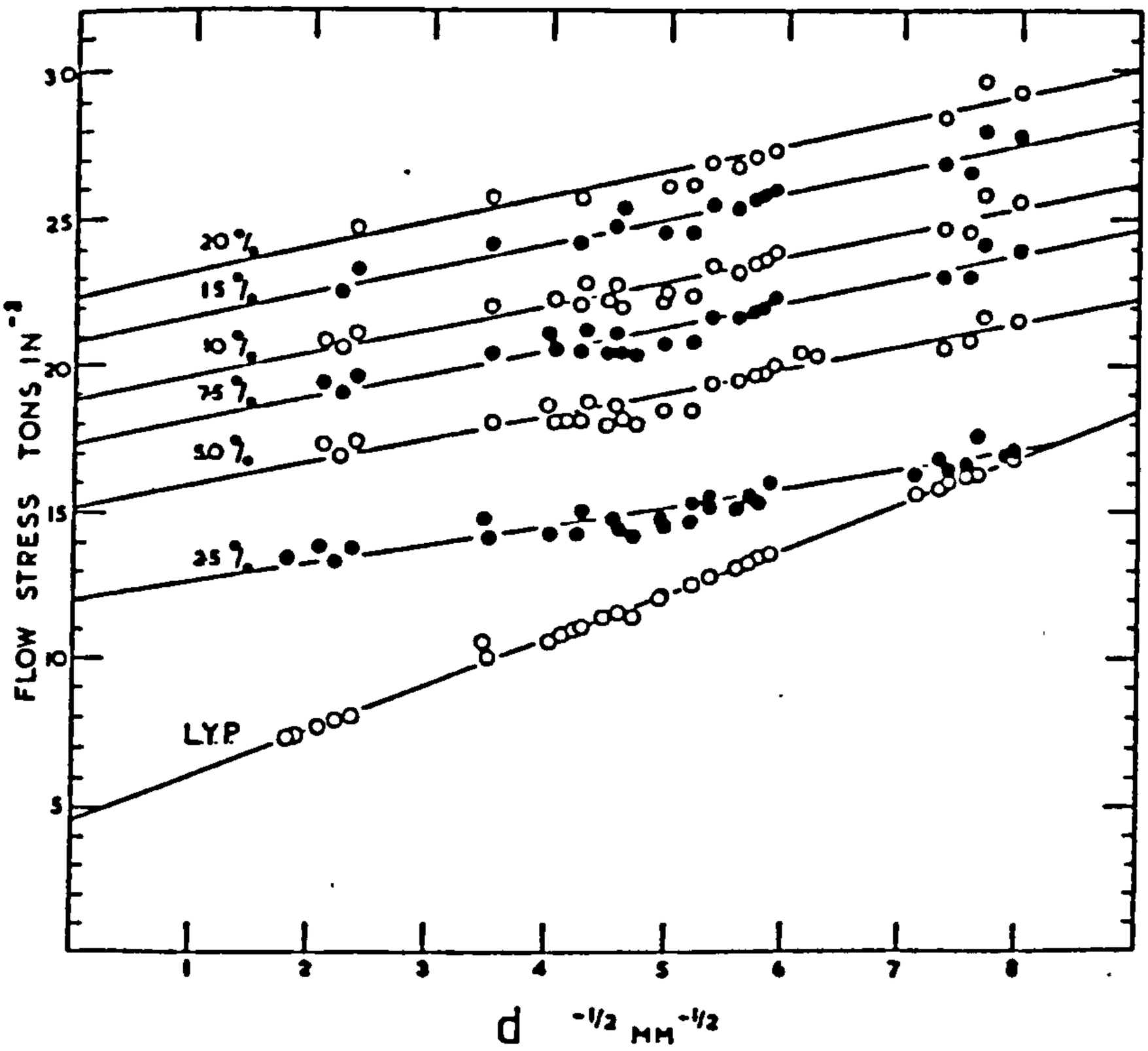

Fig 2.2 The relationship between the grain diameter(d) and the flow stress at constant strain for mild steel at room temperature. (After Armstrong et al [55])

where $\sigma_{fl}(\varepsilon_p)$, $\sigma_o(\varepsilon_p)$ and $k(\varepsilon_p)$ are the flow stress, friction stress and Hall-Petch slope at a plastic strain ε_p.

Although dislocation pile-ups are fundamental to the above theory of yielding there is little or no direct evidence for the existence of such dislocation arrays in bcc metals and steels[58]. In addition, studies on Fe-3 wt.%Si alloys have observed the emission of dislocations from grain boundaries at a stress which is below the yield stress and is independent of grain size[59]. These observations have led to a number of theories which explain the grain size dependence of yield and flow stress but do not require the formation of dislocation pile-ups. Such models have been admirably reviewed elsewhere[58,60,61] and need not be detailed here. However as the work hardening[62] and grain boundary source theories[63] are of some relevance to the present work they will be discussed below.

2.1.1 Non-pile-up models.

2.1.1.1 Work hardening theories:

In the work hardening model of Meakin and Petch[62] and Conrad[64] and Johnson[65] it is assumed that a linear relationship exists between the yield or flow stress and the square root of the average dislocation density ρ, i.e.

$$\sigma = \sigma_o + \alpha\mu b\rho^{\frac{1}{2}} \qquad (2.9)$$

where σ is one half of the tensile yield or flow stress, α is a constant $\simeq 0.4$ (but dependent on the Taylor factor[56] or if forest dislocation density is used instead of an average). μ is the shear modulus and b the dislocation Burgers vector.

If the average distance of slip of a dislocation, $\bar{x}$, is proportional to the grain diameter, d, then,

$$\bar{x} = \beta d \qquad (2.10)$$

where β is a constant. Since the plastic strain, ε is given by,

$$\varepsilon = \rho b \bar{x} \qquad (2.11)$$

the total dislocation density can be calculated by assuming that all the dislocations remain in the system, i.e.

$$\rho = \varepsilon / b\bar{x} = \varepsilon / b\beta d \qquad (2.12)$$

Substituting equation 2.12 into equation 2.9 gives a Hall-Petch equation of the form:

$$\sigma = \sigma_o + \alpha\mu b \, (\varepsilon / b\beta)^{\frac{1}{2}} \, d^{-\frac{1}{2}} \qquad (2.13)$$

Although evidence has been found in support of the work hardening theory[62,64] the requirement of a dislocation density-strain relationship is only valid for certain metallic systems[58]. In addition, this theory has no provision for interpreting the effect of grain boundary structure and so the alternative, though related, grain boundary source theory has gained more favour.

2.1.1.2 Grain boundary source theory

In this theory the grain boundaries themselves are assumed to act as the source of dislocations. Li[63] proposed that the yield stress may be governed by the ability to propagate dislocations from the grain boundary regions. Metallographic evidence of grain boundary ledges led Mott[66] and later Li[63] to postulate that the removal of such ledges would result in the generation of dislocations in the matrix (Fig. 2.3). Assuming a constant ledge density, the number of dislocations generated per unit strain is

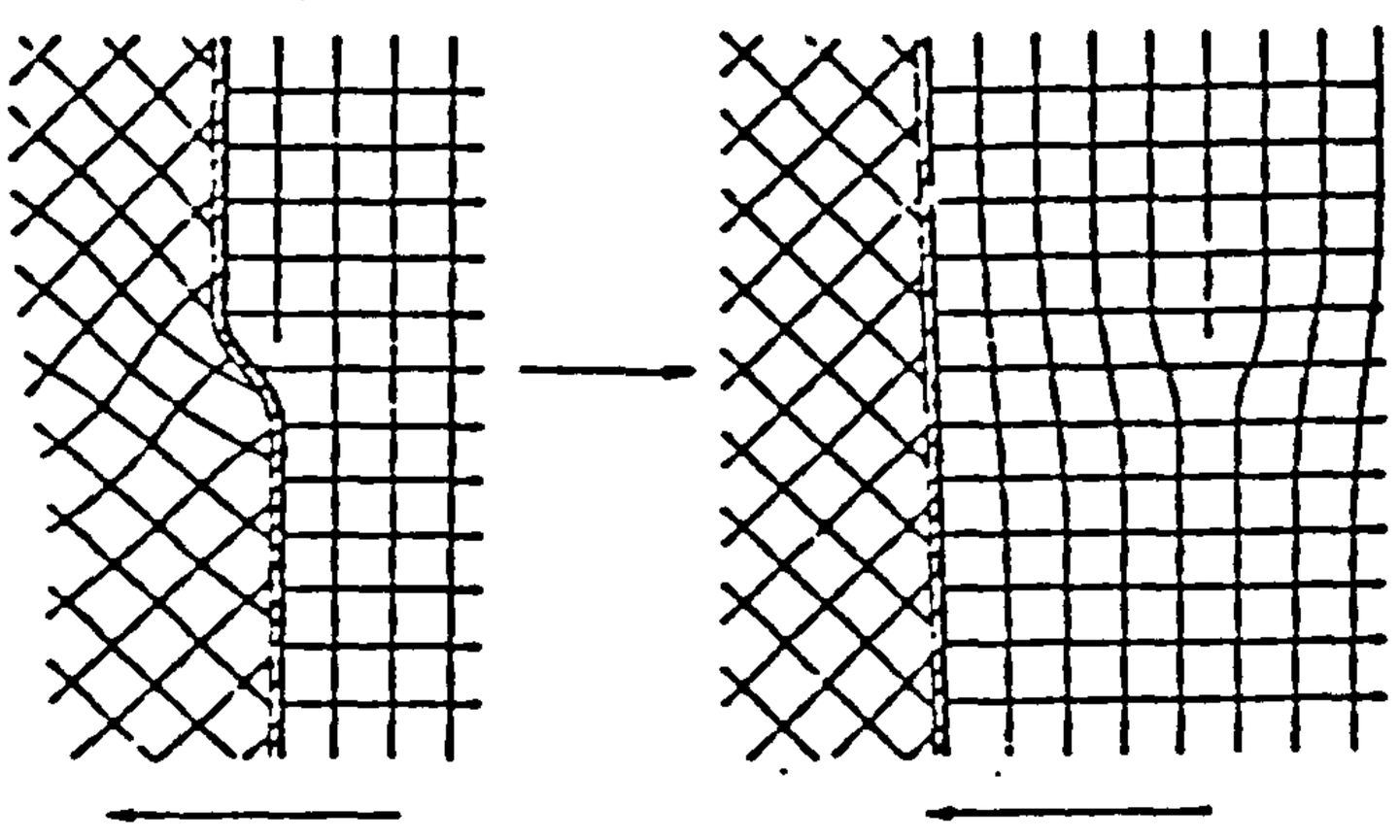

Fig 2.3 Grain boundary acting as a donor of dislocations. (After Li[63])

proportional to the grain boundary surface area per unit volume. It then follows that for small plastic strains ρ is proportional to 1/d. Substitution of 1/d for ρ in equation 2.9 gives a Hall-Petch relationship.

Li[63] also suggested that the ledge density would be critically dependent on the impurity content at the grain boundaries as impurities would stabilise ledges. Thus increasing the impurity content should raise the value of the Hall-Petch slope. This theory has enabled proposed explanations for the apparent influence of, for example, alloying elements and cooling rate on the value of k_y.

Mintz et al[67] have shown in low carbon steels that k_y values decrease with increasing silicon and manganese content. They suggested that such changes arise through the effect solute elements have on interstital segregation to grain boundaries. As both these elements will reduce the concentration of carbon and nitrogen at the boundaries, k_y should decrease with increasing silicon and manganese, as observed. Similarly Wilson[68] has reported the effect of cooling rate on k_y values for low carbon steels. Slow cooling rates were suggested to give rise to higher k_y values as more time is available for carbon segregation to grain boundaries to stabilize ledges.

Finally it should be noted that although the grain boundary source theory makes use of equation 2.9 it does not contain a plastic strain term and therefore cannot be considered as a work hardening theory. In addition,the work hardening theory in fundamental form does not require the existence of a Hall-Petch relationship.

The effect of grain size is indirect. A Hall-Petch relationship will result if ρ is proportional to $1/d$ or if $\rho^{\frac{1}{2}}$ increases linearly with $d^{-\frac{1}{2}}$(64).

2.2 THE YIELD AND FLOW STRESS OF PEARLITIC STEELS

The increase to the hardness and strength of iron as a result of introducing second phase particles is well established. As early as 1942 Gensamer et al[69] related the microstructure with the tensile properties of steels containing different carbide morphologies. The authors illustrated the experimental observation that the yield stress of spheroidite and pearlite showed a linear dependence on the logarithm of the mean free path in ferrite. This prediction was supported later by Roberts et al[70]. Of the dislocation theories which have been proposed to account for this strengthening effect the two most widely accepted models rely on either an Orowan[71] or a modified Hall-Petch[53,54] relationship.

Orowan[71] described dispersion strengthening in terms of dislocation bowing between non-deformable second phase particles. The yield stress is then the stress required to bow the dislocation between the particles to the point where they are re-established on the other side. In general, the flow stress σ_{fl} is given by,

$$\sigma_{fl} = \frac{\alpha\mu b}{\lambda_p} + \sigma_m \qquad (2.14)$$

where α is a constant μ is the shear modulus, b the dislocation Burger's vector, λ_p the interparticle spacing and σ_m the flow stress of the matrix. Although Ashby[72] has modified Orowan's model[71] to take account of the interaction between dislocations

which have bowed and the line energy of the dislocation, the prediction that the yield or flow stress should vary as the inverse of λ_p is retained.

Similarly in a modified Hall-Petch[53,54] analysis the yield stress, σ_{ys}, is a function of the reciprocal of the square root of some defined measure of the interparticle spacing, i.e.

$$\sigma_{ys} = A + B/\lambda_p^{\frac{1}{2}} \qquad (2.15)$$

where A and B are constants.

It should be noted, however, that in this case the particles behave as inpenetrable obstacles to dislocation motion in a manner similar to grain boundaries in iron. Nevertheless, common to both the Orowan[71] dispersion hardening and the Hall-Petch[53,54] models is that particles inhibit yielding by behaving as barriers to dislocation motion. Both equations 2.14 and 2.15 have therefore been applied to spheroidite and pearlite and consequently there is some debate in the literature as to whether an Orowan[71] or a modified Hall-Petch[53,54] strengthening analysis is appropriate for these systems. As more progress has been made in describing the strengthening effect of cementite particles in spheroidite than in pearlite, it will prove helpful to briefly discuss this work before considering in detail the strength of pearlitic steels.

2.2.1 The Yield and Flow Stress of Spheroidite

Following the pioneering work of Gensamer et al[69], Turkalo and Low[73] extended the study of spheroidised carbon steels to finer structures. As Turkalo[74] had previously highlighted the existence of sub-grains between cementite particles, the authors[73] were able to show that a logarithmic relationship did not apply

over a wide range of microstructures unless grain boundaries are also included in the measurement of the mean free path. In 1960, Ansell and Lenel[75] found that the yield stress data of Roberts et al[70] and Turkalo and Low[73] also followed a Hall-Petch[53,54] equation when plotted as a function of the reciprocal square root of the mean free ferrite path. In direct contrast Tyson[76] showed that the same data could be related by an Orowan[71] theory to the reciprocal of the planar interparticles spacing.

More recent studies by Kossowsky and Brown[77], Liu and Gurland[78], Hodgson[79] and Hodgson and Tetelman[80] have supported a Hall-Petch model. These authors demonstrated that both the yield and flow stress of spheroidised carbon steels vary as the reciprocal square root of the dislocation obstacle spacing, providing due care is taken over the definition and determination of this parameter in different microstructures.

Electron microscopy by Turkalo[74] revealed an initial stable dislocation network between particles in tempered medium and high carbon steels which was assumed to have resulted from fabrication or heat treatment. This led Kossowsky and Brown[77] to propose that such networks are partly responsible for the strengthening of spheroidised carbon steels as they reduce the available slip distance in the ferrite. This view is upheld by the later work of Liu and Gurland[78] who, like Hodgson[79], examined a range of microstructures. Liu and Gurland[78] studied spheroidised steels of carbon content between 0.065 and 1.46 wt.% and concluded that a transition occurred from grain boundary

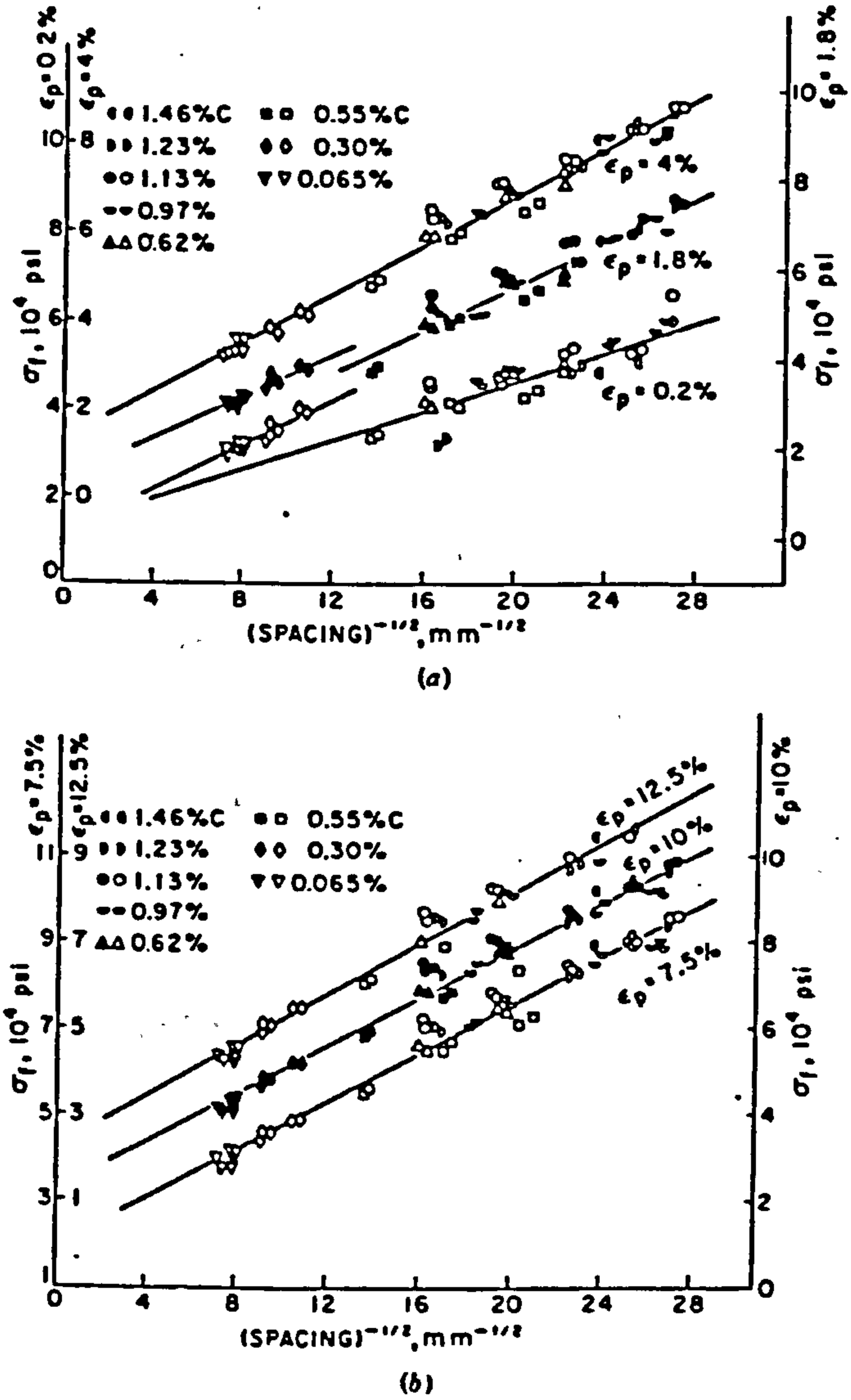

(a)

(b)

True flow stress, σ_f, at constant strain as function of reciprocal of square root of spacing in the structure. The spacing in 0.065 and 0.3 pct C alloys is the mean free ferrite path The spacing in 0.55 to 1.46 pct C alloys is the particle spacing

Fig 2.4 After Liu and Gurland[78].

strengthening in low carbon steels to particle strengthening in medium to high carbon steels. When cementite particles were confined to ferrite grain boundaries(carbon contents <0.3 wt.%) they contributed to grain boundary strengthening. When intra-granular particles predominated (>0.55 wt.%C), these particles promoted and became part of a subgrain dislocation cell structure which acts as a barrier to slip in a manner similar to grain boundaries. Liu and Gurland[78] measured the appropriate obstacle spacing for each microstructure, i.e. grain size in low carbon steels and cell size (interparticle spacing) in high carbon steels. By correcting for cell wall thickness and particle width, Liu and Gurland[78] were then able to show that the flow stress equation of Armstrong et al[55] (equation 2.8) applied for the range of carbon steels studied subject to 0.2 to 12.5% plastic strain (Fig. 2.4).

Evidence in the literature, therefore strongly suggests that the tensile properties of spheroidised steels of different carbon content obey a Hall-Petch relationship when the appropriate microstructural features are measured. As will be seen, relatively little progress has been made in the correlation of microstructure with the flow stress of pearlitic steels over a similar range of carbon contents, despite reports of dislocation cell structures in deformed pearlite[81].

As discussed in Section 1.4, it is now well established that lowering of the austenite to pearlite transformation temperature decreases the interlamellar spacing of pearlite[46,82-86]. In addition, there is evidence[46] to suggest that such a reduction is independent of prior-austenite grain size or transformation mode (isothermal or continuous cooling) and is instead entirely

dependent on the degree of undercooling as predicted by Zener[39]. Decreased interlamellar spacing results in a notable increase in the hardness and strength of pearlite, similar in effect to reduced ferrite grain size in mild steel[53,54] or fine carbide dispersions in spheroidite[78]. Pearlite spacing measurement are thus an integral part of structure-property relationship studies. A wide range of methods are available and many of these are used throughout the literature. Before going on to discuss microstructure strength relationships,it will therefore be of benefit to briefly review these methods and the terminology used with regard to the measurement of the interlamellar spacing of pearlite.

2.2.2 The Interlamellar Spacing of Pearlite

In general what is required in spacing measurements is the true distance, S_t, between the centre of parallel cementite lamellae measured perpendicular to their length and breadth as shown in Fig. 2.5. However,such an evaluation is complicated not only by the apparent variation produced by the metallographic sectioning plane with respect to the orientation of the lamellae, but also by an apparent or real variation within a given pearlite colony as well as between different colonies.

Prior to the application of electron microscopy, pearlite spacing measurements were hindered by the resolution capacity of the optical microscope. As a result Belaiew[5] mistakenly assumed that the true spacing within a sample was constant and apparent variations were due only to a sectioning effect. Furthermore,the author[6] proposed that when this true spacing was below the resolution of the microscope, the resolvable lamellae could be measured and the value related to the true spacing. Greene[87] made similar

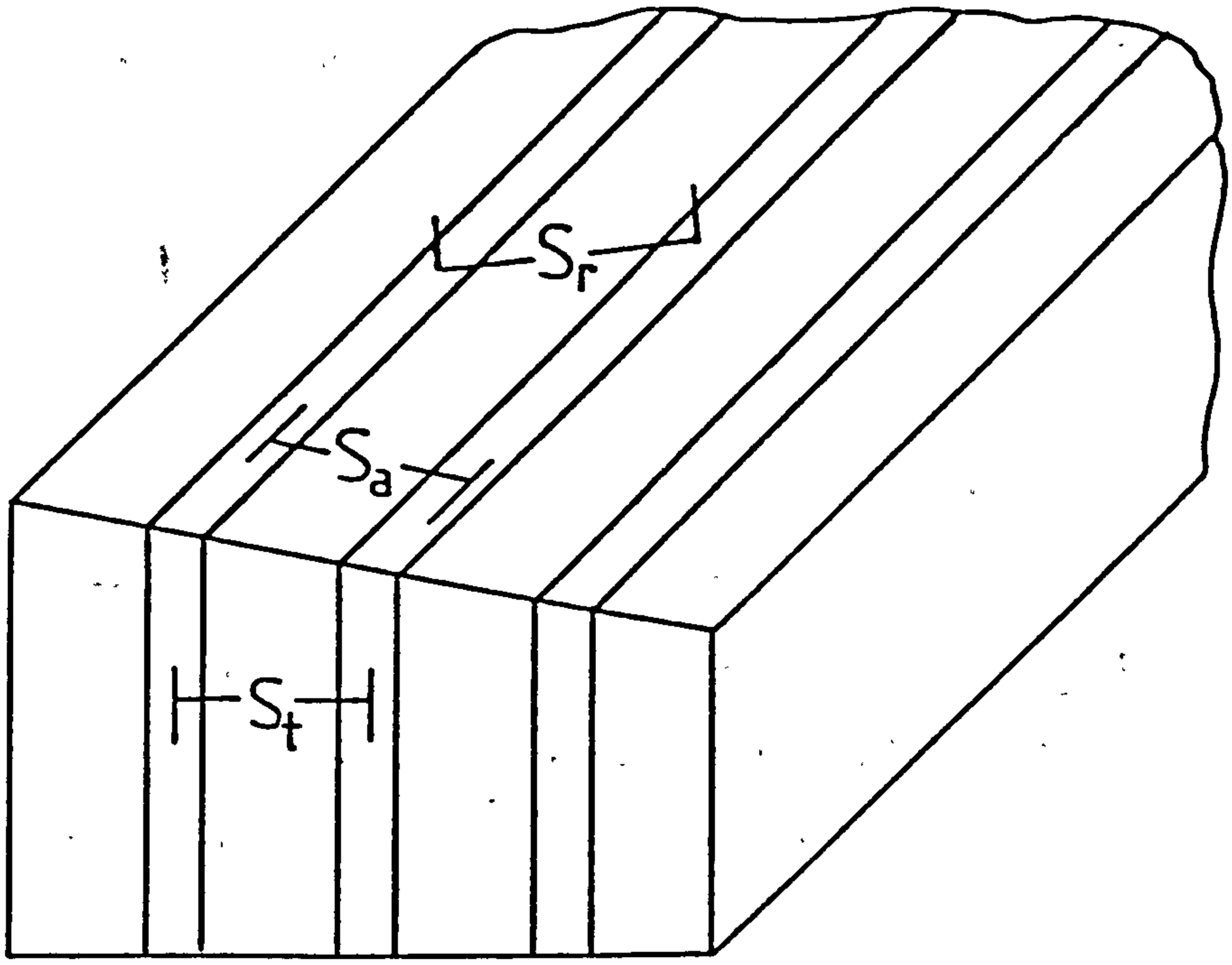

S_t true spacing

S_a apparent spacing

S_r random spacing

Fig 2.5 Classification of pearlite spacing measurements in a geometrically ideal lamellar structure

assumptions and measured the finest colony which he considered to give the true spacing. However the classic work of Pellisier et al[88] has shown that even in the case of isothermally transformed pearlite the interlamellar spacing is not constant but instead exhibits a statistical distribution about a mean true interlamellar spacing $\bar{S}_t$.

Of the available optical microscopy proceedures for measuring pearlite spacing the method of Pearsall[69] is undoubtedly the most popular. Pearsall[69] developed a technique known as the "partial resolution method" whereby the mean spacing, S_o, could be be obtained from the areal fraction of unresolved pearlite F_u, using the expression,

$$S_o = \frac{\Lambda}{2.NA} \sqrt{1 - F_u^2} \qquad (2.16)$$

where Λ is the wavelength of light forming the image and NA the numerical aperture of the optical microscope objective.

The relationship between S_o and $\bar{S}_t$ is not entirely clear in the literature, although many authors[82,89-91] employ the terms "true spacing" to the S_o measurement obtained by the method of Pearsall[69]. Vander Voort and Roosz[92] have recently reviewed spacing measurements in pearlite. Their results support the earlier conclusions of Gregory et al[93] by showing that the partial resolution method only gives an accurate measurement of the mean true spacing for the limited range 50 to 65% unresolved pearlite. With higher amounts of unresolved pearlite the estimate was poor. It would appear then, that S_o is synonymous with $\bar{S}_t$ for measurements only within the above range of unresolved microstructure. Outside these limits the connection between S_o and $\bar{S}_t$ is uncertain.

It should also be noted that equation 2.16 was derived assuming that each pearlite colony consisted of parallel platelets of ferrite and cementite, S_o was constant within each colony and for all colonies and that pearlite colonies were randomly distributed in space. The application of equation 2.16 is therefore only strictly correct for microstructures in which these assumptions are valid. As pointed out recently by Ridley[48], few experimenters would appear to consider these limitations in view of the fact that the method of Pearsall[69] is widely used to measure pearlite spacing over a range of composition and microstructures.

With the application of electron microscopy the resolution limitation of earlier optical techniques disappeared. Probably the most favoured electron metallographic method of pearlite spacings measurement is that due to Brown and Ridley[94] for the determination of the minimum, S_{min}, or average observed minimum spacing, $\bar{S}_{min}$. Using the TEM and conventional replica techniques, the specimen surface is scanned until the finest pearlite colonies are located. By applying a line of known length perpendicular to the finest lamellae, S_{min} may be evaluated. The average of a number of such measurements gives $\bar{S}_{min}$.

Although the minimum spacing is related to the mean true spacing the relationship is not constant[48,92]. Work to determine the connection between the mean true spacing and the minimum observed spacing has produced variable results. The relationship between $\bar{S}_t$ and S_{min} may depend not only on the method employed to determine $\bar{S}_t$[92] but also on the carbon content of the steel[29,88], the alloy system studied[95,96,97] and the transformation conditions[48].

Vander Voort and Roosz[92] regard the method of Brown and Ridley[94] to be dependent on the amount of effort extended in locating the finest spacing and therefore susceptible to error and lack of reproducibility. However, these authors made measurements on continuously cooled specimens where recalescence may influence the distribution of spacings in a given sample[69]. The fact that a very good agreement is obtained for S_{min} measurement by different experimenters[33,46,47,94,98] in isothermally transformed eutectoid steels (see Section 1.4), clearly indicates a need for a detailed study of the relationship between different spacing measurements in both isothermal and 'continuously' cooled specimens over a range of compositions.

Although Puls and Kirkaldy[33] and others[86] regard the method of Brown and Ridley[94] as the most reliable and consistent approach available for determining pearlite spacing alternative electron microscopy methods have been suggested. Recently Underwood[99] proposed measuring $\bar{S}_r$, the mean random spacing, a proceed-ure reported in 1941 by Gensamer et al[69]. In this case $\bar{S}_r$ is obtained from randomly applied test lines traversing a large number of lamellar (Fig. 2.5). For an 'idealised' structure Saltykov (cited in Underwood[99]) has shown that the mean random spacing is related to the mean true spacing by:

$$\bar{S}_r = 2\,\bar{S}_t \qquad (2.17)$$

Experimental verification of equation 2.17 has been reported by Gensamer et al[69] who found the ratio $\bar{S}_r/S_o$ in pearlitic steels to vary between 1.9 and 2.0. Equation 2.17 is, however, approximate and it should be noted that additional terms are required

S_a	Apparent interlamellar spacing	Visual range of pearlite spacing as a result of metallographic sectioning and true specimen variations.
$\bar{S}_r$	Mean random interlamellar spacing	Average of a number of measurements obtained from randomly applied test lines intersecting cementite lamellae at various angles.
S_o	Mean interlamellar spacing	Average pearlite spacing obtained from the method of Pearsall.[69]
S_{min}	Minimum observed interlamellar spacing	Measurement obtained perpendicular to the finest observed lamella spacing. Method of Brown and Ridley.[94]
$\bar{S}_{min}$	Average minimum observed interlamellar spacing	Average of a number of S_{min} determinations
$\bar{S}_t$	Mean true spacing	Average true distance between lamellae. $\simeq \bar{S}_r/2$

Table 2.1 Symbols, definitions and discriptions of the various pearlite spacing measurements used in the literature.

to obtain $\bar{S}_t$ from $\bar{S}_r$ in non-lamellar microstructures[99]. Vander Voort and Roosz[92] measured the mean random spacing using a number of transmission and scanning electron microscopy techniques. Their results showed that consistent and accurate values of $\bar{S}_r$ could be obtained provided measurements were made using unbiased systematic field selection.

For clarity, the definition and symbols for the various spacing measurements are summaried in Table 2.1.

The studies of pearlite growth rates and reaction kinetics in eutectoid steels by Ridley et al[48,98], Puls and Kirkaldy[33], Williams and Glover[100] and Marder and Bramfitt[46,85] were discussed in Section 1.4. In all cases the pearlite spacing was measured by the method of Brown and Ridley[94]. As a result, within this group of investigators, excellent agreement is found between interlamellar spacing and transformation data[46]. In structure-property studies on the other hand, although the method of Brown and Ridley[94] is again popular it is by no means customary. As will be seen similar agreement between pearlite spacing and mechanical properties has therefore not been reported. The methods of measurement employed, and in particular the results obtained, for microstructure-strength studies in pearlitic steels will now be discussed.

2.2.3 The Strength of Fully Pearlitic Steels

As mentioned earlier, the classic work of Gensamer et al[69] related the yield strength of pearlite to the logarithm of the mean free ferrite path. Although the authors attempted to justify this logarithmic correlation in terms of a dislocation theory their reasoning was critisised in the later study of Hugo

and Woodhead[83]. Hugo and Woodhead examined the interdependence of tensile properties and microstructure in three 3% nickel steels. The authors measured the interlamellar spacing of the pearlitic steels by the method of Pearsall[69] and showed, in accordance with the theoretical predictions of Zener[39], that S_o was proportional to the reciprocal of the degree of undercooling ΔT. As this temperature difference can be assessed more accurately than experimental values of S_o, ΔT was used by the authors as the variable to represent S_o for correlating with tensile test data.

As Eshelby, Frank and Nabarro[50] had shown theoretically that the applied stress is inversely proportional to the square root of the slip band length, and Hall[53] had identified this length with the mean grain diameter in mild steel, Hugo and Woodhead[83] considered the strength properties of pearlite to be related to the reciprocal square root of the average distance between cementite lamellae measured in all possible directions. Consequently, the mean free path of Gensamer et al[69] was regarded by the authors[83] to be the product of the measured interlamellar spacing and some constant greater than unity. They therefore suggested a relationship of the form:

$$\text{strength} = a + b\, S_o^{-\frac{1}{2}} \qquad (2.18)$$

where a and b are constants of undefined value.

A linear plot of yield stress against $\Delta T^{\frac{1}{2}}$ confirmed the above expression and thus Hugo and Woodhead[83] clearly provided one of the first arguments for the application of a modified Hall-Petch relationship to the correlation of microstructure with the strength of pearlite.

Later studies by Gladman, McIvor, Pickering and Holmes[82,89,90,91,101] have assigned numerical values to the constants in equation 2.18. These authors[90] reported that both the pearlite colony size and the prior-austenite grain size have no effect on the yield stress of fully pearlitic steels, this property being governed entirely by the interlamellar spacing. As reduced transformation temperatures result in finer pearlite, the authors concluded that increased strength could be achieved by the use of fast cooling rates. The increase in strength as a result of lower isothermal transformation temperature had already been noted by Gensamer et al[69]. By applying a multiple regression analysis to their data, Gladman, McIvor and Pickering[90] arrived at an expression for the strength of pearlite of the form:

$$\sigma_{ys}\ (\pm 48\ \text{Nmm}^{-2}) = 178 + 3.8\ S_o^{-\frac{1}{2}} \qquad (2.19)$$

where S_o is the "true" interlamellar spacing (in mm) obtained by the method of Pearsall[69]. The analogy between the numerical values in equation 2.19 and the Hall-Petch[53,54] parameters σ_o and k is implicit in the work of Gladman and co-authors[89,90,101]. It should be stated, however, that in the study of Hugo and Woodhead[83] the constant b in equation 2.18 is not simply the Petch[54] slope k but also incorporates a multiplying factor for converting S_o to the mean free ferrite distance. It may be noted that such conversions have been neglected in later studies and pearlite spacing measurements are invariably related directly to flow stress values.

The studies of Hyzak and Bernstein[86] and of Marder and Bramfitt[85] also confirmed the effect of low isothermal and low continuous cooling transformation temperatures on increasing

the strength of fully pearlitic steels. However the former authors[86] reported an additional influence of coarse austenite grain size on refining the pearlite and so increasing the strength. Hyzak and Bernstein[86] produced a regression equation in terms of the minimum observed pearlite spacing S_{min}, the pearlite colony size P, and the prior-austenite grain size L_γ, i.e.

$$\sigma_{ys}\ (Nmm^{-2}) = 52.3 - 0.4P^{-\frac{1}{2}} - 2.88\ L_\gamma^{-\frac{1}{2}} + 2.18S_{min}^{-\frac{1}{2}} \qquad (2.20)$$

Similarly Querales and Byrne[102] reported a regression equation, in this case containing terms for L_γ and pearlite spacing only. However, as pointed out recently by Gladman and Pickering[101], it is difficult to understand why colony size or prior austenite grain size should have any influence on σ_{ys} given that they are on a much coarser scale than the pearlite spacing. In fact Hyzak and Bernstein[86] did suggest that the effect of austenite grain size was indirect through its apparent influence on the pearlite spacing. Thus such multi-variable equations should be viewed with some suspicion as they probably result from insufficient isothermal temperature control or because heat treatment variables which influence the pearlite spacing simultaneously change the pearlite colony size.

In support, Marder and Bramfitt[85] found that prior-austenite grain size had no effect on pearlite spacing, which was only dependent on the transformation temperature. Plots of interlamellar spacing against yield stress data gave linear relationships for both $S_{min}^{-\frac{1}{2}}$ and S_{min}^{-1}. However as the correlation of σ_{ys} with $S_{min}^{-\frac{1}{2}}$ resulted in a negative friction stress the strength of pearlite was written as,

$$\sigma_{ys} = \sigma_o + kS_{min}^{-1} \qquad (2.21)$$

Based on similar regression analysis Marder and Bramfitt[85] obtained values for σ_o of 139 Nmm^{-2} and k of 46.4 Nmm^{-1}.

More recent studies have supported the conclusions of the latter authors, and the occurrence of a negative friction stress for yield stress versus $S_{min}^{-\frac{1}{2}}$ correlations is well documented. (Bouse et al[84], Servillano[103], Flugge and Heller[104], 1979 and Sunwoo et al[105]).

It is therefore clear from the literature that pearlite spacing primarily controls the yield strength of fully pearlitic steels, the precise nature of the strengthening albeit rather uncertain. Although Hall-Petch[53,54] relationships are popular, negative friction stress values are obviously contradictory. Tentative suggestions in the literature indicate the alternative possibility of an Orowan[71] dispersion strengthening model applying to fully pearlitic steels, and accordingly further work is needed in this area.

2.2.4 The Strength of Ferrite-Pearlite Steels

Comparatively few studies have considered the problems associated with precisely relating the microstructure to the yield stress of ferrite-pearlite steels. Hugo and Woodhead[83] expanded equation 2.18 to take account of the percentage of pro-eutectoid ferrite, F, where,

$$\text{Strength} = a + b\, S_o^{-\frac{1}{2}} + cF \qquad (2.22)$$

and c is a constant.

Although these authors obtained good agreement between micro - structure and mechanical properties for hypo-eutectoid steels, they only considered various values of F in a purely additive manner and no theoretical argument for equation 2.22 was postulated.

Gladman, McIvor and Pickering[90] examined the strength of ferrite-pearlite steels containing 20 to 100% pearlite. They expressed the composite yield stress, σ_c as a modified law of mixtures,

$$\text{i.e. } \sigma_c = F_\alpha^n \sigma_\alpha + (1 - F_\alpha^n)\sigma_P \qquad (2.23)$$

where F_α is the mass fraction of ferrite, σ_α and σ_P the yield stress of ferrite and pearlite respectively and the index 'n' is a parameter allowing for the non-linear variation of σ_c with pearlite content. A multiple regression analysis gave a least residual error for a value of n = 1/3, and yielded an equation of the form[91]:

$$\sigma_c\ (\pm 48\ \text{Nmm}^{-2}) = F_\alpha^{1/3}\left[53.9+32.3\text{wt.\%Mn}+7.7\text{wt.\%Si}+17.5d_\alpha^{-\frac{1}{2}}\right] + (1-F_\alpha)^{1/3}\left[178.6+63.1\text{wt.\%Si}+3.8S_o^{-\frac{1}{2}}\right] \qquad (2.24)$$

where d_α is the mean linear intercept ferrite grain size and d_α and S_o are in millimetres.

This equation is useful for determining the effect of compositional and microstructural variations on σ_c and is consistent with the observation that the yield (proof) stress of ferrite and pearlite are inversely related to d_α and S_o respectively. In addition it may be noted that equation 2.24 gives rise to equation 2.19 for the case of a fully pearlitic steel (i.e. $F_\alpha = 0$) when the solid solution strengthening effect of silicon is neglected.

However the use of multiple regression analysis is not entirely satisfactory from a theoretical standpoint and more rigorous micro-structural models have been sought.

Karlsson et al[106,107] have applied finite element methods to study the deformation of ferrite-pearlite steels with particular attention being paid to the relative deformation of the individual constituents. Such procedures, however, require a very detailed knowledge of the microstructure and are therefore too complex for immediate use. Although the topological approach of Gurland[108,109] is somewhat simpler, it does require an understanding of phase continuity which is difficult to assess. An alternative approach, due to Reuben and Baker[110], returns to a more fundamental statement of strength in two phase materials. This model is particularly relevant to the present study and is outlined in some detail in Appendix A.

The work of Reuben and Baker[110] considered the deformation of two phase materials in terms of the continuity and grain size of the component materials. Their treatment is based on the original statement of the flow stress in polycrystals by Hall[53] and Petch[54] and the modifications of Armstrong et al[55], Smith and Worthington[52] and Wilson and Chapman[57]. Reuben and Baker considered a ferrite-pearlite composite to compromise a bimodal distribution of grain size in what is effectively a single phase (ferrite) material. They arrived at an expression for the yield stress of the composite, σ_c of the form[110],

$$\sigma_c = \sigma_o + [k_\alpha + (k_p - k_\alpha)(1-V_\alpha)]d_c^{-\frac{1}{2}} \qquad (2.25)$$

d_c is the composite ferrite 'grain size' and is given by:

$$d_c^{-\frac{1}{2}} = (1 - V_\alpha)\, d_\alpha^{-\frac{1}{2}} + V_\alpha\, d_{II}^{-\frac{1}{2}} \qquad (2.26)$$

d_{II} is the average ferrite width in the pearlite and k_P is the Hall-Petch slope for a plot of the proof stress of pearlite against $d_{II}^{-\frac{1}{2}}$. As before σ_o, k_α, V_α and d_α are respectively the friction stress, Hall-Petch slope, volume fraction and grain size for pure ferrite. A full account of the derivation of equations 2.25 and 2.26 can be found in Appendix A. The end points of equation 2.25, at $V_\alpha = 1$ and $V_\alpha = 0$, are obviously of similar form to the end points of the general regression equation of Gladman et al[90,91] (equation 2.24), although the former has been obtained from a more theoretical basis. It may be noted that equation 2.25 predicts that the Hall-Petch slope for a ferrite-pearlite steel will increase as V_α increases. This prediction will be tested in the present study using microstructural and mechanical property data.

2.2.5 The Flow Stress of Pearlite

Although there are abundant reports in the literature on the subject of deformation and fracture of pearlitic steels, very few studies have considered the relationship between microstructure and flow stress. Those studies which have, have dealt specifically with fully pearlitic steels.

As in the case of spheroidised carbon steels, electron microscopy studies of pearlite subjected to large deformations have revealed dislocation sub-grains within the pearlitic ferrite[81,105,111,112]. The work of Embury and Fisher[81] has shown that the flow stress of deformed pearlite is governed by these sub-grains, the size of which is determined by the imposed strain and the

resultant interlamellar spacing. The flow stress was found by the authors[81] to be dependent on the sub-grain size through a modified Hall-Petch[53,54] relationship where the Petch slope increased with strain. Takahashi and Nagumo[112] made a similar study of fully pearlitic steels subjected to smaller strains of up to 7%. The flow stress was shown by these authors to be linearly dependent on the inverse square root of the pearlite spacing, a result supported by the unpublished work of Slater and Pickering (cited in reference 101).

The present study will now attempt to expand on previous results by examining the role of pearlite spacing and ferrite volume fraction on the flow stress of pearlitic steels.

CHAPTER 3

EXPERIMENTAL PROCEDURE

3.1 MATERIAL AND ANALYSIS

The materials used in the present investigation were provided in two forms:

(a) rail section, and

(b) hot-rolled bar.

The rail section was supplied by British Steel Corporation, Teesside Laboratories, following rolling on the Workington Mill and the hot rolled bar was air-melted by B.S.C. Hoyle Street, Sheffield.

The chemical analysis of the rail steel fell within the specification for UIC 860-0 Wear Resisting Quality 'A', and this composition together with the bar compositions are given in Table 3.1

3.2 HEAT TREATMENT

As already mentioned in the introduction one of the main objectives of this study is the investigation of the microstructure-mechanical property relationships in medium to high-carbon steels, with particular reference to rail steels. Because conventional rails are continuously (air) cooled from the last mill pass, it was decided in the present study to limit the heat treatment variations to changes in re-austenitising temperature and cooling rate.

SAMPLE	wt % C	wt % Si	wt % Mn	wt % P	wt % S	wt % Cr	wt % Mo	wt % Cu	wt % Sn
SL174A	0.42	0.19	0.77	0.03	0.016	< 0.02	< 0.02	< 0.05	< 0.005
SL175A	0.59	0.21	0.84	0.038	0.016	< 0.02	< 0.02	< 0.05	< 0.005
Completed Rail	0.74	0.23	0.89	0.023	0.028	< 0.01	-	-	-
SL175B	0.82	0.21	0.82	0.036	0.02	< 0.02	< 0.02	< 0.05	< 0.005

Table 3.1 Compositions of bar and rail steels.

This said however, a heat treatment program was designed with the aim of producing a wide range of microstructures for each of the compositions listed in Table 3.1.

Specimen tensile blanks of 15 and 20mm diameter and 60mm in length were machined from the centre of the rail head or bar material. Each specimen was taken with the long axis parallel to the rolling direction. To obtain an accurate thermal history for a given heat treatment 2mm diameter Chromel-Alumel and Pt-Pt 13%Rh mineral insulated thermocouple probes were embedded in one end of each specimen. The thermocouples were manufactured by BICC Pyrotenax Limited with a tested accuracy ±3/4% above 400°C. A 2mm diameter hole was drilled axially from one end to a depth of 20mm and the thermocouple inserted and secured using furnace cement paste and Nichrome wire wound around the specimen. The thermocouple was connected to a chart recorder, the accuracy of which was checked periodically using a millivolt source.

In all heat-treatments large electrically heated muffle furnaces were used for re-austenitising treatments. The size of the hot zone was determined and found to greatly exceed that required for specimen blanks. Although no controlled atmosphere was used, decarburisation was more than compensated for in tensile blanks and was not considered a problem, even at 1200°C.

Specimens were austenitised at 900, 1000 and 1200°C for 20 minutes at temperature, and three methods were employed to obtain a range of cooling rates from the furnace.

3.2.1 Vermiculite Cooling ($\simeq 0.5^{\circ}C\ S^{-1}$)*

The slowest cooling rates were obtained using the larger diameter specimens. After austenitising, specimens were removed

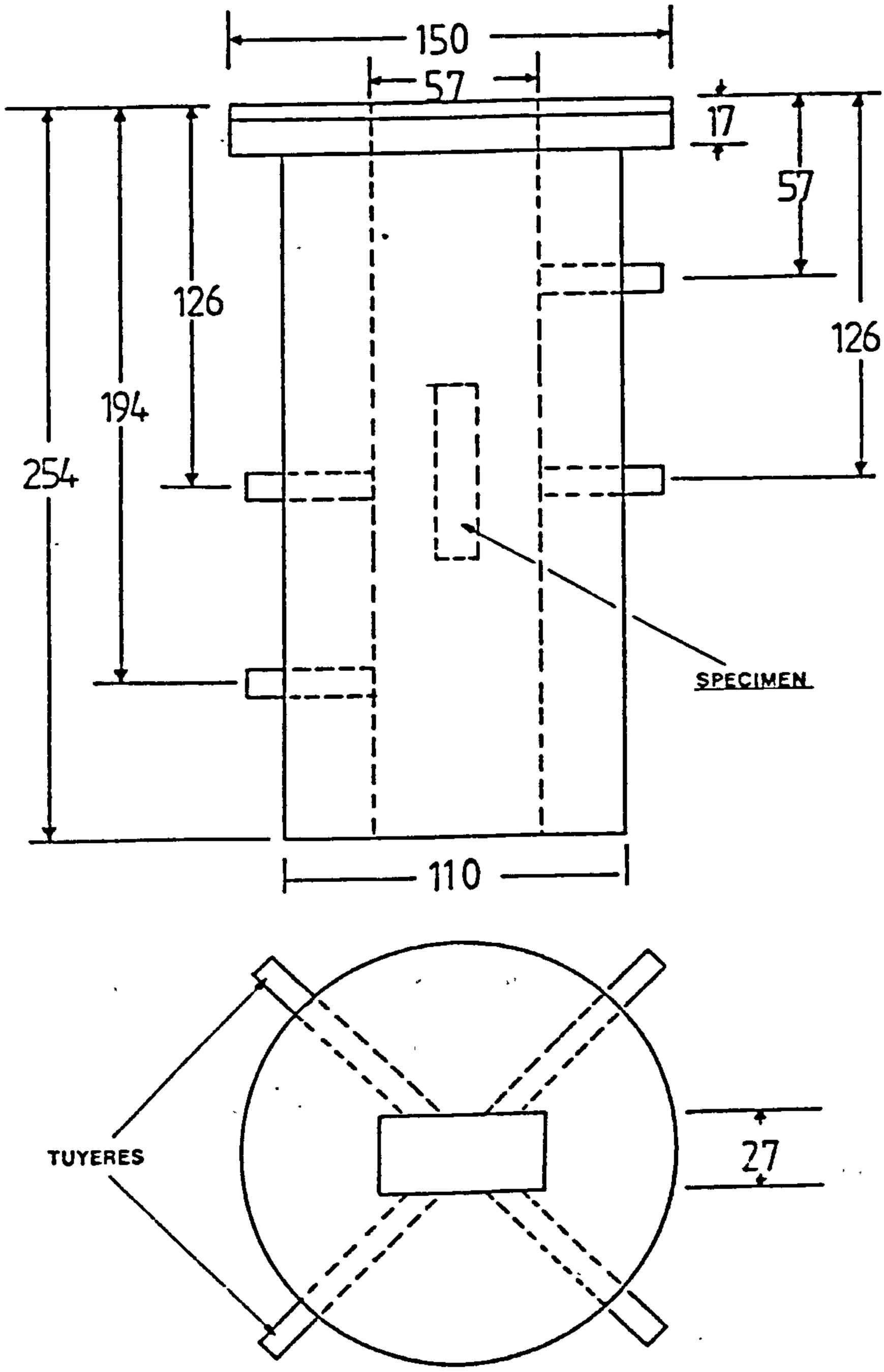

Fig 3.1 Forced gas cooling chamber. (Dimensions in mm)

from the furnace and embedded in a container packed with vermiculite. This heat treatment was performed to simulate the typical cooling rate in rail steel production[113,114].

3.2.2 Air Cooling ($\simeq 3^{o}C\ S^{-1}$)*

One specimen from each austenitising temperature was removed from the furnace and allowed to cool to room temperature in still air.

3.2.3 Accelerated Cooling

Cooling rates in excess of $\simeq 3^{o}C\ S^{-1}$* were obtained using the smaller tensile blanks and a cooling chamber constructed for this purpose at B.S.C. Laboratories. The rig comprised a metal cylinder with a central hollow and tuyeres arranged as shown in Fig. 3.1. Pipes were connected to a compressed air cylinder via a central junction and the chamber was raised on supporting blocks at the base to ensure uniform gas circulation. After austenitising at the required temperature, the air was turned on to a pre-determined pressure, allowed to stabilise and the specimen suspended in the centre of the chamber (Fig. 3.1) using a retort clamp attached to the thermocouple. By the use of an appropriate chart speed, the cooling rate at various gas pressures and the transformation data were recorded.

3.2.3.1 Interrupted Cooling

In addition, one specimen austenitised at $900^{o}C$ and $1200^{o}C$ was cooled rapidly in the chamber until the start of the austenite to pearlite transformation, as indicated on the chart recorder, when it was quickly removed and allowed to transform in the still air. This treatment is referred to as "Interrupted Cooling".

(* pre-transformation cooling rate).

3.2.4 Heat Treatment to Determine the Prior-Austenite Grain Size "Thermal Etching"

Following the approach of Park and Bernstein[115] and similar to that described by Halliday[116], a separate heat treatment was employed to obtain the prior-austenite grain size in fully pearlitic steels. Small specimens of 0.74 and 0.82 wt.%C steels were polished by conventional metallographic methods and sealed in an evacuated quartz capsule. Specimens were then austenitised at 900, 1000 and 1200^{o}C for 15 to 20 minutes followed by furnace cooling to room temperature. The prior-austenite grain boundaries were then clearly visible on the polished surface under the optical microscope.

3.3 MECHANICAL TESTING

3.3.1 Hardness Testing

Although this section is detailed prior to Section 3.4 hardness testing was normally carried out after final metallographic examination. This ensured that hardness tests were conducted on material of which an accurate heat-treatment and metallographic record had been taken. Using a Vickers testing machine and a 30 kg load, hardness was measured from ten suitably spaced indentations traversing the specimen surface. The mean and standard deviation were recorded for each specimen. Care was taken to check the accuracy of readings on a standard test plate prior to testing and to avoid decarburised edges during testing. The latter consideration was aided considerably by the fact that most specimens were in the polished and etched condition.

3.3.2 Tensile Testing

Standard Hounsfield No.12 specimens (approx. gauge length 16mm) were machined from the centre of heat-treated blanks. The average diameter of each specimen was measured to the nearest 0.01mm using a micrometer gauge. Specimens were then tested to failure on an Instron machine at a constant cross-head speed of 0.05cm min^{-1}. Load-displacement graphs were measured to obtain the percentage elongation, the stress corresponding to 0.2 (0.2% proof stress), 2 and 5% plastic strain. As these stresses correspond to deformation at or before the UTS the engineering strain was assumed to be approx. equal to the true strain. In only three cases was a slight yield point detected and this was recorded. Finally, the reduction in cross sectional area was gauges from broken test pieces using a standard tensometer instrument. To avoid non uniform cooling along the length of the specimen, a size restriction (i.e. 60mm long) was placed on tensile blanks for cooling chamber experiments. As a result, only one tensile test could be conducted on specimens which had undergone forced air cooling. In all other cases the average of two tests was taken.

3.4 METALLOGRAPHIC EXAMINATION

To ensure microstructural measurements were conducted on specimens for which an accurate temperature record existed, metallographic specimens were cut from one end of the bar to a depth of approximately 25mm (i.e. close to the prior position of the end of the thermocouple probe). Specimens were polished and then etched in 2% Nital, and a number of metallographic parameters were measured, depending on composition and heat treatment. Although random field selection was ensured for most metallographic measurements, some care was taken to conduct measurements within a close proximity of the specimen centre where tensile test specimens would be taken.

This avoided the complication of any effect on metallographic parameters of more rapid surface cooling rates, particularly in forced air cooled specimens.

3.4.1 Optical Metallography

The following parameters were measured using optical microscopy.

3.4.1.1 Ferrite Volume Fraction (V_α)

The volume fraction of pro-eutectoid ferrite was obtained by systematic two dimensional point counting on a Zeiss Ultraphot II projection microscope using a rectangular grid. 20 fields were taken for each specimen amounting to approximately 2000 counts. Care was taken to select an appropriate magnification to ensure that no two points fell within the same phase area. The relative error in point counting is then given by[117],

$$\frac{S.D.}{V_\alpha} = \left| \frac{1}{P_\alpha} (1 - V_\alpha) \right|^{\frac{1}{2}} \qquad (3.1)$$

where S.D. is the standard deviation of the determination, V_α is the volume fraction of the phase being counted (ferrite) and P_α is the total number of intersections on the grid falling in the phase of interest. In most cases this gave a relative error of ≃±5%. However, in near fully pearlitic microstructures, where fewer counts are taken per field of view the relative error is ≃±10%.

3.4.1.2 Grain Size Measurements

Prior-austenite grain size ($\bar{L}_\gamma$): In specimens of hypo-eutectoid composition , the grain boundary network of pro-eutectoid ferrite allowed the relatively simple determination of the prior-austenite grain size by a linear intercept technique. In fully

pearlitic microstructures, measurements were made on thermally-etched specimens and compared with values obtained from decarburised edges. In all cases a minimum of 500 grains were counted per specimen. The 95% confidence limits in grain size determination is then given by[117],

$$95\% \text{ Confidence limits} = \pm \frac{140}{n^{\frac{1}{2}}} \qquad (3.2)$$

where n, is the number of grains counted. Values were therefore accurate to ±6%.

Ferrite grain size (d_α): In some specimens having a large volume fraction of ferrite, pro-eutectoid ferrite was not confined to the prior-austenite grain boundaries and the ferrite grain size, d_α, was obtained from[117],

$$d_\alpha = \frac{LV_\alpha}{N_\alpha} \qquad (3.3)$$

where V_α is the volume fraction of ferrite and N_α is the number of ferrite grains in a total traverse line of length L. If the error in evaluating d_α is assumed to be the sum of the error in measuring V_α and that arising from the number of intercepts counted, then the 95% confidence limit in the determination of d_α is ≈±16%.

3.4.2 Scanning Electron Microscopy

A Philips PSEM 500 scanning electron microscope was used to measure the pearlite interlamellar spacing from polished and etched specimens. The minimum observed, S_{min}, average minimum interlamellar spacing $\bar{S}_{min}$ and the mean random intercementite spacing, $\bar{S}_r$, were measured within the pearlite.

S_{min} values were obtained by a method similar to that used

by Brown and Ridley[94] whereby a thorough examination of the specimen was made to locate pearlite colonies of minimum lamellae spacing . Using the adjustable horizontal line generated on the SEM screen together with the scanned image rotation and tilt correction features, such areas could be traversed perpendicular to the lamellae by a test line of known length. This was performed at a suitable magnification to give complete resolution. The number of cementite lamellae intercepts was counted along the test line and the maximum number of lamellae counted from 20 separate fields was used to calculate S_{min} from,

$$S_{min} = \frac{L}{n} \times \frac{1}{M} \qquad (3.4)$$

where n is the total number of cementite lamellae counted and M is the magnification. The average of the 20 S_{min} determinations gave the value of $\bar{S}_{min}$. Care was taken in hypo-eutectoid steels to avoid areas near the pro-eutectoid ferrite, where carbon concentration gradients can influence spacing measurements[94].

The mean intercementite spacing, $\bar{S}_r$, was measured in the pearlite by a random linear intercept technique. Forty randomly selected fields were measured at magnifications between X1250 and X20,000 resulting on average in approximately 1200 intercepts per specimen. In contrast to the S_{min} measurements, no selection of fields was made and cementite lamellae were traversed at randomly occurring angles. In addition, no attempt was made to avoid regions on non-lamellar pearlite of areas close to pro-eutectoid ferrite. To assess the accuracy of pearlite spacing measurements it was assumed that the errors involved were similar to those incurred in grain size determination. The statistical significance of

measured values was then obtained from the number of intercepts using equation 3.2. The values of S_{min}, $\bar{S}_{min}$ and $\bar{S}_r$ are therefore expressed with 95% confidence limits of $\simeq\pm20\%$, $\pm5\%$ and $\pm4\%$ respectively.

CHAPTER 4

RESULTS

Heat treatment and transformation data together with corresponding microstructural measurements and mechanical test results are recorded in Tables 4.1 to 4.8. These tables can be found at the end of Chapter 5.

4.1 COOLING CURVES AND TRANSFORMATION DATA

As expected, cooling curves were characterised by recalescence and temperature increases during transformation of up to 40°C were recorded. Consequently the cooling rates given in Tables 4.1, 4.3, 4.5 and 4.7 are those for the temperature range 850°C to 670°C, prior to transformation.

Gensamer et al[69] have shown that during recalescence the austenite progressively transforms to pearlite. It is clear, therefore, that under more "continuous" cooling conditions the transformation temperature is variable. As it is then inappropriate to assign a single transformation temperature to reactions showing recalescence both the minimum (T_{min}) and maximum (T_{max}) transformation temperatures were recorded (see Fig. 4.1). These temperatures are given in Tables 4.1, 4.3, 4.5 and 4.7.

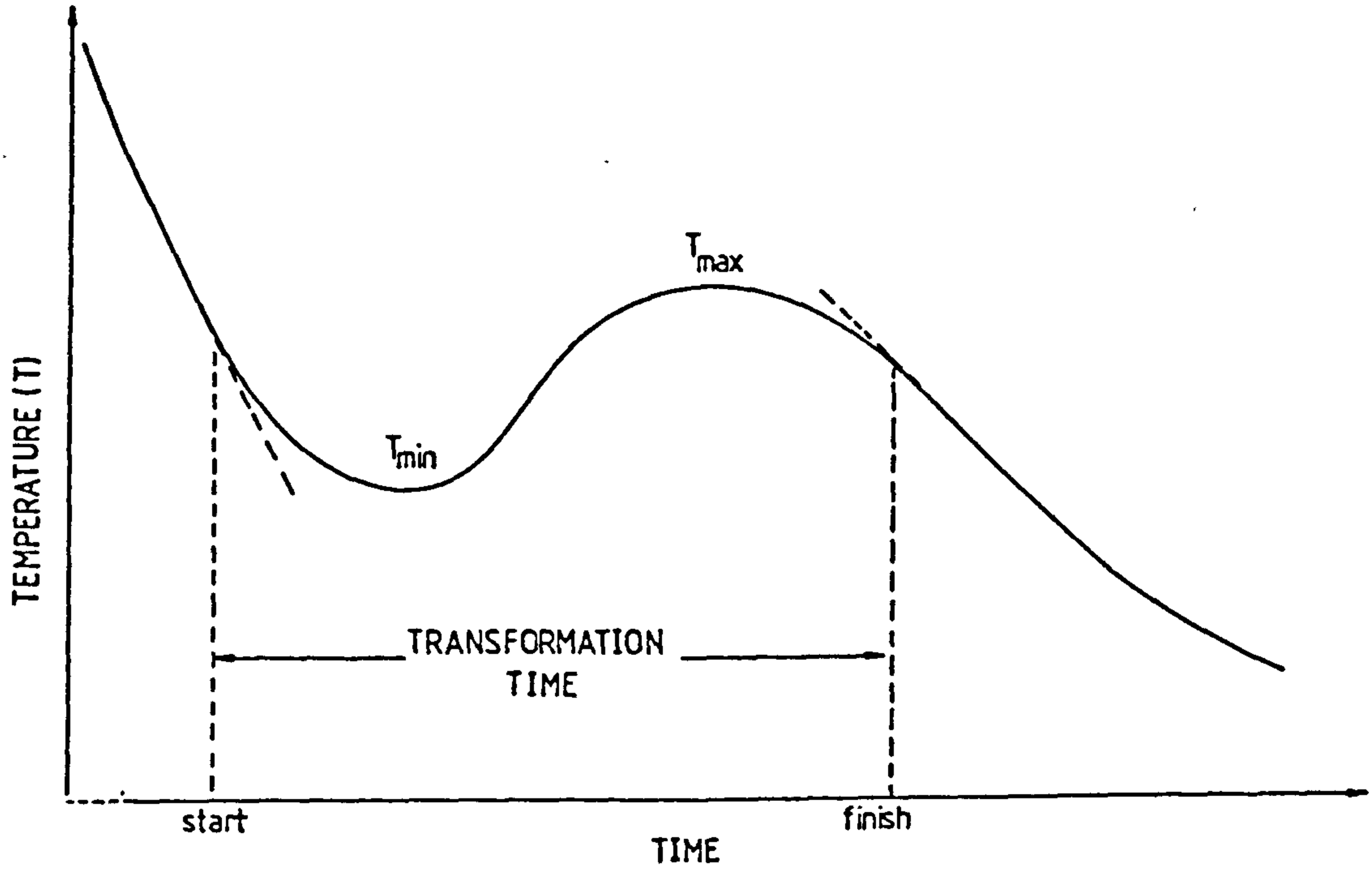

Fig 4.1 Schematic diagram of a typical cooling curve in a high-carbon pearlitic steel showing recalescence.

The occurrence of recalescence also permits the transformation time to be measured, as shown in Fig. 4.1. By assuming that the cooling curve is linear before and after recalescence tangents can be drawn as indicated, and the time taken for the transformation to go to completion measured. These times for all heat treated specimens are given in Tables 4.1, 4.3, 4.5 and 4.7.

In all cases, except possibly specimens cooled slowly at $0.5^{o}C^{-1}$, high austenitising temperatures resulted in lower transformation temperatures for a given cooling rate, with samples cooled from $1200^{o}C$ transforming (both T_{min} and T_{max}) approximately 15 to $20^{o}C$ lower than those cooled from $900^{o}C$. Such an effect is to be expected due to the influence of prior-austenite grain size on the nucleation of pearlite.

In general, faster chamber cooling rates resulted in lower transformation temperatures and shorter transformation times as would be expected. In specimens which had been cooled rapidly until the start of transformation and then removed from the cooling chamber (interrupted cooling) the transformation times were 5 seconds longer than those for equivalent rates of continuous chamber cooling. (c.f. specimens 4A9 - 4A13, 5A1 - 5A6 and R8 - R13).

4.2 MICROSTRUCTURE

4.2.1 General Observations

The typical ferrite-pearlite and fully pearlitic microstructures of air cooled specimens of 0.42, 0.59 and 0.82 wt.%C steels are shown in the optical micrographs in Fig. 4.2 to 4.4. In agreement with a number of similar studies[82,84,90], the volume fraction of pearlite increased with increasing carbon content for a

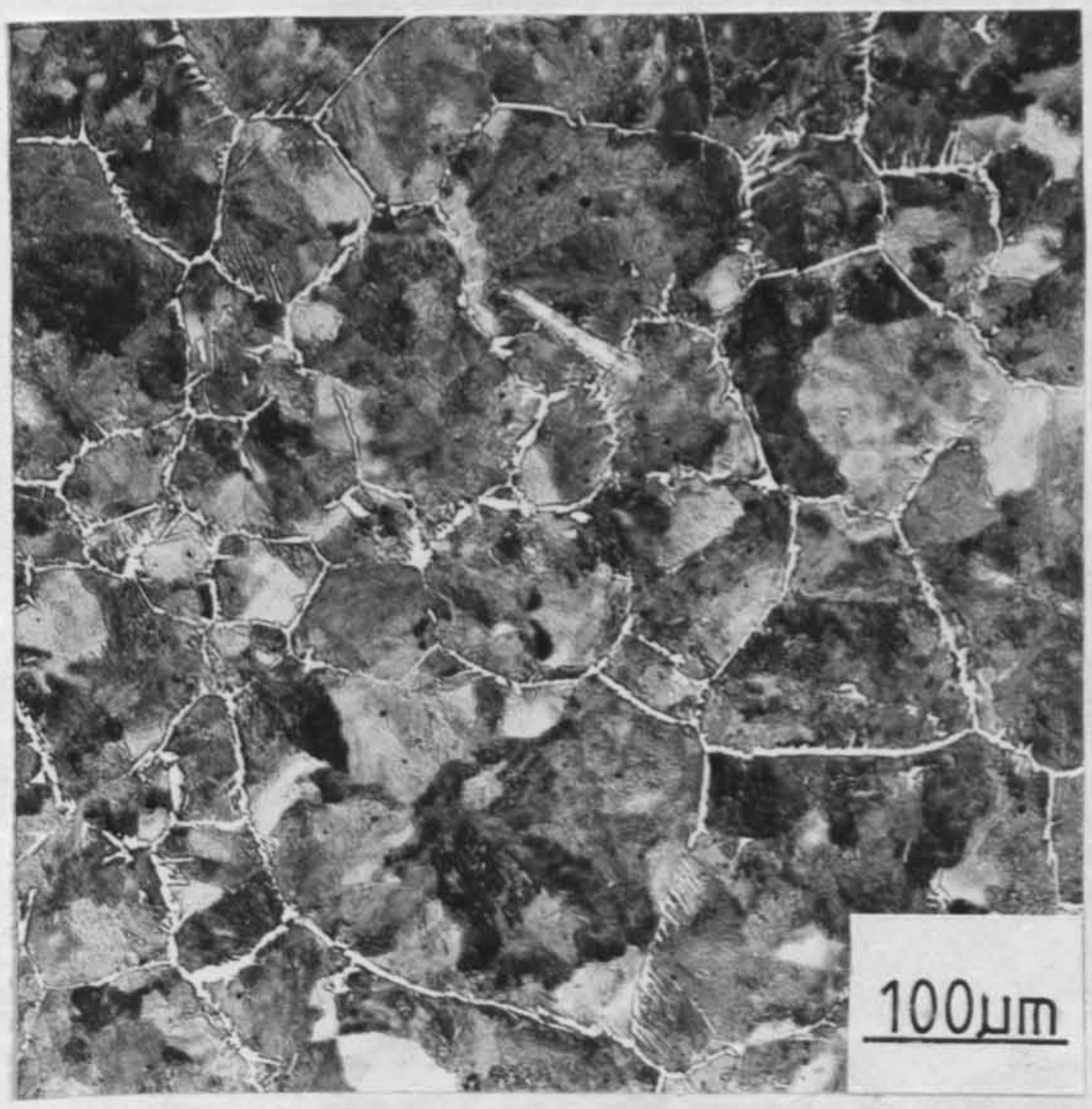

Fig 4.2 Optical micrograph of a 0.42wt%C steel air cooled from 1200°C.(Specimen 4A11)

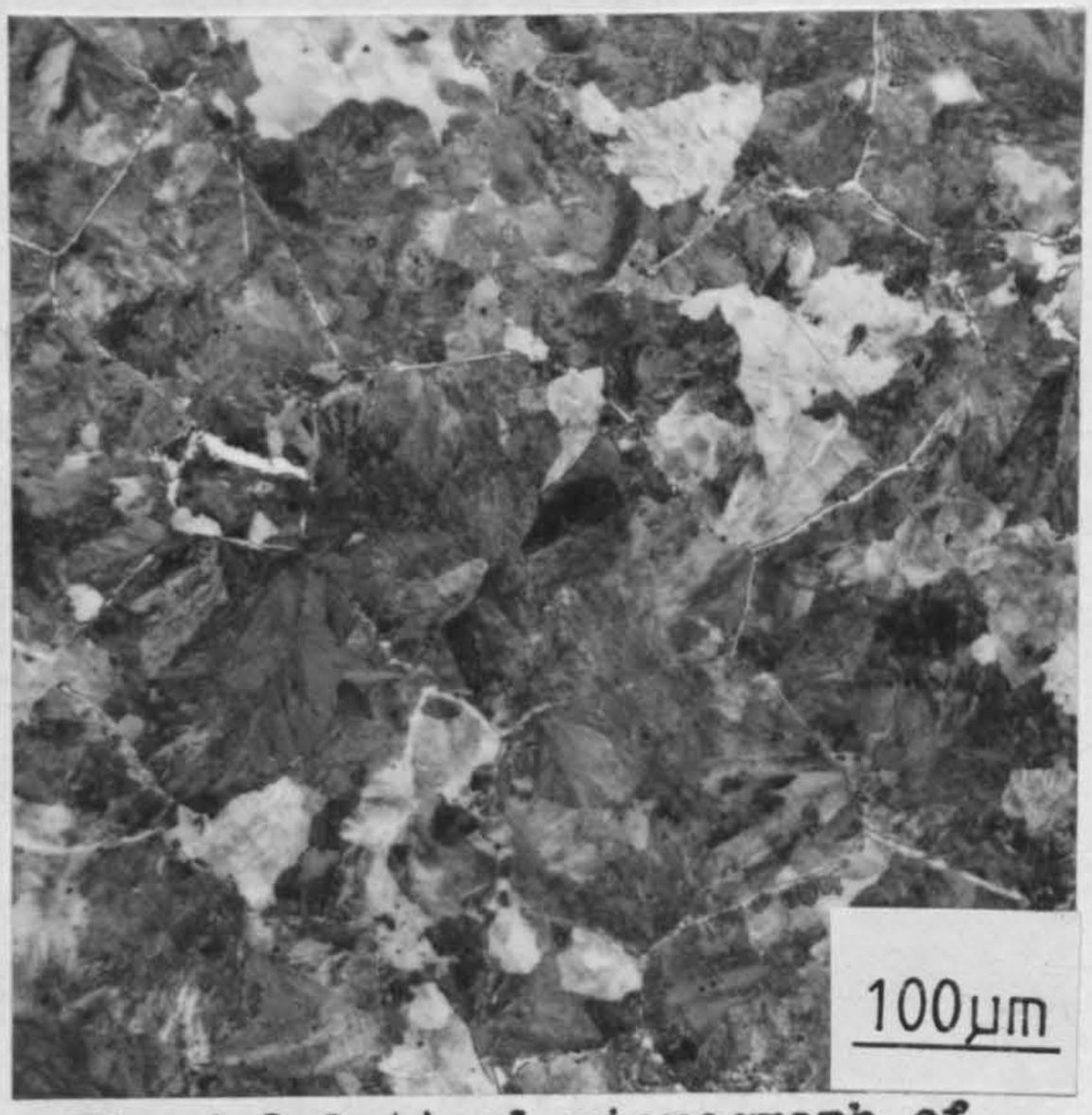

Fig 4.3 Optical micrograph of a 0.59wt%C steel air cooled from 1200°C.(Specimen 5A11)

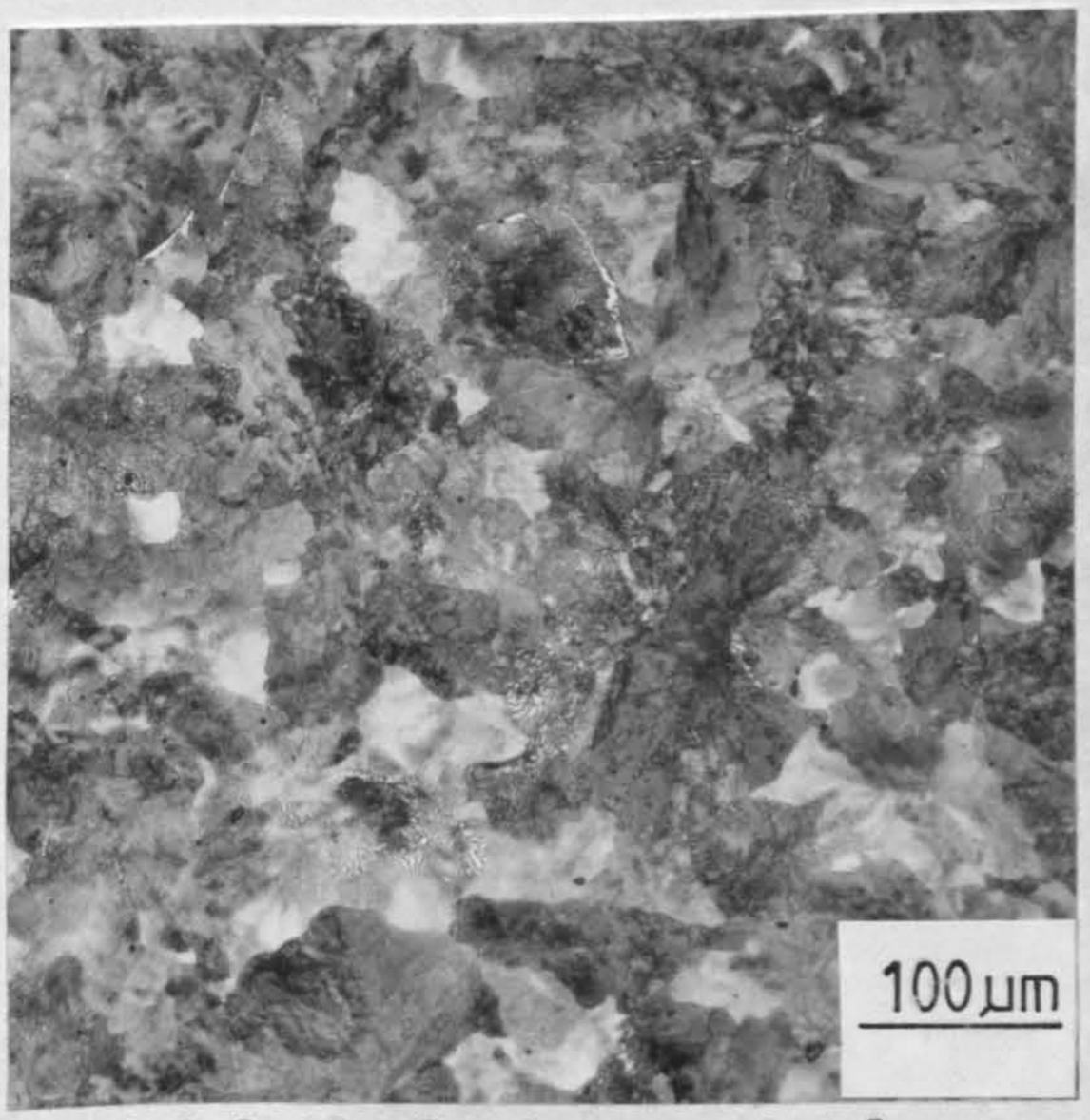

Fig 4.4 Optical micrograph of a 0.82wt%C steel air cooled from 1200°C. (Specimen 5B11)

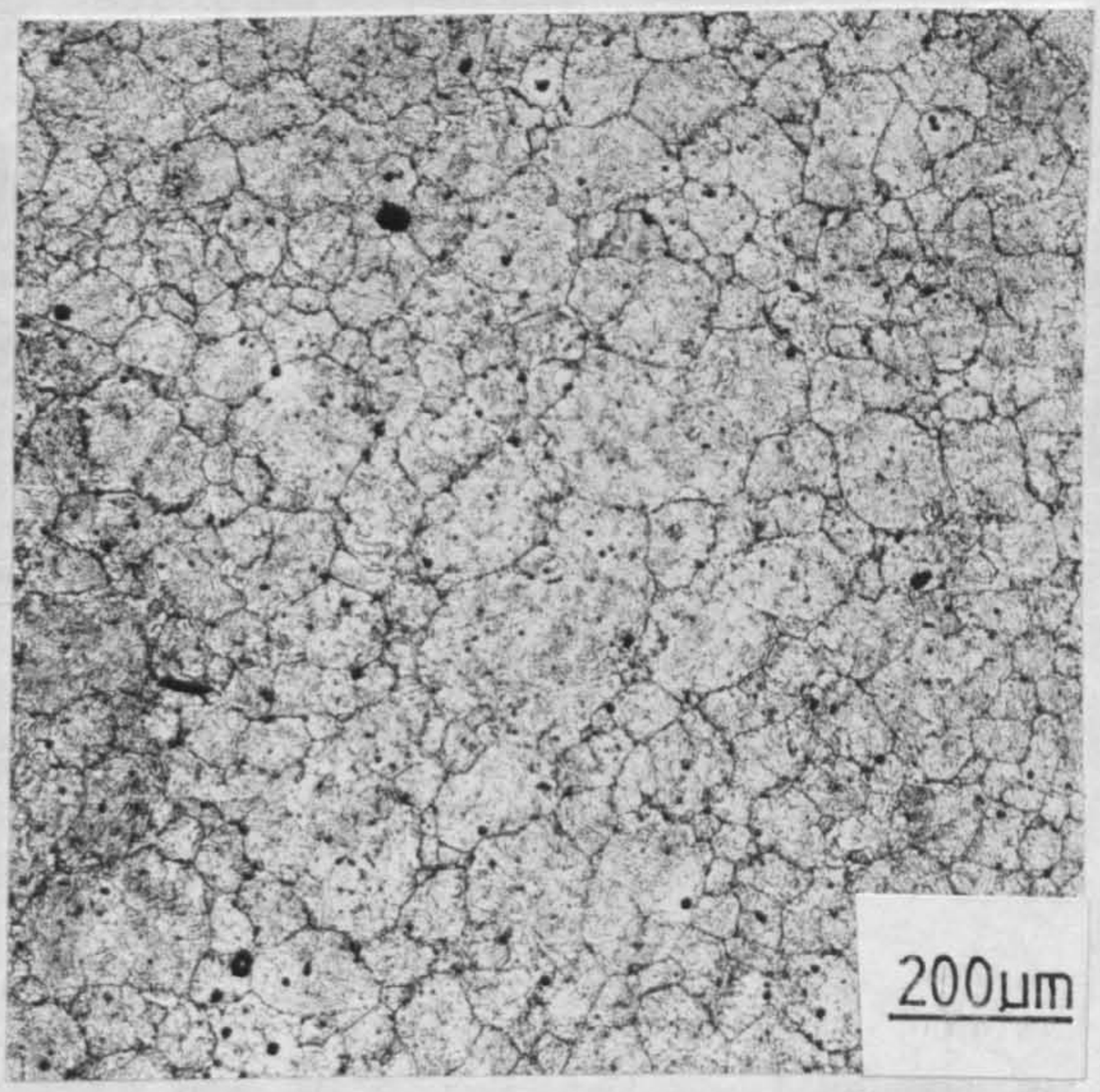

Fig 4.5 Typical optical micrograph of a thermally etched specimen (Specimen R7, Austenitised 1000°C)

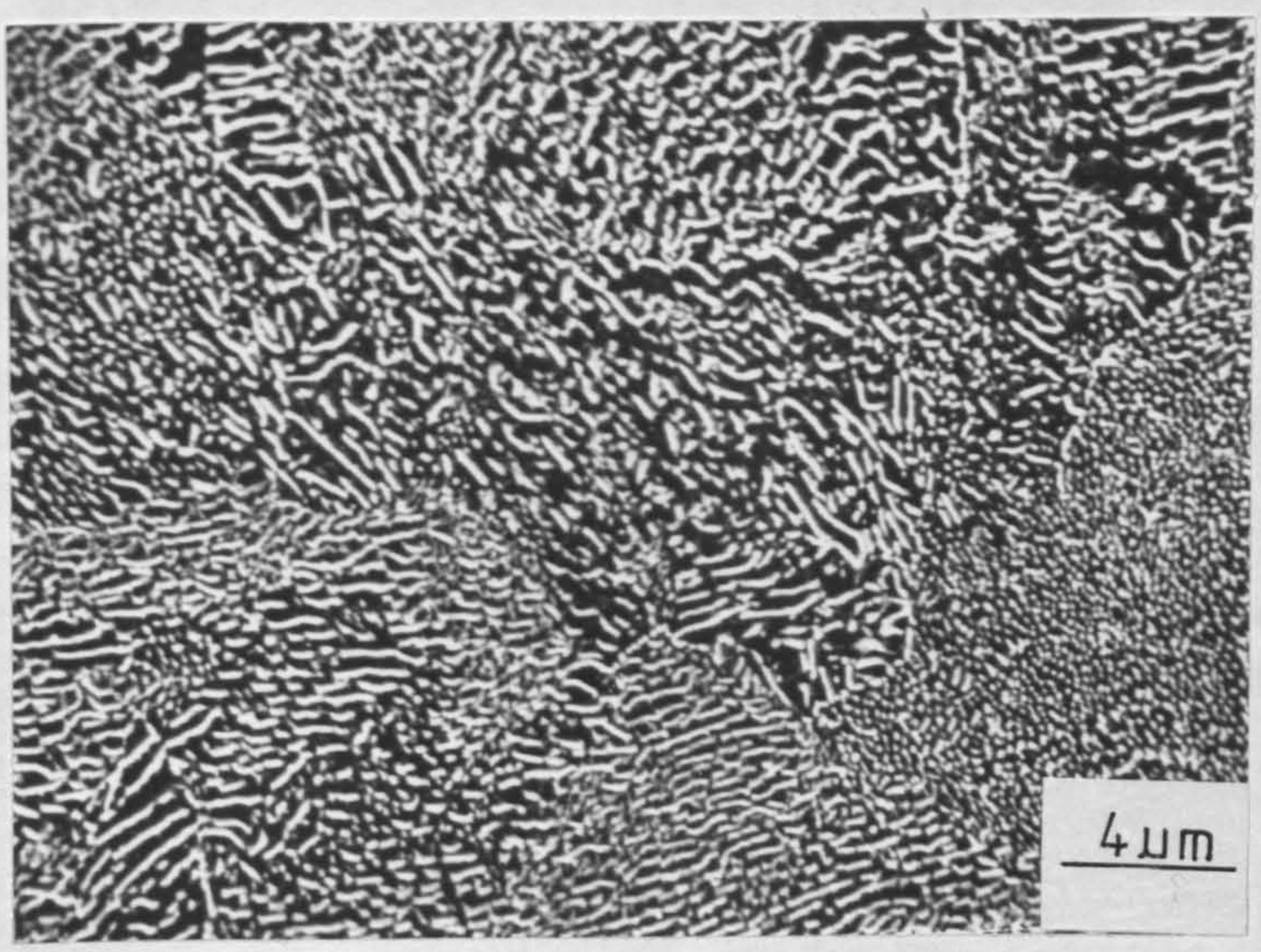

Fig 4.6 SEM micrograph of non-lamellar pearlite in a vermiculite cooled specimen of 0.59wt%C steel. (Specimen 5A5)

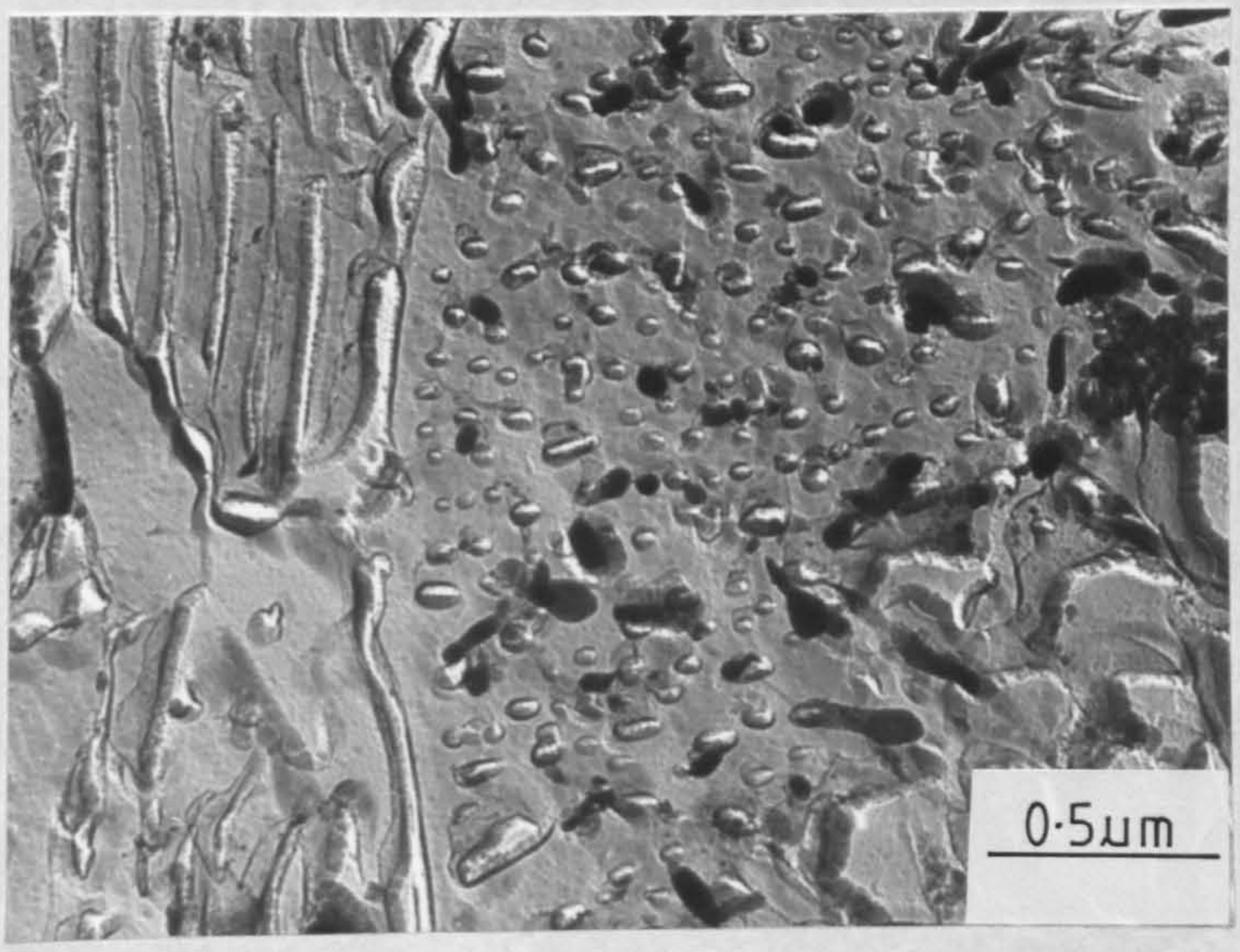

Fig 4.7 Two-stage replica of non-lamellar pearlite in a rapidly cooled specimen of 0.74wt%C steel. (Specimen R2)

given cooling rate. In addition fast cooling rates in the hypo-eutectoid compositions,0.42 and 0.59 wt.%C, resulted in lower transformation temperatures and higher volume fractions of pearlite. The occurrence of dilute pearlite in rapidly cooled hypo-eutectoid alloys is well documented[82,84,90].

Increasing the austenitising temperatures as expected resulted in an increase in the prior-autenite grain size, this feature being independent of cooling rate. As mentioned earlier, the prior-austenite grain size in fully pearlitic microstructures was obtained from thermally etched specimens. A typical example of the microstructure resulting from this heat treatment is shown in Fig. 4.5. The general trends in microstructure as a result of varying the austenitising temperature and cooling rate can be obtained from Tables 4.1, 4.3, 4.5 and 4.7.

As the pearlite colony size has little bearing on the strength of pearlitic steels, this microstructural feature is not recorded. However, the variation of colony size with austenitising temperature and cooling rate is discussed in Part 2.

4.2.2 Pearlite Morphology and Interlamellar Spacings

The pearlite morphology was in general lamellar, although non-lamellar regions were identified in both slow and rapidly cooled samples of all compositions. In addition,the occurrence of such areas varied with the carbon content of the steel, with the lowest carbon level (0.42 wt.%C) steel least likely to exhibit a fully lamellar microstructure.

Very slow cooling rates (i.e. in vermiculite $0.5^{o}C^{-1}$) resulted in areas of non-lamellar pearlite which closely resembled an annealed or spheroidised microstructure. A typical example in

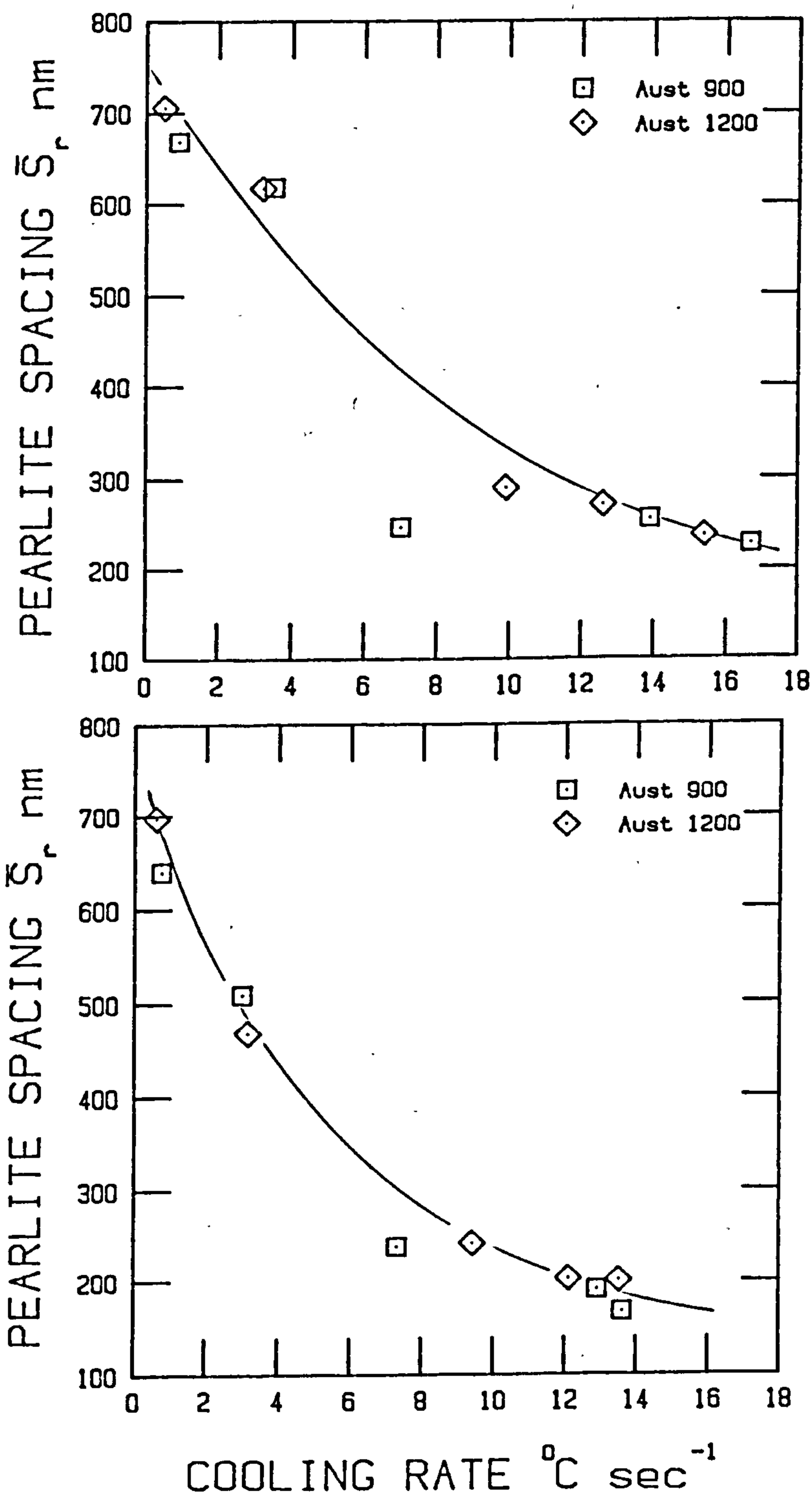

Fig 4.8 The mean random pearlite interlamellar spacing as a function of the cooling rate prior to transformation.(0.59(top) & 0.82 wt%C steels.)

a hypo-eutectoid steel is given in Fig. 4.6. Rapidly cooled specimens, on the other hand, produced carbide dispersions similar in appearance but considerably finer than non-lamellar regions in slow cooled specimens (Fig. 4.7).

Mean random pearlite spacing measurements varied between approximately 170 and 800nm, depending on composition and cooling rate (Tables 4.1, 4.3, 4.5 and 4.7). In general a decrease in the carbon content of the steel gave coarser pearlite for a given cooling rate, particularly at low transformation temperatures. This is in agreement with the isothermal transformation studies of Cheetham and Ridley[30]. In accordance with many published studies on pearlitic steels, a faster continuous cooling rate resulted in finer pearlite, as shown in Fig. 4.8 for the case of 0.59 and 0.82 wt.%C steels. This effect appears to be independent of prior-austenite grain size. Not included in Fig. 4.8 are the results for specimens which had undergone "interrupted cooling". The measured pearlite spacings for these specimens were in most cases characteristic of slower rates of continuous cooling.

4.3 MICROSTRUCTURE, HARDNESS AND STRENGTH

As would be expected, increased carbon content resulted in higher hardness and strength levels for a given cooling rate. Within each composition increasing the continuous cooling rates from $0.5^{o}C\ s^{-1}$ to $18^{o}C\ s^{-1}$ resulted in a non-linear increase in hardness and strength (Tables 4.2, 4.4, 4.6 and 4.8). The effect of cooling rate on the 0.2% proof stress is shown in Fig. 4.9. As anticipated from the pearlite spacing results, the strength (and

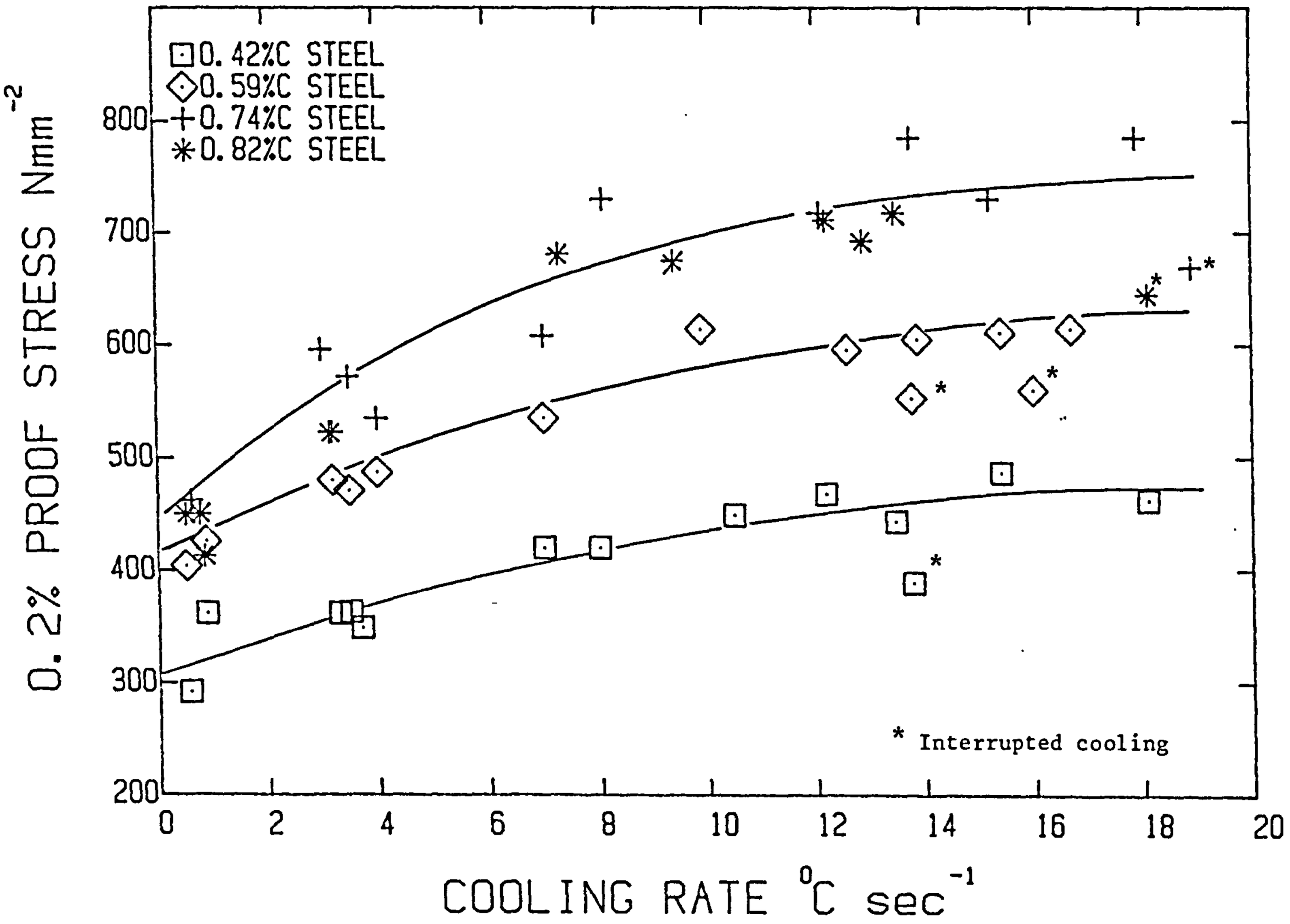

Fig 4.9 The 0.2% proof stress as a function of the cooling rate prior to transformation.(All data)

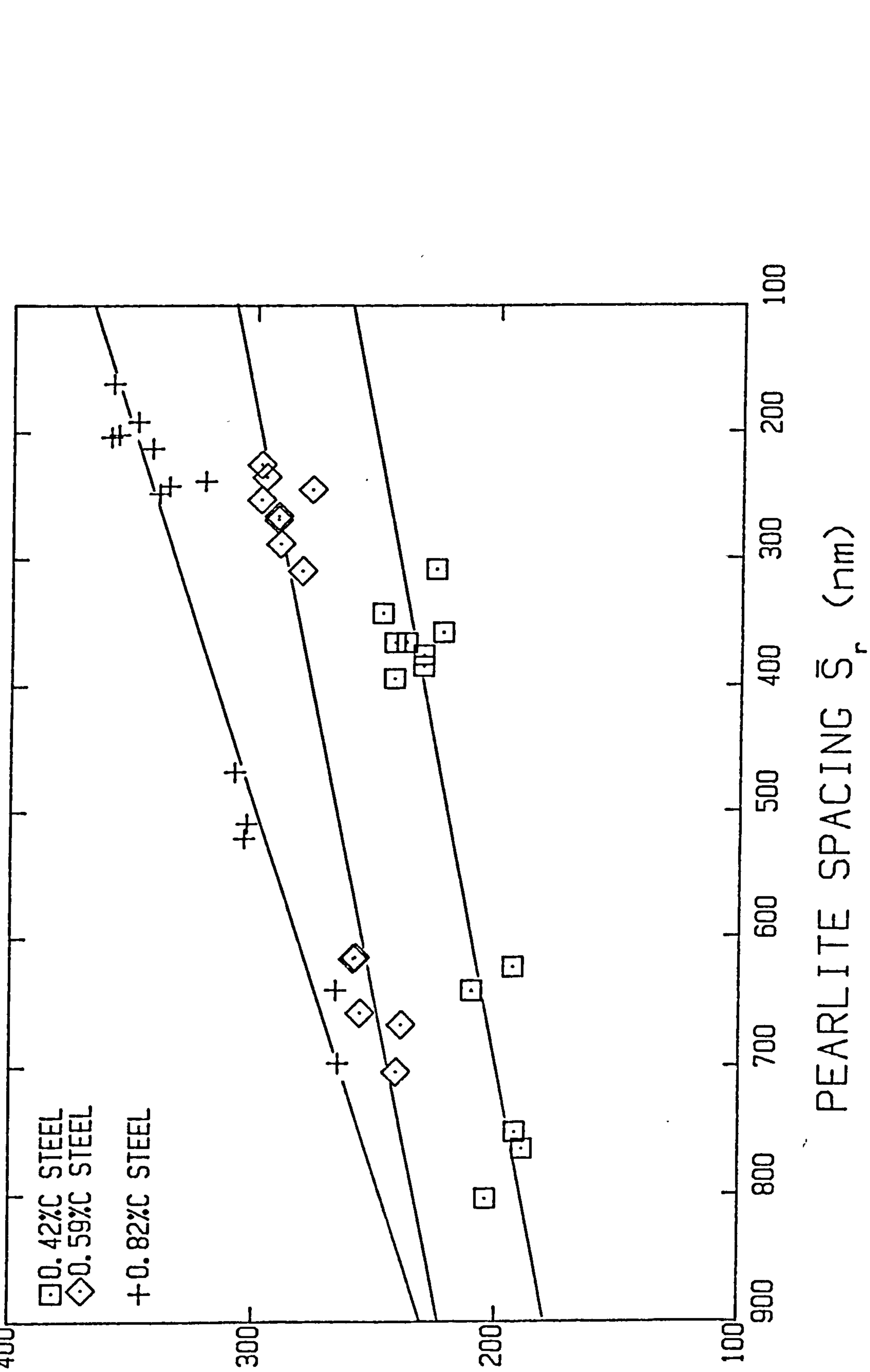

Fig 4.10 Vickers hardness as a function of the mean random pearlite interlamellar spacing.

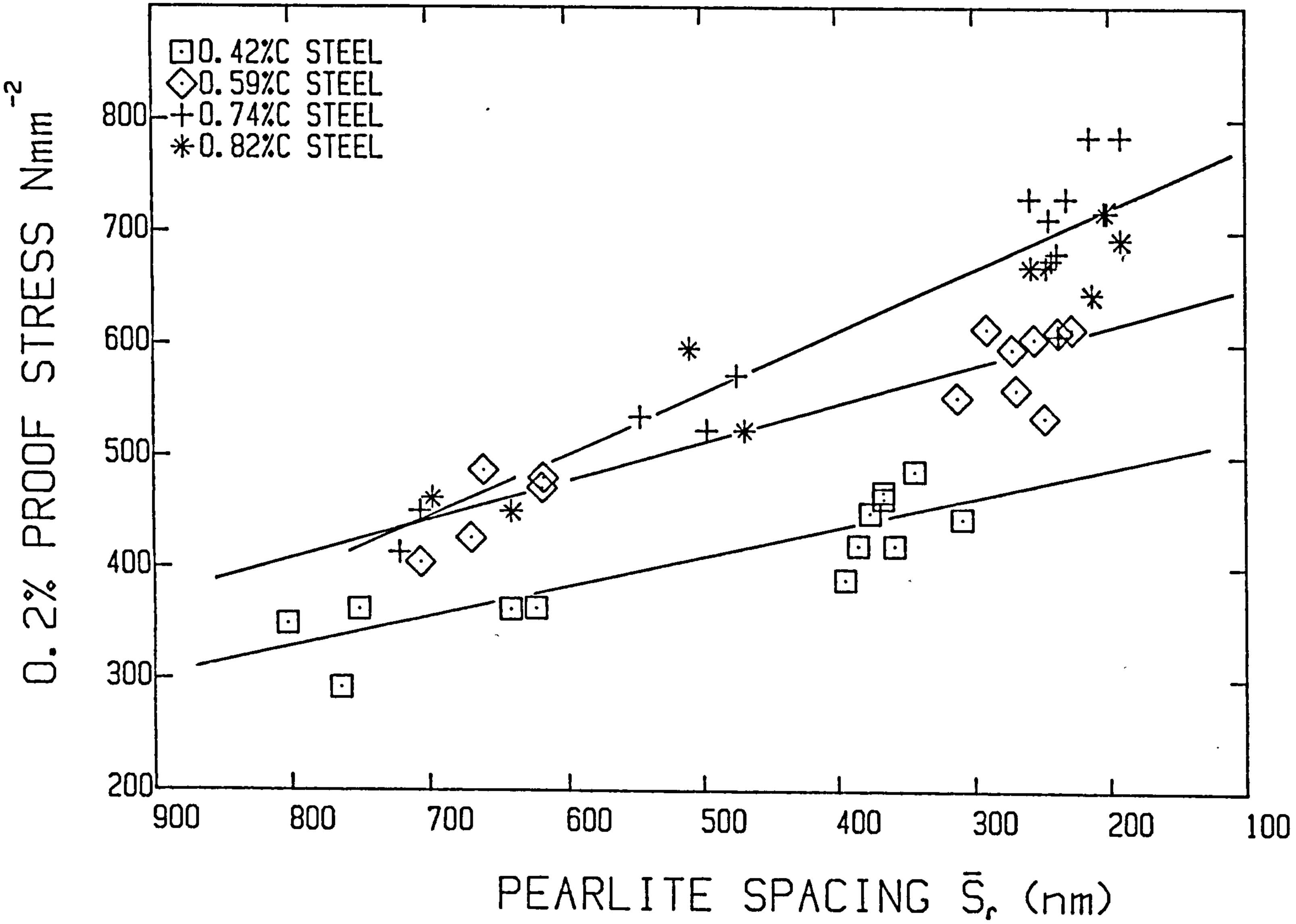

Fig 4.11 The 0.2% proof stress as a function of the mean random pearlite interlamellar spacing.

hardness) levels of specimens which had been cooled in the interrupted manner were similar to those cooled continuously at slower rates.

It is clear from Fig. 4.9 that a more substantial increase in strength of each steel occurred in the cooling rate range $\simeq$0.5 to 4 $^{o}C\ s^{-1}$ prior to transformation. This is consistent with the results given in Fig. 4.8 for the effect of cooling rate on pearlite spacing. As $\bar{S}_r$ decreases non-linearly with increased cooling rate, and pearlite spacing primarily governs both the hardness and strength, it is not surprising that a linear relationship is obtained for a plot of $\bar{S}_r$ against both these properties (Fig. 4.10 and 4.11). However, the fact that the results for each composition fall on separate lines, demonstrates that $\bar{S}_r$ does not fully describe the microstructure-strength relationship over the range of compositions. It is anticipated that other features such as the carbide thickness and particularly the amount of pro-eutectoid ferrite should be taken into account when correlating microstructure with the strength and hardness of pearlitic steels. Such considerations form the main body of the discussion which now follows.

CHAPTER 5

INTERPRETATION AND DISCUSSION OF RESULTS

5.1 PEARLITE MORPHOLOGY

The occurrence of non-lamellar pearlite in hypo-eutectoid and eutectoid steels is discussed in Chapter 1, Section 1.3. The observation in the present study of an increase in the degeneracy of the pearlite as the carbon content of the steel decreased is in good agreement with the work of Cheetham and Ridley[30] and others[24]. As discussed in Section 1.3 Cheetham and Ridley[30] argue that the formation of dilute pearlite in hypo-eutectoid steel will result in a lower volume fraction of cementite than in a eutectoid alloy. This may then give rise to a transition from lamellar to aligned discontinuous or "rod like" cementite,as observed in specimens in the present study. This form of pearlite is, however, distinct from non-lamellar pearlite formed in specimens cooled slowly in vermiculite (see Fig. 4.6).

The pearlite morphology of these specimens is undoubtedly the result of the prolonged reaction time (up to ~5 minutes) and the slow cooling after the transformation has reached completion. This will render the lamellar morphology unstable and result in cementite spheroidisation. The driving force for this post reaction morphology change is thought to be the decrease in interface boundary area giving a decrease in interface boundary energy. As Chadwick[1] has pointed out, even though an orientation

relationship exists between the eutectoid phases, and despite the fact that the interfacial boundary energy is possibly of the order of only 0.1 Jm^{-2}, this is sufficient to render the primary eutectoid microstructure unstable.

Such an explanation is clearly acceptable given that some of the lamellae in vermiculite cooled specimens were observed to be only partially spheroidised, resulting in parallel rows of spheroidal carbides. This type of microstructure is then dissimilar to that previously described for dilute hypo-eutectoid steels in that the former is a result of the pearlite growth and the latter due to a post-transformation morphology change.

The non-lamellar pearlite formed in the rapidly cooled high carbon (0.74 and 0.82 wt.%C) steels (e.g. Fig. 4.7) was, in some cases, similar to the transitional pearlite discussed by Smith and Fletcher[26] and others[27]. This decomposition product may be due to insufficient diffusion of carbon to maintain continuous cementite formation[14,15,16] at the low transformation temperatures and high transformation velocities. Alternatively, as Hillert[2] points out, transitional pearlite may be the result of a limited degree of coherency being established at the austenite-pearlite interface thus preventing satisfactory cooperative growth of ferrite and cementite.

The observations of the present study therefore suggest that a fully lamellar microstructure forms only within a limited range of cooling rates and transformation temperatures, and is dependent on the carbon content of the steel. Large amounts of non-lamellar pearlite form preferentially in low carbon hypo-eutectoid steels. High carbon near eutectoid or eutectoid steels

on the other hand give predominantly lamellar pearlite,although both very slow and rapid cooling rates can lead to degenerate microstructures.

Rough estimates of the proportion of non-lamellar regions in the microstructure of each specimen gave values between 0% and 20%. An attempt was made to categorise the decomposition products formed in each specimen in terms of the amount of lamellar pearlite, spheroidised pearlite, transitional pearlite and upper bainite. However, comparison with the many published micrographs of non-lamellar pearlite and upper bainite made unambiguous identification of each of the forementioned two phase ferrite-cementite mixtures difficult. From an examination of transformation data in relation to CCT and TTT diagrams it would seem unlikely that substantial amounts,if any,of upper bainite would be found in some of the microstructures investigated. Nevertheless, strengthening in pearlite[90], spheroidite[78] and bainites[81,118,119,120] are similarly considered in terms of their carbide spacing. The microstructure-strength analysis considered in Section 5.3 should, therefore, be relatively unaffected by the fraction of non-lamellar structure,provided due care is taken in the method of quantifying each microstructure.

5.2 THE RELATIONSHIP BETWEEN THE PEARLITE SPACING AND THE TRANSFORMATION TEMPERATURE

The role of transformation temperature in determining the pearlite interlamellar spacing is well established[69]. Reducing the transformation temperature,by either accelerated continuous cooling or lowering the isothermal bath temperature,

results in a refinement of the interlamellar spacing. According to the work of Marder and Bramfitt[46] and the theoretical predictions of Zener[39] this effect should be independent of prior-austenite grain size or transformation mode and should instead be solely dependent on the degree of undercooling.

The effect of continuous cooling rate on the pearlite spacing was highlighted earlier (see Fig. 4.8). The fact that increasing the cooling rate resulted in finer pearlite, irrespective of the austenitising temperature, is surprising given the fact that specimens of a large prior-austenite grain size transform to pearlite at lower temperatures ($\simeq$15 to 20^{o}C) and should therefore give finer pearlite. This effect is made clear in Fig. 5.1. A comparison of the mean random spacing with the average transformation temperature, taken to be the mid point between T_{min} and T_{max}, is shown in Fig. 5.1 for the 0.74 and 0.82 wt.%C steels. Although the general form of the relationship is in agreement with the work of Marder and Bramfitt[46] the apparent effect of prior-austenite grain size is clearly inconsistent with the results of these authors and the theory of Zener[39]. If the $\bar{S}_r$ values of the 0.82 wt.%C steel were converted to S_{min} values using the approximate relationships $\bar{S}_r = 2\ \bar{S}_t$ and $\bar{S}_t = 1.65\ S_{min}$[92], and then plotted against the degree of undercooling on Fig. 1.7 all points would appear to fall within the scatter band of Marder and Bramfitt[46]. This is not surprising however, given that this scatter band may contain data with the same undercooling but S_{min} values which differ by as much as 100%.

Specimens which had undergone interrupted cooling did not always have pearlite spacings which were characteristic of their

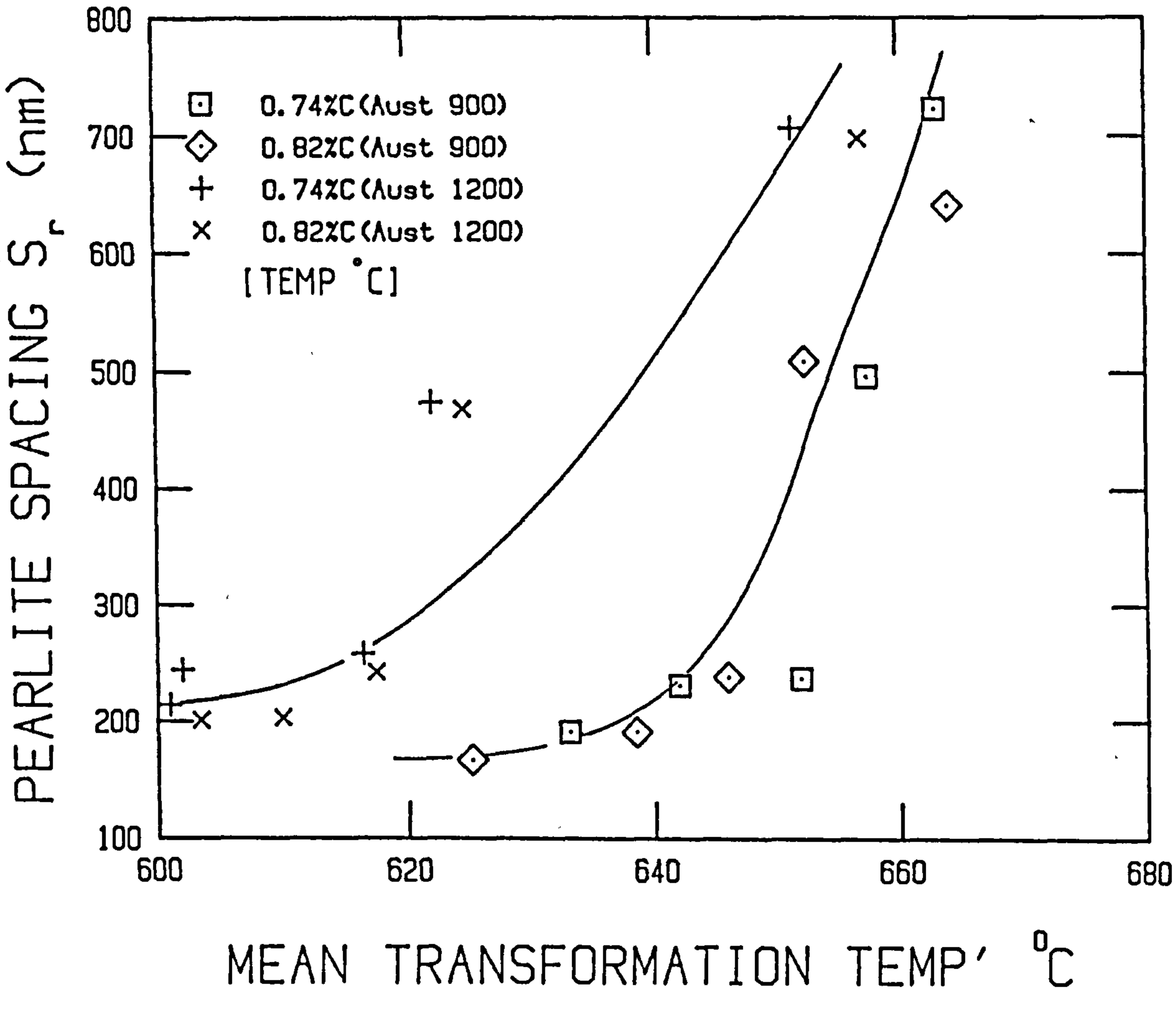

Fig 5.1 Mean random pearlite spacing as a function of the average transformation temperature for continuously cooled specimens of 0.74 & 0.82wt%C steel.

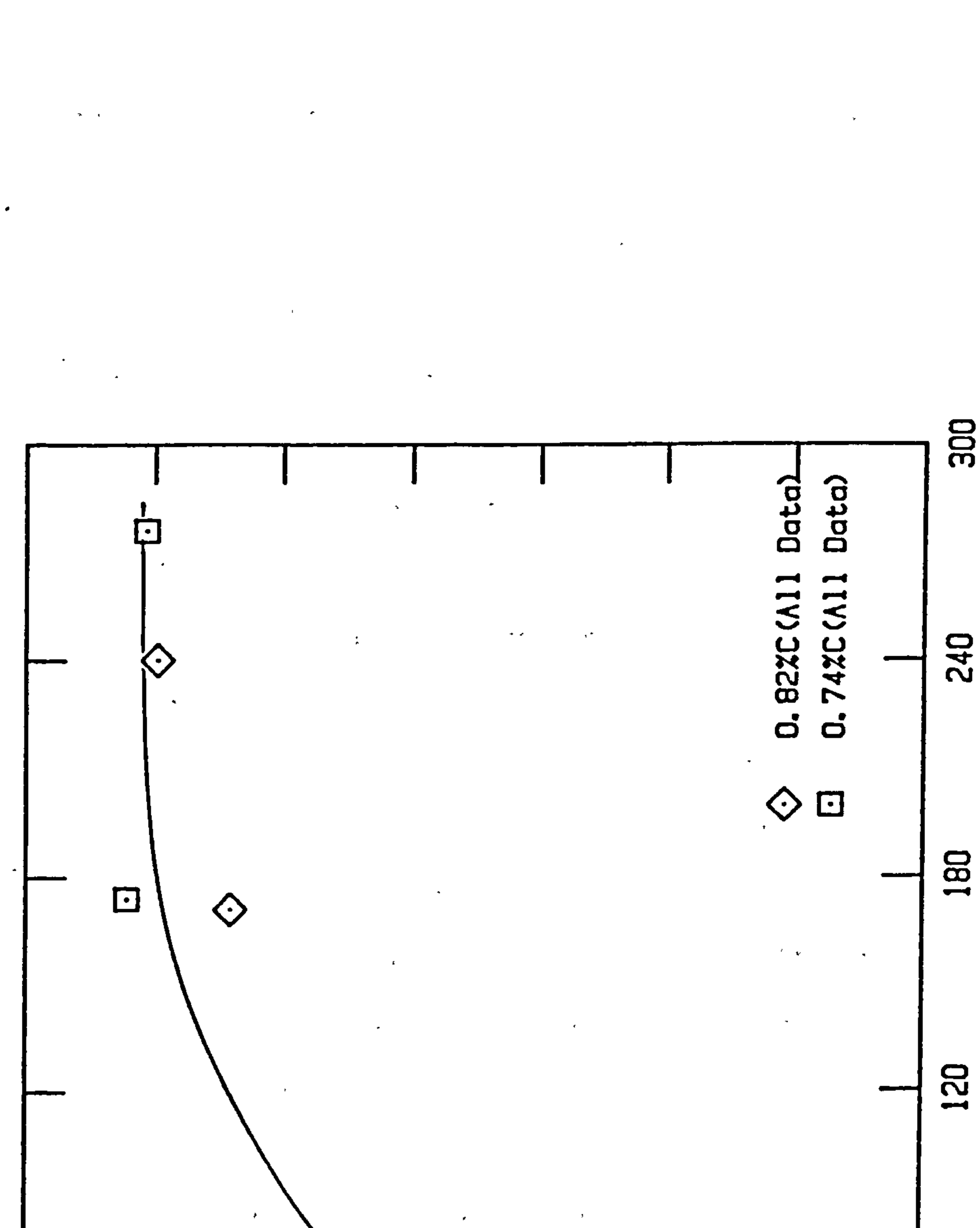

Fig 5.2 Mean random pearlite spacing as a function of the transformation time for the 0.74 & 0.82 wt%C steel.

transformation temperatures. For example, although specimens 4A5 and 4A6 have essentially the same mean transformation temperatures, $\bar{S}_r$ values are respectively 751nm and 308nm. Similar differences occurred between specimens 5A5-5A6 and R3-R6. However, when the time taken for the transformation to go to completion is examined, it is clear that this variable is important in determining the pearlite spacing. Specimen 4A5 transformed to ferrite and pearlite over a time interval of approximately two minutes whereas in specimen 4A6 the transformation was complete over the same temperature range in around 17 seconds. In fact when the mean random spacing values are compared with transformation times a satisfactory agreement is obtained for all data, irrespective of the prior-austenite grain size or the cooling mode (interrupted or continuously cooled samples). This correlation between transformation time and pearlite interlamellar spacing is illustrated in Fig.5.2 for the case of the 0.74 and 0.82 wt.%C steels.

Thus it seems that the mean random pearlite spacing is determined by the time available for the transformation to go to completion, i.e. the transformation velocity. In continuous cooling this velocity is governed primarily by the transformation temperature but does not always appear to correspond to it. The present study suggests that, although the transformation temperature in specimens of large grain size austenite are lower for a given continuous cooling rate, the cooling rate (particularly for chamber cooled specimens) rather than the transformation temperature determines the velocity of the reaction which controls the pearlite spacing. In the specimens which have been cooled rapidly to low transformation start temperatures and then allowed to cool

in still air, the pearlite spacing values were characteristic more of the transformation times than of the temperatures.

Both these observations suggest that the growth rate determines the time available for the diffusion of carbon which in turn dictates the pearlite interlamellar spacing. A decrease in the growth rate as a result of slower continuous cooling rates increases the time available for diffusion. This enables carbon to diffuse over greater distances thus promoting a coarser interlamellar spacing. This conclusion is obviously contrary to the theory of Zener[39] which states that interlamellar spacing controls the growth rate. More work is therefore needed on continuously cooled pearlitic steels to verify these conclusions. Nevertheless, the main body of the present study is concerned with the relationship between microstructure, hardness and strength. As both these mechanical properties correlate well with measured values of pearlite spacing within a given composition (see Figs. 4.10 and 4.11), considerable confidence can be placed in the accuracy of mean random spacing measurements. The remainder of this discussion will now consider in some detail the role of microstructure in determining the hardness and flow stress of pearlitic steels. A number of microstructural features are defined and used throughout the next section. To aid the reader a general summary of symbols and definitions can be found at the beginning of the thesis.

5.3 THE RELATIONSHIP BETWEEN THE MICROSTRUCTURE HARDNESS AND STRENGTH

At this point it is useful to compare microstructure-

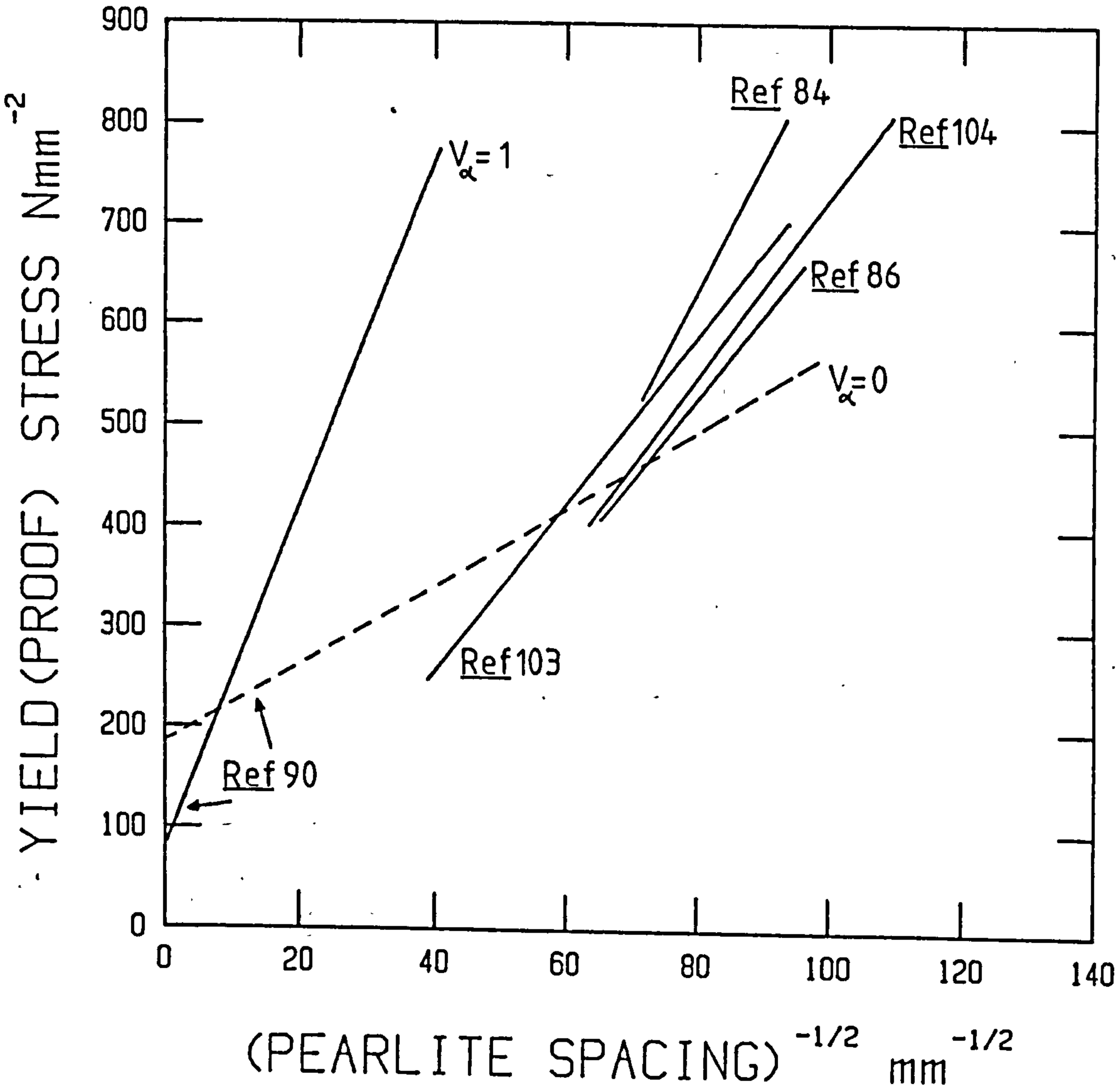

Fig 5.3 Pearlite spacing-strength relationships from the literature for the case of fully pearlitic steels.

strength relationships gathered from the literature. Fig. 5.3 shows a number of minimum interlamellar spacing versus 0.2% proof stress plots for the case of eutectoid 0.82 wt.%C steels. As discussed in Section 2.2.4 Gladman et al[90,91] suggested relationships between the yield (proof) stress of ferrite, σ_α, and pearlite, σ_p, with composition and microstructural variables to be the form[91],

$$\sigma_\alpha \ (Nmm^{-2}) = 53.9 + 32.3 \text{ wt.\%Mn} + 7.7 \text{ wt.\%Si} + 17.5 \ d_\alpha^{-\frac{1}{2}} \qquad (5.1)$$

$$\sigma_p \ (Nmm^{-2}) = 178.6 + 63.1 \text{ wt.\%Si} + 3.8 \ S_o^{-\frac{1}{2}} \qquad (5.2)$$

where S_o is the 'true' interlamellar spacing and d_α is the mean ferrite grain diameter.

It might be noted that equations 5.1 and 5.2 are the end points of a more general regression equation at 0% pearlite and 100% pearlite respectively. If, as is implicitly assumed in previous studies[84,86,103,104], pearlite is to be considered as a very fine grained ferritic material, then the microstructure-strength relationship should be compatable with the behaviour of pure ferrite. For this purpose, using the manganese and silicon contents present in the steels examined in this study, the line for ferrite volume fraction $V_\alpha = 1$, calculated from equation 5.1, and Gladman et al's[90,91] 100% pearlite line $V_\alpha = 0$, calculated from equation 5.2, are included in Fig. 5.3.

Although there is general agreement on strength-structure behaviour in the normal range of interlamellar spacings in all but one case, that of Gladman et al[90,91], the long extrapolation to $S^{-\frac{1}{2}} = 0$ leads to a negative value for the friction stress with consequent theoretical difficulties. This observation is seen to

be true even when correction is made for differences in solid solution elements between studies.

It is worth noting that the pearlite spacing values of Gladman et al[90,91] were not determined by the method of Brown and Ridley[94] as were references 84, 86, 103 and 104, but were instead measured by the procedure of Pearsall[69]. The fact that these authors obtained a positive friction stress may be due in part to this, but can also be attributed to the fact that equations 5.1 and 5.2 are derived from a more general regression equation that covers the entire range of volume fractions of pearlite (see Section 2.2.4).

Figure 5.3 clearly illustrates the general inadequacy of conventional spacing measurements in describing the microstructure-strength relationship in terms of a Hall-Petch[53,54] analysis, even for the relatively simple case of a fully pearlitic microstructure. As negative friction stress values are inconsistent with definition, many experimenters[84,85,103] have postulated a proof stress dependence on S^{-1}. Such relationships are seldom explained from any theoretical background although an Orowan[71] dispersion strengthening model may be inferred. A plot of proof stress as a function of S^{-1} results in a positive friction stress together with a good statistical fit for the experimental data[85].

Apart from the work of Gladman et al[90,91], the only other reports found to give positive friction stresses from Hall-Petch plots were those of Takahashi and Nagumo[112] and Langford[121]. The common feature of their work is that both studies measured the mean intercementite spacing and this link may give an important clue to the reason behind the many negative friction

stress values obtained from proof stress minimum spacing correlations.

If the ferrite grain size in mild steel is assumed to be measured by a mean linear intercept, it is then of some importance to carefully consider the method of quantifying the microstructures of the present study to obtain the corresponding ferrite 'grain size' in pearlite. When dealing with non-equiaxed 'grains', as in the case of lamellar microstructures, an uncertainty may arise as to whether the ferrite width perpendicular to the cementite lamellae or the average width should be measured. What is obviously required is the mean slip distance in the ferrite. This point was appreciated by Gensamer et al[69], Hugo and Woodhead[83] and later by Embury and Fisher[81].

Gensamer[69] regarded the mean free path as the average slip distance in ferrite and showed this to be approximately twice the pearlite spacing. However, as Embury and Fisher[81] have pointed out, this assumes that no orientation relationships exist between cementite and ferrite, and slip in the ferrite of some colonies could then theoretically occur parallel to the carbide lamellae. However, as discussed in Section 1.2, this is not the case and a fixed orientation relationship does exist. In the Pitsch[17] relationship, the plane of the lamellar particle is parallel to (001) cementite planes and approximately parallel to (521) ferrite planes so that the ferrite slip planes make angles from about 20 to 70° to the lamellae[81]. Thus the assumption made by Gensamer et al[69] that the mean free distance (or mean random spacing $\bar{S}_r$) is twice the mean true spacing ($\bar{S}_t$) is quite reasonable. In fact, as the multiplicity of slip systems in the

Wt % C	AUSTENITISING TEMPERATURE °C	COOLING METHOD	AVERAGE MINIMUM SPACING $\bar{S}_{min}$ (nm)	MINIMUM OBSERVED SPACING S_{min} (nm)	MEAN RANDOM SPACING $\bar{S}_r$ (nm)	MEAN TRUE SPACING $\bar{S}_t$ (nm)	$\bar{S}_t / S_{min}$	$\bar{S}_t / \bar{S}_{min}$
0.42	1000	AIR	307	243	788	394	1.62	1.28
0.42	1160	"	333	281	806	403	1.43	1.21
0.59	800	"	267	238	878	439	1.84	1.64
0.59	1000	"	382	310	674	337	1.09	0.88
0.59	1160	"	273	237	784	392	1.65	1.43
0.82	800	"	250	115	549	275	2.39	1.10
0.82	1000	"	281	222	369	185	0.83	0.66
0.82	1160	"	307	240	384	192	0.80	0.62
95% confidence limits			± 5%	± 20%	± 4%	± 4%		

Table 5.1 Comparison on pearlite spacing values obtained by different methods.

bcc structure should effectively randomise orientation effects[101], the mean free distance measurement will be a good approximation of the ferrite slip distance in pearlite.

Although Embury and Fisher[81] employed a multiplication factor of 2 to convert spacing measurements to mean slip distances this is only strictly correct when the measurement of pearlite spacing is the mean true spacing $\bar{S}_t$. It therefore does not apply to measurements of S_{min}, $\bar{S}_{min}$, some measurements of S_o and non-lamellar microstructures.

A preliminary investigation was conducted to examine the relationship between S_r, S_t and S_{min} for the relatively simple case of air cooled specimens of 0.42, 0.59 amd 0.82 wt.%C steels (prepared for Part 2, Section 8.1.1). Conversion of $\bar{S}_t$ to the mean true spacing using the relationship $\bar{S}_r = 2\ \bar{S}_t$ allows a direct comparison between S_{min} and $\bar{S}_t$ as well as $\bar{S}_r$ (Table 5.1 opposite). Although some agreement was reached between these parameters, within a given composition, the overall relationship is poor. Whether this is due to the effect of recalescence producing a large variation in true spacing, or to the fact that $\bar{S}_r$ measurements may incorporate non-lamellar regions, is not clear. In isothermally transformed specimens the variation in spacings might be expected to be somewhat less than in continuously cooled materials and therefore a closer relationship between $\bar{S}_t$ and S_{min} may be found. However as data in this area have apparently not been published a thorough investigation is obviously warranted.

Measurements of pearlite spacings by the method of Brown and Ridley[94] are clearly of considerable use in reaction kinetic

studies, on isothermally transformed high purity eutectoid alloys, where some measure of the true distance between cementite lamellae is required. However, when relating mechanical properties to the microstructure of commercial alloys and rail steels, particularly those 'continuously cooled', minimum spacing measurements are inappropriate. What is required is a measure of the mean random intercementite spacing. This is probably not obtainable from measurements of S_{min} which, by definition, are selective and therefore avoid non-lamellar regions when present. Such non-lamellar regions may markedly influence the value obtained for $\bar{S}_r$.

Given these limitations, it would appear that the only truly accurate method of determining the average slip distance in ferrite is to measure the mean random cementite spacing as in the work of Gensamer et al[69], Takahashi and Nagumo[112], Langford[121] and the present study.

5.3.1 Mean Free Ferrite Distance $\bar{\lambda}_\alpha$

Following their approach, it was decided to treat the present microstructures in terms of $\bar{\lambda}_\alpha$, the average mean free distance in ferrite. In fully pearlitic steels the mean free ferrite distance (m.f.f.d) is simply the mean ferrite width. In the case of a ferrite-pearlite microstructure $\bar{\lambda}_\alpha$, is to a first approximation, the volume fraction weighted mean of the m.f.f.d. in the pearlite and in the pro-eutectoid phase averaged over all orientations. $\bar{\lambda}_\alpha$ is then easily measured by a mean linear intercept along a random straight line in a random section. In the present study the m.f.f.d. in the pearlite was measured and that in the pro-eutectoid phase calculated from the volume fraction of ferrite, assuming

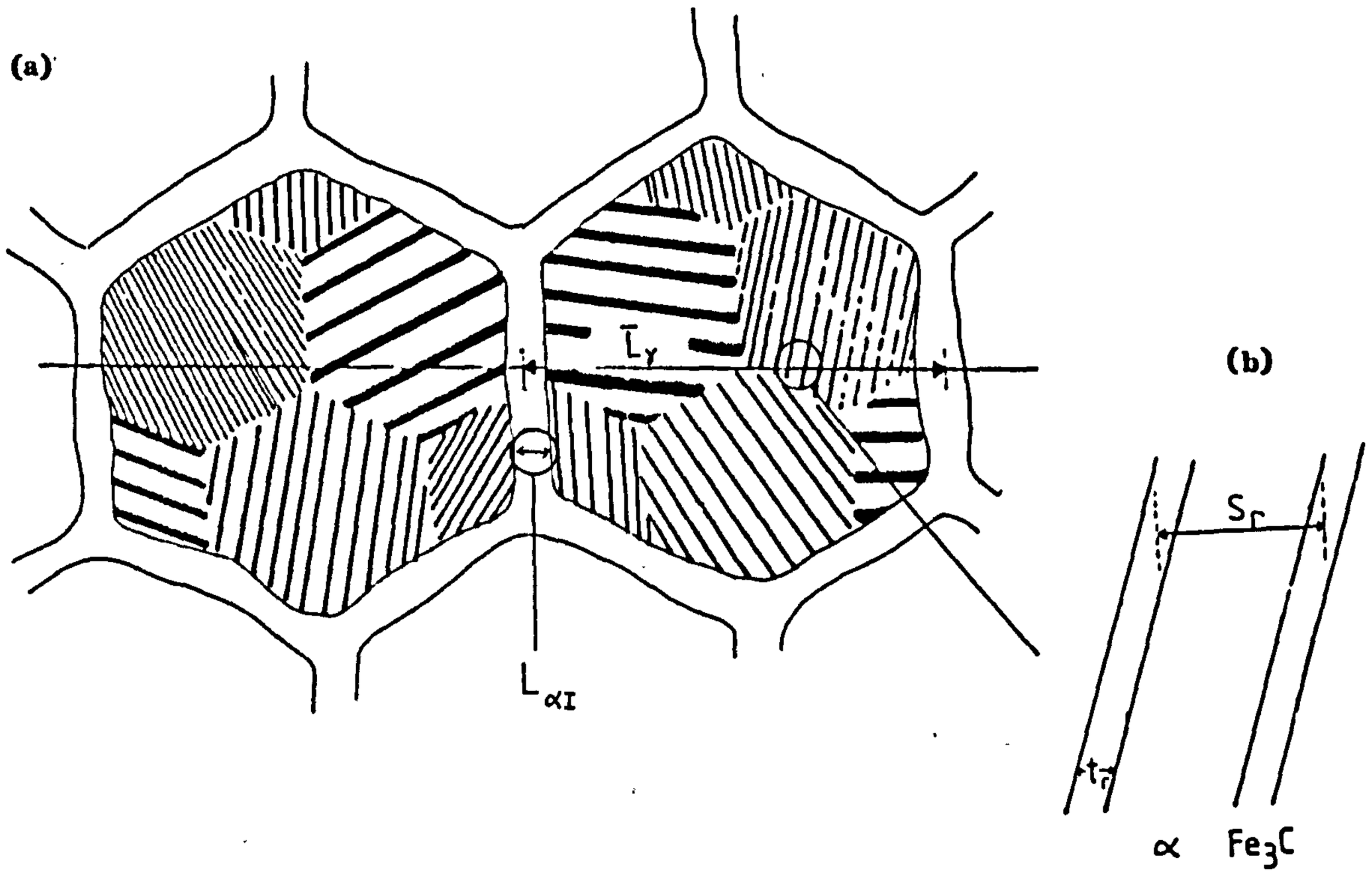

Fig 5.4 Schematic diagram of a ferrite-pearlite aggregate illustrating the various microstructural parameters,

this to be distributed as a boundary free network around the prior-austenite grains.

Following established stereological techniques[99] the pro-eutectoid m.f.f.d, $\bar{L}_{\alpha I}$, can be expressed by considering a random line of length L drawn through the structure, Fig. 5.4 (a), where;

$$\bar{L}_{\alpha I} = \frac{\text{total length of pro-eutectoid ferrite}}{\text{number of prior-austenite grain boundaries}}$$

$$= \frac{L_{\alpha I}}{N_{\gamma}} \qquad (5.3)$$

However, the prior-austenite grain diameter, $\bar{L}_{\gamma}$, can also be measured along such a line and;

$$\bar{L}_{\gamma} = \frac{L}{N_{\gamma}}$$

$$\text{i.e. } N_{\gamma} = \frac{L}{\bar{L}_{\gamma}} \qquad (5.4)$$

The volume fraction of pro-eutectoid ferrite, V_{α}, is also obtainable by measurement along the same line,

$$V_{\alpha} = \frac{L_{\alpha I}}{L}$$

$$\text{i.e. } L_{\alpha I} = LV_{\alpha} \qquad (5.5)$$

Substituting equation 5.3 and 5.4 into equations5.5 gives

$$\bar{L}_{\alpha I} = V_{\alpha}\bar{L}_{\gamma} \qquad (5.6)$$

If $\bar{L}_{\alpha II}$ is the ferrite mean free distance in pearlite then,

$$\bar{L}_{\alpha II} = \bar{S}_{r} - \bar{t}_{r} \qquad (5.7)$$

where $\bar{S}_{r}$ is the mean random pearlite or intercementite spacing and

$\bar{t}_r$ the average random cementite width. Considering equations 5.6 and 5.7 we arrive at an expression for the average m.f.f.d. in the ferrite-pearlite aggregate;

$$\bar{\lambda}_\alpha = (1 - V_\alpha)\bar{L}_{\alpha II} + V_\alpha \bar{L}_{\alpha I}$$

$$\text{or } \bar{\lambda}_\alpha = (1 - V_\alpha)(\bar{S}_r - \bar{t}_r) + V_\alpha^2 \bar{L}_\gamma \qquad (5.8)$$

Some difficulty may be encountered when trying to obtain an accurate value for the prior-austenite grain size in fully pearlitic steels. In hypo-eutectoid compositions ferrite separation prior to the formation of pearlite clearly delineates the prior-austenite grain boundaries. Transformation in eutectoid steels, on the other hand, results in an almost fully pearlitic microstructure and special etching or a heat treatment is required to outline the grain boundaries. Fortunately, however, an inaccurate estimate of $\bar{L}_\gamma$ in the latter case will not seriously influence the value of $\bar{\lambda}_\alpha$ obtained from equation 5.8. The ferrite volume fraction will be very close to zero, making $\bar{\lambda}_\alpha$ in effect entirely dependent on the mean free distance in pearlite.

5.3.1.1 Evaluation of $\bar{t}_r$

The only parameter in equation 5.8 which is not readily obtainable is $\bar{t}_r$, the mean random cementite width. Mintz et al[122] have compared values of grain boundary carbide thickness measured by scanning electron and optical microscopy. For the case of low carbon ferrite-pearlite steels, these authors obtained SEM values which were in general half the size measured optically by Gladman et al[89]. Mintz and co-authors[122] attributed this discrepancy to the superior resolution of the SEM relative to the optical microscope.

Since optical microscopy would not be suitable for the fine microstructures of the present study, a preliminary examination was made of direct cementite lamella thickness measurements by scanning electron microscopy. Typical values of $\sim$0.2μm, for the case of an air cooled 0.82 wt.%C steel were approximately an order of magnitude larger than those values calculated by Gladman et al[90] for similar compositions and heat treatments. Indeed it is rather obvious from close inspection that the SEM greatly exaggerates the width of the cementite lamellae compared to the ferrite, with both phases appearing to have equal width. This is believed to be due both to preferential etching of ferrite leaving the cementite protruding and to an enhanced backscattered signal from the cementite phase.

Therefore, contrary to the findings of Mintz et al[122], the SEM is regarded as unsuitable for the measurement of carbide width in high carbon-pearlitic steels. Although replicas and thin foils would undoubtedly yield more realistic values of $\bar{t}_r$, particularly for degenerate structures, such procedures are excessively time consuming considering the number of specimens to be measured, the statistical counts required and the accuracy obtainable. It was therefore decided to calculate the mean cementite width from a knowledge of the carbon content of the steel and the measured values of $\bar{S}_r$ and V_α. $\bar{t}_r$ is quite simply obtained following an analysis similar to that of Gladman et al[90].

In the case of dilute pearlite, as in some of the microstructures of this study, the eutectoid weight per cent carbon content(wt.%C)is not predictable but can be obtained from weight fraction of pearlite. Assuming all the carbon to be in the

pearlite, the eutectoid carbon content, wt% C_E, is given in terms of the total alloy carbon content, C(in wt.%), and the weight fraction of pearlite W_p by,

$$\text{wt.\%}C_E = \frac{\text{wt.\%}C}{W_p} \tag{5.9}$$

$$\text{where } W_p = \frac{V_p/\rho_p}{\frac{(1-V_p)}{\rho_\alpha} + V_p/\rho_p} \tag{5.10}$$

V_p is the volume fraction of pearlite and ρ_p and ρ_α are the densities of pearlite and ferrite respectively.

The densities of ferrite and cementite are 7.86 gcm^{-3} and 7.40 gcm^{-3} respectively. Assuming the density of ferrite, cementite and therefore pearlite to be the same, equation 5.10 reduces to,

$$W_p = V_p \tag{5.11}$$

Substituting 5.11 into 5.9 gives,

$$\text{wt.\%}C_E = \text{wt.\%}C/V_p \tag{5.12}$$

Consider a unit volume of pearlite as represented schematically in Fig. 5.4(b). Along a random line, the volume-fraction of cementite in pearlite,

$$V_{cem} = \frac{\bar{t}_r}{\bar{S}_r} \tag{5.13}$$

therefore,

$$\bar{t}_r = \bar{S}_r V_{cem} \tag{5.14}$$

100 g of pearlite will contain $\left| \frac{3 \times 56}{12} + 1 . \text{wt.\%}C_E \right|$ g of

cementite and the weight fraction or volume fraction of cementite is,

$$W_{cem} = V_{cem} = \frac{100\ (0.15\ wt.\%C_E)}{100 - 100\ (0.15\ wt.\%C_E) + 100\ (0.15\ wt.\%C_E)}$$

$$\therefore\ V_{cem} = 0.15\ wt.\%C_E \qquad (5.15)$$

Substituting equation 5.12 in equation 5.15 gives,

$$V_{cem} = \frac{0.15\ wt.\%C}{V_p} \qquad (5.16)$$

and substituting for V_{cem} into 5.4 gives finally,

$$\bar{t}_r = \frac{\bar{S}_r\ 0.15\ wt.\%C}{V_p} \qquad (5.17)$$

Equation 5.17 differs somewhat from that given in the literature by Gladman, McIvor and Pickering[90]. However, as is shown in Appendix B, the differences in calculated values of $\bar{t}_r$ are relatively insignificant given the accuracy limits of $\bar{S}_r$ and V_p measurements.

Using equation 5.17, $\bar{t}_r$ values were calculated for each specimen and are given in Tables 4.1, 4.3, 4.5 and 4.7. This parameter, together with measured $\bar{L}_\gamma$, $\bar{S}_r$ and V_α values, can now be substituted in equation 5.8 to give the mean free ferrite distance $\bar{\lambda}_\alpha$ for each microstructure (Tables 4.1, 4.3, 4.5 and 4.7).

5.3.1.2 Hardness

Vickers hardness values as a function of $\bar{\lambda}_\alpha^{-1}$ and $\bar{\lambda}_\alpha^{-\frac{1}{2}}$ are given in Figs. 5.5 and 5.6. Clearly an excellent correlation is obtained for the microstructural and compositional range studied. Although Fig. 5.5 is non-linear, a single linear relationship is

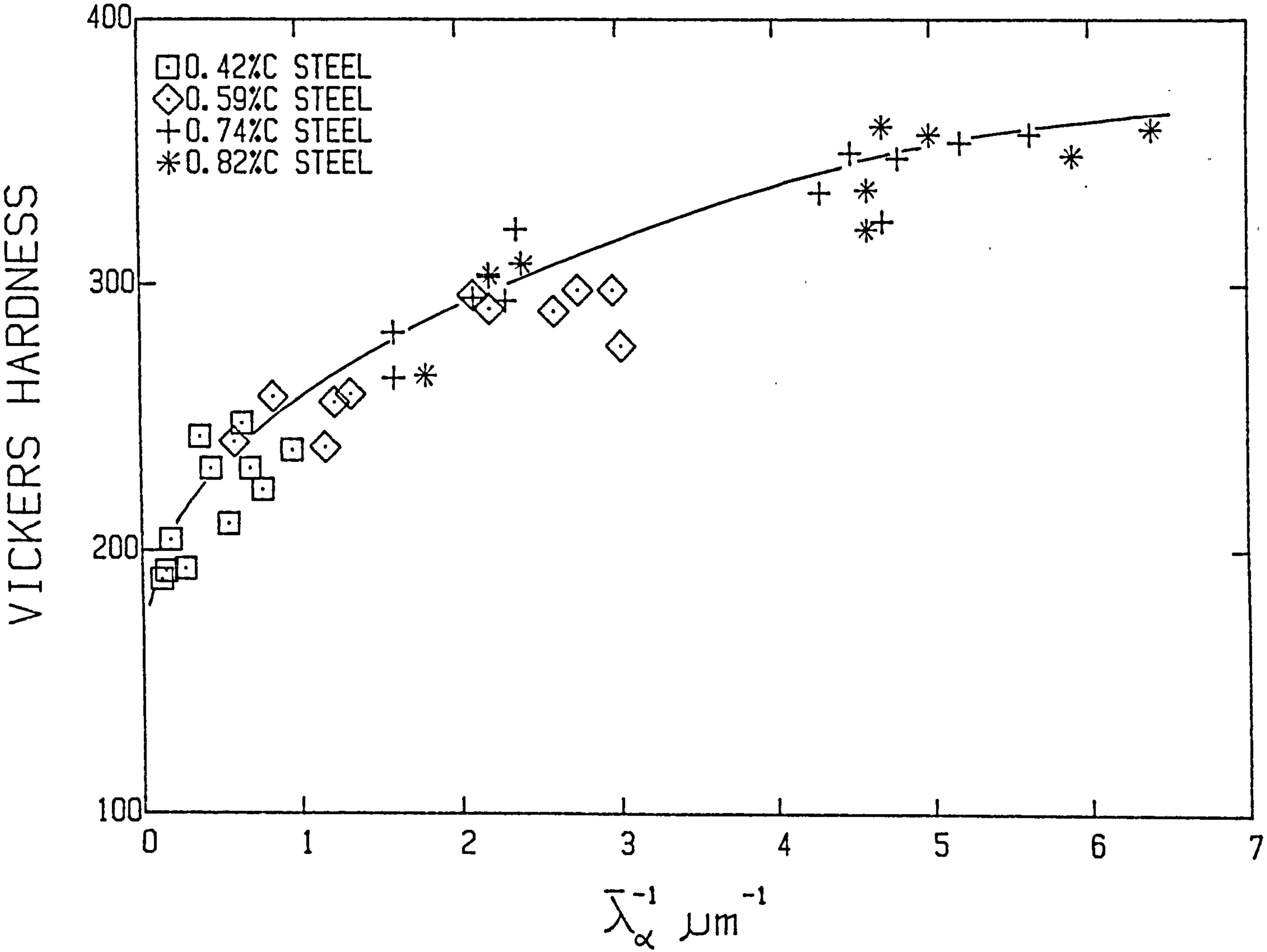

Fig 5.5 Vickers hardness as a function of the reciprocal mean free ferrite distance. (All data).

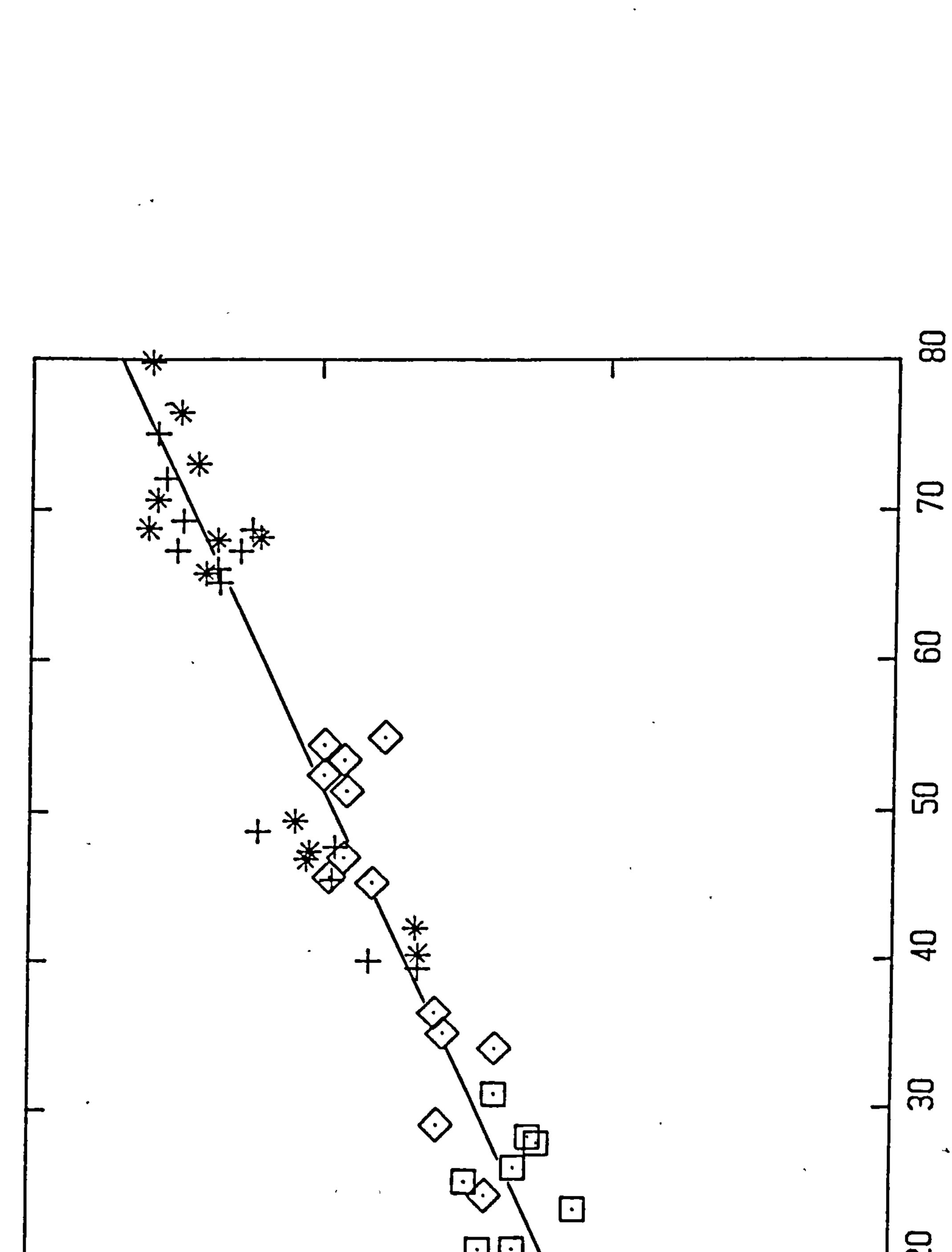

Fig 5.6 Vickers hardness as a function of the reciprocal square root of the mean free ferrite distance. (All data)

is obtained for the Hall-Petch plot. In the case of hardness, where testing may be viewed as an averaging process, the weighted mean approach of $\bar{\lambda}_\alpha$ is obviously useful. A similar study by Jindal and Gurland[123] examined the hardness-microstructure relationship in a range of tempered and spherodised carbon steels (0.065 to 1.23 wt.%C)and obtained an equivalent single linear relationship of the form,

$$H = H_o + K_H \lambda^{-\frac{1}{2}} \qquad (5.18)$$

where H is the hardness, H_o and K_H are constants, and λ is the carbide spacing.

Although differences in heat treatment and microstructural interpretation prevent a direct comparison, it is clear that the hardness of spherodised, lamellar and mixed lamellar non-lamellar carbon steels obey a Hall-Petch relationship when plotted against the reciprocal square root of the appropriate mean slip distance in the ferrite.

5.3.1.3 Yield and Flow Stress

The corresponding 0.2% proof stress $\bar{\lambda}_\alpha^{-1}$ and $\bar{\lambda}_\alpha^{-\frac{1}{2}}$ correlations are given in Figs. 5.7 and 5.8. Although both display linear relationships, Fig. 5.7 is probably more accurately described by a curve, particularly at large values of $\bar{\lambda}_\alpha$. On this basis it would appear that the Orowan[71] dispersion strengthening model is inappropriate for the microstructures of the present study, As will be seen later, rejection of this model is justified when large 'grain size' (i.e. $\bar{\lambda}_\alpha^{-1} \rightarrow 0$) data points are included in the graphs. When $\bar{\lambda}_\alpha$ is regarded as the effective ferrite grain diameter in a Hall-Petch relationship with the 0.2% proof stress,

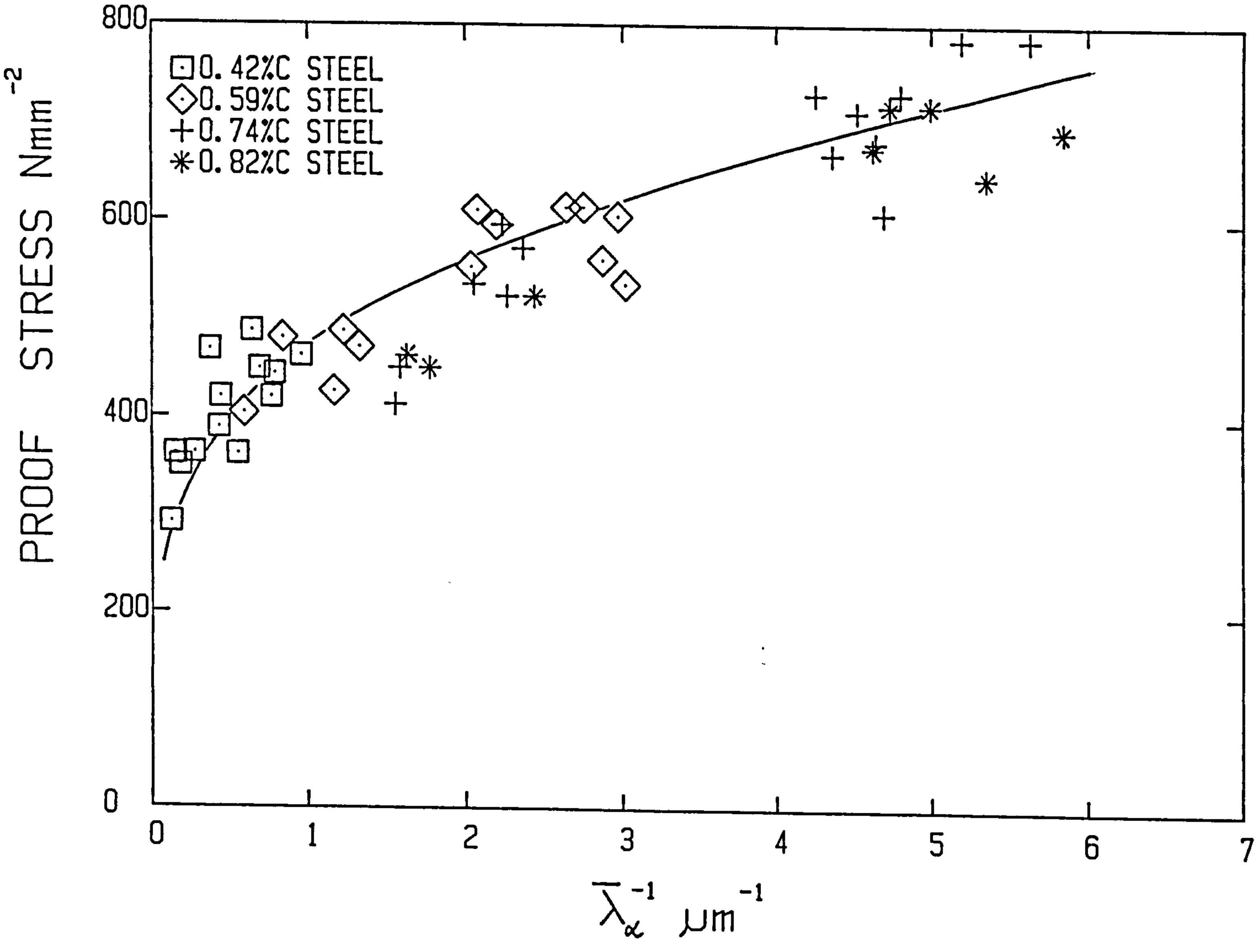

Fig 5.7 The variation in 0.2% proof stress with the reciprocal mean free ferrite distance. (All data).

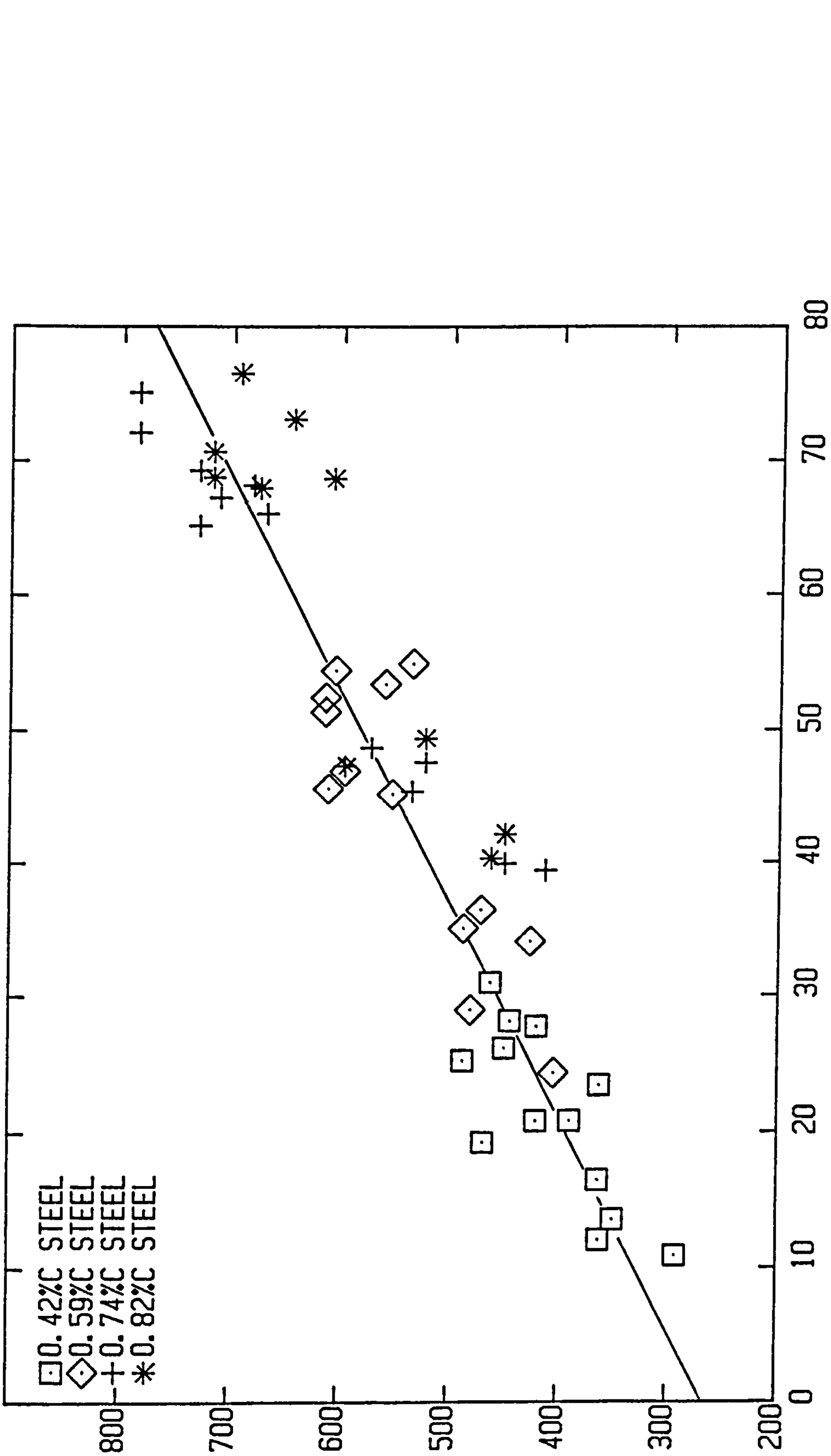

Fig 5.8 **The variation in 0.2% proof stress with the reciprocal square root of the mean free ferrite distance. (All data)**

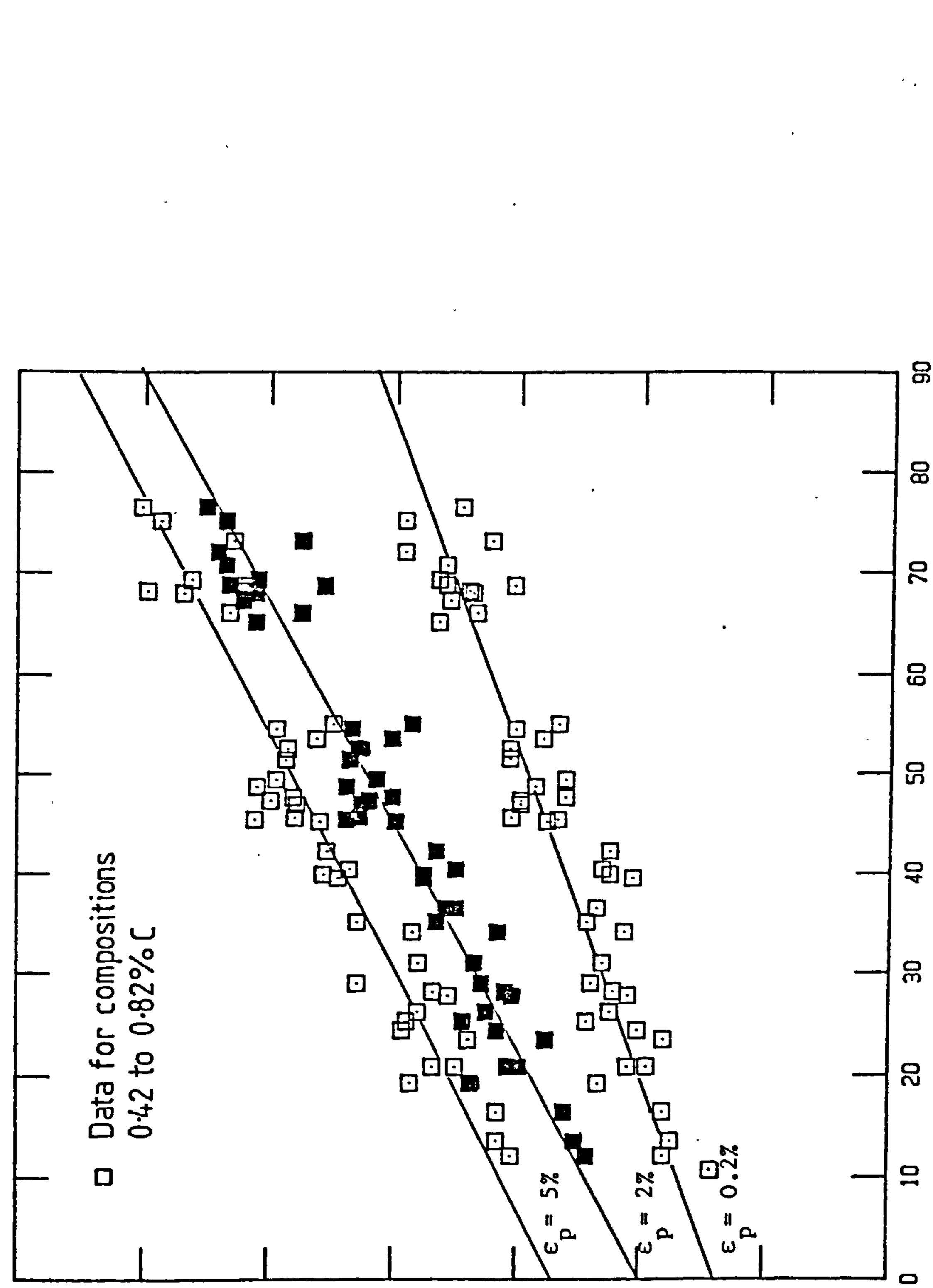

Fig 5.9 The correlation between the mean free ferrite distance and the flow stress at constant strain. (All data for compositions 0.42 to 0.82 wt%C)

a linear plot and a positive friction stress is found, In addition the flow stress at 2% and 5% plastic strain also give linear relationships with $\bar{\lambda}_\alpha^{-\frac{1}{2}}$ (Fig. 5.9) and thus fit the above model.

It should be noted at this point that deformation in ferrite-pearlite steels is assumed to be macroscopically homogeneous. As discussed by Karlsson et al[107], this is not strictly correct and the flow stress of the aggregate is more precisely described in terms of load transfer between the easier deformed ferrite and the more rigid pearlite. Nevertheless, such an approximation does lead to a highly predictive structure-property model, and on these grounds may be acceptable.

The fact that the Hall-Petch slope in Fig. 5.9 increases with strain is contrary to the work of Armstrong et al[55] on mild steel but is in agreement with the studies on fully pearlitic steels by Embury and Fisher[81] and Tukahashi and Nagumo[112]. Using the work hardening theory[62,64] as outlined in Section 2.1.1 and the grain boundary source model of Li[63], the latter authors[112] have explained this change in slope as follows. Using a similar approach to that given in Section 2.1.1.1, Takahashi and Nagumo[112] argue that the dislocation density ρ is proportional to the imposed strain ϵ and is inversely proportional to the average distance of slip of a dislocation. Although these authors only considered the case of fully pearlitic steels where the mean slip distance was the average width of the pearlitic ferrite, their model may be extended to ferrite-pearlite microstructures by assuming that ρ is also proportional to $\epsilon/\bar{\lambda}_\alpha$.

From equation 2.9 the flow stress is given by,

$$\sigma_f(\epsilon) = \sigma_o(\epsilon) + \alpha\mu b\rho^{\frac{1}{2}} \qquad (5.19)$$

where μ is the shear modulus, b the dislocation Burgers vector and α is a constant.

Substitution for ρ in equation 5.19 gives a Hall-Petch equation. The Hall-Petch slope k is then proportional to $\varepsilon^{\frac{1}{2}}$ and should increase with strain,as is observed. The argument of Takahashi and Nagumo is discussed further in Section 5.3.3.

It would appear therefore from Fig. 5.6 that the flow stress of pearlitic steels in the range 0.42 to 0.82 wt.%C steel can be described by an equation of the form:

$$\sigma_{fl}(\varepsilon_p) = \sigma_o(\varepsilon_p) + k(\varepsilon_p)\bar{\lambda}_\alpha^{-\frac{1}{2}} \qquad (5.20)$$

where $\sigma_{fl}(\varepsilon_p)$, $\sigma_o(\varepsilon_p)$ and $k(\varepsilon_p)$ are the flow stress, friction stress and Hall-Petch slope at a given plastic strain ε_p. This equation is similar to that given by Armstrong et al[55] (see Section 2.1) where the ferrite grain size is replaced by $\bar{\lambda}_\alpha$, the mean free distance in ferrite. As was discussed in Section (2.2.1), precisely the same conclusion was reached by Lui and Gurland[78] for spheroidised carbon steels. Although the results of the present study are for considerably finer structures, there is good agreement between both studies, given the differences in composition, heat treatment and microstructural interpretation.

The fact that the friction stress value of $\simeq 260$ Nmm^{-2} obtained from the plot of 0.2% proof stress versus $\bar{\lambda}_\alpha^{-\frac{1}{2}}$ is much larger than that for ferrite ($\simeq 82$ Nmm^{-2} for the manganese and silicon levels of the present study) needs some explanation. Apart from the use of 0.2% proof stress as opposed to the true yield stress, one possible reason lies in the assumption implied earlier that the pro-eutectoid ferrite contains no grain boundaries. This

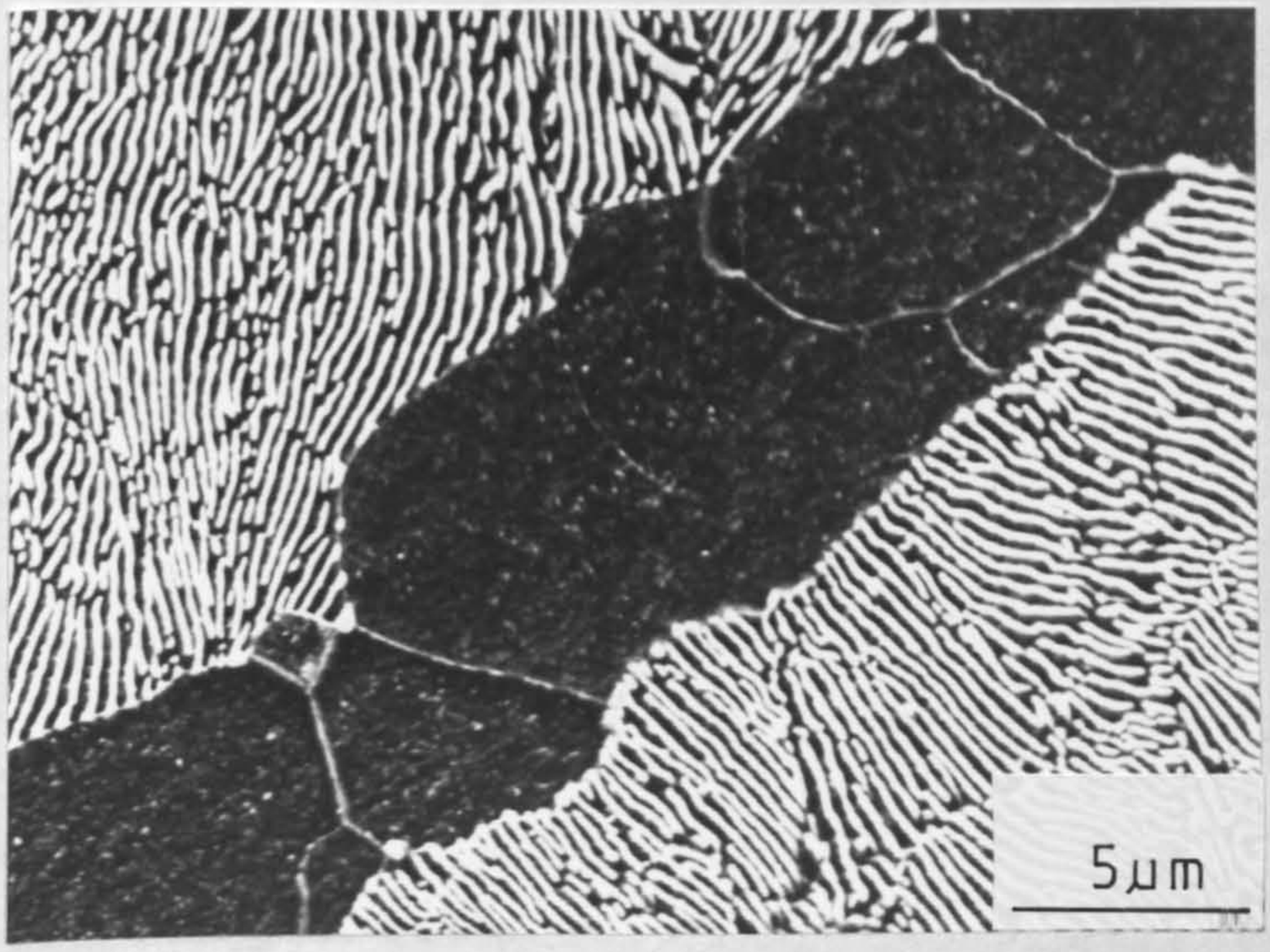

Fig 5.10 SEM micrograph showing grain boundaries in pro-eutectoid ferrite. (Specimen 4A5).

where $d_p = (\bar{S}_r - \bar{t}_r)$ is the m.f.f.d in pearlite, σ_o is the friction stress and k_α and k_p are the Hall-Petch parameters for ferrite and pearlite respectively. As shown in Appendix A, the model of Reuben and Baker[110] leadsto an equation, for the yield stress of a ferrite-pearlite composite, of the form,

$$\sigma_c = \sigma_o + [k_\alpha + (k_p - k_\alpha) V_p] d_c^{-\frac{1}{2}} \quad (5.24)$$

where the composite ferrite 'grain size' d_c is given by,

$$d_c^{\frac{1}{2}} = V_p d_p^{\frac{1}{2}} + V_\alpha d_\alpha^{\frac{1}{2}} \quad (5.25)$$

k_p, the corresponding stress intensity factor for pearlite will weakly reflect the pearlite or grain or nodule size.

As will be seen later in Part 2 of this study,there is substantial evidence in the literature to show that the crystallographic orientation of ferrite is constant within a given colony, and constant or closely aligned between a number of colonies of common parentage[21]. Thus, as there will be little or no misorientation between adjacent lamellar within a pearlite colony, the major misorientation between slip planes in pearlitic ferrite should occur at high angle pearlite nodule (or grain) boundaries and to a lesser extent across colony boundaries. As the Taylor[56] parameter accounts for the orientation difference between the existing slip system and those in the neighbouring unyielded grains, the average value of m should be somewhat less in pearlite than in ferrite. k_α is therefore expected to be greater than k_p and since $d_c^{-\frac{1}{2}}$ is not much different from $\bar{\lambda}_\alpha^{-\frac{1}{2}}$, it is anticipated from equations 5.24 and 5.25 that the single linear relationship shown in Fig. 5.8 is in fact a family of lines each with a slightly different slope according

to the volume fraction of pearlite. In support of this conclusion other experimenters have noticed variations in the Hall-Petch slope at high[84] and low[124] volume fractions of pearlite. The consequence of having a number of lines would be to decrease the effective slope for a given set of results, thus giving a high intercept. This may then contribute to the high friction stress obtained from Fig. 5.8.

To test such a conjecture the data for the fully pearlitic microstructures were plotted against $d_c^{-\frac{1}{2}}$, where $d_c^{-\frac{1}{2}} = (\bar{S}_r - \bar{t}_r)^{-\frac{1}{2}}$, (Fig. 5.11) and the slope taken as the value of k_p (i.e.≃7.8 $Nmm^{-3/2}$). This value, together with k_α from equation 5.1, allows lines to be drawn through the extreme ends of the volume fraction range of the present study ($V_p \simeq 0.65$ to 1.0) Fig. 5.11. Although insufficient results are available at each volume fraction for a two variable linear regression analysis, there does appear to be some evidence to substantiate the prediction of equation 5.24 and this is made clearer by considering the work of Preston[124].

Preston[124] examined the effect of pearlite on the yield stress of structural steels in the range 0.04 to 0.21 wt.%C. He argued that the presence of carbides or small pearlite colonies at ferrite grain boundaries might be expected to hinder the activation of dislocations in adjacent ferrite grains. Thus the value of k_α in a Hall-Petch plot should increase with volume fraction of pearlite. Preston[124] postulated a relationship of the form,

$$\sigma_c = \sigma_o + k_\alpha(1 + KV_p)d^{-\frac{1}{2}} \qquad (5.26)$$

where K is a constant.

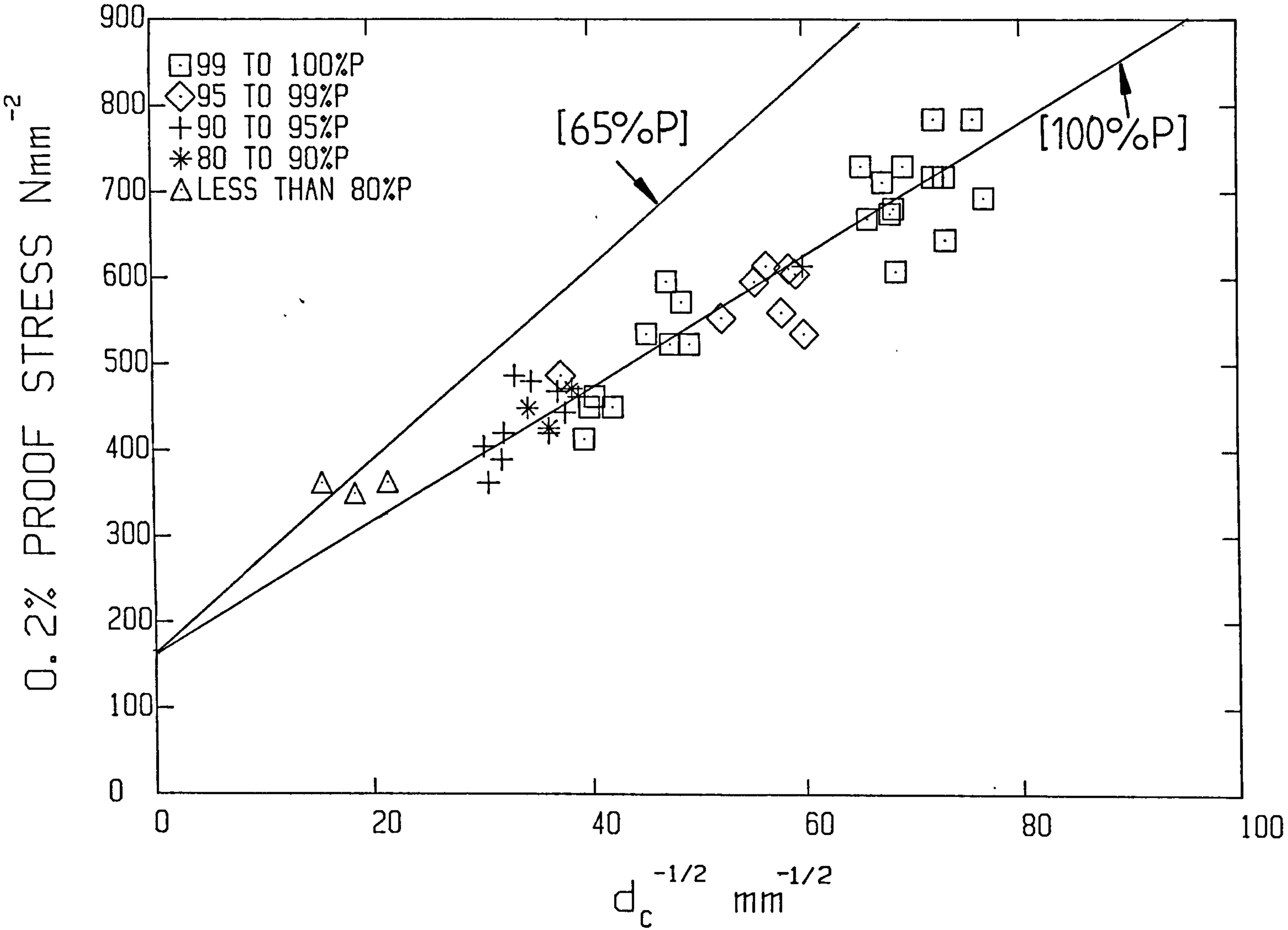

Fig 5.11 The 0.2% proof stress as a function of the composite mean ferrite grain size.

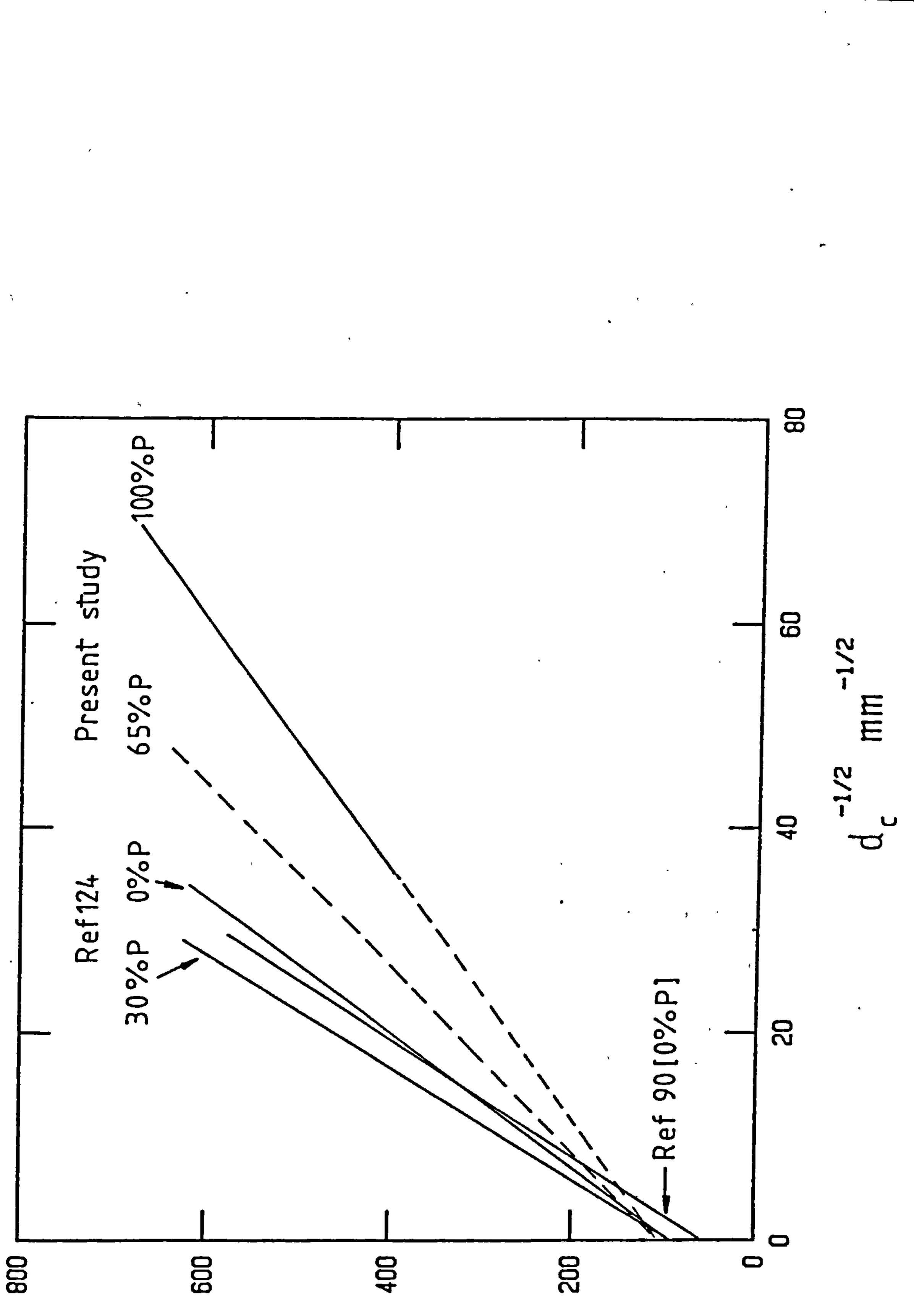

Fig 5.12 The yield & 0.2% proof stress as a function of the composite mean ferrite grain size(d_c) for the data of Preston[124] and the present study.

Multiple regression analysis performed on measured data gave[124],

$$\sigma_c \ (Nmm^{-2}) = 114 + 26.7 \text{ wt.\%Mn} + 15.0 \ (1 + 0.58 \ V_p) d_\alpha^{-\frac{1}{2}} \qquad (5.27$$

The lines for 0 and 30% pearlite, corrected for solid solution strengthening, are given in Fig. 5.12. Although there appears to be an inconsistency over the direction of the slope change with increasing volume fraction of pearlite, Reuben and Baker[110] have shown that this can be attributed to the fact that Preston[124] measured only d_α in ferrite-pearlite microstructures whereas the present study used the composite grain size d_c. Since $(\bar{S}_r - \bar{t}_r) < d_\alpha$, employing d_α only, gives $d_c^{\frac{1}{2}} = (1 - V_p) d_\alpha^{\frac{1}{2}}$ and equation 5.24 may be rearranged to give,

$$\sigma_c = \sigma_o + k_\alpha \left[1 + \frac{k_p}{k_\alpha} \frac{V_p}{1-V_p} \right] d_\alpha^{-\frac{1}{2}} \qquad (5.28)$$

This equation is very similar to equation 5.26 and understandably the volume fraction dependence could be regarded as linear over a small range. It is worth noting that the value of 0.58 for K obtained by Preston[124] (see equation 5.27) is close to the value of 0.45 calculated for k_p/k_α using k_p (0.78 $Nmm^{-3/2}$) from the present study and the k_α of Gladman et al[90]. As pointed out by Reuben and Baker[110] this small difference can be explained by the fact that $V_p/1 - V_p$ is slightly larger than V_p for the range of pearlite volume fractions studied by Preston[124] (0% to 30%).

5.3.2.1 Low Carbon - Steel Data

As a further check on the validity of equation 5.24 two low carbon steels of similar manganese and silicon contents as the steels used in the main body of the work (Table 5.2) were heat treated

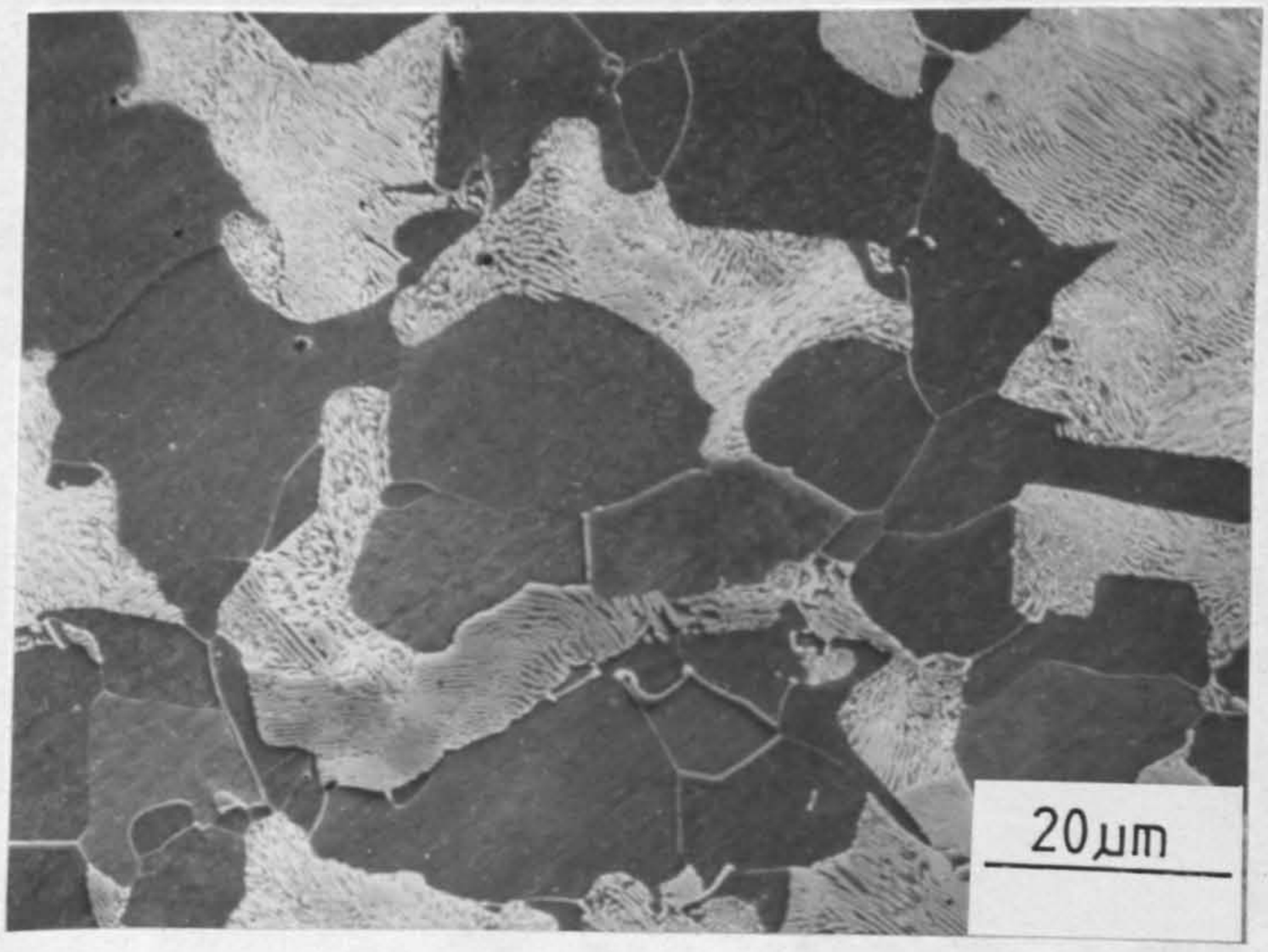

Fig 5.13 SEM micrograph of ferrite-pearlite microstructure in the low-carbon steel SM1257.

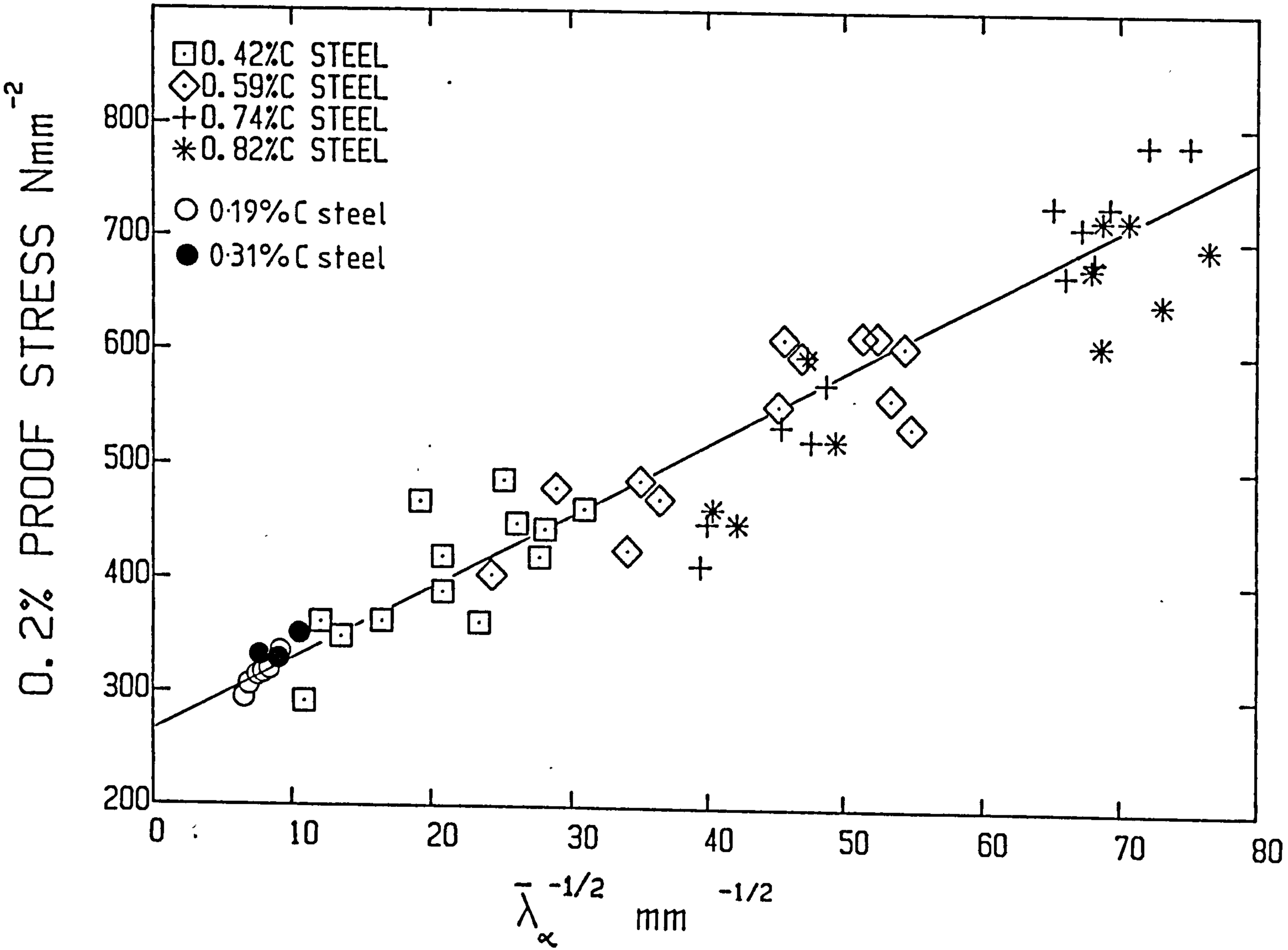

Fig 5.14 The yield stress and 0.2% proof stress as a function of the mean free ferrite distance for the range of steels studied from 0.19 to 0.82wt%C.

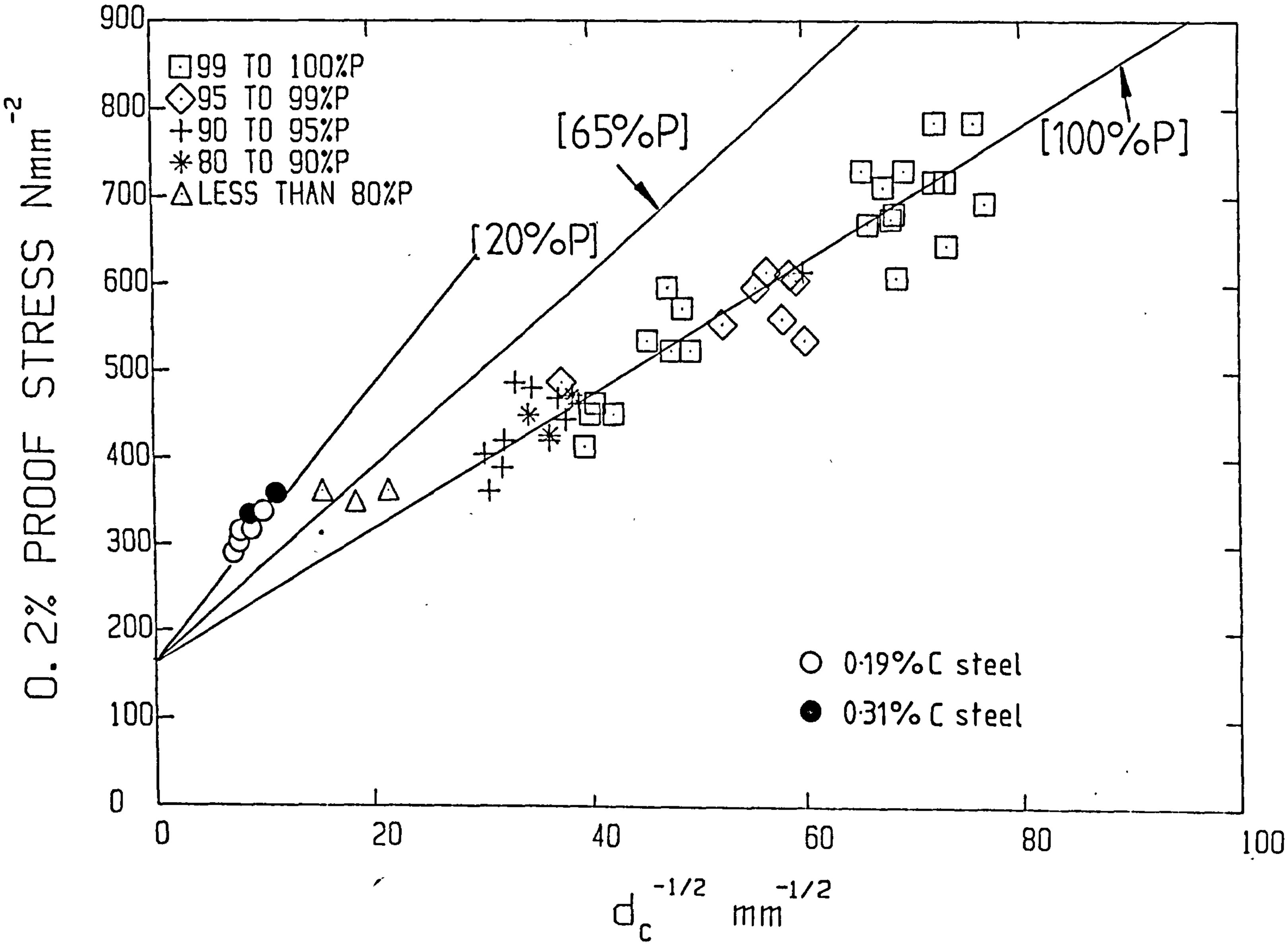

Fig 5.15 The yield stress and 0.2% proof stress as a function of the composite mean ferrite grain size. (Data for steels 0.19 to 0.82 wt%C)

as indicated in Table 5.3. Metallographic examination revealed typical ferrite-pearlite microstructures, as shown in Fig. 5.13, and measured values of V_α, d_α and $\bar{S}_r$ are also given in Table 5.3. When the lower yield stress values given in Table 5.4 are plotted against $\bar{\lambda}_\alpha^{-\frac{1}{2}}$ and $d_c^{-\frac{1}{2}}$ (Fig. 5.14 and 5.15) it is clear that the data fit Hall-Petch plots with both $\bar{\lambda}_\alpha$ and d_c. It may be noted that if $\bar{\lambda}_\alpha^{-1}$ values were plotted on Fig. 5.7 it is readily apparent that this Orowan[71] plot is indeed a curve as concluded earlier. This further supports the use of a modified Hall-Petch analysis to describe strengthening in pearlitic steels.

Unfortunately, as in the work of Preston[124], fine enough ferrite grain sizes were not obtained to give values of yield stress above 400 Nmm^{-2}. As a result, within this rather coarse range, it would be difficult on a purely predictive basis to reject $\bar{\lambda}_\alpha$ in favour of d_c. However, as shown in Fig. 5.15, when the line for $V_p = 0.2$ (the lower limit of the low carbon steel data) is drawn, a satisfactory correlation is obtained. In addition, it will be noted that the friction stress resulting from the intercept of all lines at $d_c^{-\frac{1}{2}} = 0$ is very close to the corresponding ferrite intercept predicted by equation 5.1 when solid solution effects are considered.

5.3.3 Proposed Strengthening Mechanisms

Although experimental data can be accurately defined by a Hall-Petch relationship as the present study has shown, its use has not been without criticism. The two main questions posed are firstly, whether a dislocation pile-up mechanism truly operates at such small 'grain sizes' and in a system where pile-ups have not been observed, and secondly, if so, in what way does slip by-pass cementite lamellae. It is therefore worth commenting on the nature of the strengthening in pearlitic steels.

Embury and Fisher[81], Chadwick[125,126] and Sevillano[103] regard the operation of a pile-up model in pearlite as improbable given the relatively small dimensions of the ferrite 'grain size'. However, Armstrong et al[127] have shown that the Hall-Petch relationship is in fact applicable down to very small grain sizes (i.e. ≃100 Å) providing that a modification is made to account for the significant influence of individual dislocations upon the stress concentration characteristics of the pile-up.

Langford[121] postulated a Hall-Petch relationship on the basis of the attainment of the cementite shear strength at the head of the pile-up in the pearlitic ferrite. Thus the flow stress is proportional to the reciprocal square root of the ferrite lamellae width. At extremely fine interlamellar spacings of ≃100Å, Langford[121] considered the generation of dislocations required in the pile-up as an important component of the work of deformation, and therefore the flow stress expression would contain an additional term proportional to the reciprocal of this width. It must be stated, however, that the work of Embury and Fisher[81] and Langford[121] is on heavily deformed pearlitic wire where the interlamellar spacing decreased in proportion to the wire diameter. In the present study, ferrite mean free distances were one to two orders of magnitude greater than the pearlite spacings measured by these authors (of <50nm) and accordingly a conventional dislocation pile-up model is likely to be more feasible.

As discussed in Section 2.1.1 an alternative non-pile-up explanation for a $d^{-\frac{1}{2}}$/flow stress relationship is that proposed by Li[63]. Li derived the same relationship as Hall[53] and Petch[54] by calculating the internal stress due to the dislocations generated

at grain boundaries, either by deformation of the boundary or by the generation of dislocations from grain boundary ledges. In simple terms, the flow stress is proportional to $\rho^{\frac{1}{2}}$ where ρ is the dislocation density. The application of such a model to pearlite has obvious attractions, as the ferrite-cementite interface is often regarded as a favoured nucleation site for dislocations, and heavy dislocation densities at the interface are commonly observed even at relatively low values of strain[81,105,112,128]. In addition, the semi-coherent lamellar interface of pearlite incorporates a dislocation grid and hence may be viewed as having a certain capacity for the emission of dislocations[22,103,112]. As discussed earlier Takahashi and Nagumo[112], taking the lead from the work of Li[63], have shown theoretically that ρ can be related to mean slip distance in ferrite. This gives a Hall-Petch relationship where the dislocation density is due to generation at the lamella interface and partly to multiplication within the ferrite. Beside those discussed above, other methods have been suggested in which slip can proceed through pearlite. Puttick[129] noticed that slip in pearlitic ferrite could occasionally traverse a number of lamellae at their growth faults. Takahashi and Nagumo[112] supported these observations by noting the extension of a slip band through existing gaps in cementite lamellae. Such a mechanism may be envisaged to occur in coarse spheroidised microstructures where a small yield point is often detected[69].

At higher strains, the strengthening mechanisms will involve dislocation cells which, as discussed by Embury and Fisher[81], may comprise a complex arrangement of dislocations and carbide fragments. As in the case of spheroidised carbon steels[79], the

cell walls then become the major obstacle to slip, although it should be said that the effectiveness of dislocation cell structures in spheroidite may not necessarily be the same as in pearlite. More work is therefore needed to clarify the precise nature of the strengthening mechanisms in pearlitic steels in terms of dislocation pile-ups, generation of dislocations from the ferrite-cementite interface or the formation of dislocation cells. This is obviously dependent on the scale of the microstructure, the morphology of the cementite, and the imposed strain. The mechanism of strengthening may therefore change as deformation proceeds.

Summary

The present study has thus shown that a Hall-Petch equation can be applied satisfactorily to a wide range of pearlitic steels when care is taken in obtaining the appropriate 'grain size' or obstacle spacing for a given microstructure. Mean random spacing measurements are particularly useful as they will accurately reflect the average slip distance in the pearlitic ferrite of both lamellar and non-lamellar microstructures. Furthermore, in contrast to other commonly used pearlite spacing measurements they do not rely on the application of conversion factors which are probably only suitable over a narrow range of 'ideal' lamellar structures. As similar measurements of mean obstacle spacing by Lui and Gurland[78] and Hodgson[79] have shown a Hall-Petch relationship to apply to spheroidised carbon steels, it is tempting to agree with the prediction of Gensamer et al[69], that the strength of a two-phase aggregate comprising a hard phase dispersed in a soft matrix is proportional to the mean straight path through the

continuous phase, irrespective of whether the second phase is lamellar or spheroidal. The nature of this proportionality is thus given by a Hall-Petch equation.

PART 1: CONCLUSIONS

The relationship between heat treatment variables and the microstructure, hardness and strength has been studied for a range of pearlitic steels. The conclusions drawn from this investigation are listed below.

Microstructure:

1) A study of the microstructure revealed that fully lamellar pearlite forms only within a narrow range of cooling rates and transformation temperatures and may depend on the composition of the steel studied.

2) Large amounts of non-lamellar pearlite were observed preferentially in low carbon hypo-eutectoid steels. Both very slow and rapid cooling rates lead to non-lamellar pearlite in all compositions.

Transformation temperature and microstructure:

3) The temperature for the austenite to pearlite (or ferrite and pearlite) transformation decreased with increasing prior-austenite grain size and with faster cooling rates. However, only in the latter case was the mean random pearlite spacing correspondingly refined.

4) In specimens which had been rapidly forced air cooled to the start of the transformation and then allowed to transform in still air and pearlite spacings were not directly related to the transformation temperatures.

5) Comparison of microstructure with transformation data suggested that the time taken for the transformation to go to completion dictates the mean pearlite inter-lamellar spacing, irrespective of the prior-austenite grain size or cooling mode (interrupted or continuous cooling).

6) It is suggested that the growth rate, which is dependent primarily on the cooling rate in continuously cooled specimens, determines the time available for the diffusion of carbon atoms. The diffusion rate in turn dictates the pearlite spacing.

Microstructure hardness and strength:

7) For the range of carbon contents (0.42 to 0.82 wt.%) and heat treatments used in this study refining the pearlite interlamellar spacing by accelerated cooling increased the hardness and strength of each of the steels studied. This effect was independent of the prior-austenite grain size.

8) In contrast with previous reports in the literature it was found that a modified Hall-Petch equation can be applied satisfactorily to a wide range of pearlitic steels when care is taken in obtaining the appropriate mean slip distance for a given microstructure.

9) From the limited measurements in the present study the relationship between the minimum observed, mean true and mean random pearlite interlamellar spacing is not constant and may depend on the composition of the steel studied.

10) Mean random pearlite spacing ($\bar{S}_r$) measurements are therefore believed to be the most reliable and accurate method of evaluating the mean slip distance in both lamellar and non-lamellar pearlite.

11) Using a simple law of mixtures this parameter was combined with the measured ferrite volume fraction (V_α) ferrite grain size (d_α), prior-austenite grain size ($\bar{L}_\gamma$) and calculated cementite lamella thickness ($\bar{t}_r$) to evaluate the mean slip distance in the ferrite-pearlite composite, $\bar{\lambda}_\alpha$, i.e.

$$\bar{\lambda}_\alpha = (1 - V_\alpha)(\bar{S}_r - \bar{t}_r) + V_\alpha d_\alpha (\text{or } V_\alpha^2 \bar{L}_\gamma)$$

12) When $\bar{\lambda}_\alpha$ was substituted for the ferrite grain size in a Hall-Petch equation a single linear relationship was found for a correlation with both the hardness and flow stress of pearlitic steels of carbon content between 0.19 and 0.82 wt.%.

13) The correlation of $\bar{\lambda}_\alpha$ with the 0.2% proof stress gave an improvement in the prediction of the friction stress over that when the minimum interlamellar spacing was used in a Hall-Petch equation. However, the positive value obtained for the friction stress was higher than should be expected for the case of 100% ferrite.

14) Further improvement was suggested by considering an equation of the form,

$$\sigma_c = \sigma_o + \left[k_\alpha + (k_p - k_\alpha) V_p \right] d_c^{-\frac{1}{2}}$$

where the composite ferrite grain size is given by,

$$d_c^{\frac{1}{2}} = V_p (\bar{S}_r - \bar{t}_r)^{\frac{1}{2}} + V_\alpha d_\alpha^{\frac{1}{2}}$$

15) Application of this equation to the measured microstructural and strength data for the entire range of steels studied (0.19 to 0.82 wt.%C) indicated that the single linear relationship with $\bar{\lambda}_\alpha$ may in fact be a family of lines,each with a slightly different slope according to the volume fraction of pearlite.

16) The friction stress was then found to be very close to that for pure ferrite with increasing volume fraction of pro-eutectoid ferrite having the effect of increasing the Hall-Petch slope while retaining the same value for the friction stress.

Specimen No.	Austenitising Temp. °C	Cooling Data		Transformation Data			MEASURED			CALCULATED	
		Method	Rate °Csec^{-1}	Time Sec.	Temperature °C Tmin.	Tmax.	Ferrite Volume Fraction V_α	Prior Austenite Grain Size L_γ (μm)	Mean Random Pearlite Spacing $\bar{S}_r$ (nm)	Mean Random Cementite Thickness $\bar{t}_r$ (nm)	Mean Free Ferrite Distance $\bar{\lambda}_\alpha$ (μm)
SL174A1	900	Forced air	18.1	10	649	654	0.12	51.6 ±6%	365 ±4%	26,1	1.041
" 4A2	"	"	10.5	13	658	663	0.15	"	375	27.8	1.456
" 4A3	"	"	7.0	20	660	670	0.14	"	357	26.1	1.296
" 4A4	"	air	3.5	53	638	643	0.25	"	623	52.3	3.653
" 4A5	"	vermiculite	0.9	120	660	670	0.35	"	751	72.8	6.762
" 4A6	"	interrupted	13.5	17	660	667	0.14	"	308	22.6	1.257
" 4A7	1000	air	3.7	30	643	653	0.22	100	803	64.8	5.416
" 4A8	1200	Forced air	15.4	9	633	633	0.11	197	342	23.4	1.557
" 4A9	"	"	12.2	13	633	633	0.08	"	365	25.8	2.679
" 4A10	"	"	8.0	18	638	641	0.10	"	384	26.9	2.286
" 4A11	"	air	3.3	58	631	637	0.08	"	641	43.9	1.808
" 4A12	"	vermiculite	0.6	204	653	662	0.20	"	764	60.2	8.423
" 4A13	"	interrupted	13.8	19	633	642	0.10	"	394	27.6	2.295

Table 4.1 Heat treatment, transformation data and microstructural measurements for the 0.42 wt%C steel.

Specimen No.	Vickers Hardness	TENSILE DATA (Nmm^{-2}) STRESS At ϵ_p = 0.2%	ϵ_p = 2%	ϵ_p = 5%	UTS	% Reduction in CSA	Elongation
SL174A1	238 ± 5	462	669	760	779	45	23.5
" 4A2	231 " 6	449	649	760	782	48	24.0
" 4A3	223 " 5	420	608	711	736	50	25.7
" 4A4	193 " 2	363*	523	632	706	48	31.5
" 4A5	192 " 3	362*	486	608	675	48	30.8
" 4A6	226 " 6	444	620	736	766	52	29.0
" 4A7	204 " 2	350*	505	632	693	50	33.2
" 4A8	248 " 9	487	687	778	794	27	20.9
" 4A9	243 " 7	468	675	772	787	32	21.2
" 4A10	231 " 4	420	614	736	772	33	23.4
" 4A11	210 " 3	362	553	678	729	30	25.5
" 4A12	189 " 4	292	-	-	669	44	30.1
" 4A13	243 " 7	389	596	699	730	40	27.7

*Lower yield stress.

Table 4.2 Tensile test results for the 0.42 wt %C steel

Specimen No.	Austeni-:tising Temp. °C	Cooling Data		Transformation Data			MEASURED			CALCULATED	
		Method	Rate °Csec^{-1}	Time Sec.	Temperature °C Tmin.	Tmax.	Ferrite Volume Fraction V_α	Prior Austenite Grain Size L_γ (μm)	Mean Random Pearlite Spacing $\bar{S}_r$ (nm)	Mean Random Cementite Thickness $\bar{t}_r$ (nm)	Mean Free Ferrite Distance $\bar{\lambda}_\alpha$ (μm)
SL175A1	900	Forced air	16.7	7	647	652	0.06	47.1±6%	227±4%	21.4	0.363
" 5A2	"	"	13.9	10	649	654	0.05	"	255 "	23.8	0.337
" 5A3	"	"	7.0	23	648	673	0.05	"	247 "	23.0	0.331
" 5A4	"	air	3.5	48	643	667	0.07	"	618 "	58.8	0.751
" 5A5	"	vermiculite	0.9	264	639	661	0.08	"	669 "	64.3	0.858
" 5A6	"	interrupted	16.0	12	646	657	0.05	"	268 "	25.0	0.349
" 5A7	1000	air	4.0	50	619	639	0.05	97 "	660 "	61.5	0.811
" 5A8	1200	Forced air	15.4	7	628	628	0.04	136 "	237 "	21.8	0.481
" 5A9	"	"	12.6	12	623	632	0.04	"	271 "	25.0	0.454
" 5A10	"	"	9.9	14	618	623	0.03	"	290 "	26.5	0.378
" 5A11	"	air	3.2	58	625	649	0.07	"	617 "	58.7	1.187
" 5A12	"	vermiculite	0.5	240	653	669	0.09	"	706 "	68.7	1.684
" 5A13	"	interrupted	13.8	19	623	642	0.04	"	311 "	28.7	0.489

Table 4.3 Heat treatment, transformation data and microstructural measurements for the 0.59 wt %C steel.

Specimen No.	Vickers Hardness	TENSILE DATA (Nmm^{-2}) STRESS At ϵ_p = 0.2%	ϵ_p = 2%	ϵ_p = 5%	UTS	% Reduction in CSA	% Elongation
SL175A1	298 ± 6	614	857	970	985	42	24.3
" 5A2	298 " 8	605	867	988	1007	38	23.7
" 5A3	277 " 4	535	772	897	918	45	25.9
" 5A4	259 " 3	471	699	715	876	40	25,7
" 5A5	238 " 1	426	632	769	815	35	27.3
" 5A6	291 " 10	560	803	924	943	42	25.9
" 5A7	256 " 3	487	730	857	891	35	24.0
" 5A8	296 " 7	611	854	958	960	15 *	17.6
" 5A9	291 " 8	596	851	955	967	10 *	16.9
" 5A10	290 " 3	614	870	973	979	~9 *	16.3
" 5A11	258 " 6	480	657	857	894	23	20.0
" 5A12	241 " 5	404	632	785	833	30	25.0
" 5A13	281 " 5	553	797	918	955	15 *	19.0

*Fractured just after UTS.

Table 4.4 Tensile test results for the 0.59 wt%C steel.

Specimen No.	Austeni-:tising Temp. °C	Cooling Data		Transformation Data			MEASURED			CALCULATED	
		Method	Rate °Csec^{-1}	Time Sec.	Temperature °C Tmin.	Tmax.	Ferrite Volume Fraction V_α	Prior Austenite Grain Size L_γ (μm)	Mean Random Pearlite Spacing S_r (nm)	Mean Random Cementite Thickness $\bar{t}_r$ (nm)	Mean Free Ferrite Distance $\bar{\lambda}_\alpha$ (μm)
R1	900	Forced air	17.9	7	620	645	0.010	96 ±6%	191 ±4%	21.4	0.177
R2	"	"	15.2	9	635	650	0.007	"	231 "	25.8	0.208
R3	"	"	7.0	17	642	662	0.006	"	237 "	26.5	0.213
R4	"	air	3.2	48	641	674	0.0	"	496 "	55.6	0.441
R5	"	vermiculite	0.9	174	648	678	0.0	"	721 "	80.1	0.641
R6	"	interrupted	18.9	15	640	659	0.003	"	257 "	28.6	0.229
R7	1000	air	4.0	45	608	642	0.002	97 "	546 "	60.7	0.485
R8	1200	Forced air	13.8	14	597	604	0.004	199 "	214 "	23.9	0.193
R9	"	"	12.2	16	600	604	0.005	"	244 "	27.2	0.220
R10	"	"	8.1	24	617	626	0.006	"	258 "	28.8	0.235
R11	"	air	3.5	72	615	629	0.003	"	474 "	52.8	0.421
R12	"	vermiculite	0.5	276	641	663	0.0	"	706 "	78.4	0.628
R13	"	interrupted	13.8	20	609	628	0.008	"	236 "	26.4	0.221

Table 4.5 Heat treatment, transformation data and microstructural measurements for the 0.74 wt%C rail steel.

Specimen No.	Vickers Hardness	TENSILE DATA (Nmm^{-2}) STRESS At ϵ_p = 0.2%	ϵ_p = 2%	ϵ_p = 5%	UTS	% Reduction in CSA	% Elongation
R1	357 ± 11	785	1070	1174	1174	33	22.0
R2	348 " 10	730	1019	1125	1131	35	21.7
R3	324 " 5	608	912	1034	1046	32	23.2
R4	294 " 1	523	803	961	985	18	22.1
R5	265 " 3	413	751	888	912	13	21.7
R6	336 " 11	669	949	1064	1070	38	24.3
R7	295 " 6	535	875	1022	1046	17	19.9
R8	354 " 10	785	1082	-	1143*	< 5	13.2
R9	350 " 8	712	1043	-	1122*	< 5	13.7
R10	335 " 6	730	1022	-	1086*	< 5	14.0
R11	321 " 5	572	1019	-	1030*	< 5	14.6
R12	282 " 5	450	751	912	943	8	17.3
R13	328 " 5	-	-	-	-	-	-

* Specimen fractured at or before UTS.

Table 4.6 Tensile test results for the 0.74 wt%C rail steel

Specimen No.	Austeni-:tising Temp. °C	Cooling Data		Transformation Data			MEASURED			CALCULATED	
		Method	Rate °Csec^{-1}	Time Sec.	Temperature °C Tmin.	Tmax.	Ferrite Volume Fraction V_α	Prior Austenite Grain Size L_γ (μm)	Mean Random Pearlite Spacing $\bar{S}_r$ (nm)	Mean Random Cementite Thickness $\bar{t}_r$ (nm)	Mean Free Ferrite Distance $\bar{\lambda}_\alpha$ (μm)
SL175B1	900	Forced air	13.6	7	615	635	0.014	65 ±6%	167 ±4%	20.8	0.157
" 5B2	"	"	12.9	11	630	647	0.009	"	191 "	23.7	0.171
" 5B3	"	"	7.3	17	632	660	0.012	"	238 "	29.6	0.215
" 5B4	"	air	3.0	48	636	669	0.0	"	509 "	62.6	0.446
" 5B5	"	vermiculite	0.7	171	650	678	0.001	"	642 "	78.8	0.561
" 5B6	"	interrupted	18.1	14	620	660	0.006	""	212 "	26.2	0.187
" 5B7	1000	air	2.9	66	633	665	0.002	69 "	521 "	64.2	0.456
" 5B8	1200	Forced air	13.5	13	601	606	0.013	160 "	201 "	25.0	0.200
" 5B9	"	"	12.1	10	605	615	0.015	"	203 "	25.3	0.211
" 5B10	"	"	9.4	23	615	620	0.006	"	242 "	29.9	0.216
" 5B11	"	air	3.1	58	615	634	0.0	"	468 "	57.6	0.410
" 5B12	"	vermiculite	0.6	240	645	669	0.0	"	697 "	85.8	0.612
" 5B13	"	interrupted	14.2	18	600	621	0.01	"	248 "	30.8	0.231

Table 4.7 Heat treatment, transformation data and microstructural measurements for the 0.82 wt%C steel.

Specimen No.	Vickers Hardness	TENSILE DATA (Nmm^{-2}) STRESS At ϵ_p = 0.2%	ϵ_p = 2%	ϵ_p = 5%	UTS	% Reduction in CSA	% Elongation
SL175B1	359 ± 12	-	-	-	-	-	-
" 5B2	349 " 10	693	1101	1204	1204	20	19.9
" 5B3	321 " 5	681	1040	1195	1195	25	22.6
" 5B4	303 " 7	596	839	997	1028	23	22.1
" 5B5	266 " 8	450	730	906	949	15	20.1
" 5B6	343 " 12	645	949	1058	1071	35	22.3
" 5B7	304 " 3	-	-	-	-	-	-
" 5B8	357 " 6	718	1070	-	1149*	<5	12.6
" 5B9	360 " 5	718	1064	-	1162*	<5	14.0
" 5B10	336 " 5	675	1022	1137	1137*	<5	14.9
" 5B11	308 " 3	523	827	988	1010	10	20.0
" 5B12	265 " 3	462	699	870	918	13	18.7
" 5B13	340 " 5	-	-	-	-	-	-

* Specimen fractured at or before UTS.

Table 4.8 Tensile test results for the 0.82 wt%C steel.

SAMPLE	wt % C	wt % Si	wt % Mn	wt % P	wt % S	wt % Cr	wt % Mo	wt % Cu	wt % Sn
SM1256	0.19	0.46	0.89	0.017	0.015	0.03	0.02	0.06	0.006
SM1257	0.31	0.36	0.86	0.019	0.016	0.03	0.004	0.05	0.007

Table 5.2 Compositions of low carbon steels

Specimen No.	Austenitising Temp. °C	Cooling Data		Transformation Data			MEASURED			CALCULATED	
		Method	Rate °Csec^{-1}	Time Sec.	Temperature °C Tmin.	Tmax.	Ferrite Volume Fraction V_α	ferrite Grain Size d_α (μm)	Mean Random Pearlite Spacing $\bar{S}_r$ (nm)	Mean Random Cementite Thickness $\bar{t}_r$ (nm)	Mean Free Ferrite Distance λ_α (μm)
56/9V	900	vermiculite	0.2	-	654	654	0.751	17.2 ± 16%	577 ± 4%	66.0	13.04
56/9A	900	air	3.3	-	631	631	0.743	15.5 "	475 "	52.7	11.62
56/95V	950	vermiculite	-	-	-	-	0.760	23.0 "	497 "	59.0	17.58
56/95F	950	furnace	0.1	-	-	-	0.771	27.6 "	597 "	74.3	21.40
56/10V	1000	vermiculite	-	-	-	-	0.784	26.2 "	542 "	71.5	20.64
56/10A	1000	air	-	-	-	-	0.765	19.1 "	486 "	58.9	14.71
57/9V	900	vermiculite	0.3	-	657	662	0.624	15.1 "	582 "	72.0	9.61
57/95V	950	vermiculite	0.3	-	653	657	0.615	25.0 "	622 "	75.1	15.58
57/95F	950	furnace	0.1	-	-	-	0.630	24.1 "	617 "	77.5	15.38
57/10F	1000	furnace	0.3	-	654	660	0.599	20.6 "	578 "	67.0	12.54

Table 5.3 Heat treatment, transformation data and microstructural measurements for the 0.19 & 0.31 wt%C steels.

SPECIMEN No	TENSILE DATA Nmm^{-2}	
	YIELD STRESS	UTS
56/9V	330	529
56/9A	337	550
56/95V	318	526
56/95F	288	515
56/10V	305	525
56/10A	317	539
57/9V	356	610
57/95V	332	592
57/95F	324	579
57 10V	328	593

Table 5.4 Tensile test results for the 0.19 & 0.31 wt%C steels.

APPENDIX A

THE MODEL OF REUBEN AND BAKER[110]

As discussed previously in Section 2.1 yielding in a single phase material occurs when the concentrated shear stress which is relaxed across a grain reaches a critical value at some distance, r, into an adjacent grain. From equation 2.4 this condition is described by,

$$(\tau - \tau_i)\left(\frac{d}{4r}\right)^{\frac{1}{2}} = \frac{m\tau_c}{2}$$

Addition of a second phase has the effect of introducing a second superimposed distribution of strengths as schematically illustrated in Fig. A1. In this case it is assumed that the type II grains have a lower average strength than do type I grains. However, it should be noted that in situ average strengths are not necessarily the same as the average strengths of the corresponding single phase materials since conformity criterion may require that either type I or type II grains deform on unfavourable slip systems. The probability P_I that a given yielding grain is of type I, will be related to the volume fraction of type I grains and to the degree of overlap between the strength distribution of type I and type II grains. The left hand side of equation 2.4, written for the two phase case in terms of the probabilities, is then,

$$P_I(\tau - \bar{\tau}_i^I)\frac{d_I}{4\bar{r}_I}^{\frac{1}{2}} + (1 - P_I)(\tau - \tau_i^{II})\frac{d_{II}}{4\bar{r}_{II}}^{\frac{1}{2}} \qquad (A.1)$$

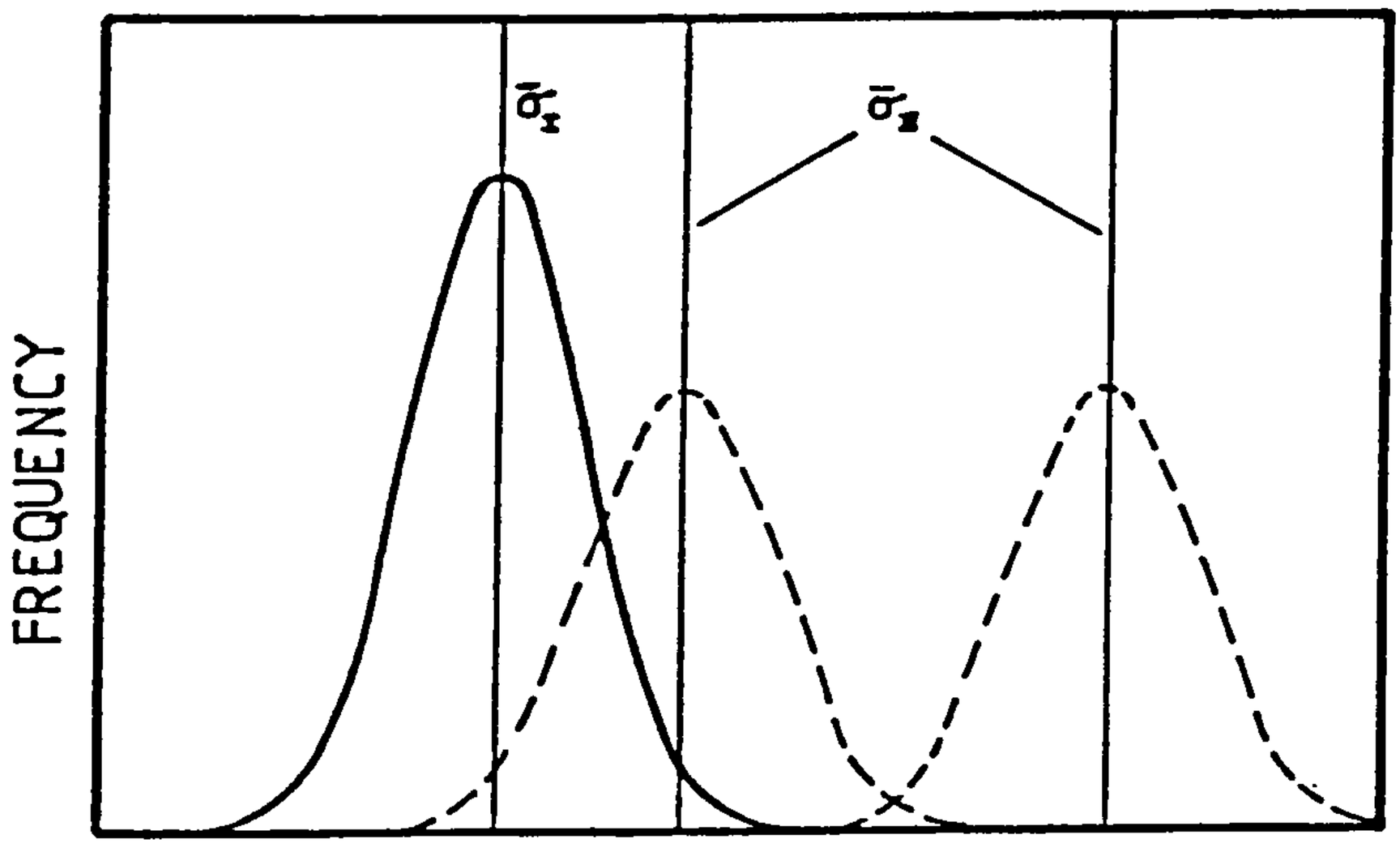

Fig A1 Bimodal distribution of strength in a two-phase structure. (After Reuben and Baker[110])

The average distances $\bar{r}_I$ and $\bar{r}_{II}$ into the adjacent grain at which propagation may occur can be expressed as,

$$\bar{r}_I = C_I r_I + (1 - C_I) r_{II} \qquad (A.2)$$

and,

$$\bar{r}_{II} = C_{II} r_{II} + (1 - C_{II}) r_I$$

where r_I and r_{II} are the average distances required to be traversed in grain type I and II before an active source is encountered. C is the contiguity and is defined by Gurland[108,109] as the fractional area of a grain surface occupied by adjacent grains of the same type. The right hand side of equation 2.4, designated Z, can then be written as,

$$Z = P_I \{C_I \frac{m_{11}}{2} \tau_c^I + (1 - C_I) \frac{m_{12}}{2} \tau_c^{II}\}$$

$$+ (1 - P_I)\{C_{II} \frac{m_{22}}{2} \tau_c^{II} + (1 - C_{II}) \frac{m_{21}}{2} \tau_c^I\} \qquad (A.3)$$

The first term represents propagation from type I grains into type I and II respectively and the second term represents propagation from type II grains into type II and I respectively. These differences are reflected in the inter-orientation factors m_{ii}. Rearranging equations A.1 and A.3 and converting to tensile stress gives,

$$\sigma = \dot{m} \frac{Z + P_I \left(\frac{d_I}{4\bar{r}_I}\right)^{\frac{1}{2}} \tau_i^I + (1 - P_I) \left(\frac{d_{II}}{4\bar{r}_{II}}\right)^{\frac{1}{2}} \tau_i^{II}}{P_I \left(\frac{r_I}{4\bar{r}_I}\right)^{\frac{1}{2}} + (1 - P_I) \left(\frac{d_{II}}{4\bar{r}_{II}}\right)^{\frac{1}{2}}} \qquad (A.4)$$

where m is the macro-orientation factor and is dependent on the average slip plane orientation relative to the applied tensile axis rather than on orientation differences between adjacent grains in the assemblage.

Reuben and Baker[110] therefore arrived at a general statement for the flow stress of a two phase material in terms of the grain size of the constituent materials. Although the unacceptable parametric level would preclude the general use of equation A.4, the authors showed that considerable simplification would result when applying this equation to ferrite-pearlite steels.

By regarding pearlite as a very fine grained ferrite material, the composite may then be treated as a bimodal distribution of grain size in a single phase material. Consequently;

$$\tau_c^{II} = \tau_c^{I}, \quad \tau_i^{II} = \tau_i^{I} \text{ and } \bar{r}_{II} = \bar{r}_I = r \qquad (A.5)$$

As the second phase is also ferrite, P_I can be related simply to the volume fraction of pearlite, V_f^{II} i.e.

$$P_I = 1 - V_f^{II} \text{ and } 1 - P_I = V_f^{II} \qquad (A.6)$$

Substituting A.5 and A.6 into A.4 gives,

$$\sigma = \frac{m}{d_c^{\frac{1}{2}}} \{(4r)^{\frac{1}{2}} Z + \tau_i^{I} d_c^{\frac{1}{2}}\} \qquad (A.7)$$

where d_c is the composite ferrite 'grain size' and is given by,

$$d_c^{\frac{1}{2}} = (1 - V_f^{II}) d_I^{\frac{1}{2}} + V_f^{II} d_{II}^{\frac{1}{2}} \qquad (A.8)$$

and d_{II} is the average ferrite width in the pearlite. As the orientation differences going from II to I should be the same as going

from I to II, $m_{21} = m_{12}$. By considering $m_{12} = m_{11}$ and using equations A.5 and A.6 equation A.3 reduces to ;

$$Z = \frac{\tau_c^{I}}{2} \{ m_{11} + V_f^{II} C_{II} (m_{22} - m_{11}) \} \qquad (A.9)$$

Since the deforming phase is always ferrite, the macro-orientation factor will be equivalent to that observed for ferrite. Combining A.7 and A.9 and re-arranging gives the yield stress of the ferrite-pearlite composite as,

$$\sigma_c = m\tau_i^{I} + \left[mm_{11} r^{\frac{1}{2}} \tau_c^{I} + m(m_{22} - m_{11}) r^{\frac{1}{2}} \tau_c^{I} V_f^{II} C_{II} \right] d_c^{-\frac{1}{2}} \qquad (A.10)$$

The end points of equation A.10 provide an expression for the yield stress of pure ferrite and pure pearlite. For ferrite this gives,

$$\sigma_I = m\tau_i^{I} + mm_{11} \tau_c^{I} r^{\frac{1}{2}} d_I^{-\frac{1}{2}} \qquad (A.11)$$

or

$$\sigma_I = \sigma_i^{I} + k_I d_I^{-\frac{1}{2}}$$

which is the Hall-Petch equation as discussed in Section 2.1.

Similarly for pearlite,

$$\sigma_{II} = m \tau_i^{I} + mm_{22} \tau_c^{I} r^{\frac{1}{2}} d_{II}^{-\frac{1}{2}} \qquad (A.12)$$

or

$$\sigma_{II} = \sigma_i^{I} + k_{II} d_{II}^{-\frac{1}{2}}$$

The contiguity C_{II} can be written as[108,109]

$$C_{II} = 1 - \frac{d_{II}}{L_{II}} \qquad (A.13)$$

where L_{II} is the 'grain' diameter of the pearlite. As pearlite 'grains' always contain a very large number of lamellae, except at

very low volume fractions of pearlite $C_{II} \simeq 1$ and equation A.10 can be rewritten more clearly as;

$$\sigma_c = \sigma_i^{I} + \left[k_I + (k_{II} - k_I)\, V_f^{II}\right] d_c^{-\frac{1}{2}} \qquad (A.14)$$

APPENDIX B

CEMENTITE LAMELLA WIDTH CALCULATION

The difference between equation 5.17 and that of Gladman et al[90] appears to lie in the definition of a pearlite unit as represented below.

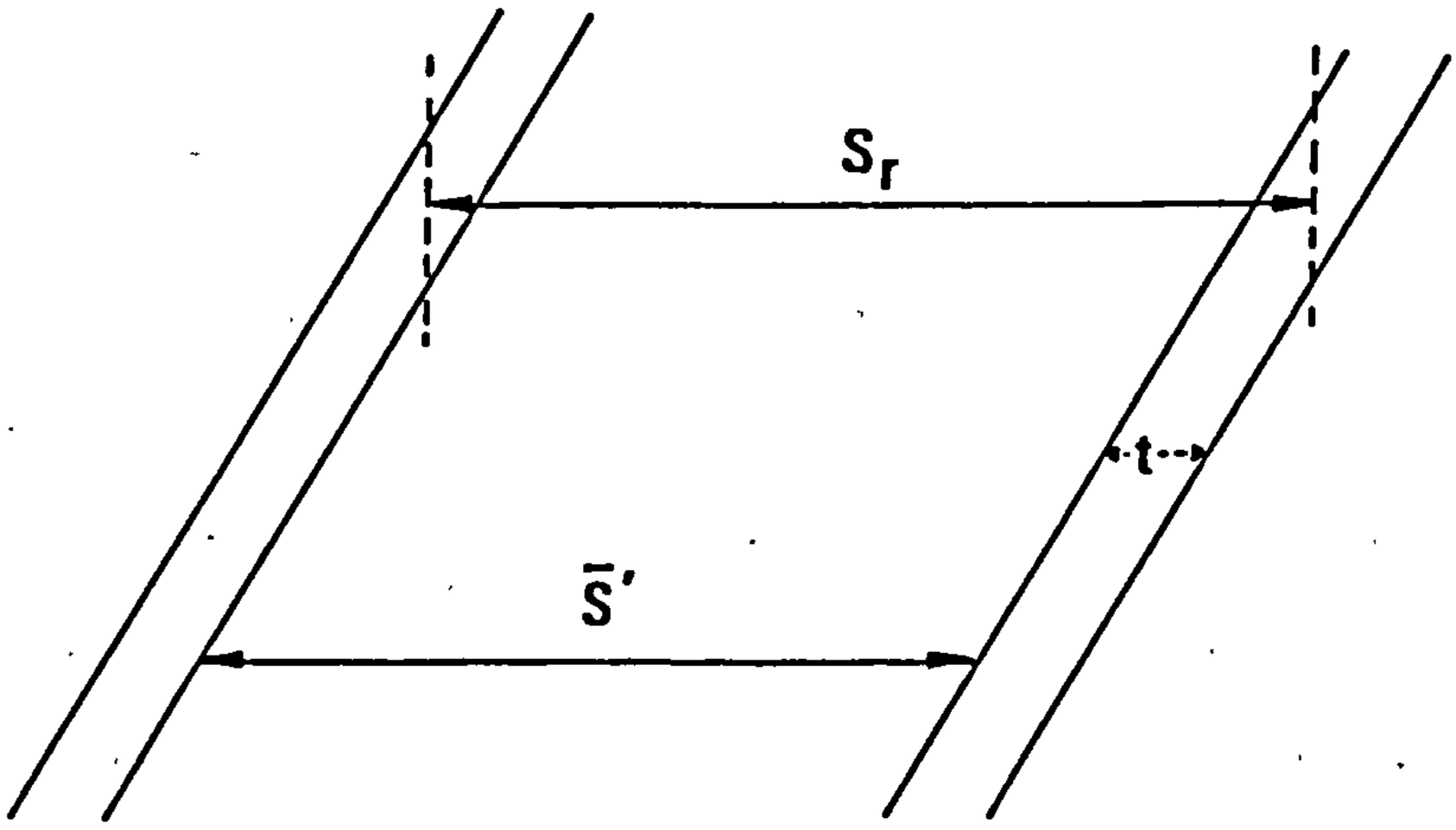

Equation 5.13 was derived from the assumption that this pearlite unit comprises one S_r which includes one t_r thus

$$V_{cem} = \frac{t_r}{S_r} \qquad (B\ 1)$$

The work of Gladman et al[90] considered the pearlite spacing measurement technique of Pearsall[69] to more accurately give a measure of the surface to surface spacing $\bar{S}'$. As the authors obtained pearlite spacing values from this method, they regarded* the pearlite unit to contain one $\bar{S}'$ and one $\bar{t}$.

Equation B1 is therefore,

$$V_{cem} = \frac{\bar{t}}{\bar{S}' + \bar{t}} \qquad (B.2)$$

From equation 5.16,

$$V_{cem} = \frac{0.15 \text{ wt.\%C}}{V_p}$$

therefore,

$$\frac{\bar{S}'}{\bar{t}} = \frac{V_p}{0.15 \text{ wt.\%C}} - 1 \qquad (B.3)$$

and,

$$\bar{t} = \frac{S'}{\left| \frac{V_p}{0.15 \text{ wt.\%C}} - 1 \right|} \qquad (B.4)$$

Equation B 4 is then the expression given in the literature by Gladman, McIvor and Pickering[90].

To examine the implications of $\bar{t}$ calculations from the different equations for the case of equilibrium and dilute pearlite, it is best to consider the dilution factor D, as defined by Gladman et al[90] as,

$$D = \frac{0.8 \ V_p}{\text{wt.\%C}} \qquad (B.5)$$

Equation 5.17 and B 4 then become respectively,

$$\bar{t}_r = \frac{0.12 \ \bar{S}_r}{D} \qquad (B.6)$$

and

$$\bar{t} = \frac{0.12 \ S'}{(D-0.12)} \qquad (B.7)$$

For equilibrium pearlite where D = 1.0 equations B.6 and B.7 give 0.12 $\bar{S}_r$ and 0.136 $\bar{S}'$ respectively. Using $\bar{S}'$ instead of $\bar{S}_r$ will result

in a difference in $\bar{t}$ of ≃12%. Similarly for dilute pearlite, say D = 2.0 this difference is ≃6%.

Thus the differences between the values obtained from each equation decreases with increasing dilution i.e. as $\bar{t}_r$ decreases with respect to $\bar{S}_r$. Given the errors involved in pearlite volume fraction and spacing measurement this difference is negligible.

(* Private communications with F.B. Pickering, 1982)

PART 2

CHAPTER 6

THE USE OF LINEAR ELASTIC FRACTURE MECHANICS AS A TEST FOR BRITTLE FRACTURE.

It is well established that the existence of a notch or crack increases the likelihood of cleavage fracture[130]. The stress concentration at the tip of the notch or crack creates a state of triaxial stress and raises the local value of the tensile stress (in some cases to as much as three times the uniaxial yield stress), thereby suppressing gross yielding[130,131]. Brittle failure then occurs at a critical value of tensile stress, the fracture stress, σ_f. At the atomistic level, the fracture strength of a purely elastic material depends on the strength of the atomic bonds of the material. The tensile stress required to separate the atomic planes, the theoretical cohesive stress, σ_c, has been calculated by Griffith[132] to be approximately E/6, where E is Young's Modulus.

In practice, this theoretical strength is rarely obtained due mainly to the presence or formation of stress concentrators such as cracks or notches. Unfortunately, the usual information gained from a "blunt notch" Charpy impact test cannot be applied directly to assess the resistance of service components to fast fracture[130]. As a result, much work is being carried out in determining the resistance of metals and alloys to the propagation of sharp cracks. The subject of Fracture Mechanics has gone a long

way, in a relatively short time, to provide quantitative information which can be used in failure prevention and design calculations.

Linear Elastic Fracture Mechanics (L.E.F.M.) provides a means of relating the stress necessary to cause failure in a structure or testpiece with the size of any defect or precrack that may be present. Before discussing the micromechanisms of brittle fracture in steels and the results obtained from L.E.F.M. tests, it is necessary to outline the underlying principles of such tests in relation to the assessment of the plane strain fracture toughness parameter, K_{IC}.

Sharp crack fracture mechanics was initially viewed by Griffith[132] from an energy balance consideration but was later developed by Irwin[133] into its present form, the stress intensity factor approach.

6.1 THE ENERGY BALANCE APPROACH

Griffith[132] suggested that although σ_c was seldom obtained on a macroscopic scale this theoretical maximum stress was reached microscopically at the tip of an inherent crack. Griffith[132] considered the fracture of glass from a thermodynamic viewpoint. His basic premise was that unstable propagation of a crack occurred when the increment of crack growth resulted in more stored elastic energy being released than is absorbed by the creation of new crack surface.

By considering an infinite plate containing a central crack of length 2a, an energy balance gave the fracture stress σ_f in terms of the crack length and surface energy, γ_s i.e.

$$\sigma_f = \left[\frac{2E\gamma_s}{\pi a}\right]^{\frac{1}{2}} \qquad (6.1)$$

where E is again Young's Modulus.

Equation 6.1 describes the necessary condition for elastic crack propagation in a completely brittle solid. Although experimental verification of this criterion has been given by Griffith[132], most metals do not fail in a completely brittle manner and some plastic deformation in the crack tip region occurs even in an apparently fully brittle failure[134].

The nature and importance of this localised plastic deformation accompanying crack propagation was first appreciated by Orowan[134,135] and Irwin[133]. These authors realised that a certain amount of plastic work, γ_p, is expended during the propagation of a crack which was additional to the elastic work required to create new fracture surfaces. Orowan[136] noted that this plastic energy term $\gamma_p >> \gamma_s$. Thus, if the Griffith[132] energy balance approach is appropriate γ_s may be neglected. Orowan[134,135] argued that, provided plastic deformation takes place in a zone which is small in comparison with the crack length and the component thickness, the energy released by crack extension could still be calculated with sufficient accuracy by elastic analysis. The energy balance for fracture between the elastic strain energy released and the plastic work done therefore gives,

$$\sigma_f = \left[\frac{2E\gamma_p}{\pi a}\right]^{\frac{1}{2}} \qquad (6.2)$$

The application of the Griffith[132] equation, which is based on linear elastic theory, to fracture involving some degree of plasticity is still in doubt. Consequently, modern fracture

mechanics approached the fracture problem from an alternative viewpoint, focusing attention instead on the stress environment near the tip of the crack. This interpretation was originally developed by Irwin[133] from the calculations of Westergaard[137].

6.2 STRESS INTENSITY CONCEPT

Westergaard[137] considered the stress distribution in the vicinity of a sharp crack. For the notation shown in Fig. 6.1, the crack tip stresses were found to be:

$$\begin{vmatrix} \sigma_x \\ \sigma_y \\ \tau_{xy} \end{vmatrix} = \sigma \left(\frac{a}{2r}\right)^{\frac{1}{2}} \cos \theta/2 \begin{vmatrix} 1 - \sin \theta/2 \sin 3\theta/2 \\ 1 + \sin \theta/2 \sin 3\theta/2 \\ \sin \theta/2 \cos 3\theta/2 \end{vmatrix} \qquad (6.3)$$

Irwin[133] realised the importance of the term $\sigma a^{\frac{1}{2}}$ in specifying the stress distribution and σ_x, σ_y and τ_{xy} were then given in terms of,

$$\frac{K \cos \theta/2}{\sqrt{2\pi r}} \quad |\text{terms as above}| \qquad (6.4)$$

where K was the stress intensity factor defined as,

$$K = \sigma_{app} \sqrt{\pi a} \qquad (6.5)$$

and σ_{app} is the applied tensile stress.

Although not a material property, K uniquely describes the elastic stress distribution near the crack tip for a given geometry.

Irwin[133] defined a parameter G, the crack extension force or strain energy release rate, and showed that G was related to the stress intensity factor K by,

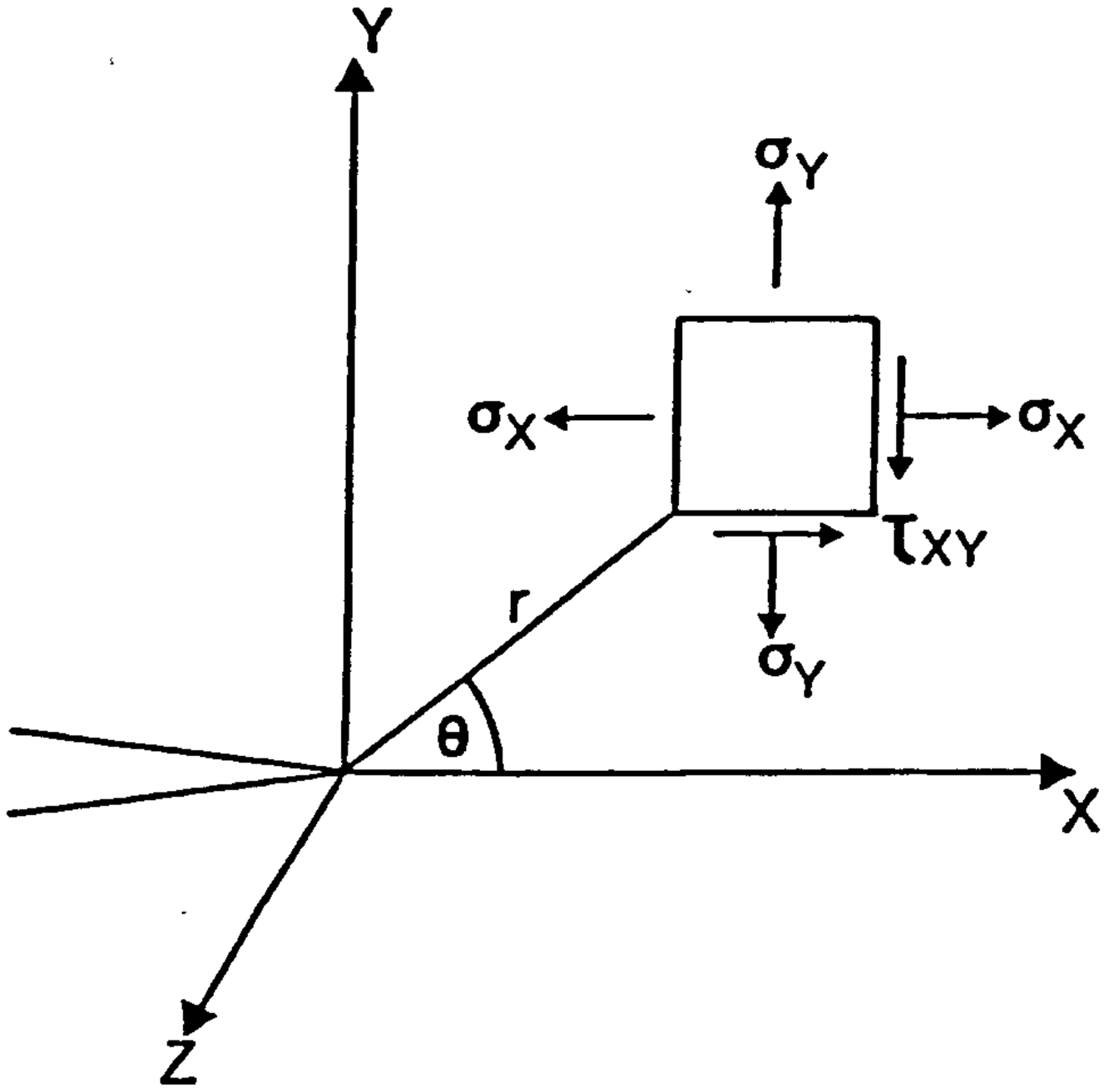

Fig 6.1 Crack tip co-ordinate system.

$$G = \frac{K^2}{E} \quad \text{(plane stress)} \tag{6.6.}$$

or,

$$G = \frac{K^2(1 - \nu^2)}{E} \quad \text{(plane strain)} \tag{6.7}$$

where ν is Poisson's ratio.

Plane strain is defined as a state of two dimensional strain, i.e. no strain in the through thickness direction. This also corresponds to a state of triaxial stress. Plane stress on the other hand is a state of two dimensional stress with no stress existing in the through thickness direction[130,138].

Substituting for K from equation 6.5 into equation 6.6. gives,

$$G = \frac{\sigma_{app}^2 \pi a}{E} \quad \text{(plane stress)} \tag{6.8}$$

If the critical values of G and σ_{app} at fracture are represented by G_c and σ_f then:

$$\sigma_f = \left[\frac{EG_c}{\pi a}\right]^{\frac{1}{2}} \tag{6.9}$$

Thus for the completely elastic condition the Griffith[132] energy balance (equation 6.2) and the Irwin[133] stress intensity approach (equation 6.9) are equivalent where $G_c = 2\gamma_p$. As Irwin[133] considered fracture to occur at the critical value of G, G_c this obviously implies failure at a critical value of K, K_c. However, Irwin's theory[133] like that of Griffith[132] applies to the elastic condition and any plasticity developed at the crack tip will alter the elastic stress distribution from that predicted by linear elastic theory. Experimental data revealed that it was

necessary to test specimens with preinduced fatigue cracks as even the sharpest machined notches gave substantially higher values of K than those obtained from fatigue cracked specimens[130]. Initial testing also indicated that K_c was geometry dependent and for a given temperature and strain rate, K_c was found to decrease with increasing specimen thickness[130,138]. The main reason for the observed thickness effect was the change from plane stress to plane strain dominated conditions. The accompanying decrease in plastic zone size ahead of the crack requires less energy to be dissipated as a result of plastic deformation under plane strain than plane stress conditions[130,138]. It was therefore found that G_c and K_c decreased to a minimum value, as the thickness of the specimen increased and created a state of predominantly plane strain at fracture. This is discussed further in Section 6.3.

In developing the stress intensity approach, it was realised that the presence of free surfaces at finite boundaries modifies the general distribution of stress. This changes the value of K obtained for given values of σ_{app} and a (equation 6.5). The application of the theory to practical situations would thus required K-calibrations for specific cases. The general expression for K_c is therefore[130,138],

$$K_c = Y \sigma_{app} (\pi a)^{\frac{1}{2}} \qquad (6.10)$$

where Y is a geometric factor which varies with the ratio of the crack length to specimen width (a/W). Values of Y can be obtained from K-calibration curves which have been calculated for many geometries[139].

When values of Y, σ_{app} and a are known for a particular case, the calculated K_c describes the materials resistance to fracture under plane strain conditions and is widely regarded as a material property[130,138]. Three distinct cracking modes have been considered, as shown in Fig. 6.2. The most common condition favouring unstable brittle fracture occurs when the stress acts normal to the crack plane causing the crack surfaces to move apart. Under this 'opening or tensile' mode (Mode I, Fig. 6.2), the crack tip stress intensity factor is termed K_I. Thus when fracture occurs under plane strain conditions the critical level of K is given the notation K_{IC} and is called the plane strain fracture toughness. Similarly Modes II and III, the 'sliding' mode and 'tearing' mode respectively, have appropriate critical stress intensity factors denoted K_{IC} and K_{IIIC}. These are discussed by Tetelman and McEvily[131]. The procedure; specimen dimensions and validity criteria for conducting K_{IC} testing of metallic materials are summarised in the proposed British Standard BS5447:1977 [140].

It is worth adding at this point, that in cases where toughness shown by K_{IC} tests are sensitive to loading rate, or the value of K_I at a particular strain rate is required, alternative high strain rate tests have been used. Unlike K_{IC}, there is yet no standard test procedure, although fatigue pre-cracked instrumented Charpy tests are probably the most common[141]. The value of K_I under such 'dynamic' loading conditions is termed K_{Id}, the dynamic fracture toughness.

6.3 DETERMINATION OF K_{IC}

K_{IC}, plane strain fracture toughness testing, is conducted in order to arrive at a reproducible value of the lower limiting critical toughness of a material in Mode I failure. Of the main type of test specimens recommended by BS5447:1977[140], the single-edge notched bend testpiece is probably the most widely used[130,138]. This is shown schematically in Fig. 6.3. Limitations are imposed on the testpiece dimensions and the shape and depth of notch. These are discussed later.

To simulate an ideal plane crack, a fatigue crack is grown at the root of the machined notch to a depth greater than 1.25 mm. Strict regulations apply to the fatigue precracking operations and to the acceptable crack configuration. These are fully described in the British Standard[140]. In the case of 3-point bend tests, specimens are normally loaded as shown in Fig. 6.3. Such loading produces the required Mode I crack opening. During bending, the crack opening displacement is measured from the change in distance across the open ends of the notch. This displacement is recorded as a function of the applied load and the load-displacement record is used to calculate the fracture toughness of the material.

Unlike most other forms of mechanical test, K_{IC} tests have to be completed and the results analysed before it can be ascertained whether the test is valid[140]. As discussed earlier, a limitation is placed on the plastic zone size for its effect to become negligible. To allow elastic analysis to be used, standard specimen size requirements demand that the plastic zone should be

less than 0.02 a[130,138]. In addition, empirical criteria have been specified which aim to ensure plane strain conditions exist at fracture, and to indicate when a candidate K value, K_Q, is equal to K_{IC}[140]. It is generally accepted that these conditions are satisfied when both the crack length, a, and specimen thickness, B, are

$$\geq 2.5 \left[\frac{K_Q}{\sigma_{0.2}}\right]^2 \qquad (6.11)$$

where K_Q is the candidate stress intensity factor and $\sigma_{0.2}$ is the 0.2% proof stress of the material in uniaxial tension. If the above criteria are satisfied, then the K_Q value is considered to be sufficiently close to the true elastic value for the effect of plasticity at the crack tip to be neglected[130,138]. K_Q therefore equals K_{IC}. Equation 6.11 is widely used in testing, although there is some evidence that this is either over or under conservative[138,142].

The effect of specimen thickness can also be rationalised in terms of load-crack displacement records and specimen fracture appearance[142] (Fig. 6.4). When test pieces are thick enough to preclude yield at the surface spreading laterally to the centre of the crack front, high triaxial stresses are developed and plane strain conditions prevail at fracture. Under such condictions, the fracture appearance is almost completely 'square' (i.e. normal to tensile axis, e.g. cleavage) with only a small proportion of slant (i.e. $\simeq 45^{o}$ to tensile axis e.g. shear lip) at the edge. In this case, the load displacement record is essentially linear to failure (Fig. 6.4(C)). Conversely, when specimens are not sufficiently thick, the triaxial stress state is relaxed due to the close proximity of the free surface; the slant fracture and central

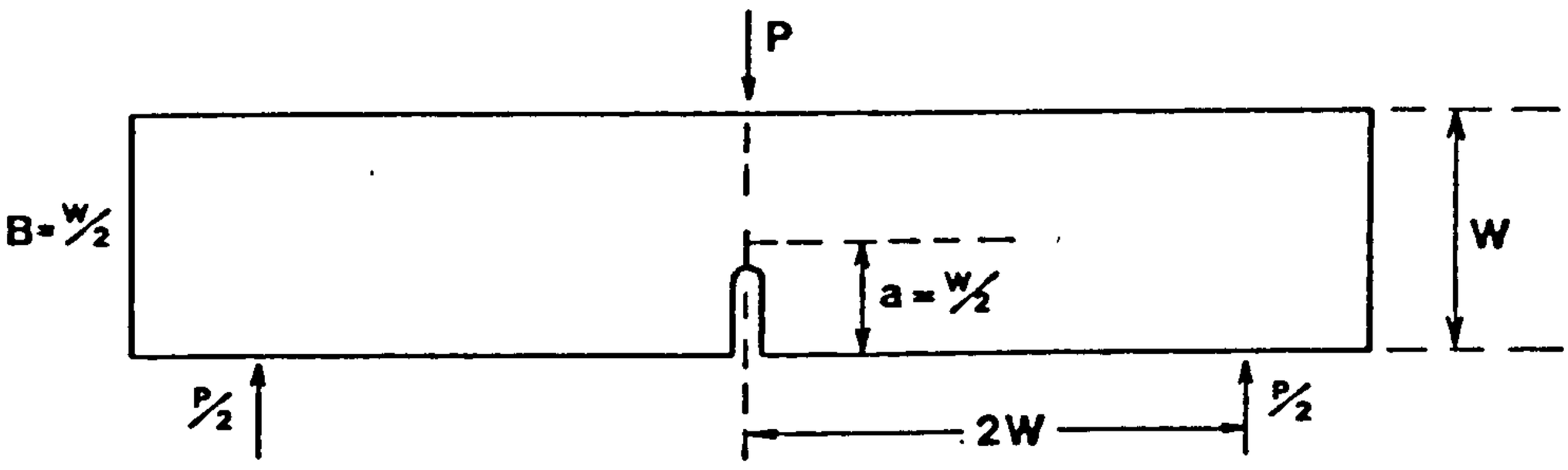

Fig 6.3 3-point bend test specimen.

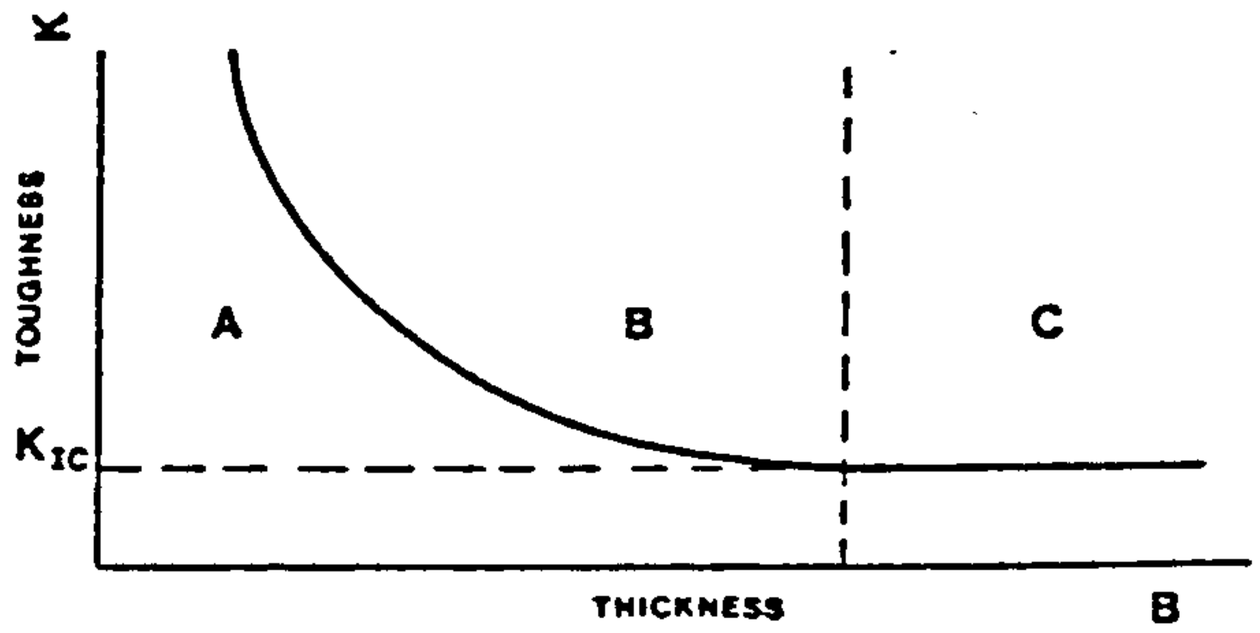

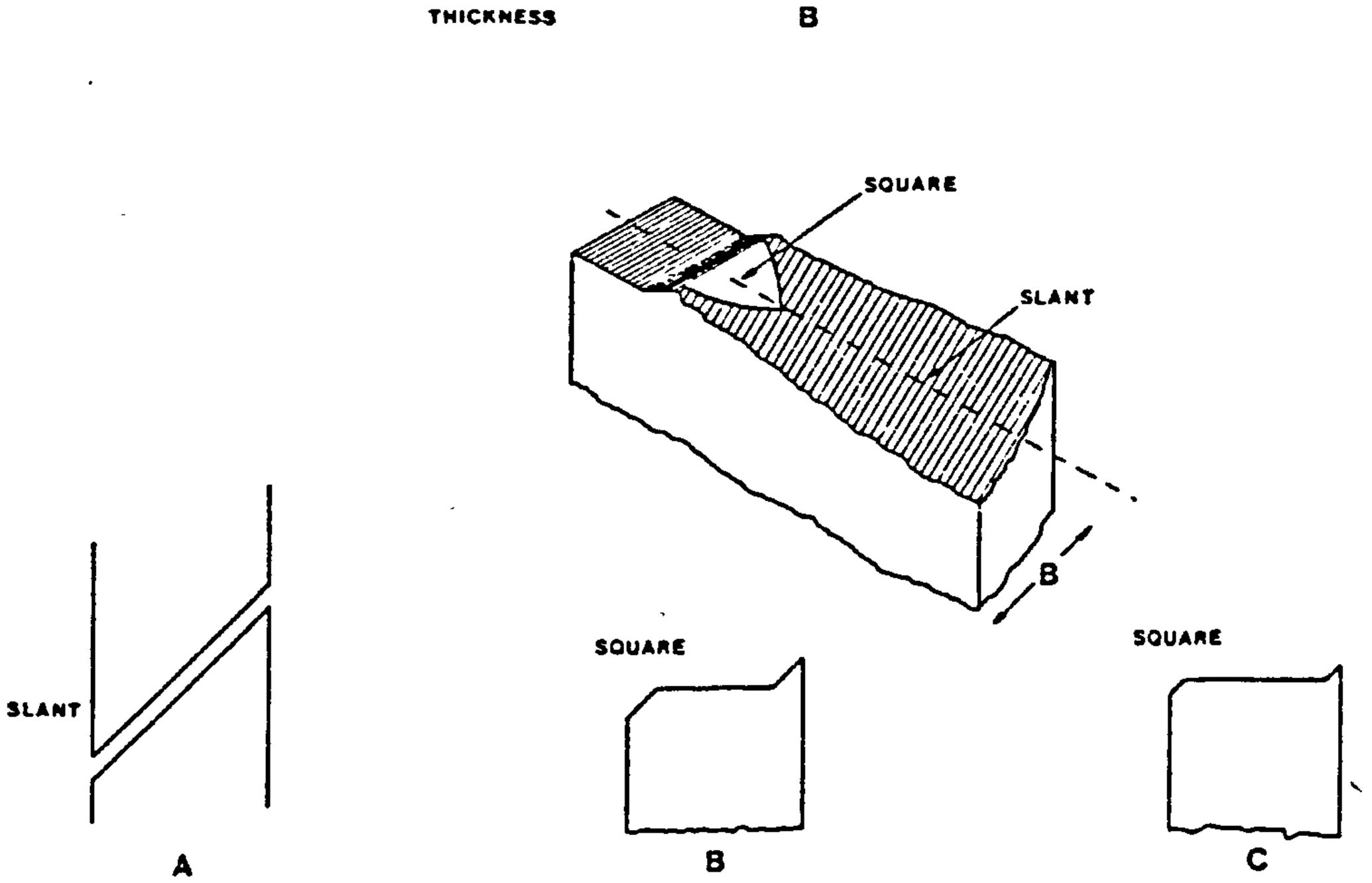

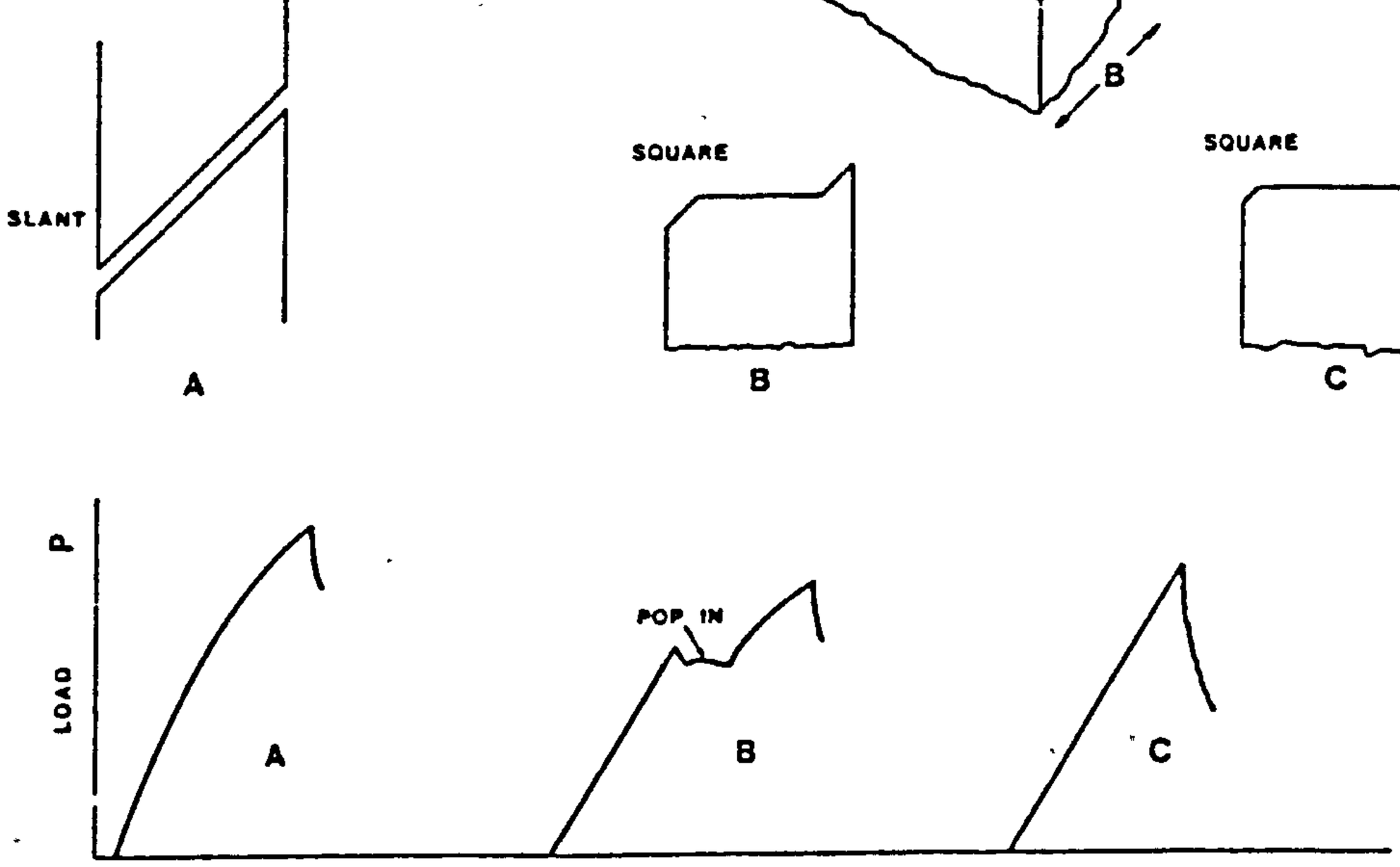

Fig 6.4 The effect of specimen thickness on the fracture profile and load-crack tip displacement records. (After Knott[130])

square fracture area become of comparable size. The load displacement curve is then characterised by meta-instability or 'pop-in' behaviour[143], where the square fracture tunnels ahead rapidly and produces a sudden extension (Fig. 6.4(B)). Further reduction in specimen thickness makes identification of the 'pop-in' behaviour difficult. When the through thickness stress is reduced to zero, throughout the sample (plane stress), fully slant or shear fracture results and the load displacement record exhibits characteristics of general plastic deformation (Fig. 6.4(A))[130,138].

6.3.1 Calculation of K_{IC}

The provisional value of fracture toughness for a three-point bend geometry is given by[130,140]:

$$K_Q = \frac{3P_Q L}{BW^{3/2}} \left[1.93\left(\frac{a}{W}\right)^{\frac{1}{2}} - 3.07\left(\frac{a}{W}\right)^{3/2} + 14.53\left(\frac{a}{W}\right)^{5/2} - 25.11\left(\frac{a}{W}\right)^{7/2} + 25.80\left(\frac{a}{W}\right)^{9/2}\right] \quad (6.12)$$

However the half load span, L = 2W. (Fig.6.3). Hence,

$$K_Q = \frac{P_Q}{BW^{\frac{1}{2}}} \cdot Y \quad (6.13)$$

where P_Q is the failure load and B and W are the specimen cross section dimensions. The stress intensity factor coefficient Y[140], is a function of (a/W) and is obtained for the measured value of (a/W) from standard tables, for the particular loading and test-piece geometry[130,140].

For linear load displacement records the maximum load is taken as P_Q, the fracture load, and substitution of this value together with B, W and Y in equation 6.13, gives the value K_Q.

When the trace shows slight non-linearity, criteria have been specified in the British Standard[140] to check whether or not the plasticity preceding total failure, or the 'pop-in', is permissible. The value of K_Q calculated from equation 6.13 is equal to K_{IC} only if the specimen dimensions, the thickness criteria (equation 6.11), the fatigue crack growth procedure and crack configuration, all comply with BS5447:1977[140]. If any one of the validity criteria is not satisfied, the test is deemed invalid and only a K_Q value can be reported.

CHAPTER 7

CLEAVAGE FRACTURE IN HIGH-CARBON PEARLITIC STEELS

Much progress has been made in understanding the micro-mechanics of brittle fracture in mild steel. It is therefore worth examining this work before considering in detail fracture in pearlitic steels.

7.1 CLEAVAGE FRACTURE IN MILD STEEL

As mentioned in Chapter 6, it is now generally accepted that cleavage fracture occurs when the local tensile stress exceeds some critical value termed the fracture stress, σ_f. However, even in the case of fully brittle fracture in tension, σ_f is coincident with the uniaxial yield stress in compression. Similarly, in brittle notched specimen cleavage fracture is preceded by a small amount of local yielding at the notch root. Plastic flow is therefore a necessary precursor to cleavage crack nucleation[130,131]. This conclusion has prompted a number of proposed mechanisms in which cleavage cracksnucleate as a result of the blocking of slip bands by obstacles in the form of grain boundaries or second phase particles.

Stroh[144] postulated a dislocation model for cleavage fracture which relied on the pile-up of dislocations on a slip band squeezing together to produce a crack nucleus (Fig. 7.1). The critical value of the effective shear stress for cleavage, τ_{eff}, is given by

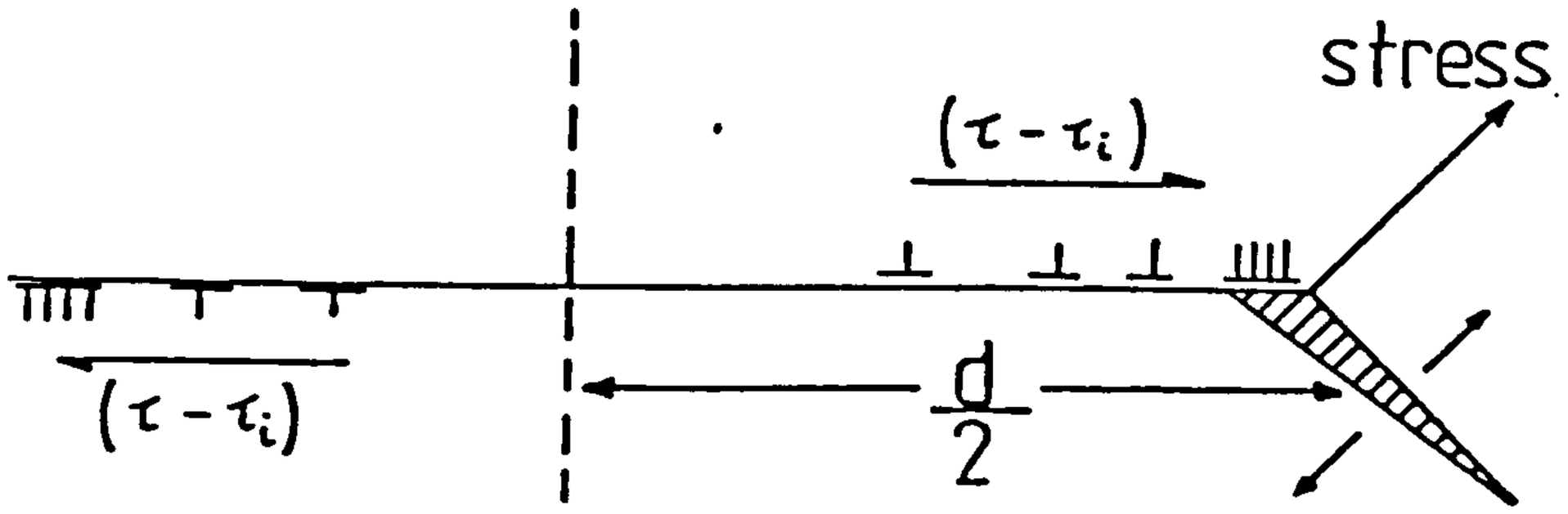

Fig 7.1 Cleavage fracture nucleation ahead of a dislocation pile-up. (After Stroh[144])

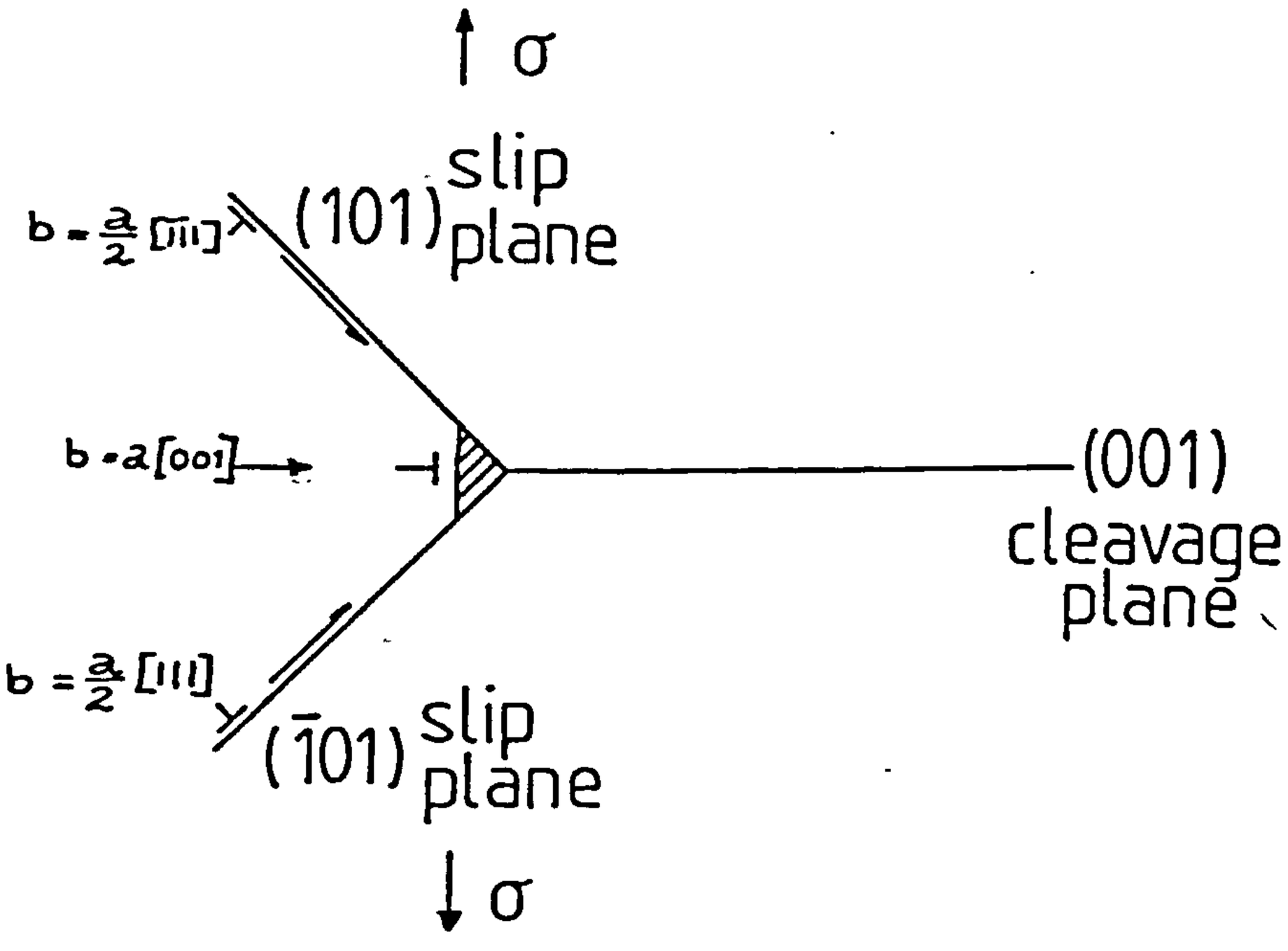

Fig 7.2 A model for cleavage fracture according to Cottrell[145]

$$\tau_{eff} = \tau_y - \tau_i \geq \left[\frac{\pi\mu\gamma}{2(1-\nu)d}\right]^{\frac{1}{2}} \qquad (7.1)$$

where τ_y is the shear yield stress, τ_i the friction (shear) stress, μ the shear modulus, ν Poisson's ratio, γ the surface energy for ferrite and d the slip band half length. From this result it may be deduced that if a crack nucleus can form any increase in its length it will lead to a decrease in the energy of the system, provided that the surface energy encountered by the growing crack remains constant. This implies that cleavage fracture is nucleation controlled.

However, Stroh's model[144] does not explain the predominance of cleavage fracture at low temperatures where the tensile yield stress is high, but the value of $(\tau_y - \tau_i)$ is similar to that at room temperature[130]. Furthermore, a model based on a shear stress criterion cannot account for the necessary attainment of a critical tensile stress for fracture. Since tensile stresses govern the propagation of crack nuclei Cottrell[145] suggested that crack growth, as opposed to nucleation, was the controlling factor in brittle fracture.

In Cottrell's model[145] (Fig. 7.2) edge dislocations with Burger's vectors of type $\frac{a}{2}\langle 111\rangle$ on intersection {101} slip planes may interact as follows,

$$\frac{a}{2}[\bar{1}\bar{1}1]_{(101)} + \frac{a}{2}[111]_{(\bar{1}01)} \rightarrow a[001]_{(001)} \qquad (7.2)$$

The resultant sessile dislocation has a Burger's vector normal to the cleavage plane (001) and the relative motion of material above and below the slip planes produces the effect of driving a 'wedge' into this plane. The dislocation reaction given

in equation 7.2 is energetically favourable and therefore produces an easy nucleation process[145]. The critical event for fracture is then the attainment of the cleavage fracture stress, σ_f, where,

$$\sigma_f > \frac{\mu\gamma}{k_S} d^{-\frac{1}{2}} \qquad (7.3)$$

k_S is the Hall-Petch constant pertaining to the shear stress state and d is the grain diameter.

This model can be applied to notched specimens, producing a simple expression for the influence of the various parameters on the ductile-brittle transition temperature[146].

When $\sigma_y = \sigma_f$,

$$\sigma_y k_S d^{\frac{1}{2}} = \mu\gamma\beta \qquad (7.4)$$

where β is a factor relating the tensile yield stress to the maximum tensile stress below the notch.

Increasing the left hand side of equation 7.4 promotes brittle failure. It can be seen, therefore, that strengthening other than by grain refinement will have a deleterious effect on toughness. Cottrell's model[145] thus appears adequate in accounting for the role of tensile stress, grain size and yielding parameters on fracture. However, as pointed out by McMahon and Cohen[147], it does not anticipate the important effect of grain boundary carbide particles.

McMahon and Cohen[147] demonstrated marked differences in the cleavage fracture behaviour of two steels of identical grain size and yielding characteristics, but containing different thicknesses of grain boundary carbides. In addition, the authors

observed that cleavage crack nuclei had invariably formed in these carbides. Taking the lead from this work, Smith[148] developed an alternative growth controlled mechanism for cleavage fracture (Fig. 7.3). In this case a brittle grain boundary carbide of width C_o will crack under the influence of the applied stress, σ, and the concentrated shear stress ahead of the dislocation pile-up, τ_{eff}. The condition for failure is therefore,

$$\frac{C_o}{d}\ \sigma_f^{\,2} + \tau_{eff}^{\,2}\left[1 + \frac{4}{\pi}\ \frac{C_o}{d}\right]^{\frac{1}{2}}\ \frac{\tau_i}{\tau_{eff}} > \frac{4E\gamma}{\pi(1-\nu^2)d} \qquad (7.5)$$

where E is Young's Modulus, d is the ferrite grain diameter and ν is Poisson's ratio.

This model[148] not only shows the importance of yielding parameters and grain size, but in addition demonstrates the necessary role of grain boundary carbides in the fracture process. At constant grain size equation 7.5 predicts low fracture stresses for coarse carbides, as observed by McMahon and Cohen[147].

A further carbide cracking mechanism is that proposed by Lindley et al[149]. In contrast to Smith's approach[148] it does not rely as heavily upon dislocation pile-ups, but instead postulates that cracking of long thin carbides occurs when the strain in the ferrite matrix due to plastic deformation reaches a critical value. The energy released on cracking may then be sufficient to cause the crack to propagate a short distance into the matrix. The final fracture is again, however, growth controlled and should therefore occur at a critical value of the applied tensile stress.

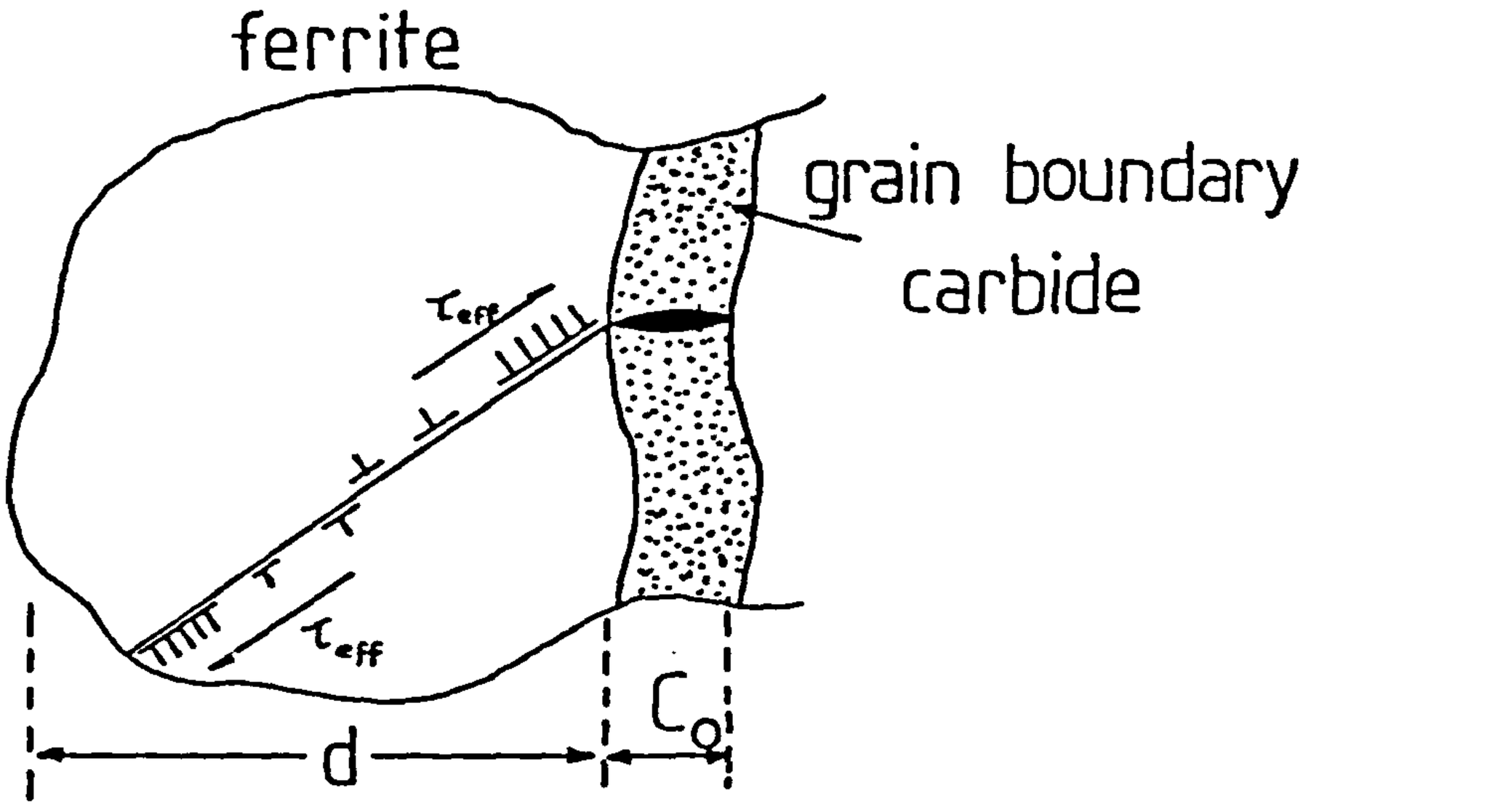

Fig 7.3 Smith's[148] model for cleavage fracture in mild steel.

7.1.1 The Observed Relationship between Grain Size σ_f and K_{IC} in Mild Steel

The grain size dependence of the cleavage fracture stress in mild steel has been studied by Curry and Knott[150]. As predicted by equations 7.1, 7.3 and 7.5 a relationship was found between these parameters. This is shown in Fig. 7.4 for notched-specimen bend tests on mild steel. The fact that the relationship between σ_f and $d^{-\frac{1}{2}}$ is in general non-linear has been taken as evidence that the carbide thickness, C_o, rather than the grain size, d, is the controlling variable. In most cases however d and C_o are also related and large grain sizes usually give rise to coarse carbides and therefore low fracture stress[130].

The relationship between d and K_{IC} in mild steel is complicated by the stress conditions at the crack tip and at the present time is not fully understood. In notched specimen, as used to determine σ_f, the maximum tensile stress below the notch is maintained over a distance which is large compared with the ferrite grain size. Cleavage fracture is therefore thought to occur when a microcrack nucleus in the thickest and most suitably orientated carbide particle within this region can propagate catastrophically[130,150]. Ahead of a sharp crack however, as is the case in a K_{IC} test, the rapid stress gradient influences the cleavage fracture conditions. Ritchie, Knott and Rice[151] have therefore argued that for cleavage fracture to occur in a K_{IC} test, the peak tensile stress must exceed the fracture stress over some 'characteristic distance' ahead of the crack tip. Ritchie et al[151] have suggested that it is the microstructural significance of this characteristic distance which controls fracture toughness.

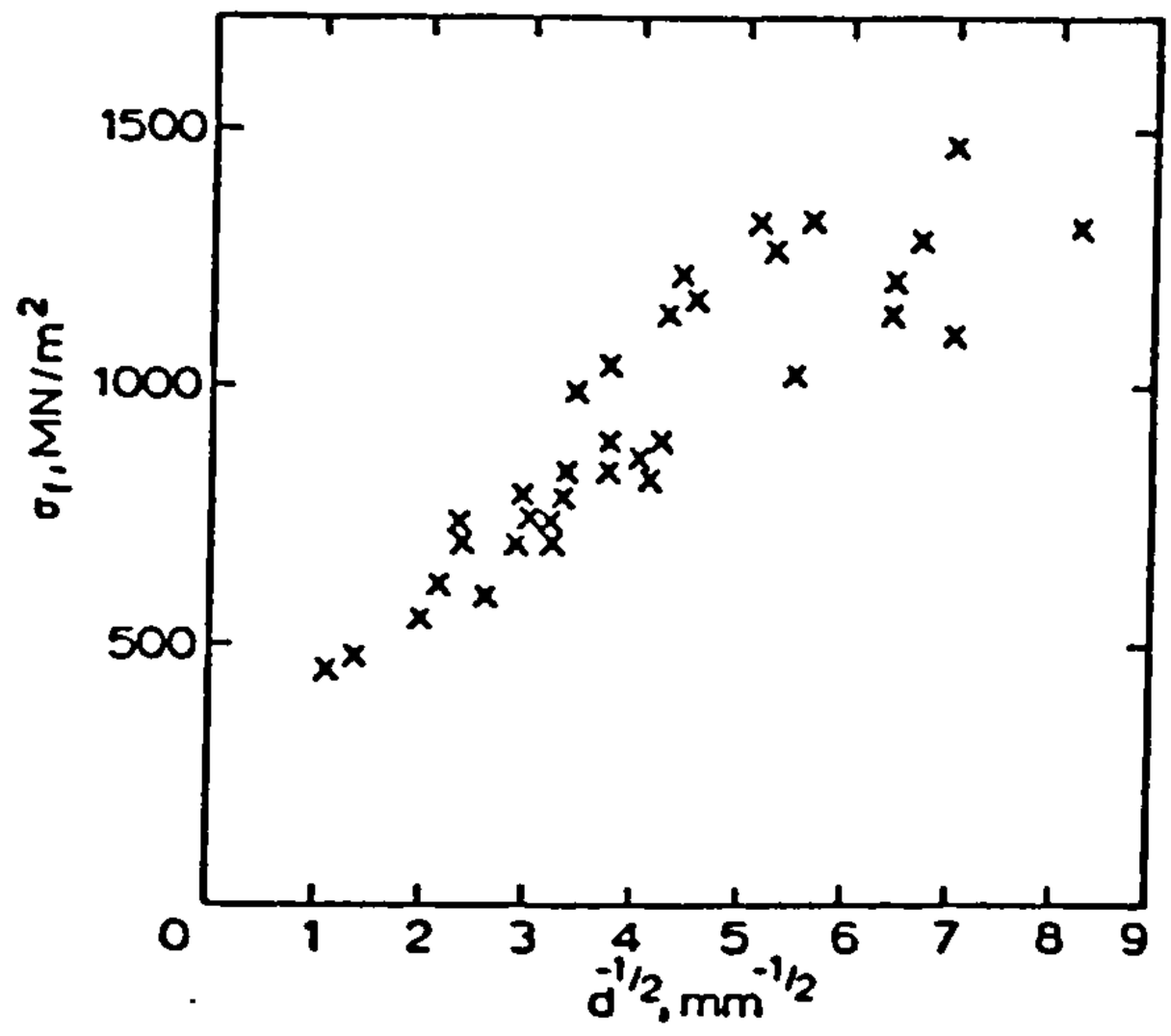

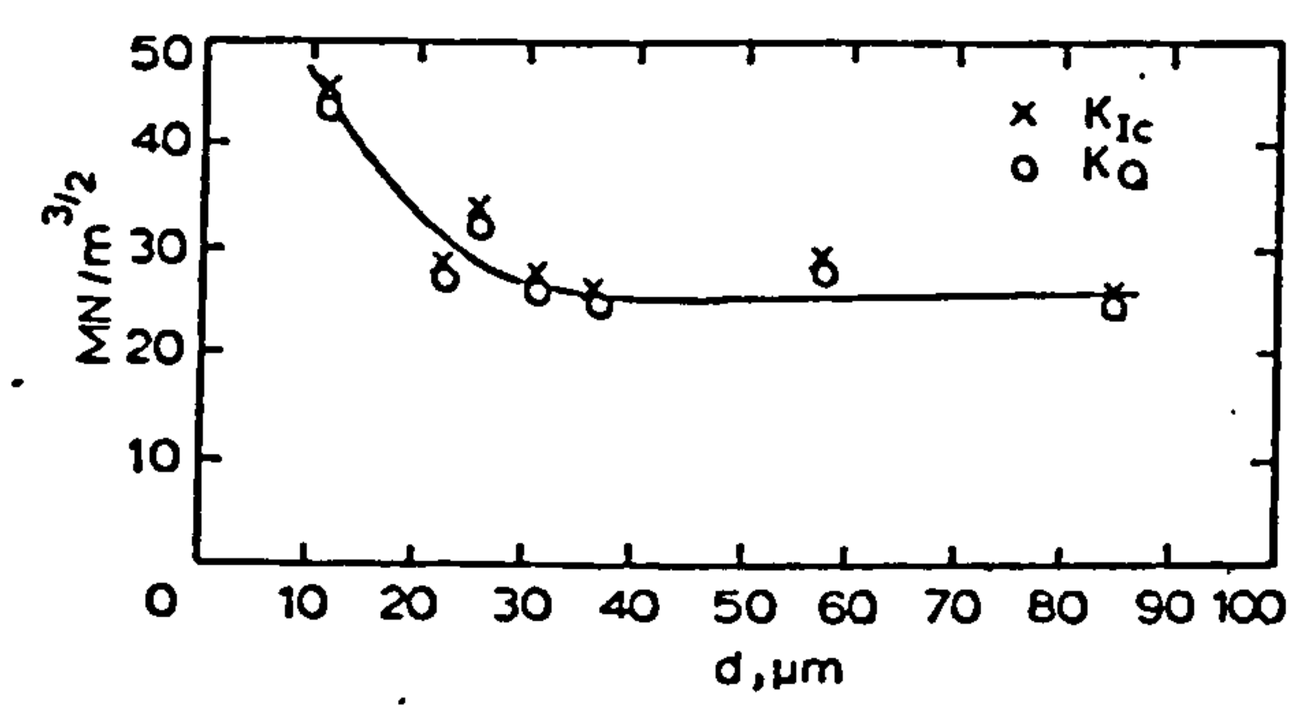

Fig 7.4 & 7.5 The variation in cleavage fracture sress(σ_f) and fracture toughness(K_Q & K_{IC}) with grain size(d) in mild steel. (After Curry and Knott[150])

Initially this distance was found to be of the order of two grain diameters[130,151]. However, the characteristic distance was later shown to be independent of $d^{\frac{1}{2}}$ and to vary between materials[152]. Although a microstructural significance has still to be attached to this distance, the presently accepted explanation is that the characteristic distance is associated with the volume of material needed to assure the presence of an 'eligible' carbide particle whose fracture condition is satisfied[152,153,154]. The observed effect of fine ferrite grain size on improving K_{IC} in mild steel (Fig. 7.5) has therefore been attributed to the increase in both σ_f and the distribution of 'eligible' carbide particles with decreasing grain size[150].

7.2 CLEAVAGE CRACK INITIATION IN PEARLITIC STEELS

Similarly the initiation of cleavage cracks in pearlitic steels has been the subject of a number of investigations. Early studies by Gross, Danko, Stout[155,156] and Linburg[157] suggested that microcracks in pearlite form during tension or compression by the process of lamella kinking in which both ferrite and cementite deform plastically. Although kinks have been observed in compressed pearlite[158], there is little evidence to support or explain kink formation in tension. In fact it is now accepted from the work of Buckner[159], Miller and Smith[160] and Park and Bernstein[161] that microcracks form instead by a process of shear cracking.

Buckner[159] reported that microcracks occurred preferentially in colonies where the cementite lamellae were aligned parallel to the tensile axis. As these microcracks were invariably

found to lie at 45° to this axis, the author[159] suggested that cementite cracking was the result of the concentrated stress on the ferrite planes of maximum resolved shear stress. Statistical measurements by Miller and Smith[160] confirmed Buckner's observations and led the former authors[159] to propose a mechanism for the cracking of pearlite, as shown in Fig. 7.6. Sequentially this entails slip in the ferrite when the specimen is stressed. Then due to the stress concentration at the ferrite-cementite interface.initial cracking occurs in the cementite plates. The cracked cementite promotes shear of the ferrite (Fig. 7.6(a) on the slip planes and finally, when the stress becomes large enough the initial cementite 'holes' link up to form a macroscopic microcrack (Fig. 7.6(c and d).

As pointed out recently by Park and Bernstein[161] some confusion has arisen in attempting to correlate this shear cracking to the subsequent process of brittle cleavage fracture. Although Ohmori and Terasaki[162] believe shear cracking resulted in cleavage cracks, the mechanisms of Miller and Smith[160] illustrate a typical sequence of events for ductile fracture. The fact that cleavage occurs on {100} ferrite planes in pearlite[115] and not {110},{112} or {123}operative slip planes[131], further supports the belief that shear cracking promotes ductile rather than cleavage fracture. From observations of dimple rupture at the initiation sites of cleavage facets in tensile specimens, Park and Bernstein[161,163] therefore suggested that fibrous cracks, formed by the shear cracking of pearlite, behave instead as Griffith[132] cracks in the initiation of unstable cleavage. Although relatively large fibrous cracks (~2 microns) were a prerequisite to cleavage

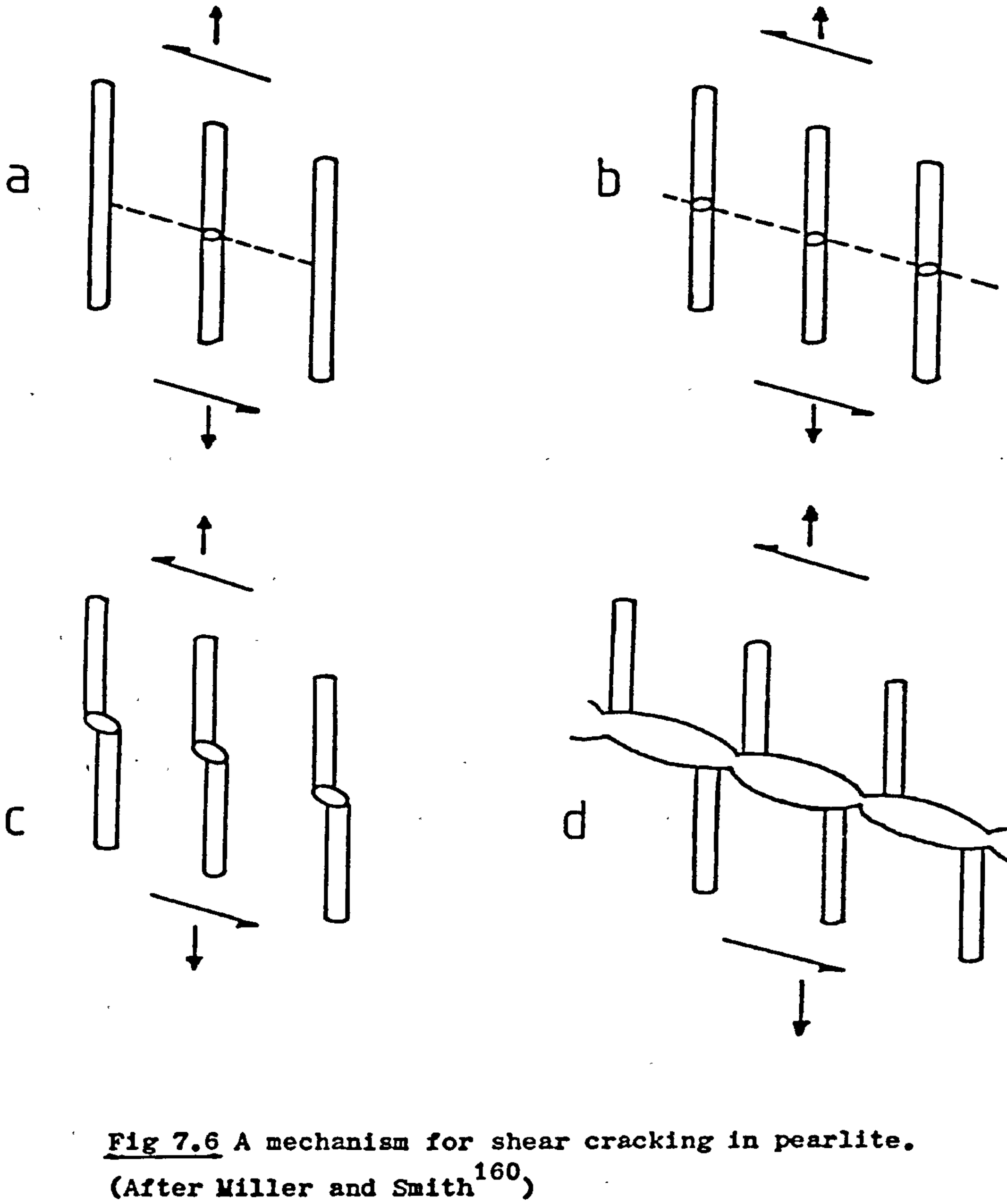

Fig 7.6 A mechanism for shear cracking in pearlite.
(After Miller and Smith[160])

in tensile specimen, the shear cracking of a few lamellae was able to initiate unstable cleavage in fatigue precracked impact specimens.

7.3 CLEAVAGE CRACK PROPAGATION AND THE EFFECT OF MICROSTRUCTURE ON THE TOUGHNESS OF PEARLITIC STEELS

Much of the work on the toughness of pearlitic steels has focused attention on the correlation of microstructure with the Charpy impact transition temperature. It is therefore worth discussing what progress has been made in this area.

The linear relationship between the impact transition temperature and the grain size in polygonal ferrite structures is well established[101,146]. The cleavage fracture stress in steels is virtually independent of temperature if fracture is induced by slip[130]. The occurrence of a ductile-brittle transition temperature is therefore predominantly the result of the marked temperature dependence of the yield stress[130,131]. The ductile-brittle transition temperature is conventionally defined as the temperature where the yield stress exceeds the fracture stress[101]. As lower transition temperatures result from a finer grain size, it should be expected the cleavage fracture stress is more grain size dependent than the yield stress. This effect has been explained by the fact that cleavage cracks have to be reorientated or renucleated at high angle grain boundaries. Smaller grain sizes therefore offer more resistance to a propagating cleavage crack[101]. Consequently, determination of the major obstacles to cleavage crack propagation has been an important part of the investigation of the role of microstructure on the toughness of pearlitic steels.

As the pearlite lamellae apparently have little effect on a cleavage crack,[157,161] a major emphasis has been placed on the influence on pearlite colony size and prior-austenite grain size on continuous cleavage crack propagation.

Danko and Stout[155] examined microcracks near the fracture surface in Charpy specimens of a eutectoid steel and concluded that these cracks were mainly limited in length to a single pearlite colony diameter. The work of Burns and Pickering[128] and Gladman et al[90] support this observation. These authors reported that cleavage cracks terminate within or change direction at, the boundaries of pearlite colonies. In addition, Gladman et al[90] found that the magnitude of the colony size effect on the impact transition temperature was virtually the same as for the ferrite grain size in low carbon steels.

The application of electron microscopy to the study of cleavage crack propagation in pearlitic steels has resulted in some controversy over the role of pearlite colonies in obstructing cleavage crack propagation and therefore determining the toughness of pearlitic steels. Observations by Turkalo[164] in high-carbon pearlitic steels indicated that although the fracture path may change direction at colony boundaries it more often continued as a single cleavage facet across many pearlite colonies extending over part, or in some cases, the whole of one prior-austenite grain. These findings led Tetelman and McEvily[131] to suggest that there may be some preferred orientation between the cleavage planes in adjacent colonies within a prior-austenite grain. The prior-austenite grain size is then the effective grain size for fracture in pearlitic steels.

A more recent study by Hyzak and Bernstein[86] examined the effect of pearlite colony and prior-austenite grain size on the impact-transition temperature of eutectoid steels. While heat treatments produced a range of prior-austenite grain sizes between approximately 14 and 170 microns, the pearlite colony size only varied between 4 and 7 microns. These results are notably different from the colony size measurements of Gladman et al[90] which, for a similar composition air cooled from 1100°C, ranged between 45 and 132 microns. Nevertheless such differences were overlooked by Hyzak and Bernstein[86]. As they obtained a wide variation in mechanical properties for different heat treatments, the latter authors[86] considered the pearlite colony size to exert little, if any, influence on the toughness of eutectoid steel. The impact transition temperature was found to be related to the prior-austenite grain size, and independent of transformation temperature (Fig. 7.7).

Recently Bernstein and fellow workers[84,86,161,163] have made a detailed study of cleavage fracture in isothermally transformed hypo-eutectoid and eutectoid high-carbon rail steels. By etching the fracture surface, Park and Bernstein[115,116] revealed that a fracture facet was composed of a number of pearlite colonies. This observation was therefore consistant with the report of Turkalo, and the conclusions of Tetelman and McEvily[131]. As cleavage cracks have been shown to propagate along {100} ferrite planes in pearlite[115], as also observed in pure iron[131] and low carbon steels[165], the fractographic observation of a number of colonies within a given facet clearly implies that cleavage planes in some adjoining colonies must be continuous.

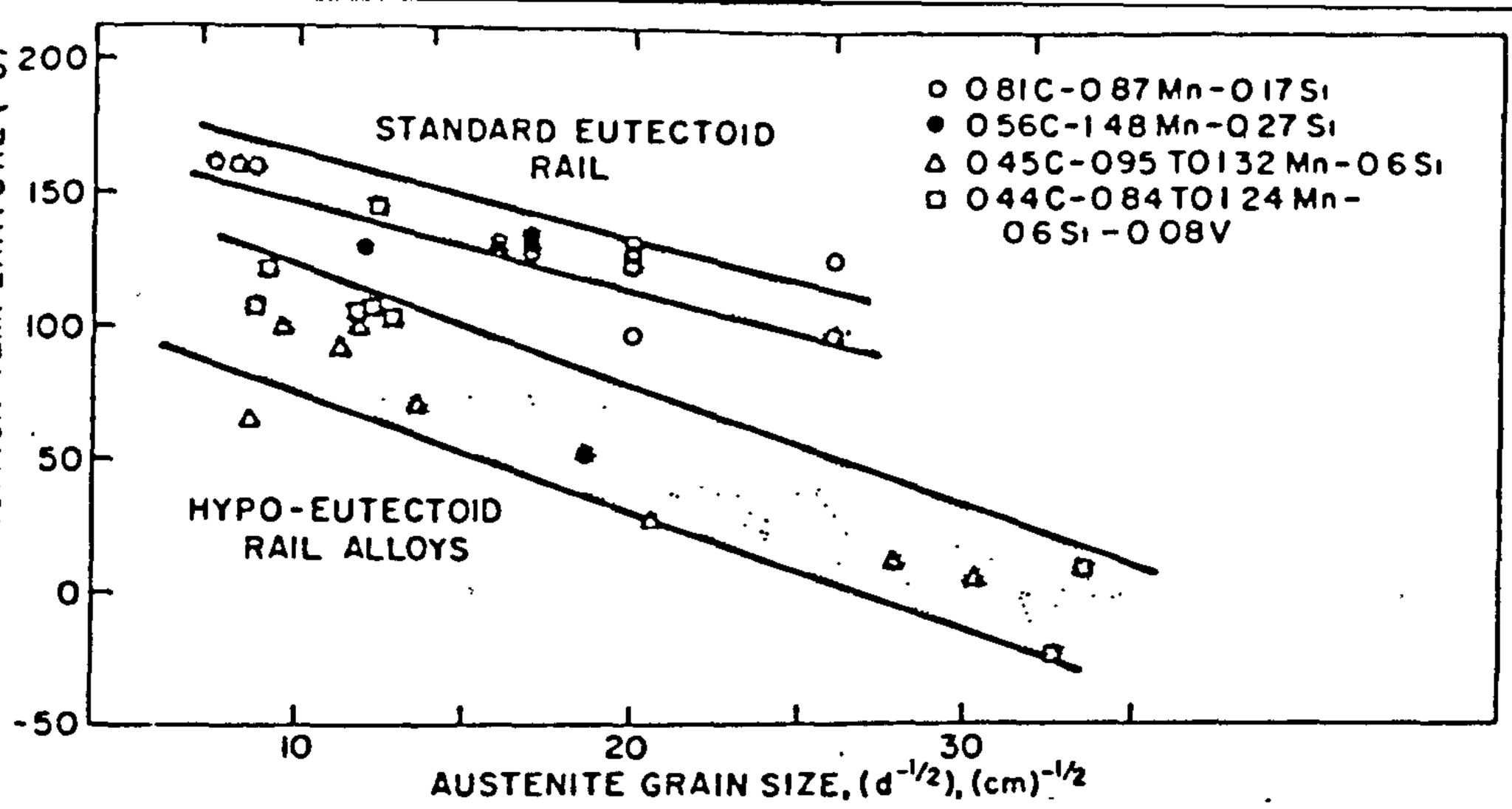

Fig 7.7 The relationship between the impact transition temperature and the prior-austenite grain size in hypo-eutectoid and eutectoid steels. (After Bouse et al[84])

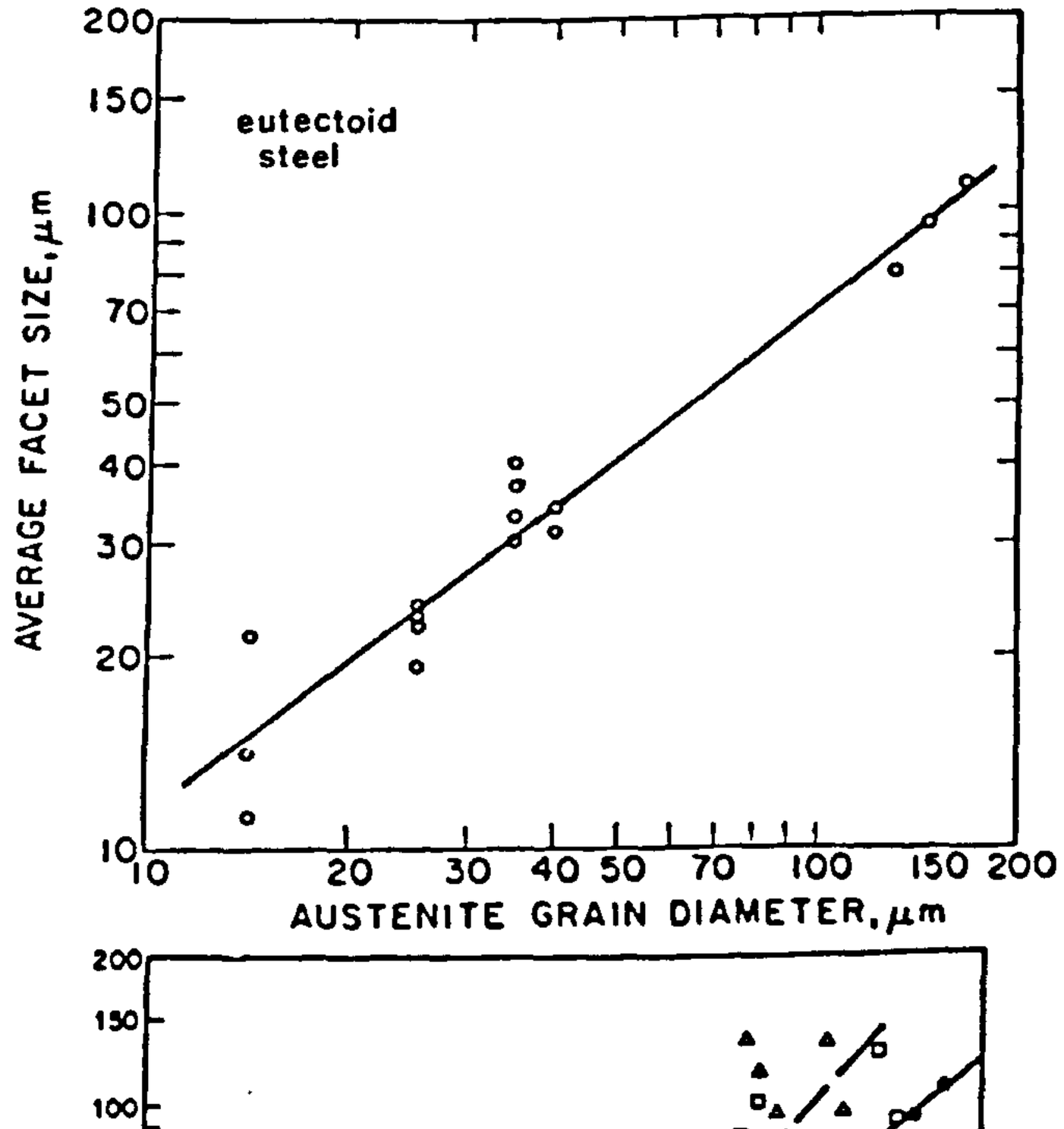

Fig 7.8 & 7.9 The relationship between the cleavage facet size and the prior-austenite grain size in hypo-eutectoid and eutectoid steels.(After Bernstein et al[84,163])

In support of this hypothesis, thin foil transmission electron microscopy studies by Bernstein et al[115,151,163,166] and others[167,168] have shown that {100} ferrite planes are indeed closely aligned across the 'boundaries' of a number of pearlite colonies. With reference to Smith's hypothesis[11] (see Section 1.1.1) Park and Bernstein[161] suggested that the size and orientation of such 'units', consisting of adjacent colonies of common parentage, would be directly related to the prior-austenite grain size. The measurement of the cleavage facet size by scanning electron microscopy gave a reasonable correlation with prior-austenite grain size (Fig. 7.8 and 7.9) for both hypo-eutectoid and eutectoid steels. Thus Bernstein et al[84,86,115,161] concluded that fine austenite grain size gave small 'orientation units' and therefore explained the observed improvement in toughness (Fig. 7.7). Park and Bernstein[161] argue that in practice the size of such 'orientation units', and therefore the effective grain size governing toughness, can be obtained by measuring the cleavage facet size.

In a recent review of the role of microstructure on the toughness of high-carbon pearlitic steels, Gladman and Pickering[101] confirmed their early conclusion that the pearlite colony size is the major microstructure feature determining toughness. It would therefore appear that despite the numerous studies of Bernstein et al and the work of Turkalo[164] some debate still remains. Even though very little variation in colony size was obtained by Bernstein and fellow workers[84,86,171] for a range of transformation temperatures and prior-austenite grain sizes, transformation temperature as well as prior austenite grain size have been

suggested to have an influence on the colony size[82,90]. Further work is therefore needed to resolve such controversy and to obtain a measurable microstructural, rather than a post fracture parameter to correlate with toughness.

In addition, the work of Bouse et al[84] on hypo-eutectoid steels is not entirely satisfactory. As discussed by Gladman and Pickering, variables other than prior-austenite grain size should be taken into account when considering toughness in these steels. Gladman and Pickering[90,101] have examined the effect of microstructural parameters on the ductile-brittle transition temperature (T_C) of ferrite-pearlite steels. Such a relationship was shown to be complex, involving the proportions of ferrite and pearlite, the pearlite spacing (S_o), the cementite lamella thickness (t), the ferrite grain size (d) and the pearlite colony size (P). In a similar fashion to their work on strength, (see section 2.2.4) the authors obtained a regression equation of the form:

$$T_{C(\pm 30)}{}^{\circ}C = (1-V_P)\left[-46-11.5d^{-\frac{1}{2}}\right] + V_P\left[-335+5.6S_o^{-\frac{1}{2}} - 13.4P^{-\frac{1}{2}} + (3.48\times10^{-6})t\right] \quad (7.6)$$

where d, S, P and t are expressed in mm and V_P is the volume fraction of pearlite.

Gladman and Pickering[101] argued that decreasing S_o would tend to increase T_C by virtue of the increased strength. As the pearlite spacing, S, is related to t, by,

$$t = \frac{0.15 \text{ wt.\%C}.S}{V_P}$$

as shown earlier (see section 5.3.1.1), decreasing S will result in

a simultaneous decrease in t for a given carbon content and V_P. Drawing on evidence in the literature for the plastic deformation of fine cementite lamellae, the authors concluded that a decrease in t will reduce T_C because the cementite will deform rather than crack. Gladman and Pickering[101] thus suggested that the influence of either S or t may predominate or be self-cancelling. Such a prediction might then explain why some studies have suggested that decreasing S, increases[169,170,171], decreases[155,156] or has no effect[86] on the impact transition temperature of pearlitic steels.

In hypo-eutectoid steels the volume fraction of pearlite is of some importance to the value of T_C. In general, increasing V_P by increasing the carbon content decreases the toughness. This conclusion has been attributed to the fact that the work hardening rate increases with increasing V_P due to the decreased volume of easily deformable ferrite, which has the effect of increasing the tendency for brittle fracture. However, if V_P is increased in hypo-eutectoid steels, at a given carbon level by low transformation temperatures or by decreasing the eutectoid carbon content by alloying, the reduced value of t predicted by equation 7.7 should result in improved toughness. Evidence of low impact transition temperatures for dilute pearlitic steels has been presented by Gladman, McIvor and Pickering[90].

7.3.1 Fracture Toughness Studies

In contrast to the numerous studies dealing with Charpy impact toughness, very little work has been published on the relationship between the microstructure and fracture toughness of high-carbon pearlitic steels. The study of Hyzak and Bernstein[86],

though mainly concerned with the impact transition temperature of eutectoid carbon steel, does indicate superior room temperature K_{Id} values for specimens of fine prior-austenite grain size. Bouse et al[84] noted a similar effect in hypo-eutectoid steels, with K_{Id} again being closely related to the prior-austenite grain size. Conversely work at British Rail by Allery[172] found no effect of prior-austenite grain size in the range 30 to 300 microns for air-cooled specimens of 0.28 to 0.6 wt.%C steel. Further work is therefore needed to clarify the influence of this micro-structural parameter on the fracture toughness of pearlitic steels. In addition the role of pearlite spacing has not been fully investigated, although there is some evidence[173] that it may affect the value of K_{IC}.

CHAPTER 8

EXPERIMENTAL PROCEDURE

It is the intention of this part of the present study to examine the effect of varying the re-austenitising temperature and cooling rate on the Charpy impact and plane strain fracture toughness properties of high-carbon pearlitic steels. Three of the compositions investigated in Part 1 were chosen, as indicated in Table 8.1. In addition, a large plate (30 x 203 x 500 mm) of composition similar to that of SL175A was supplied by British Steel Corporation through the Skinningrove Works. The composition of this steel is also given in Table 8.1

8.1 HEAT TREATMENT

The heat treatment program for standard Charpy, instrumented-impact and fracture toughness tests was essentially the same as that carried out in Part 1, that is,

(a) a varied austenitising temperature and a constant cooling rate, and,

(b) a constant austenitising temperature and a varied cooling rate.

To avoid unnecessary repetition, the experimental details of individual heat treatments have been kept to a minimum. Heat treatment variations are summarised in the tables of results collected at the end of Chapter 9.

SAMPLE	wt% C	wt% Si	wt% Mn	wt% P	wt% S	wt% Cr	wt% Mo	wt% Cu	wt% Sn
SL174A	0.42	0.19	0.77	0.03	0.016	< 0.02	< 0.02	< 0.05	< 0.005
SL175A	0.59	0.21	0.84	0.038	0.016	< 0.02	< 0.02	< 0.05	< 0.005
SL175B	0.82	0.21	0.82	0.036	0.02	< 0.02	< 0.02	< 0.05	< 0.005
RS518	0.59	0.22	0.77	0.03	0.017	< 0.05	< 0.05	< 0.01	< 0.010

Table 8.1 Compositions of bar and plate steels.

SPECIMEN No	*COOLING RATE $^{o}Cs^{-1}$	TRANSFORMATION TEMP'	
		T_{min}	T_{max}
1	4.3	623	639
2	4.8	623	638
3	4.8	627	644
4	3.9	623	639
5	4.5	623	639
MEAN $\pm$ St Dev	4.5 ± 0.4	624 ± 2	640 ± 2
* Cooling rate prior to transformation			

Table 8.2 Comparison of cooling rates and transformation temperatures for a number of similar heat treatments.(Specimen 5A19)

8.1.1 Standard Charpy Impact Specimens

Following the approach of Hyzak and Bernstein[86] a number of Charpy heat-treatment blanks (14 x 14 x 60 mm) were machined from the as-received bar. Eight specimens of each composition were austenitised at 800, 900, 1000 and 1160°C for 20 minutes and allowed to cool in air. The heat treatments were conducted at the beginning of this study and no cooling rates or transformation data were recorded. Nevertheless, as all blanks were of similar dimensions, the cooling conditions can be regarded as constant.

It was decided also to attempt to achieve three separate cooling rates for similar blanks of each composition after austenitising at 1200°C. 87 mm long specimen blanks were cut from the as-received bar (20 mm dia.) and a thermocouple probe was embedded in one end of each specimen, as discussed in Section 3.2. A preliminary experiment was then conducted to investigate the possibility of cooling more than one specimen at the same rate in the forced air cooling rig and the vermiculite packed chamber, as described in Section 3.2. Using the same gas flow pressure in the rig, it was found that the cooling rate prior to transformation was virtually identical for specimens of similar dimensions. In contrast, some difficulty was encountered in trying to achieve precisely the same transformation start and finish temperatures. A large number of specimens were heat treated and many specimens had to be rejected. With care, however, a number of specimens were cooled to give average transformation minimum and recalescence maximum temperatures within the limits of ±8°C. Typical examples are given in Table 8.2 and it can be seen that the majority of transformation temperatures are somewhat closer than these limits.

The slow cooling of a number of specimens in the vermiculite chamber was easier to duplicate. Transformation temperatures for specimens slow cooled from 1200°C rarely differed by more than 3°C. Such a variation is similar to that obtained on air cooling from 1200°C. As a further check hardness tests were conducted at the centre of specimens chosen to have the same heat treatment. Standard deviations between different specimens and were within the normal scatter obtained on testing individual samples. Thus six specimen blanks were obtained from each of the three cooling methods (rig, air and vermiculite).

8.1.2 Instrumented-Impact and Fracture Toughness Specimens

For compositions SL175A and SL175B instrumented-impact and fracture toughness test specimen blanks were of similar dimensions. As before, 87 mm long blanks were cut from bar material. Specimens were austenitised at various temperatures between 800°C and 1200°C for 20 minutes and then cooled in vermiculite, air and in the forced cooling chamber. In addition, four fracture toughness test piece blanks of dimensions 23 x 50 x 220 mm were cut from the plate of composition RS518. Three specimens were air cooled, following austenitising for 20 minutes at 900, 1000 and 1200°C, and one specimen was furnace cooled from 1000°C.

For reasons which will be discussed later as large a specimen as possible was needed for instrumented-impact and fracture toughness testing. Therefore to reduce decarburisation, particularly at high temperatures, argon was flushed through the furnace door inlet during austenitising. Argon was also used as the cooling gas in accelerated cooling experiments. Cooling rates and transformation data were again obtained from axially embedded thermocouple probes.

8.2 MECHANICAL TESTING

8.2.1 Standard Charpy Impact Testing

Oversized heat-treated blanks were machined to standard Charpy-V-notch impact test specifications. Testing was conducted in the temperature range -70°C to 350°C, depending on the composition of the steel being tested. Sub-zero temperatures were attained by mixtures of absolute alcohol and liquid nitrogen. Test temperatures up to 100°C were obtained using a water bath and temperatures from 100°C to 350°C using a small muffle furnace located close to the Charpy impact machine. Fracture surfaces were examined to aid the selection of test temperatures suitable for producing specimens having upper or lower shelf energies. After testing, the fracture surfaces were washed in alcohol, dried and sprayed with protective lacquer. Hardness measurements were made on all tested specimens for each composition and heat treatment. The average value from five hardness tests per specimen and the standard deviation obtained were recorded. Finally, the ductile-brittle transition temperature was taken as the temperature corresponding to a mean energy between upper and lower shelf values.

8.2.2 Instrumented-Impact Testing

In this section of the work it was proposed to examine the suitability of instrumented-impact testing in the ranking of steels which fail in a predominantly brittle manner. Evidence from the literature indicated that room temperature tests on 0.59 and 0.82 wt.%C steelswould give energy values at or close to the lower shelf[128]. Thus the effect, if any, of different heat treatments is not readily apparent from conventional Charpy V-notch tests.

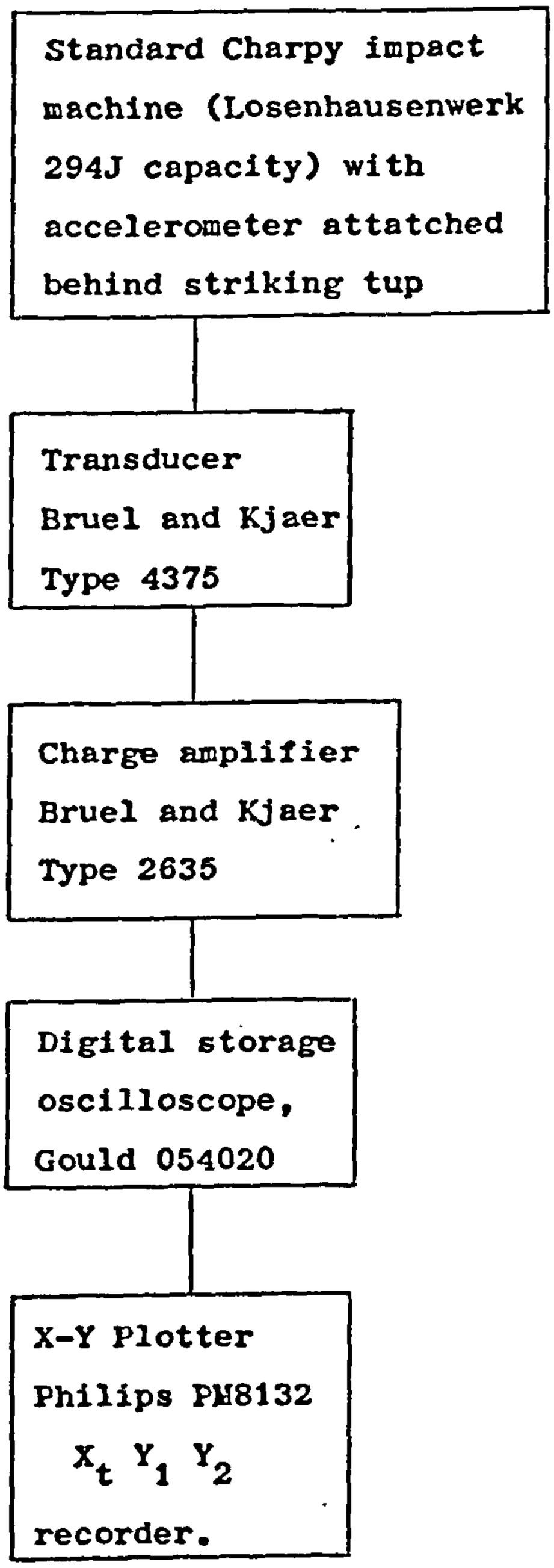

Fig 8.1 Test equipment used for instrumented impact testing.

The testing equipment and procedure was a modification of that used at the British Steel Sheffield Laboratories for the instrumented-impact testing of carburised steels. The test equipment comprised:

(a) an impact machine,

(b) a load sensor, and

(c) a signal display unit

and is similar to that used in a number of other studies[141,175]. All testing was carried out on a standard Charpy impact machine. To measure the force-time history during the test an accelerometer was attached behind the striking head of the Charpy hammer (tup). Initially, cyanoacrylate cement was used to attach the accelerometer, but better damping of the hammer vibration was obtained using a plasticine mount. Attachment cables from the accelerometer were firmly secured to the impact pendulum and connected via a transducer to a charge amplifier. The signal from the amplifier was fed to a digital storage oscilloscope and a hard copy was obtained by printing the stored voltage-time signal using an X-Y plotter. Details of the component parts of the system are shown in Fig. 8.1

Initial testing of standard Charpy specimens revealed that extraneous pendulum and impact hammer vibrations masked the signal arising from the true mechanical response of the specimen. To reduce this interference to a minimum, heat-treated blanks were machined to oversized Charpy specimens of standard V-notch and dimensions 14 x 14 x 77 mm . In addition, a reduced striking velocity (i.e. hammer energy) was used. Specimen duplicates were tested to determine the maximum oscilloscope triggering sensitivity (triggering occurring only from the initial contact of the tup with the

specimen) and to evaluate the most suitable striking velocity which gave the least vibrational interference. The chosen striking velocity was 2.54 ms^{-1}, equivalent to a hammer energy at point of specimen contact of 63 Joules (see Appendix C). This was obtained by holding the Charpy pendulum 54° from the vertical rest position. This position was marked and used in the testing of all specimens. The specimens were placed in the impact machine, making sure the notch was directly opposite the point of contact of the tup. The hammer was then held at the predetermined position, the oscilloscope 'armed' and the specimen broken. The signal held on the oscilloscope was then transferred to the X-Y plotter. After obtaining a permanent record of the signal trace, the procedure was repeated for further tests. Conversion of the voltage-time signal to a force-time record and the calculation of the energy absorbed is discussed in Appendix C.

It is appreciated that the use of large test specimens would give results only comparable with other values obtained from identical testing procedures and specimen geometry. However, this does not constitute a problem as the main aim of this part of the work was the ranking of specimen toughness arising from different heat treatments within a given composition.

Specimen fracture surfaces were examined to ensure that a fully brittle failure had occurred. Hounsfield No. 12 tensile specimens were then machined from broken specimen halves and tested at room temperature, as described in Part 1 (Section 3.3.2).

8.2.3 Fracture Toughness Testing

In BS5447:1977 empirical criteria have been specified which aim to ensure plane strain conditions at fracture during K_{IC}

testing. As discussed in Section 6.3 it is generally accepted that this condition is satisfied when,

$$a \text{ and } B \geq 2.5 \left[\frac{K_Q}{\sigma_{0.2}}\right]^2 \qquad (8.1)$$

where a is the crack length including the machined notch, B is the specimen thickness, K_Q is the candidate stress intensity factor and $\sigma_{0.2}$ is the 0.2% proof stress of the material in uniaxial tension[130].

From the literature[174] a value of 35 $MNm^{-3/2}$ is a good estimate of K_{IC} for BS11 rail steel (0.5-0.6 wt.%C, 0.05-0.35 wt.%Si and 0.9-1.25 wt.%Mn). It was assumed therefore that the K_Q value for the composition SL175B (0.82 wt.%C steel) will be somewhat less than this. Using a provisional value of 30 $MNm^{-3/2}$ and the extreme limits of the strength values encountered in Part 1, for this composition (i.e. $\sigma_{0.2}$ 450 to 718 MNm^{-2}), it can readily be seen from equation 8.1 that a and B require to be between 4 and 11mm to ensure plane strain at fracture. The maximum machineable dimensions for heat treated bar of 20mm diameter were determined to be 14 x 14mm square, allowing for decarburisation (i.e. a ∿ 7mm). It was therefore decided to attempt to measure K_{IC} from heat treated specimens of SL175B composition. In addition tests were carried out on 14 x 14mm, 19 x 38mm and 20 x 40mm cross section specimens of 0.59 wt.%C steel, i.e. compositions SL175A and RS518 (Table 8.3). No tests were performed on 0.42 wt.%C steel as the low strength and high toughness of this composition would require a very large (>50mm thick) test specimen.

After heat-treatment, blanks were machined to single-edge notched bend specimens (Fig. 8.2) of dimensions given in Table 8.3.

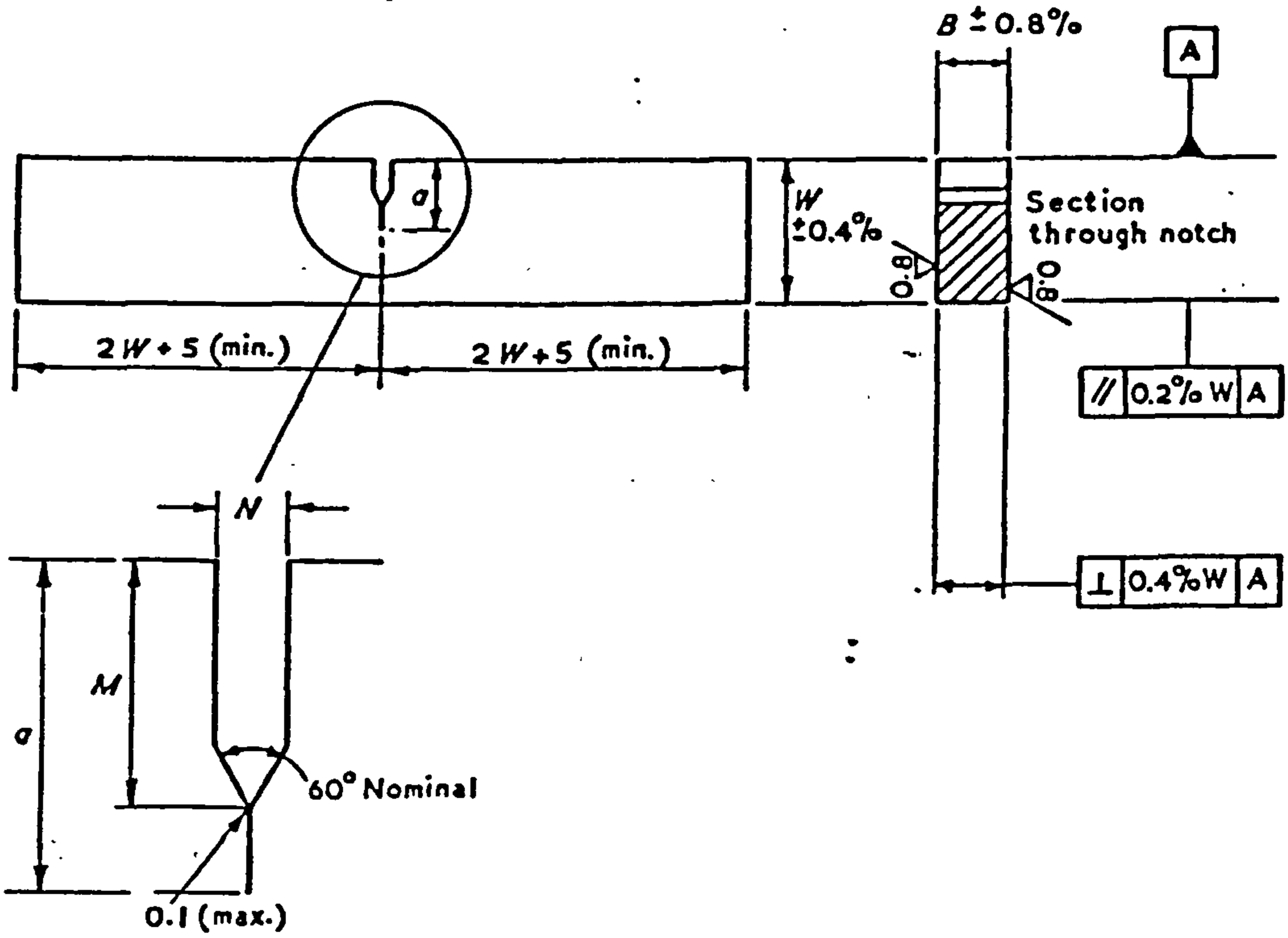

Width = W
Thickness = $B = 0.5W$
Half loading span L = $2W$
Notch width N = $0.065W$ max. (if W is over 25 mm) or = 1.5 mm max. (if W is less than or equal to 25 mm)
Effective notch length M = $0.25W$ to $0.45W$
Effective crack length a = $0.45W$ to $0.55W$

All dimensions are in millimetres.

Fig 8.2 The relationship between geometric factors for single -edge notched bend specimen.(From BS5447:1977)

SPECIMEN COMP'	SPECIMEN DIMENSIONS (mm)			NOTCH	
	WIDTH W	THICKNESS B	TOTAL LENGTH	WIDTH N	LENGTH M
SL175A & SL175B	14.0	14.0	80.0	1.0	5.0
RS518	38.0	19.0	190.0	1.0	15.0
	40.0	20.0	200.0	1.0	16.0

Table 8.3 Fracture toughness test specimen dimensions for 0.59 & 0.82 wt%C steels.

The relationship between geometric factor were in accordance with BS5447:1977 with the alternative thickness to width ration B/W = 1.0 being used for small specimens (see Fig. 8.2 and Table 8.3).

In all cases specimens were fatigue pre-cracked at room temperature, in accordance with BS5447:1977, on a 15 KN capacity Amsler Vibrophore fatigue machine. After fatigue cracking to the required length (i.e. $0.45W < a < 0.55W$), a clip displacement gauge was attached across 'knife edges' located at opposite sides of the machined notch. Specimens were then loaded on freely rotating rollers and room temperature 3 point bend tests were conducted at a loading rate of 0.75 KNs^{-1} on a Keelavite hydraulic testing machine. For the large specimens of RS518 testing was conducted at $-15^{o}C$ in a bath containing alcohol cooled to temperature by liquid nitrogen. The specimen temperature during the test was monitored from a thermocouple in contact with the test piece within 2mm of the crack tip. The temperature of the specimen during testing was within $\pm 2^{o}C$, in accordance with the requirements of BS5447:1977. For all tests the applied force versus clip gauge displacement was recorded autographically on an X-Y plotter.

After testing to failure, specimens were examined at low magnification on an optical microscope and the crack length, a, (notch plus fatigue crack) was measured at positions corresponding to 25%B, 50%B and 75%B. The specimen thickness, B, and the width, W, were also measured. The provisional value of fracture toughness, K_Q, was calculated from the expression[130],

$$K_Q = \frac{P_Q Y}{B W^{\frac{1}{2}}} \qquad (8.2)$$

where P_Q is the fracture load taken directly from linear load displacement traces. For specimens showing slight non-linearity a secant was drawn with a 5% less slope than the initial trace. The value of load, where this secant crossed the test trace, (P_5) was taken as the failure load only in cases where $P_{max}/P_5 < 1.10$. Test traces with value greater than 1.10 were rejected. The stress intensity factor coefficient, Y, was obtained for the appropriate value of a/W from standard tables computed at British Steel Corporation. Finally, specimen halves were machined to Hounsfield No.12 specimens and tensile tests were conducted at room temperature as described in Part 1 Section 3.3.2. Tests were also conducted at $-15^{o}C$ for specimens of composition RS518, using a cooling bath maintained at $\pm 2^{o}C$ throughout the test.

8.3 METALLOGRAPHY

Quantitative metallography was conducted on samples taken from ∿20mm below the fracture surfacesof standard Charpy and fracture toughness specimens. The ferrite volume fraction, ferrite grain size, prior-austenite grain size and the mean random pearlite spacing were measured as described in Part 1 Section 3.4.and therefore the method need not be repeated here. However, additional metallographic measurements were made in this section of the work and these are outlined below.

8.3.1 Pearlite Colony Size

Pearlite colony size measurements were conducted on specimens of 0.59 and 0.82 wt.%C steel, from Part 1,to investigate the effect of austenitising temperature and cooling rate. In addition measurements were carried out on Charpy impact and fracture toughness

specimens. The pearlite colony size was identified and measured by two distinct methods. Following the approach of Brogan and McIvor[176], the optically revolvable pearlite colony size was obtained using a 'colour tinting reagent' due to Beraha[177]. After polishing and etching in saturated Picral, samples were washed in alcohol, dried and immersed in a standard solution of 3g Potassium Metabisulphite and 10g Sodium Thiosulphate diluted to 100ml in distilled water. A normal soaking time was around 60 seconds[177], although variations in the above concentrations and immersion times were made depending on the specimen microstructure. In most cases the pearlite colonies were clearly distinguishable under the optical microscope by virtue of a crystallographic dependent colour etch tint and, in particular, by well defined boundaries. The colony size was then measured at a low magnification (X100 or X200) by a linear intercept method on a Vickers bench microscope fitted with a motorised stage. A minimum of 500 colonies were counted for a given specimen, resulting in a 95% confidence limit of ±6%. As in the case of ferrite grain size measurements, corrections had to be made to obtain the pearlite colony size in a two component ferrite-pearlite microstructure. The optical pearlite colony size, d_p, is then given by[117],

$$d_p = \frac{V_p L}{n} \qquad (8.3)$$

where n is the number of pearlite colonies crossed on a test line of length L, and V_p is the volume fraction of pearlite. As discussed in Section 3.4.1.2, if the error in d_p determination is assumed to be cumulative then d_p values are obtained with a 95% confidence limit of $\sim\pm16\%$.

The second procedure for obtaining the pearlite colony size involved taking mean linear intercept measurements of regions of constant lamella direction using a Philips PSEM 500 scanning electron microscope. This method was subject to a larger error than the previous method, as the 'boundaries' between colonies were less well defined and relatively few completely resolvable colonies could be viewed in a given field. In addition, a certain degree of selection was required in some microstructures, to obtain fields of view containing lamellar pearlite. Therefore, although this procedure cannot then be regarded as giving truly random data, the results will only be used on a comparative basis. 100 colonies were counted per specimen and using the expression of Pickering[117] (equation 3.2,Section 3.4.1.2) this gives a 95% confidence limit of $\sim\pm15\%$.

8.3.2 Fractography

8.3.2.1 Fracture Path

Broken Charpy specimens showing essentially fully brittle fracture, were selected from each composition and heat-treatment. Two separate specimens containing the fracture surfaces were cut from each half of the test-piece. Both specimens were ultrasonically cleaned in acetone in order to remove the lacquer coating which was applied to the samples after testing. One specimen was then prepared for SEM examination. The other fracture surface was nickel-plated in a standard solution of Nickel Sulphate ($Ni\ SO_4\ 6H_2O$) 240 gl^{-1}, Nickel Chloride ($Ni\ Cl_2\ 6H_2O$) 45 gl^{-1} and Boric Acid (H_3BO_3) 30 gl^{-1} at a temperature 54^{o}C and a pH of 3 to 5. The nickel-plated specimen was then mounted in bakelite with the fracture surface normal to the plane of polish and the fracture path studied by optical and scanning electron microscopy.

8.3.2.2 Cleavage Facet Size

The cleavage facet size was measured normal to the fracture plane on a Philips PSEM 500 scanning electron microscope. A random linear intercept method was used at a magnification of X160 or X320. Employing the PSEM 500 specimen tilt facility together with the tilt correction, fields of view could be inclined such that the majority of facets appeared closely perpendicular to the test line. 500 facets were counted for a given specimen. Stereo-pair fractographs were then taken by tilting the specimen through 5^{o} and were used to examine the accuracy of linear intercept measurements.

Some criticism can be made of measuring a three dimensional fracture surface from a two dimensional projection. Although stereo-pair fractographs aid the viewing of the fracture surface, linear intercept measurements are still subject to error due to the fact that the cleavage facets are not always normal to the plane of observation. As the propagation of the crack front is extremely irregular, an underestimate of the cleavage facet size will occur. When the facet is tilted with respect to this plane it can easily be shown that the error varies as the cosine of the angle of tilt. As reported by Park[21], an average incline of 20^{o} can be considered reasonable and this will give an actual cleavage facet size 6.4% larger than that measured. This error together with that arising simply from the statistical significance of the measuring technique would suggest that the fracture facet size is measured to an accuracy of approximately $\sim\pm$13%.

CHAPTER 9

RESULTS AND DISCUSSION

9.1 GENERAL METALLOGRAPHY

As found in Part 1 (Chapter 4), higher austenitising temperatures gave larger prior-austenite grain sizes, lower transformation temperatures and, in only a few cases, corresponding finer pearlite. In all cases, faster cooling rates resulted in lower transformation temperatures and finer pearlite. The general microstructural changes accompanying different heat treatments were consistent with the observations reported in Part 1, and therefore need not be discussed in detail again. The transformation data and the measured and calculated microstructural parameters are collected in tables which can be found at the end of this chapter.

In contrast to Part 1, where it was concluded that the mean free ferrite distance is the microstructural feature governing strength, the pearlite colony size is recognised to be of considerable importance in determining the toughness of pearlitic steels. Consequently the pearlite colony size measurement in this section of the work will be discussed in some detail. Initially the results are discussed with reference to cleavage crack propagation, but in the later discussion, the values are taken in conjunction with other microstructural measurements to explain the observed

effect of heat treatment on, firstly,the Charpy-V-notch and, secondly,the plane strain fracture toughness of high-carbon pearlitic steels.

9.1.1 The Pearlite Colony Size

Typical examples of pearlite colonies as defined by optical and scanning electron microscopy are shown in Fig. 9.1, 9.2 and 9.3. The results for such measurements on the 0.59 and 0.82 wt.%C steels, heat treated for the study on strength, are given in Tables 9.1 and 9.2, and these are graphically illustrated in Fig. 9.4 and 9.5. Although both sets of values are subject to error in definition and measurement it is evident that the pearlite colony size from the optical method is larger in all cases than the corresponding SEM measurements. Although both graphs show an effect of accelerated cooling, and in particular low austenitising temperature, on reducing the size of the pearlite colony, the effect is more noticeable for the optical measurements. An example of the effect of cooling rate on the optical colony size of the 0.59 wt.%C steel is given in Figs. 9.6 and 9.7.

9.2 THE INFLUENCE OF PEARLITE COLONY SIZE ON CLEAVAGE CRACK PROPAGATION

It is useful at this point to begin by considering the pearlite colony as originally defined by Belaiew[5,6]. A pearlite colony,as stated by Belaiew,is a region where in the lamellae usually have one direction, and in which the ferrite and cementite each have a single crystallographic orientation. These colonies,as pointed out by Mehl[3],make up a pearlite nodule. In the present

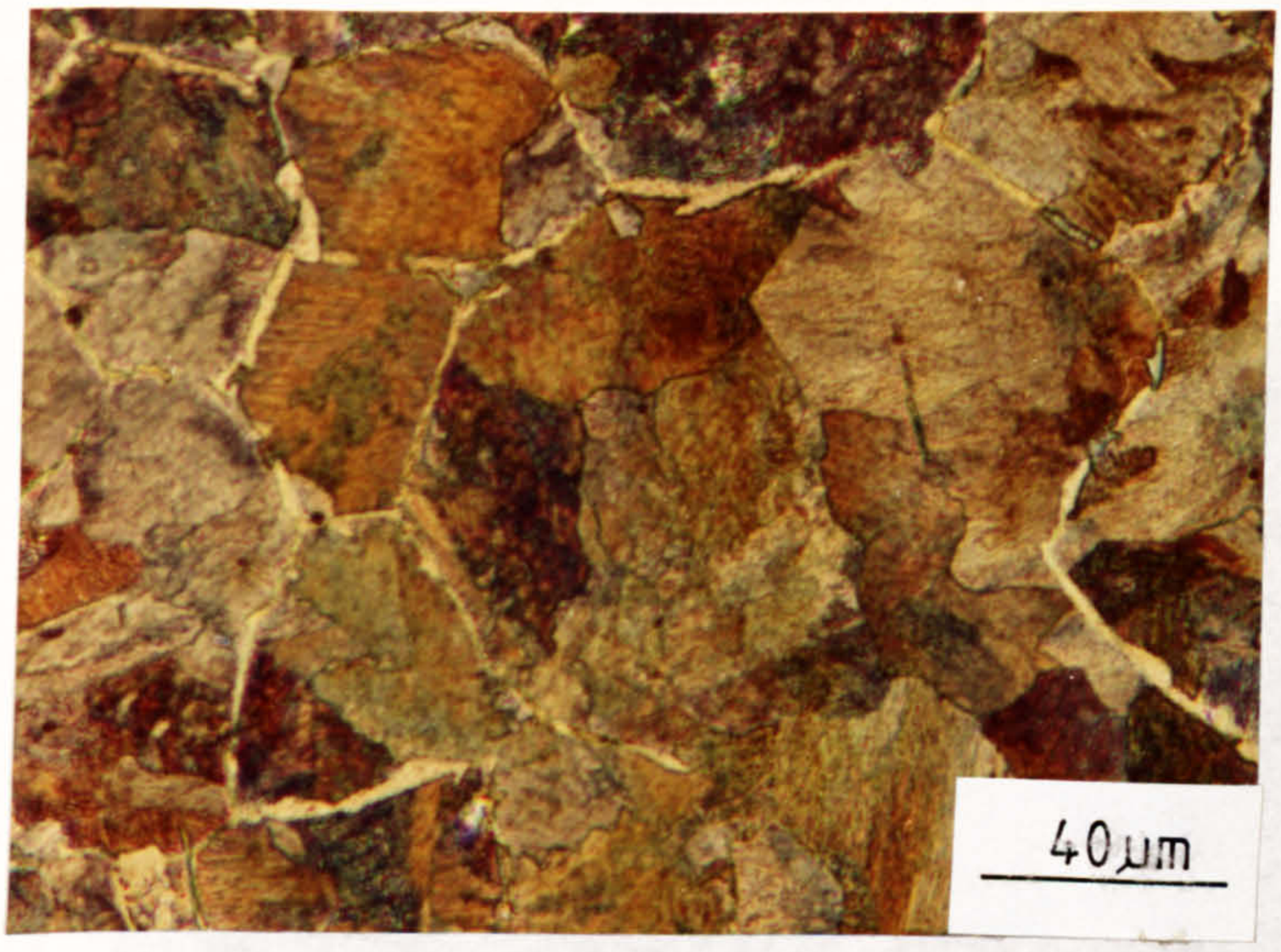

Fig 9.1 Optical micrograph showing the crystallographic dependent colour etching of pearlite grains. (Specimen 5A12)

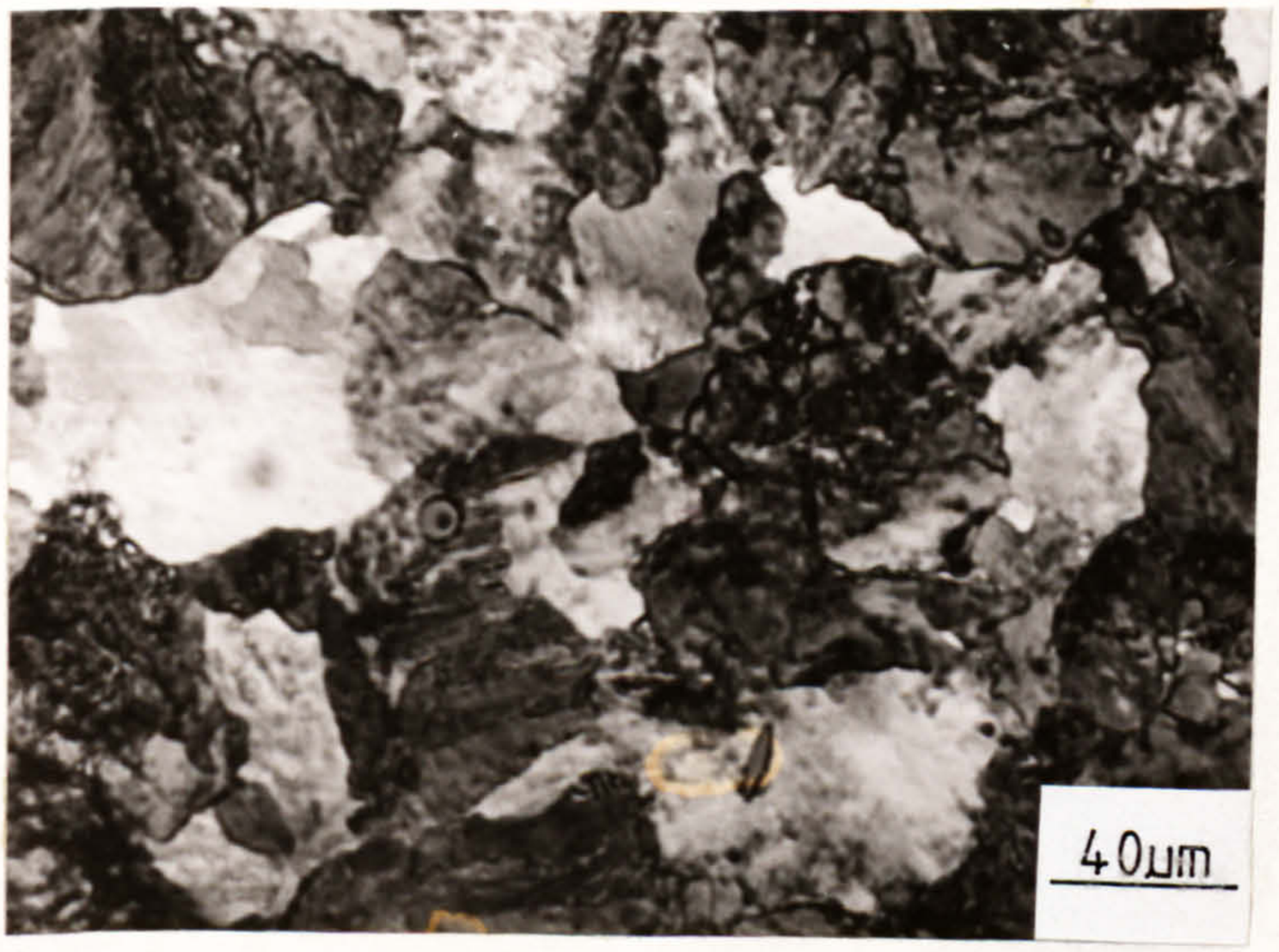

Fig 9.2 Optical micrograph of pearlite grains in a fully pearlitic microstructure. (Specimen 5B12)

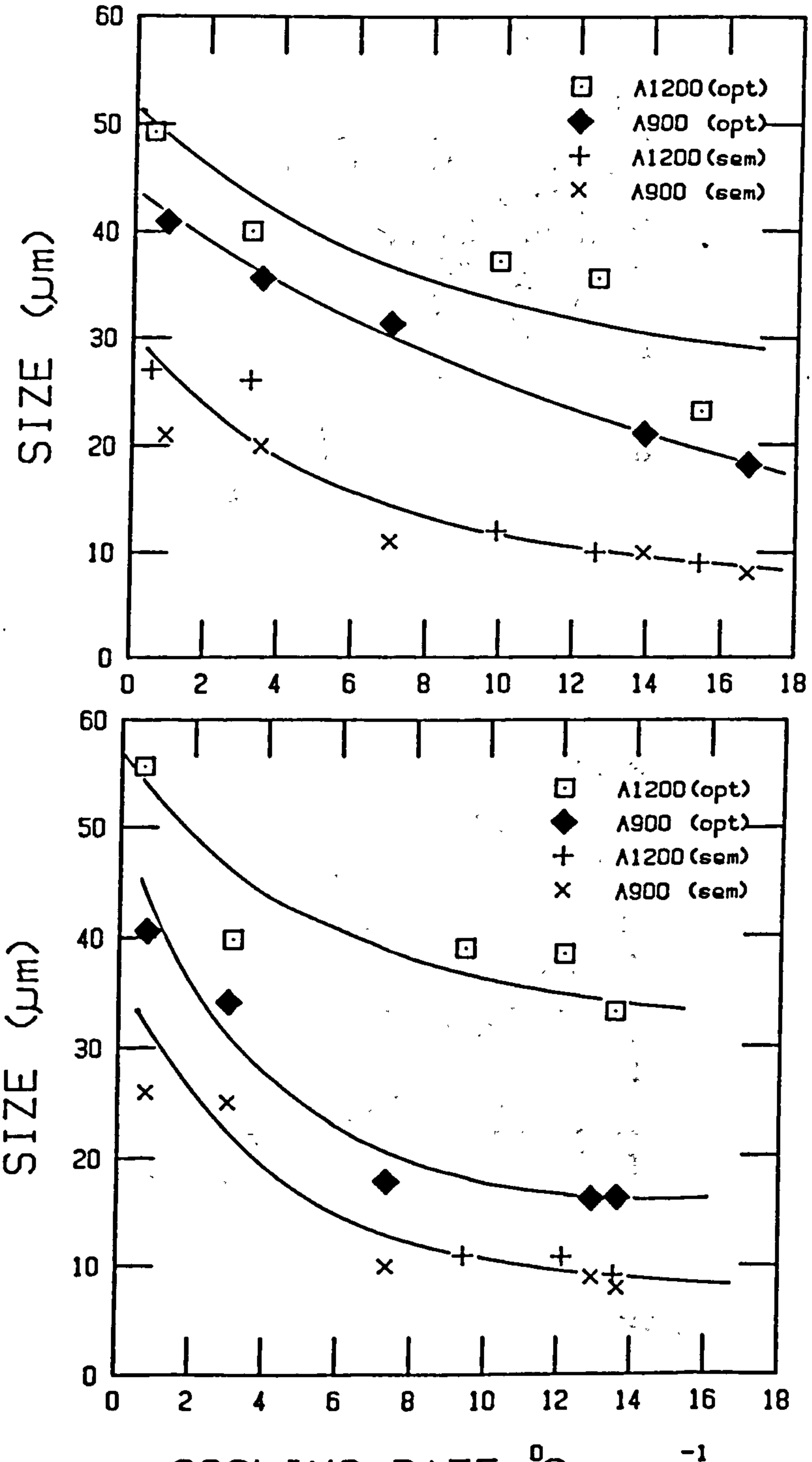

Fig 9.4 & 9.5 Pearlite "colony" size (SEM and optical) as a function of the cooling rate prior to transformation. 0.59 wt%C steel (top), 0.82 wt%C steel (bottom).

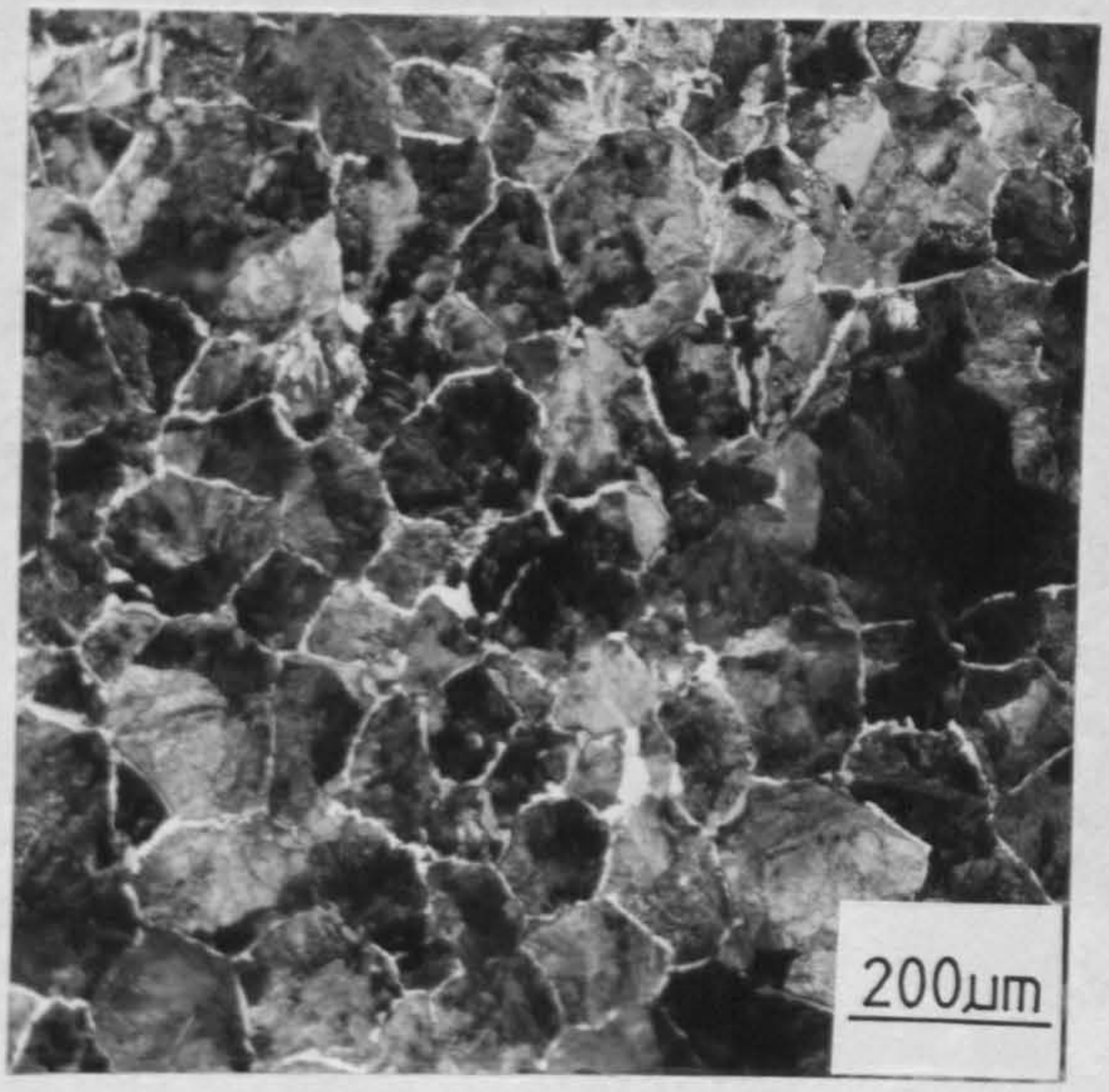

Fig 9.6 Pearlite grains in a slow cooled specimen.(5A12)

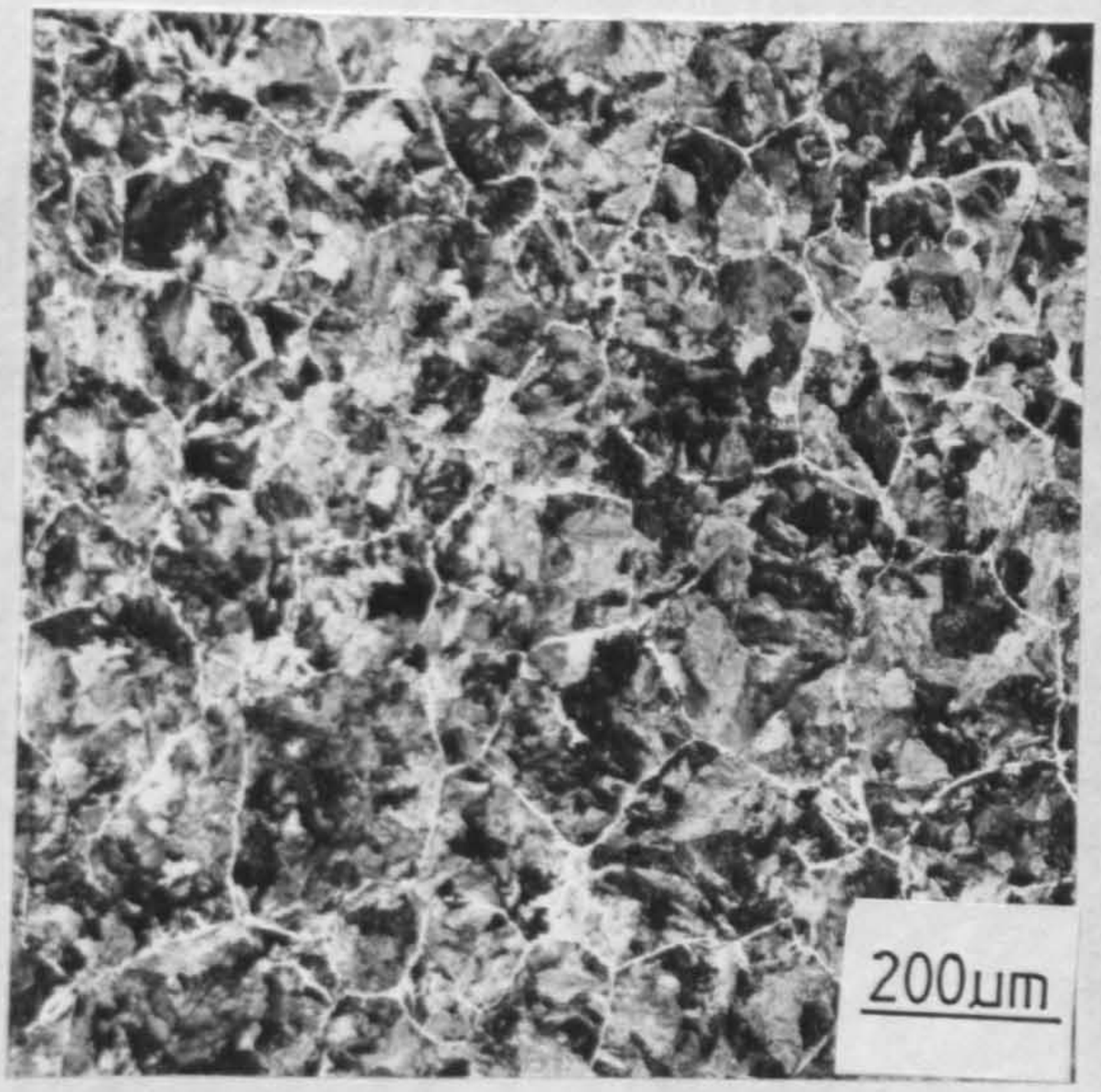

Fig 9.7 Pearlite grains in a rapidly cooled specimen.(5A10)

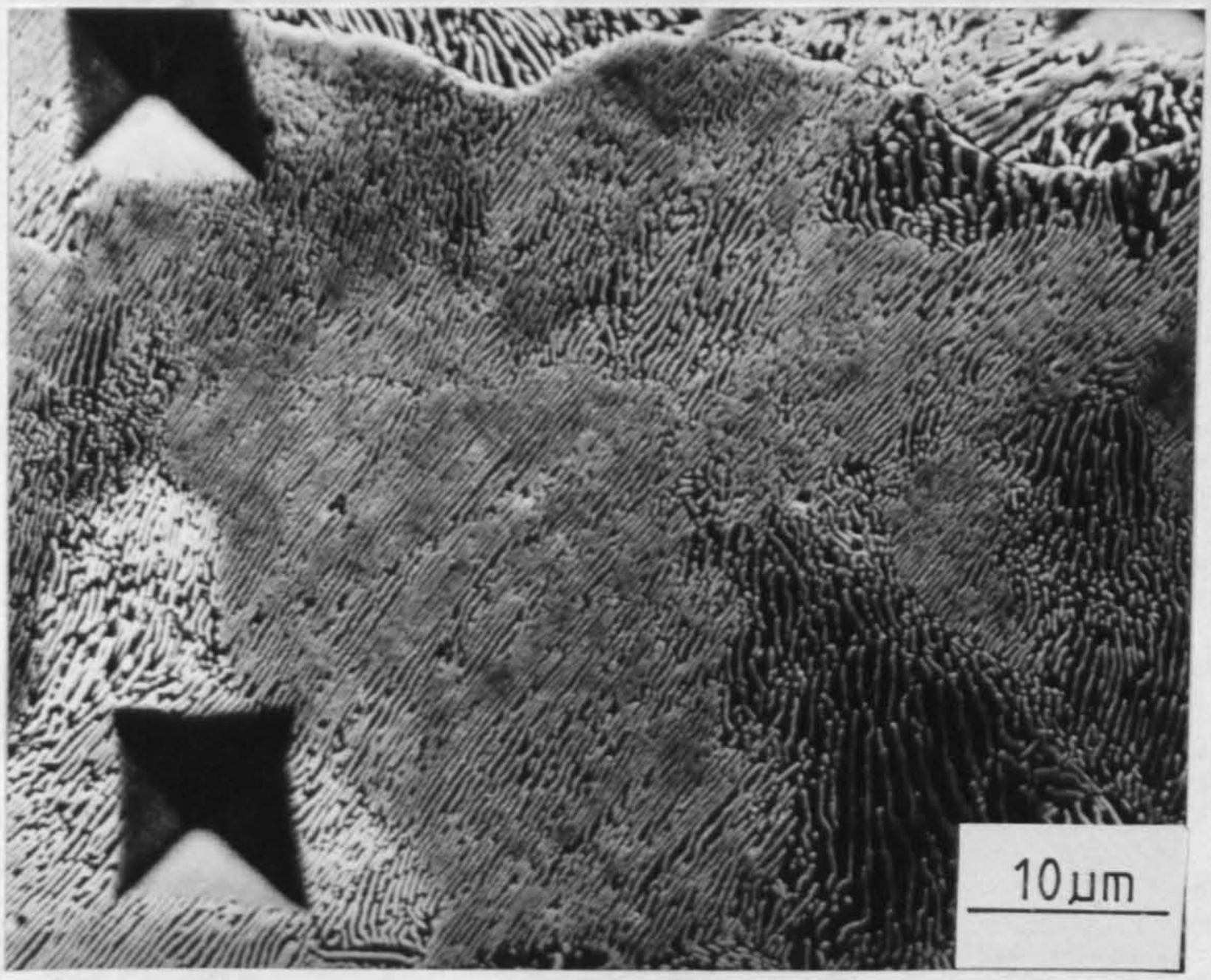

Fig 9.8 SEM micrograph showing micro-hardness indentations around optically defined pearlite grains.(5A12)

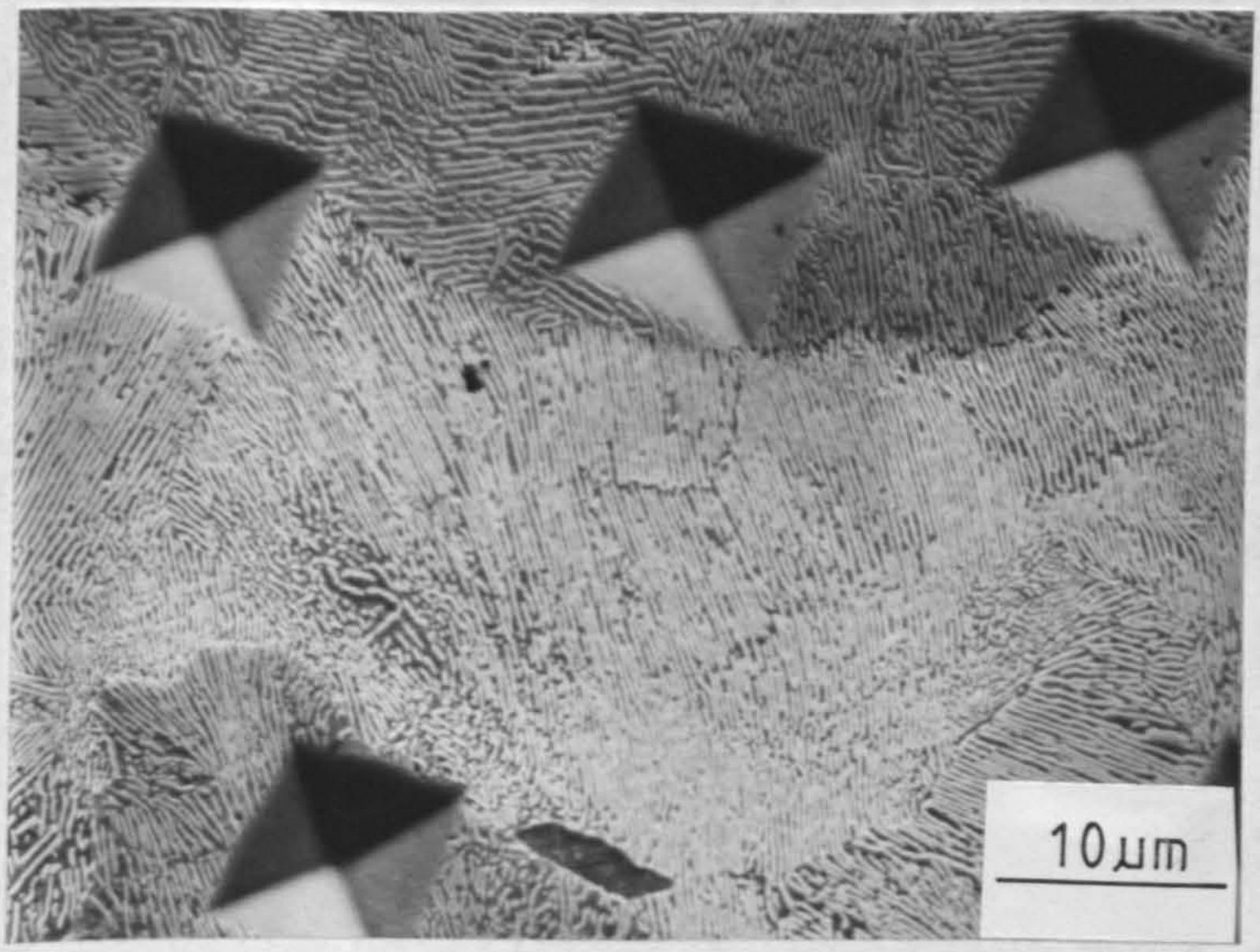

Fig 9.9 SEM micrograph as above.

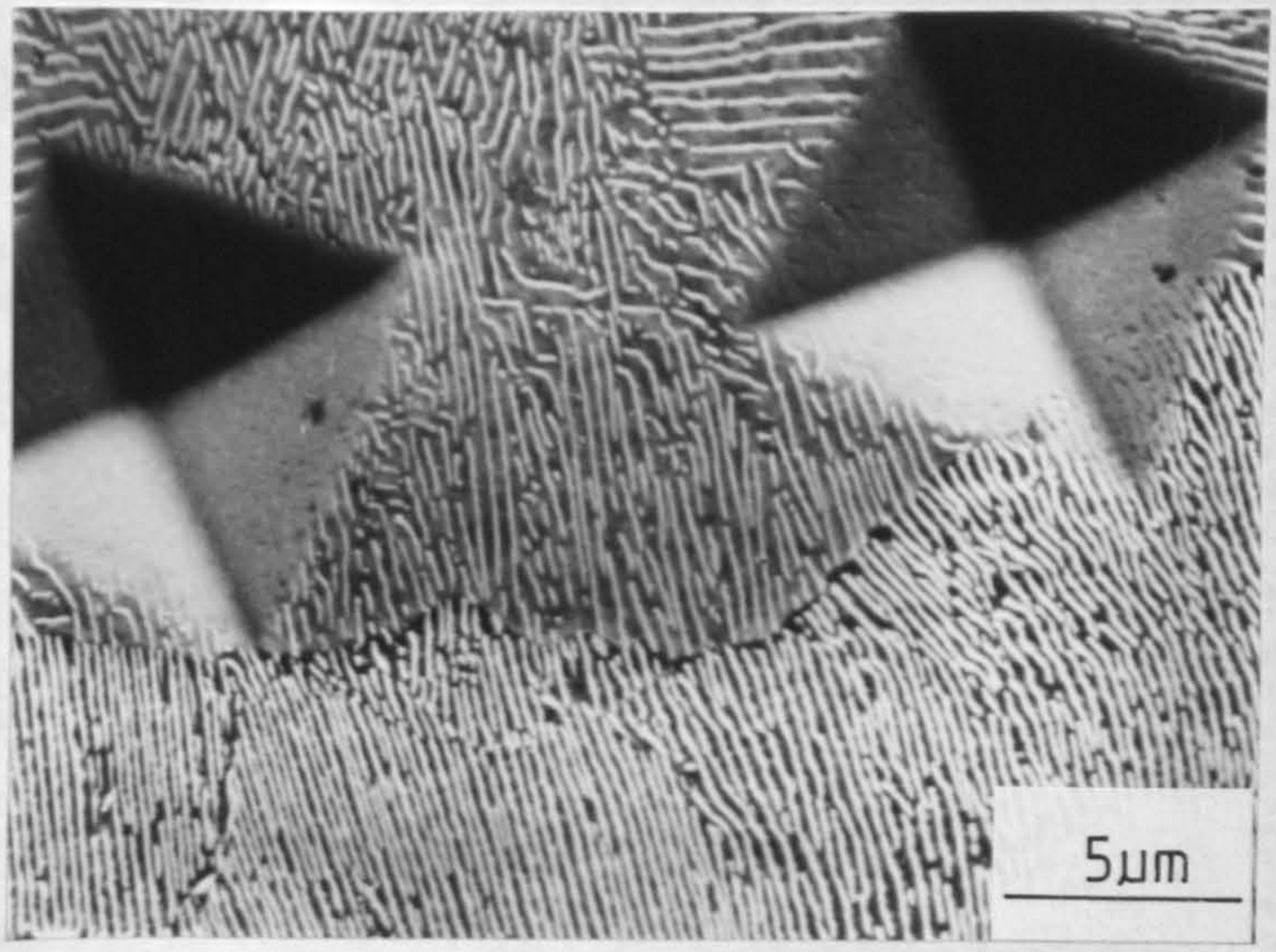

Fig 9.10 SEM micrograph showing micro-hardness indentations at the 'high-angle' boundary of two pearlite grains. (Specimen 5A12)

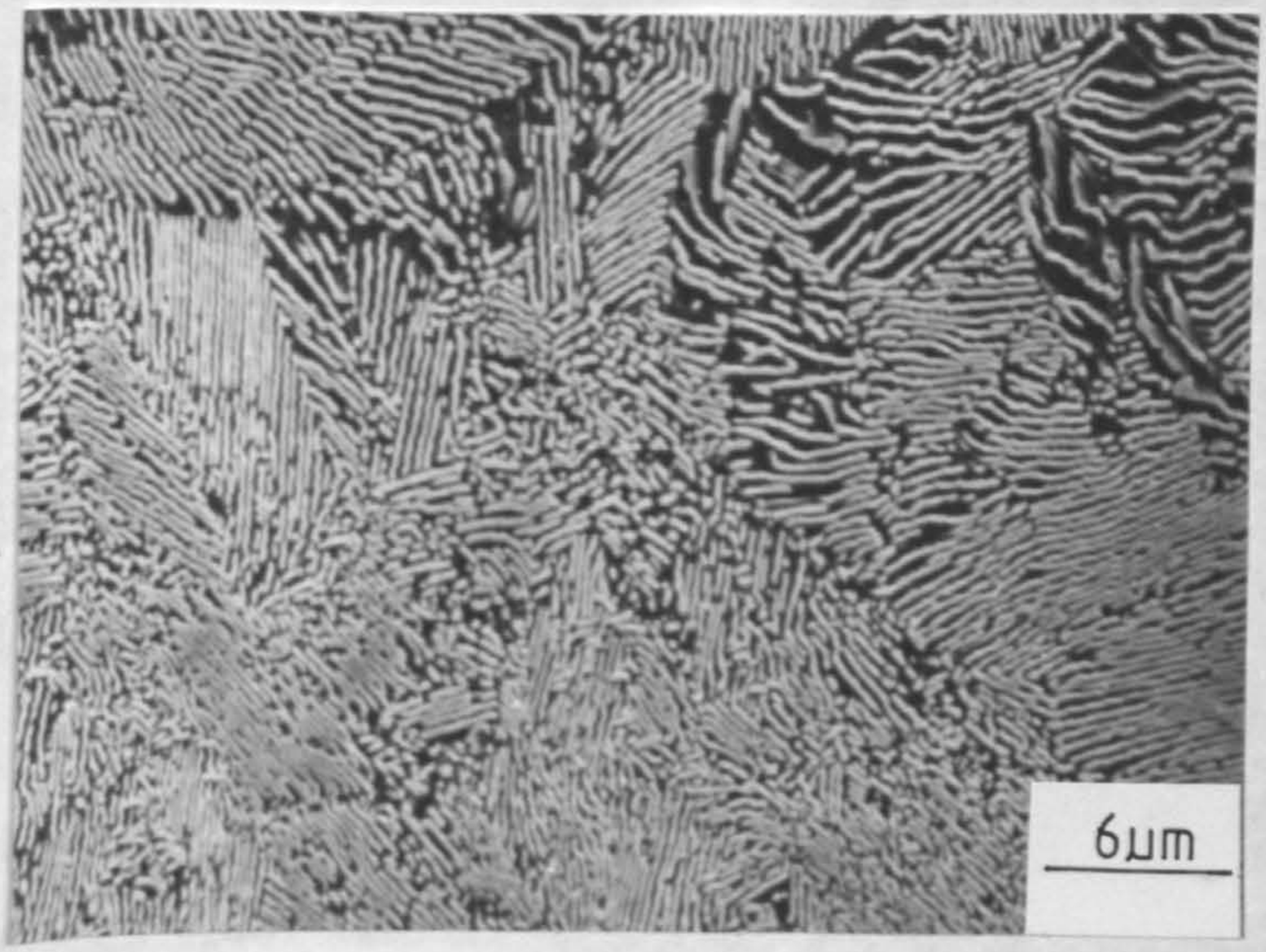

Fig 9.11 SEM micrograph showing a number of cementite lamella growth directions in a non-ideal pearlitic microstructure.(5B4)

study microhardness indentations were made around the boundaries of the optically distinct pearlite 'colonies'. By examining these areas on the scanning electron microscope, (Figs. 9.8, 9.9 and 9.10), it can be seen that optically measured regions may consist of pearlite of more than one lamella direction and therefore, in effect, a number of pearlite colonies. This is confirmed by the work of Takahashi et al[167,168] on the crystallography of eutectoid steels. Their work defined, by a similar crystallographic dependent etching reagent, a "pearlite block" which was composed of a number of pearlite colonies. This optically distinct region was considered to be the final stage of the pearlite nodule formation and thin foil work showed these 'blocks' to indicate regions of constant ferrite crystallographic orientation[167].

As discussed earlier, the series of papers by Bernstein and co-authors[84,86,115,162] on the toughness and cleavage fracture of isothermally transformed pearlitic steels have drawn attention to the frequency with which the fracture path is observed to continue as a single cleavage facet across many pearlite colonies. This observation has led Bernstein et al[84,86,115,163], Turkalo[164] and others[131] to the conclusion, contrary to the findings of Gladman et al[90], that the pearlite colony was not the primary obstacle to cleavage crack propagation. Thin foil microscopy by Park and Bernstein[161] appears to support this conclusion by showing that the {100} ferrite cleavage planes are essentially continuous across the boundaries of a number of neighbouring pearlite colonies. However, it is the difference between the colony size measurements of Gladman, McIvor and Pickering[90] and Bernstein et al[84,86,115,163] that gives an important clue to the reason behind

their apparent disagreement over the role of this microstructural feature in obstructing cleavage crack propagation.

Hyzak and Bernstein[86], as mentioned previously, have shown that large changes in prior-austenite grain size, with very little change in pearlite colony size, resulted in a large change in fracture toughness. The range of colony sizes encountered by these authors[86] was between 4 and 7 microns. Undoubtedly these measurements cannot be of the same microstructural feature as the optical measurements of Gladman et al[90], who for similar compositions, encountered a range of colony sizes up to 132 microns. Bernstein and fellow workers[84,86,115,161,163] were unable to adequately explain this difference, but suggested that it may be due to the fact that their work used isothermal transformation conditions whereas the specimens of Gladman et al[90] were continuously cooled. Such an explanation is, however, unlikely to be acceptable given that the work of Takahashi et al[167,178] also used isothermal transformations.

It is believed in the present study that the electron microscopy measurements of pearlite colony size by Bernstein et al[84,86,115,163] and Turkalo[164] and the optical measurements of Gladman et al[90] are defined in a similar manner to the corresponding measurement in the present study. Indeed, the fractographic evidence presented by Turkalo[164] and by Park and Bernstein[115,163] for cleavage across a number of pearlite colonies, leaves little doubt that these authors regarded the pearlite colony as a region of approximately parallel lamellae. The average colony diameter measured by Turkalo[164] was ≈4 microns, a figure not dissimilar

to those values quoted by Bernstein et al[84,86,115,163] and the SEM measurements given in Tables 9.1 and 9.2.

It is obviously then of some importance to clearly define which microstructural feature is regarded as a pearlite colony. Measurements based on constant lamellae direction can be both difficult to make and may be misleading. Optically defined pearlite regions may have a number of cementite lamellae directions, particularly in 'non ideal' microstructures. Fig. 9.11 illustrates this point.Clearly a great deal of difficulty would be encountered in attempting to measure the pearlite colony size in such areas. In the present study a wide scatter of colony sizes was observed when these colonies were defined as regions of parallel lamellae, and in excess of an order of magnitude size difference frequently occurred within one field of view. In other cases,optically etched regions were composed of pearlitic cementite of predominantly one lamellae direction.

Close inspection of optically defined regions of pearlite in Fig. 9.9 and 9.10 reveals that these areas are clearly outlined by high-angle boundaries. High-angle boundaries are also easily discernible on the optical micrographs in Fig. 9.1 and 9.2. These boundaries formed, in part, the basis of optical 'colony' size measurements. Regions of parallel lamellae within these areas however in general, have no apparent boundary and their size can only be measured when the lamellae are fully resolved. Before proceeding, it would be helpful therefore to make some distinction between the optical and SEM measurements. In the light of the thin foil microscopy of Takahashi et al[167] and of Park and Bernstein[161]

and the observations of the present study it is concluded that the optically measured pearlite colonies are most likely indicative of regions of constant or closely aligned ferrite planes. To avoid further confusion this optically measured parameter will be referred to hereinafter as the Pearlite Grain. In fully pearlitic microstructures the term 'grain' and 'nodule' are synonomous. In ferrite-pearlite microstructures the relationship between pearlite grains and nodules is complicated by the existence of pro-eutectoid ferrite. This point will be discussed later.

The microstructural measurements in the present study seem to imply, that the confusion in the literature regarding the role of pearlite colonies in obstructing cleavage crack propagation has arisen simply from the use of two quite different measurements and interpretations of this parameter. This view is supported by the fact that evidence in favour of pearlite colonies obstructing cleavage propagation has resulted from optical examination[90,128,155] where colonies are normally defined by their etch contrast. Evidence against has been obtained invariably from electron microscopic studies[86,115,163,164]. To test such a conjecture the pearlite grain size will now be compared to the corresponding cleavage facet size from Charpy impact specimens which have failed in a predominantly brittle manner.

9.2.1 Fracture Facet Measurements

As discussed earlier,a method of demonstrating which microstructural feature is the major barrier to crack propagation is to measure the cleavage facet size and relate it to the underlying microstructure. Such techniques have been used with considerable success in bainitic steels[179,180]. Following this

approach, the fracture facet size was measured from lower shelf Charpy specimens of 0.42, 0.59 and 0.82 wt.%C steel heat treated as given in Tables 9.3 and 9.4 (The general form of the Charpy impact curves, the ductile-brittle transition temperature and the micro-structural measurements, also recorded in Tables 9.3 and 9.4, are discussed in detail later).

The fracture facet size was found to be a strong function of the austenitising temperature and, therefore, the prior-austenite grain size. This is illustrated in Figs. 9.12 and 9.13 and in Table 9.3. Large prior-austenite grains give rise to large facet sizes. The cleavage facet size also varied with the cooling rate for a given prior-austenite grainsize as shown in Figs. 9.14 and 9.15 and Table 9.4. Faster cooling rates gave smaller facet sizes. Comparison of this parameter with the pearlite grain or nodule size in fully pearlitic steels yields a close agreement (Tables 9.3 and 9.4). Examination of nickel-plated fracture surfaces as shown optically in Figs. 9.16 and 9.17 and on the SEM, Figs. 9.18 and 9.19 clearly support the view that the high-angle boundaries of pearlite grains or nodules obstruct cleavage crack propagation. The close correspondence between the pearlite grain size and the cleavage facet size in the fully pearlitic steel also implies that the {100}$_\alpha$ ferrite planes are closely aligned or constant within a given pearlite grain.

It is therefore not surprising that the pearlite colony when defined as regions of parallel lamellae has been found to have little influence on crack propagation. This should be controlled almost exclusively by the crystallography of the pearlitic ferrite. Although the orientation of the ferrite and cementite are related

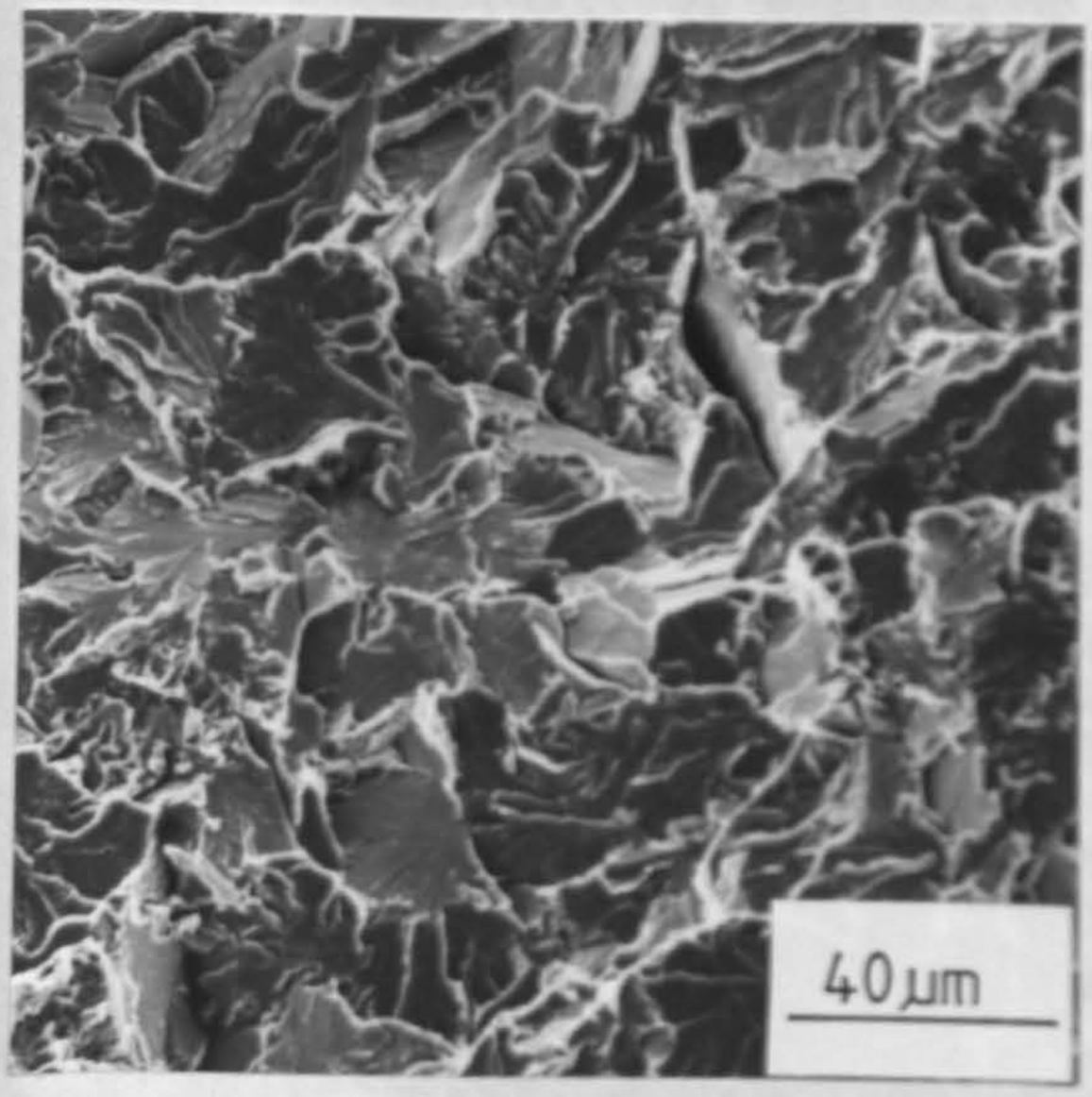

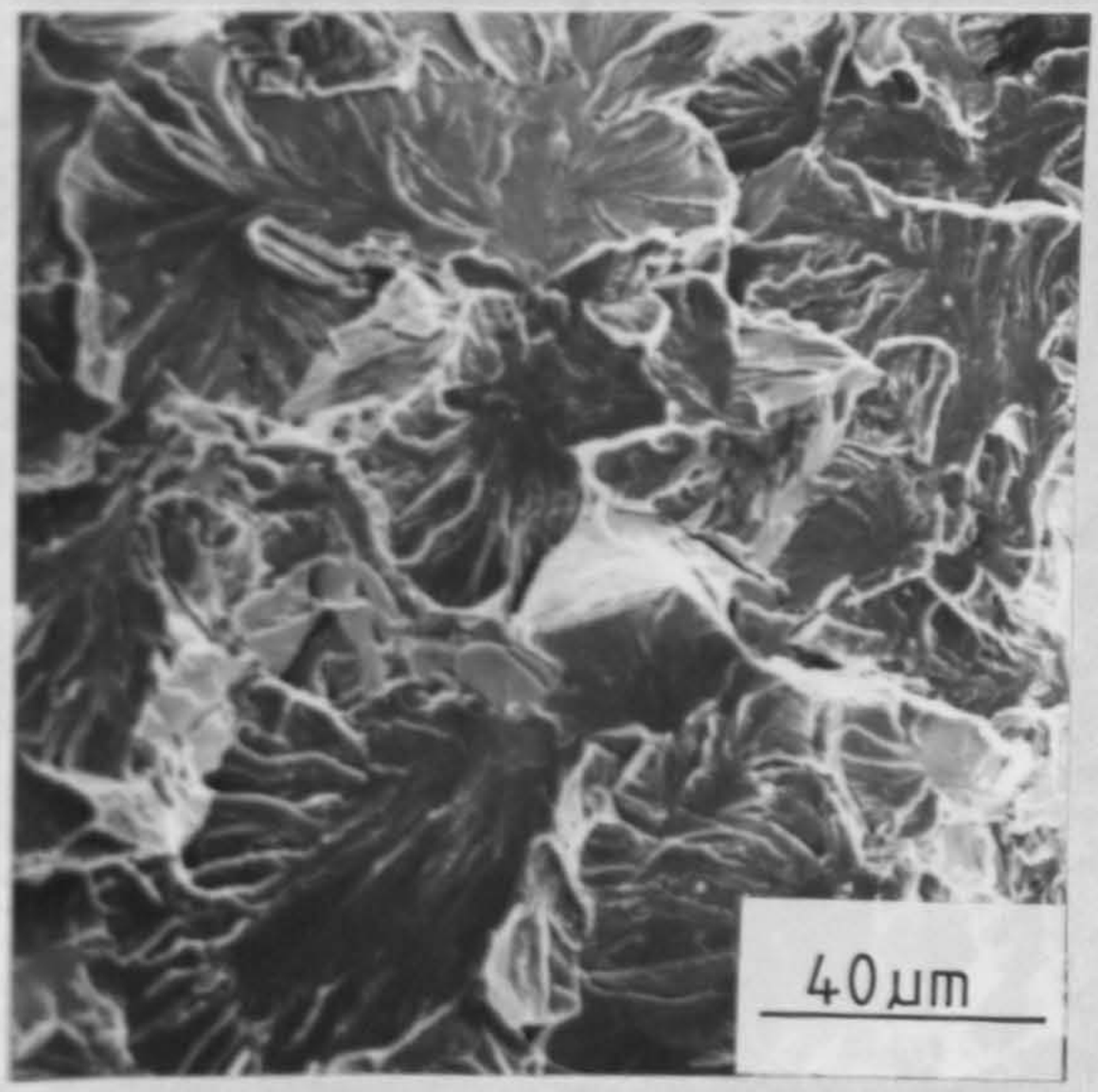

Fig 9.12 & 9.13 SEM micrographs showing the change in cleavage facet size with austenitising temperature at constant cooling rate. Air cooled specimens of 0.82wt%C steel austenitised at 800°C(LHS) and 1160°C.

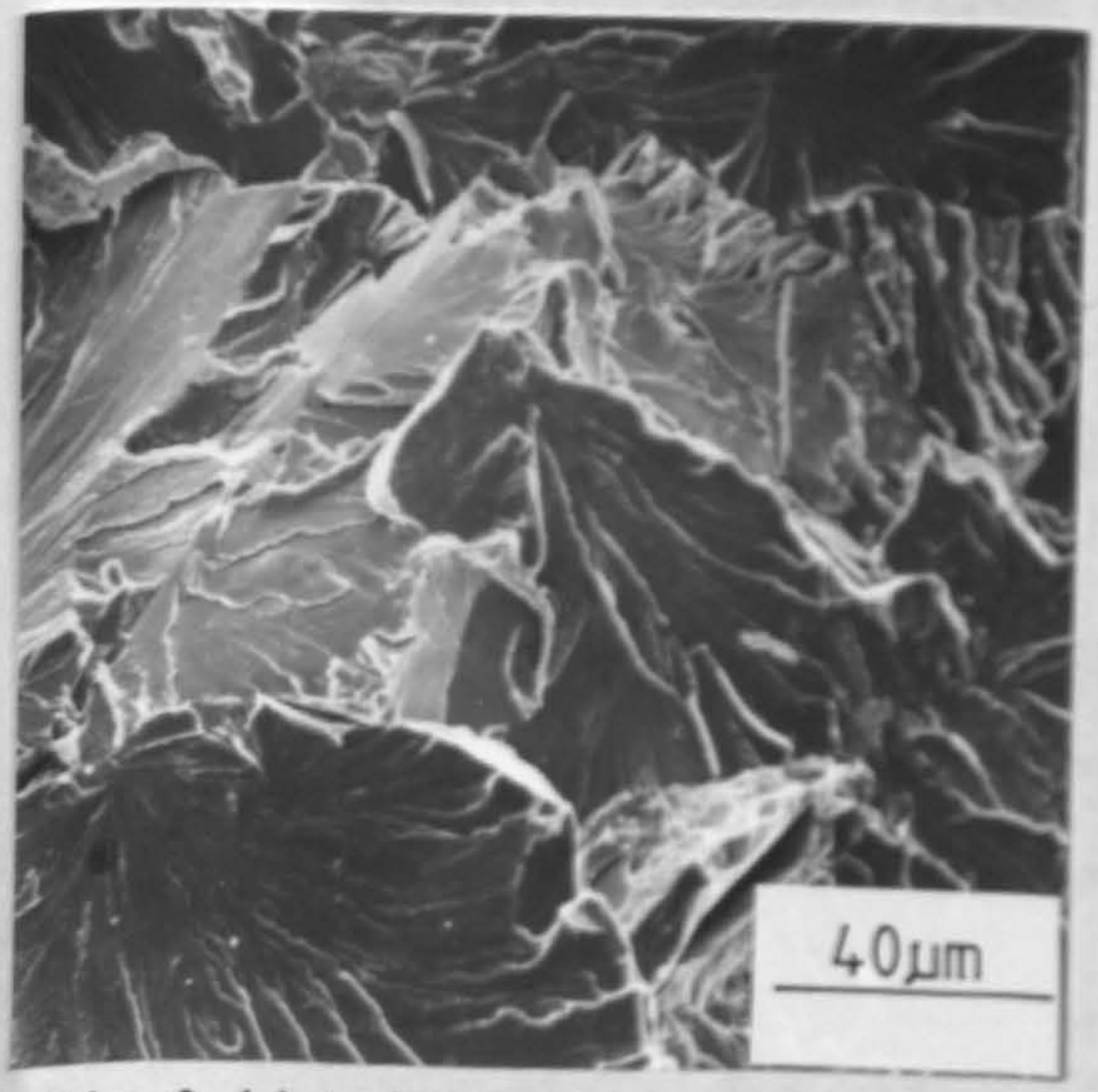

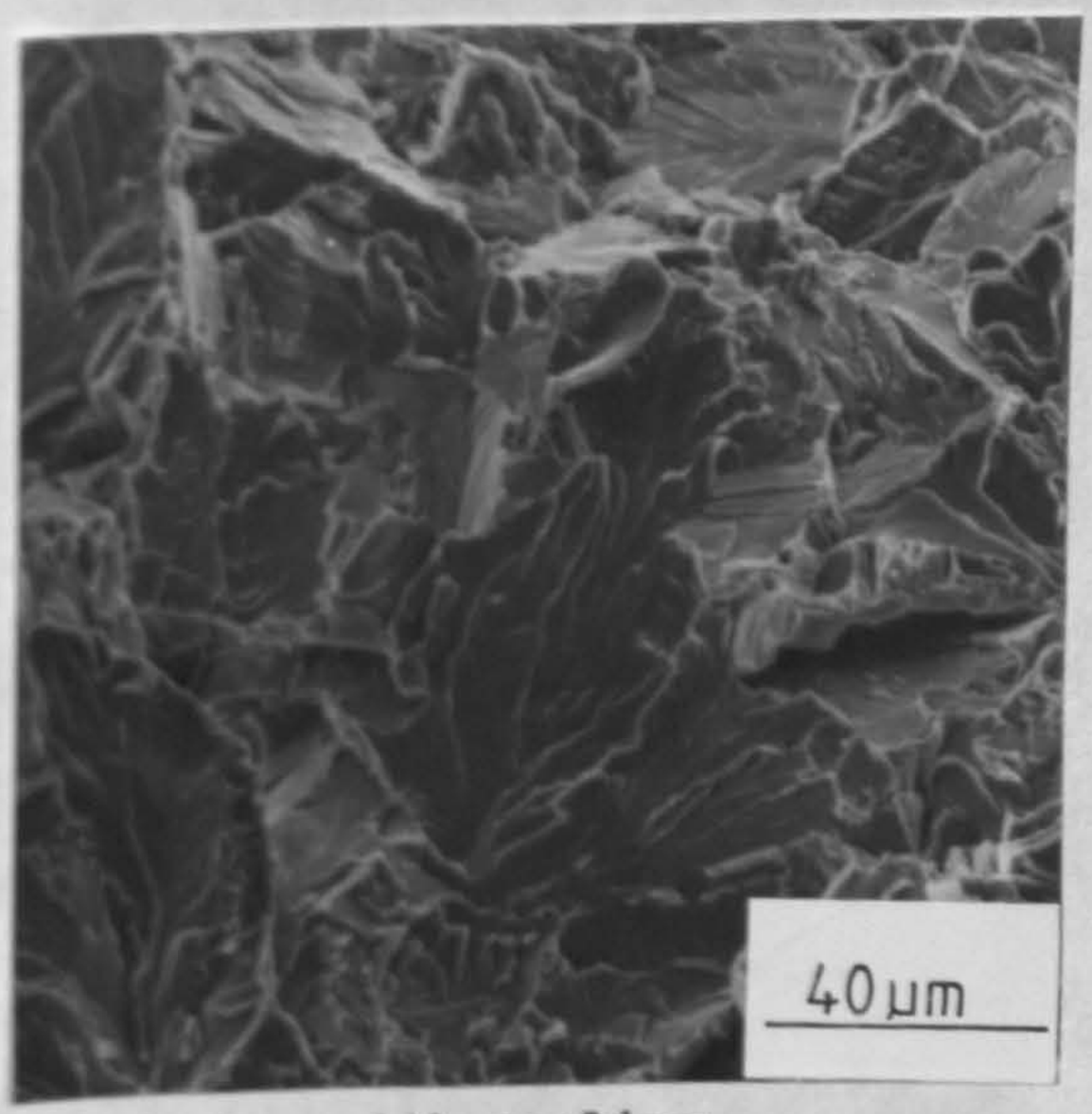

Fig 9.14 & 9.15 Change in cleavage facet size with cooling rate. Specimens of 0.59wt%C steel austenitised 1200°C, vermiculite(LHS) and rig cooled.

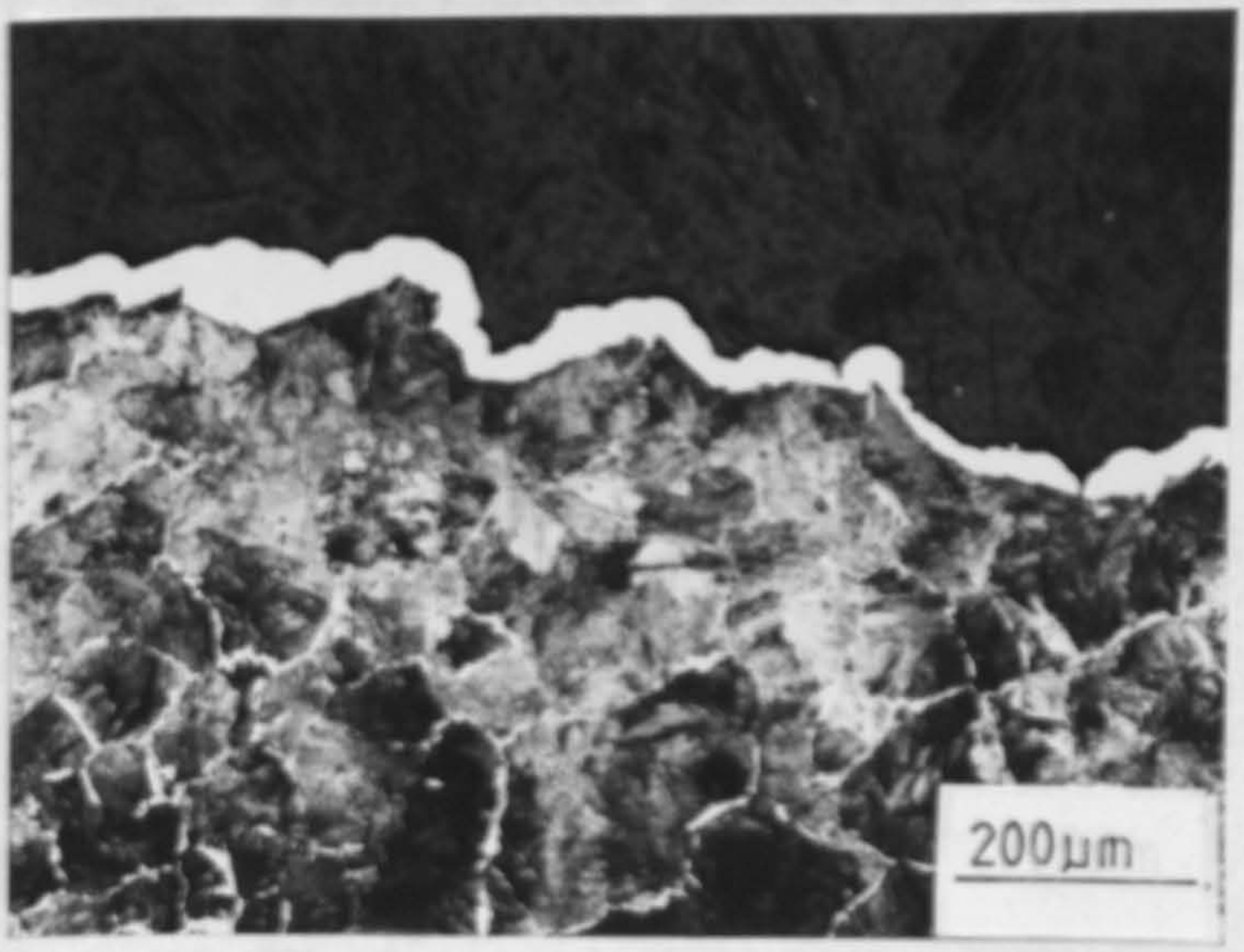

Fig 9.16 Optical micrograph showing the deviation of the fracture path at pearlite grain boundaries.(5AJ7). Note also grain size micro-cracks below the fracture surface.

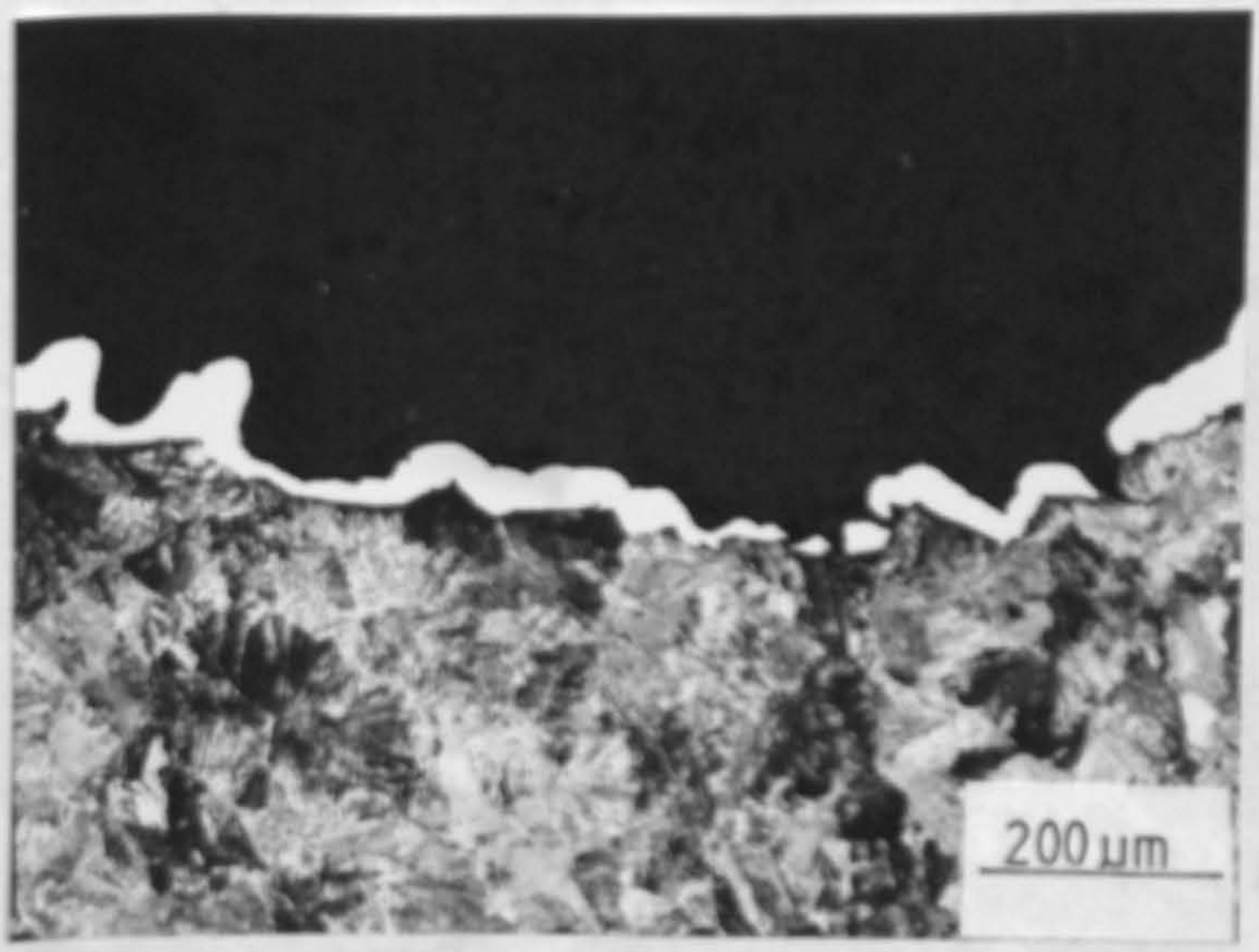

Fig 9.17 As above, specimen 5B17

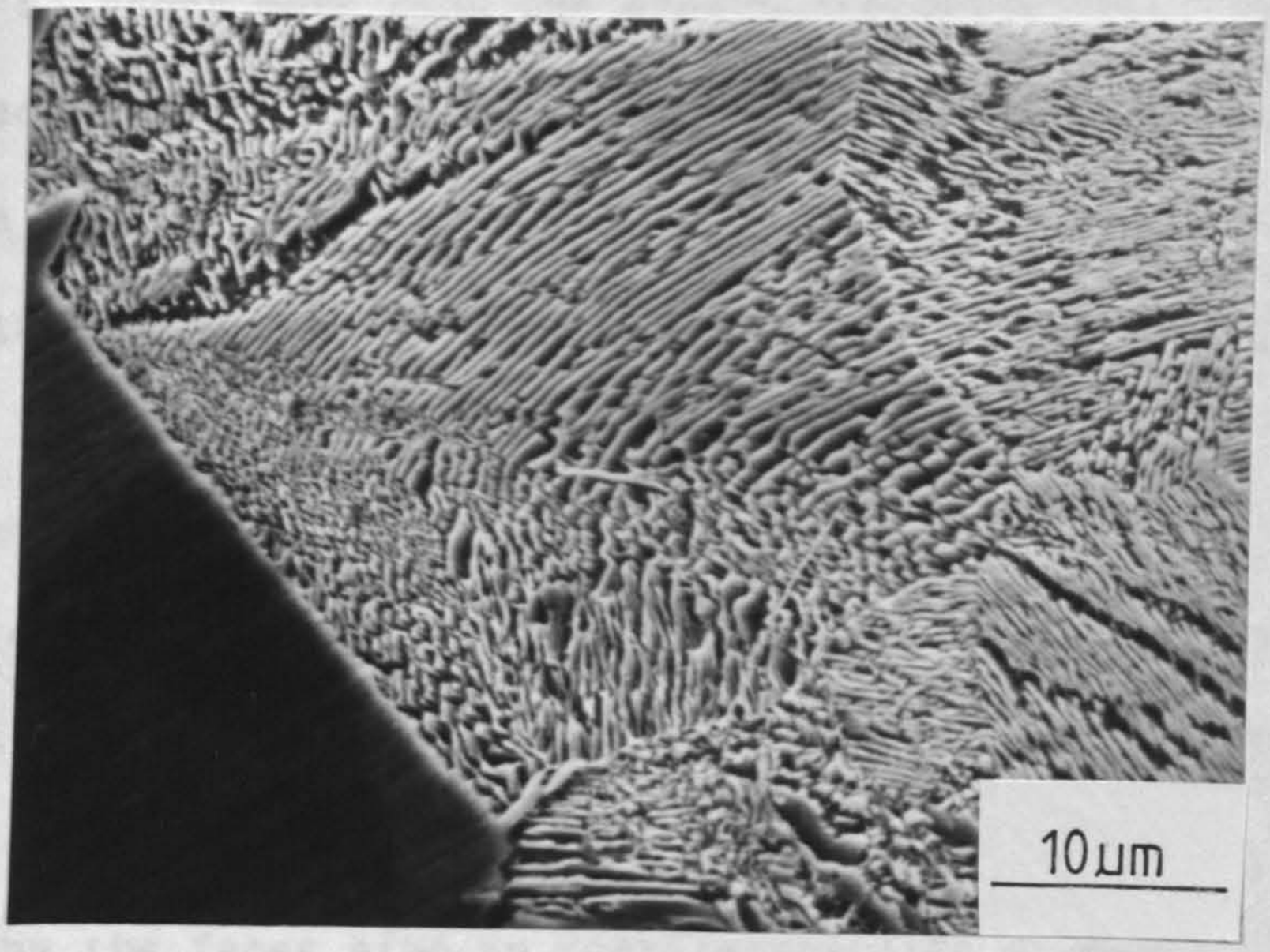

Fig 9.18 SEM micrograph showing a deviation in fracture path at a pearlite grain boundary (Specimen 5A17).

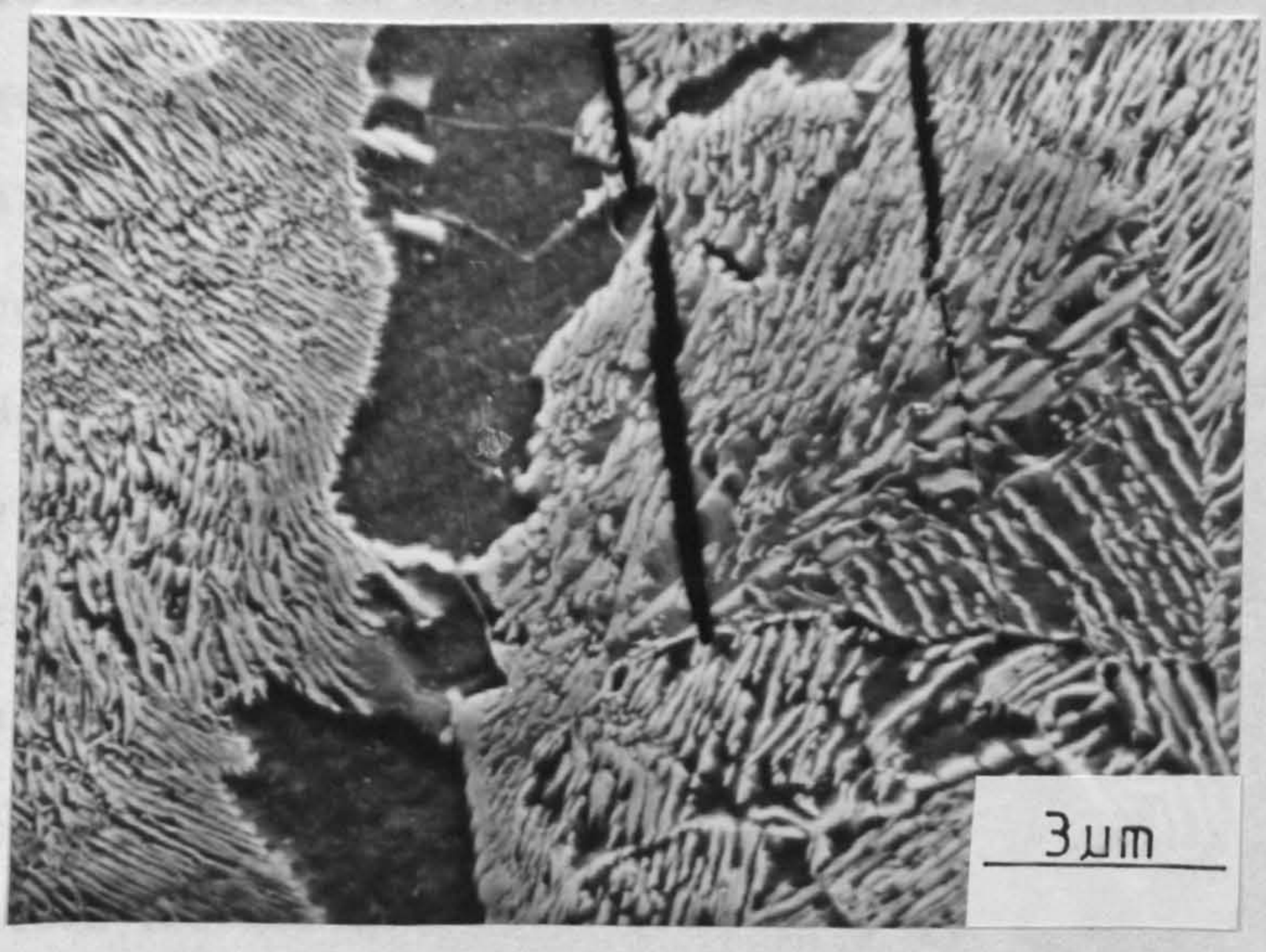

Fig 9.19 SEM micrograph showing the obstruction of micro-cracks at a high-angle pearlite grain boundary in a hypo-eutectoid steel.(4A16)

within a given pearlite colony or nodule, the cementite has been observed to adopt more than one growth direction[2]. It must be emphasised therefore that the apparent direction or alignment of the cementite is of limited value in determining which microstructural feature governs the extent of continuous cleavage propagation.

As the volume fraction of ferrite increases, the fracture facet size becomes noticeably larger than the pearlite grain size (see Tables 9.3 and 9.4). The fact that this size difference increases with increasing volume fraction of pro-eutectoid ferrite, strongly suggests an important role of pro-eutectoid ferrite in determining the facet size in ferrite-pearlite steels. It is therefore worth considering the crystallographic relationship between pro-eutectoid ferrite and adjacent pearlite grains in steels having a ferrite-pearlite microstructure.

The crystallographic relationship between the ferrite constituent of the pearlite colony and the neighbouring pro-eutectoid ferrite is discussed in Hillert's paper on the formation of pearlite[2] (see Chapter 1). The author made use of the fact that Nital attacks all ferrite crystals except those with a cube axis closely perpendicular to the specimen surface. By subsequent etching in Picral, Hillert revealed that unetched 'grains' in a hypo-eutectoid alloy may consist of a pearlite colony as well as the adjoining pro-eutectoid ferrite[2]. Confirmation of this finding by Hultgren and Ohlin[23] illustrated that the ferrite constituent of the pearlite had the same lattice orientation as some adjoining grains of pro-eutectoid ferrite in 60 to 80% of all pearlite colonies examined. These observations led Hillert[2] to the conclusion that, in cases where the pro-eutectoid ferrite had grown incoherently into the grain of austenite, further growth gives rise to pearlitic ferrite

of the same crystallographic orientation as the pro-eutectoid ferrite. Hulgren and Ohlin[23] examined partially transformed specimens in which the pearlite colonies were still relatively small and would, therefore, be close to the pro-eutectoid grain of ferrite which had served as its nucleus, either 'actively' or informally However, such an argument might equally well be applied to fully developed pearlite grains since within these grains the crystallographic orientation of the ferrite will be relatively constant[161,167].

Hillert's[2] argument is closely related to whether or not a high-angle grain boundary exists between pro-eutectoid ferrite and the adjacent peatlitic ferrite. Fig. 9.20 shows a pearlite grain close to pro-eutectoid ferrite in a slow cooled specimen of 0.59 wt.%C steel. As no grain boundary is apparent, it might be concluded from this micrograph that the adjacent pro-eutectoid ferrite was the 'active' nucleus for the pearlite grain. As discussed in Section 1.2, this situation is analogous to the growth of pearlite in the vicinity of pro-eutectoid cementite. The resulting pearlite has in this case a Bagaryatski[19] crystallography and the pearlitic cementite has the same lattice orientation as the adjacent grain boundary cementite.

As the {100} planes are the preferred cleavage planes in ferrite[165] and in pearlitic ferrite[161,165,166], a cleavage crack should only be obstructed at the 'boundary' between pro-eutectoid ferrite and a pearlite grain when there is no crystallographic alignment between these planes. If this was not the case, and cleavage propagation was obstructed by pro-eutectoid ferrite at prior-austenite grain boundaries, it might be argued that the average cleavage facet size would be smaller than the pearlite grain size and

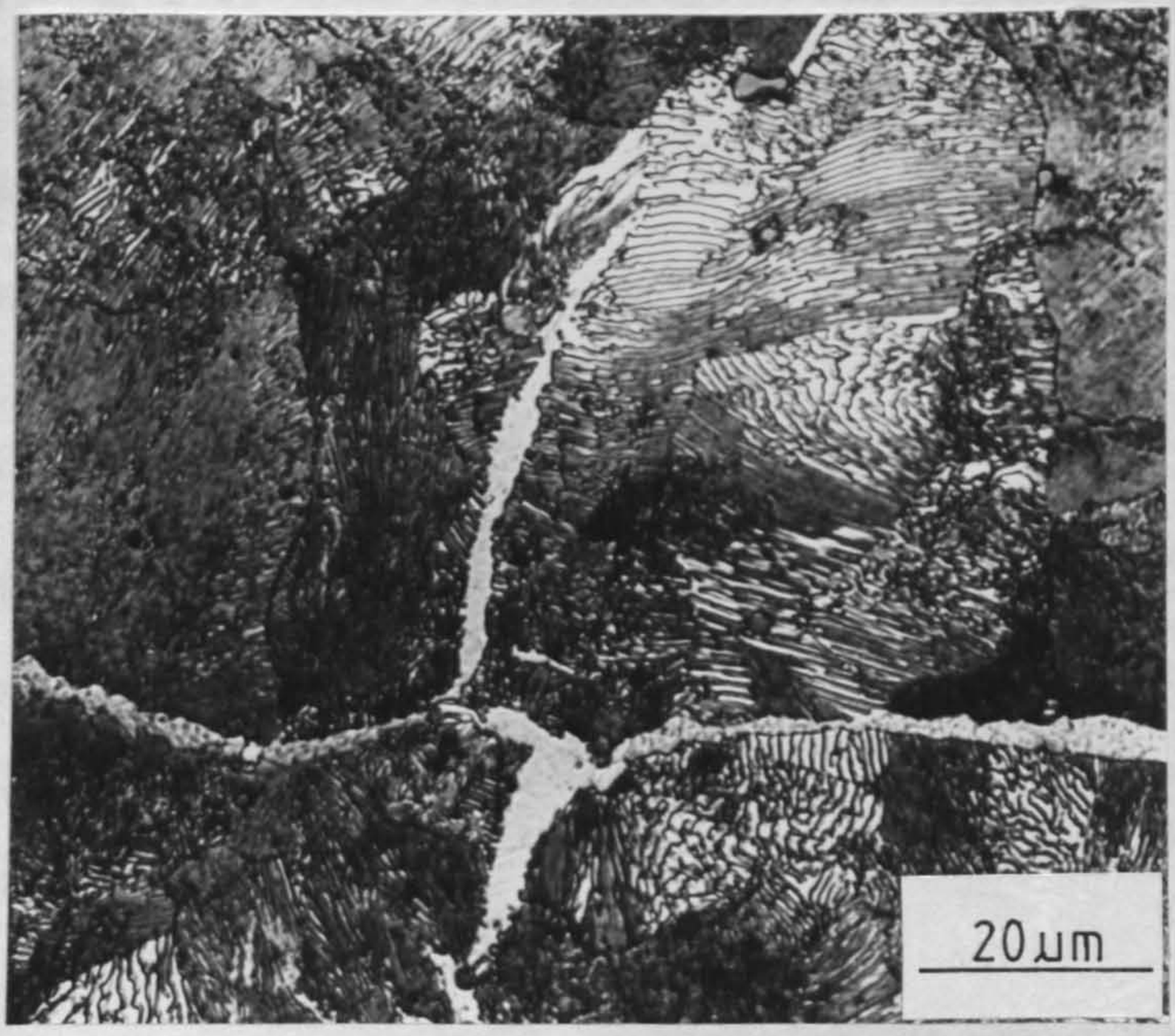

Fig 9.20 Optical micrograph of a pearlite grain and neighbouring pro-eutectoid ferrite in a slow cooled specimen of 0.59%C.(5A17)

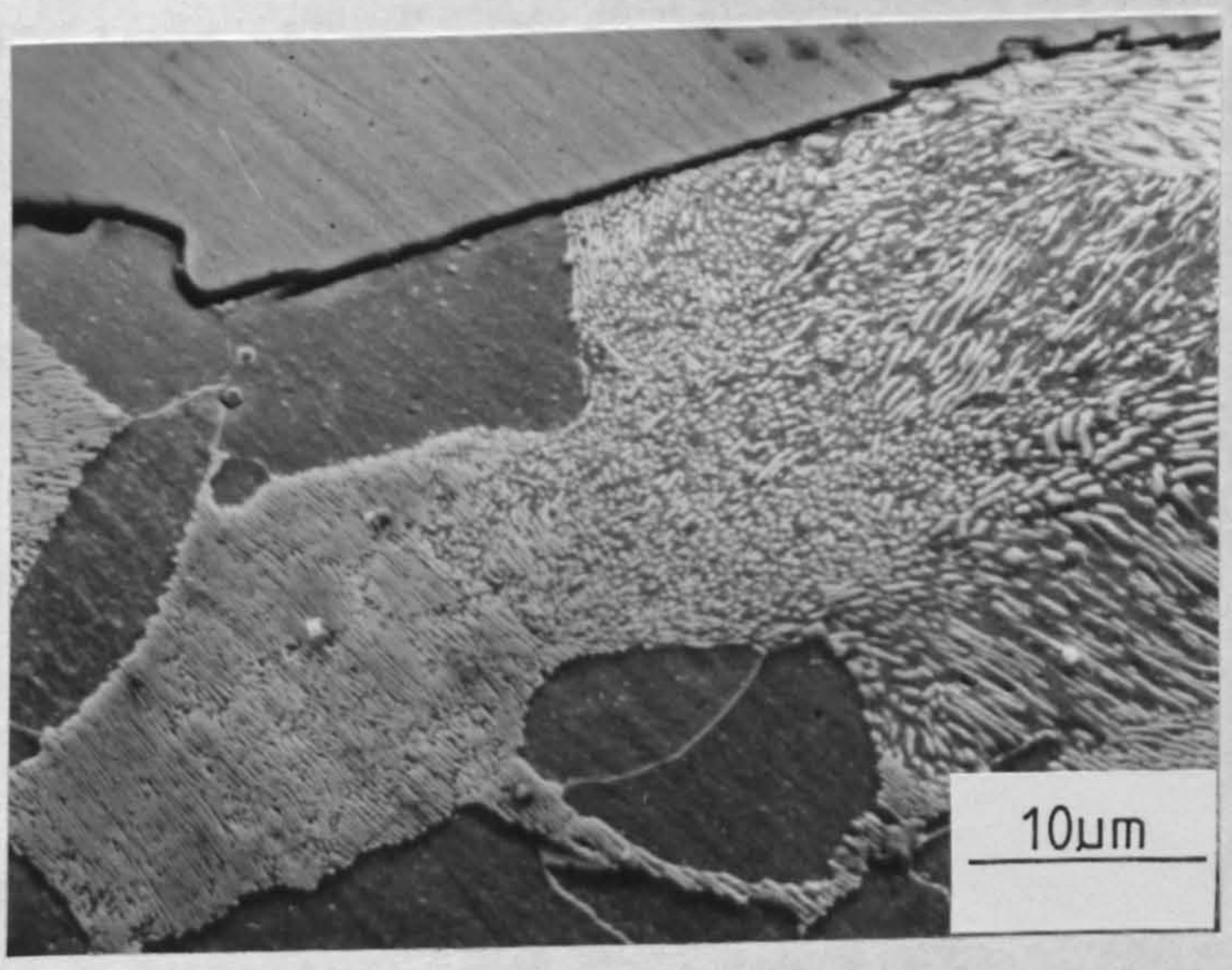

Fig 9.21 SEM micrograph showing continuous cleavage fracture between a pearlite grain and neighbouring pro-eutectoid ferrite.(4A16)

that a bimodal distribution of facet size would be evident from the fracture surface of the hypo-eutectoid steels. As can be seen from Figs. 9.14 and 9.15 this was not observed. In fact, as Fig. 9.21 shows, the fracture path may continue into the pro-eutectoid ferrite from one pearlite region (or vice versa) without the need for either a change in direction or for the nucleation of another cleavage crack. Similar observations can be found in the literature[128,162,165]. A pearlite grain formed in the neighbouring prior-austenite grain, which has no crystallographic relationship to the former pro-eutectoid ferrite will, however, constitute an effective barrier to further continuous crack propagation.

This argument obviously only applies to cases where pro-eutectoid ferrite has grown incoherently and is therefore inappropriate when considering pearlite adjacent to Widmanstätten ferrite. However, in the microstructures of the present study which have a relatively large volume fraction of ferrite, (i.e. hypo-eutectoid steels cooled slowly in vermiculite) Widmanstätten morphologies were not predominant. Therefore, although the argument which now follows is in some ways approximate, it may be justified.

If the pearlite nodule or grain in eutectoid steels is considered as a region in which the ferrite crystallographic orientations are constant or closely aligned then the corresponding nodule in hypo-eutectoid steels is the pearlite grain together with the neighbouring pro-eutectoid ferrite from which this grain nucleated. For the hypo-eutectoid steels of the present study (0.42 and 0.59 wt.%C) it can, therefore, be argued that it is necessary to include the pro-eutectoid ferrite grain size or width for a comparison to be made of the fracture facet with the size of the pearlite nodule.

Obviously it would be extremely difficult to determine optically which region of pro-eutectoid ferrite nucleated which pearlite grain. The average effective nodule size in hypo-eutectoid steels can therefore be estimated by assuming that the pro-eutectoid ferrite is a continuous grain boundary network and is only a single grain in width. As shown earlier (see Fig. 5.10) this approximation is reasonable for the relatively low volume fractions of ferrite observed in the present study.

Following well established stereological techniques[99], the optically measured pearlite grain size d_p in a ferrite-pearlite microstructure was obtained from the expression,

$$d_p = \frac{V_p L}{n} \qquad (9.1)$$

where n is the number of pearlite grains crossed on a test line of length L and V_p is the volume fraction of pearlite. V_p corrects for the fact that regions of pro-eutectoid ferrite are also included when measuring the pearlite grain size. The effective pearlite nodule size, N_p, can thus be estimated by 'adding' the size of the pro-eutectoid ferrite grains or pro-eutectoid ferrite width to the value of d_p, averaged over all orientations. This is simply evaluated by assuming $V_p = 1$ and therefore;

$$N_p = \frac{L}{n} \qquad (9.2)$$

In the fully pearlitic microstructures, as stated earlier, the pearlite grain and nodule size are equal and these values, together with corrected values of N_p for $V_p < 1$, are included in Tables 9.3 and 9.4.

A plot of pearlite nodule size against the fracture facet size is given in Fig. 9.22. As expected, this is close to a direct

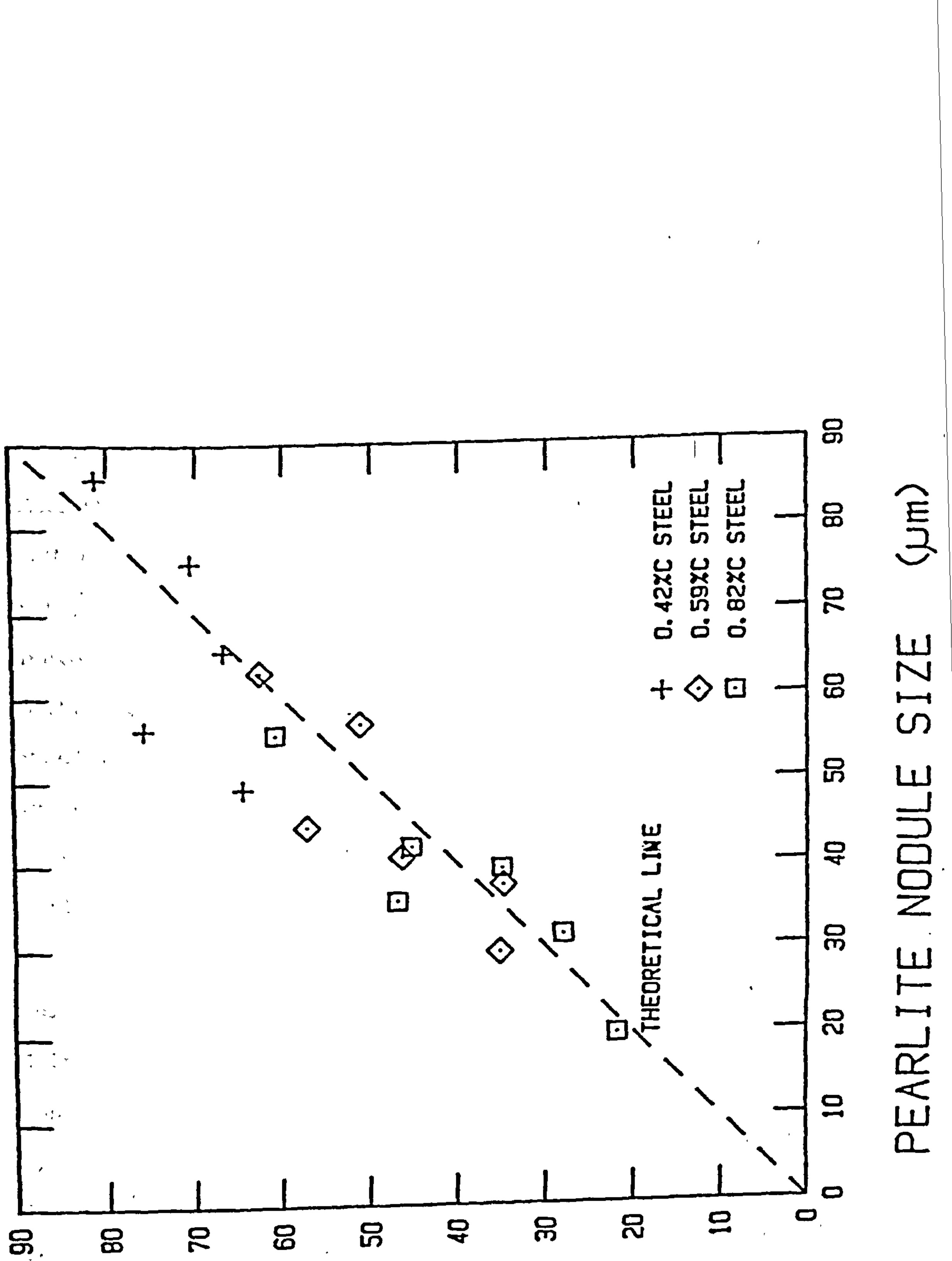

Fig 9.22 The cleavage facet size as a function of the pearlite nodule size.(0.42, 0.59 & 0.82 wt%C steels)

relationship given the accuracy with which the cleavage facet size can be measured. It should be noted,however,that with increasing amounts of pro-eutectoid ferrite a number of ferrite grains will be associated with a given pearlite grain and the above argument breaks down.

These conclusions are not entirely in agreement with those of Park and Bernstein[115,163] and of Bouse et al[84] who suggested that the fracture facet size is related solely to the prior-austenite grain size(see Fig. 7.8 and 7.9). In the hypo-eutectoid alloys studied by Bouse et al[84] the fracture facet size was approximately 12% larger than the prior-austenite grain size. In contrast, the results of Park and Bernstein[115,163] on a eutectoid steel gave facet sizes around 21% smaller than the prior-austenite grain size. However, the difference between the results of the present study and both these sets of authors can be explained as follows.

Smith's hypotheses[11] concerning the orientation relationship between pearlite and austenite is discussed in Section 1.1.1. Smith proposed that pearlite grown from the austenite grain boundary would bear a specific orientation relationship to a neighbouring grain of austenite, this grain being the parent grain for the pearlite nodule. In addition, as the size of a given pearlite nodule should be dependent on the size of the prior-austenite grain, (related to the number of nucleation sites),it is to be expected that the fracture facet size will be related to the prior-austenite grain size. However, as pointed out by Mehl[3], Brown and Ridley[94] and more recently by Marder and Bramfitt[46,85], the pearlite nodule size is also strongly influenced by the transformation temperature through

its effect on the rate of nucleation and growth. This is the reason for the observed effect of cooling rate, in the present study, on the size of pearlite grains at constant prior-austenite grain size (see Figs. 9.4 and 9.5). Faster cooling rates give lower transformation temperatures and higher pearlite growth velocities. This gives rise to smaller pearlite nodules and possibly smaller colonies. On the other hand, at high transformation temperatures, pearlite nodules in eutectoid steels can grow to be considerably larger than the austenite grains from which they are nucleated. The fact that, in the present study, pearlite grains were always of a size smaller than the prior-austenite grains is probably due to the relatively high rates of nucleation and growth in continuously cooled specimens.

It therefore follows that the comparisons of fracture facet size with prior-austenite grain size, even in the comparatively simple case of eutectoid steels, should only be strictly accurate if the transformation conditions are constant, and vice versa. This may explain why a large number of points on the graph of Park and Bernstein[115,163], Fig. 7.8, appear to be for specimens which have the same prior-austenite grain size but quite different fracture facet sizes.

To conclude, the present study has shown that the pearlite nodule by virtue of it's high-angle boundaries and crystallographic orientation is the relevant microstructural feature in determining the cleavage facet size. Lower austenitising temperature and/or fast cooling rates give smaller facet sizes. How this effects toughness can now be discussed in detail.

9.3 TOUGHNESS AND MICROSTRUCTURE

9.3.1 Charpy V-Notch Toughness

Microstructural measurements and mechanical properties obtained from Charpy impact specimens are given in Tables 9.3 and 9.4. In general, specimens air cooled from 1000°C and 1160°C had similar pearlite spacings. This is predicted by the results in Part 1. Specimens cooled in the same manner from 800°C, however, appear to have coarser spacings and this may be due to the small austenite grain size giving a higher transformation temperature and slower pearlite growth rates. Unfortunately no transformation data were recorded for these heat treatments and a definite conclusion cannot be made.

As expected, from the conclusions in Part 1, increasing the cooling rate, from $\simeq 0.3^{o}C\ s^{-1}$ in vermiculite to $\simeq 4^{o}C\ s^{-1}$ in the accelerated cooling chamber, increased the volume fraction of pearlite and decreased the pearlite spacing. Measured microstructural parameters were used to calculate the mean free ferrite distance, $\bar{\lambda}_{\alpha}$, (from equation 5.8, Section 5.3). and these values are given in Tables 9.3 and 9.4. The mean Vickers hardness measured from the Charpy impact specimens is plotted as a function of $\bar{\lambda}_{\alpha}^{-\frac{1}{2}}$ in Fig. 9.23. Given also in Fig. 9.23 is the line obtained from the correlation of hardness with $\bar{\lambda}_{\alpha}^{-\frac{1}{2}}$ in Part 1, Fig 5.6. It is clear that a good agreement is found between these results, and this further substantiates the use of $\bar{\lambda}_{\alpha}$ in correlating microstructure with the hardness (and strength) of pearlitic steels.

The Charpy impact curves for heat treated specimens of the 0.42, 0.59 and 0.82 wt.%C steels are given in Figs. 9.24 to 9.29. In all cases, lower ductile-brittle transition temperatures were

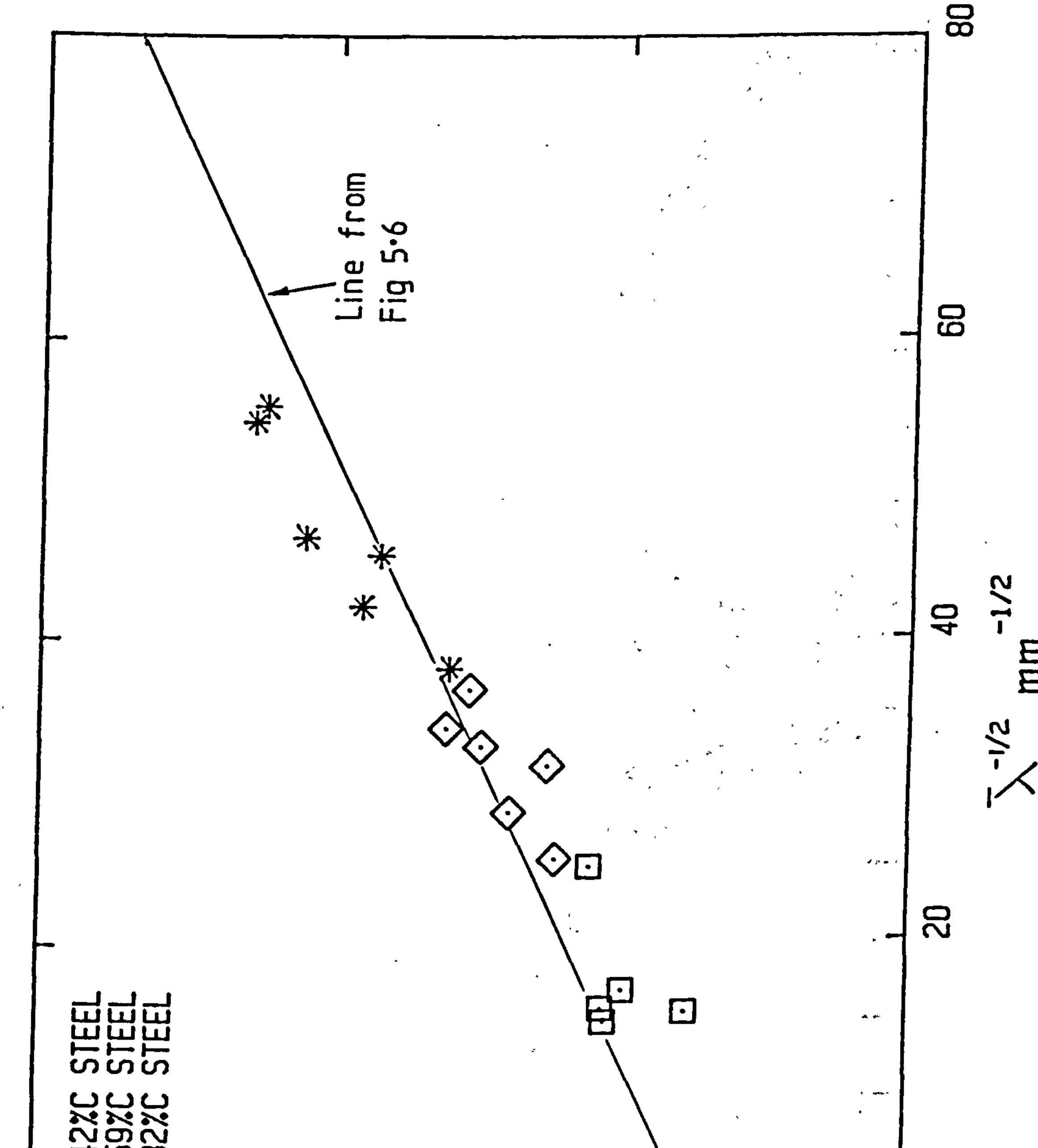

Fig 9.23 The Vickers hardness data for Charpy impact specimens as a function of the mean free ferrite distance.

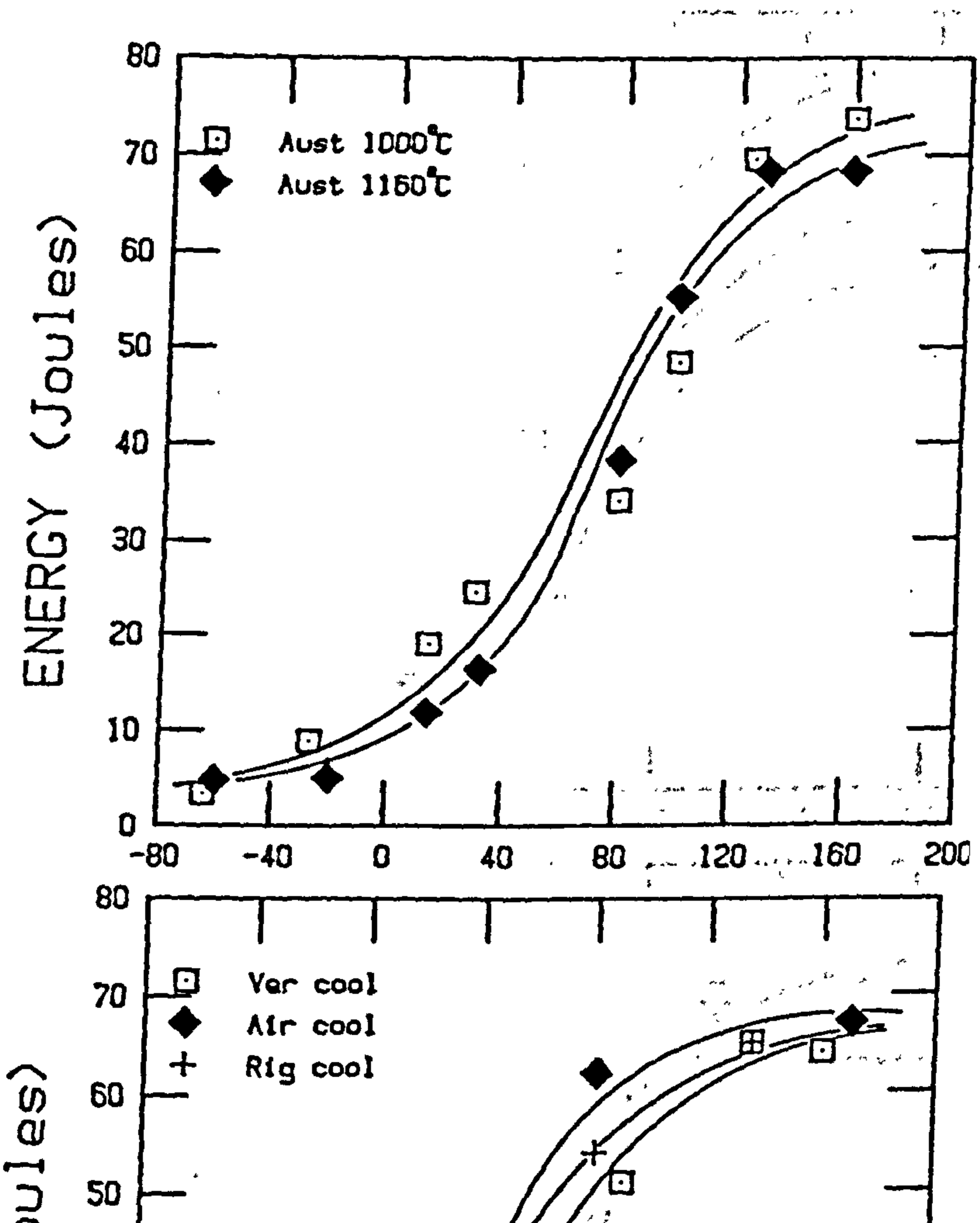

Fig 9.24 & 9.25 The effect of changes in austenitising temperature and cooling rate on the standard Charpy impact curves for the 0.42 wt%C steel.(SL174A)

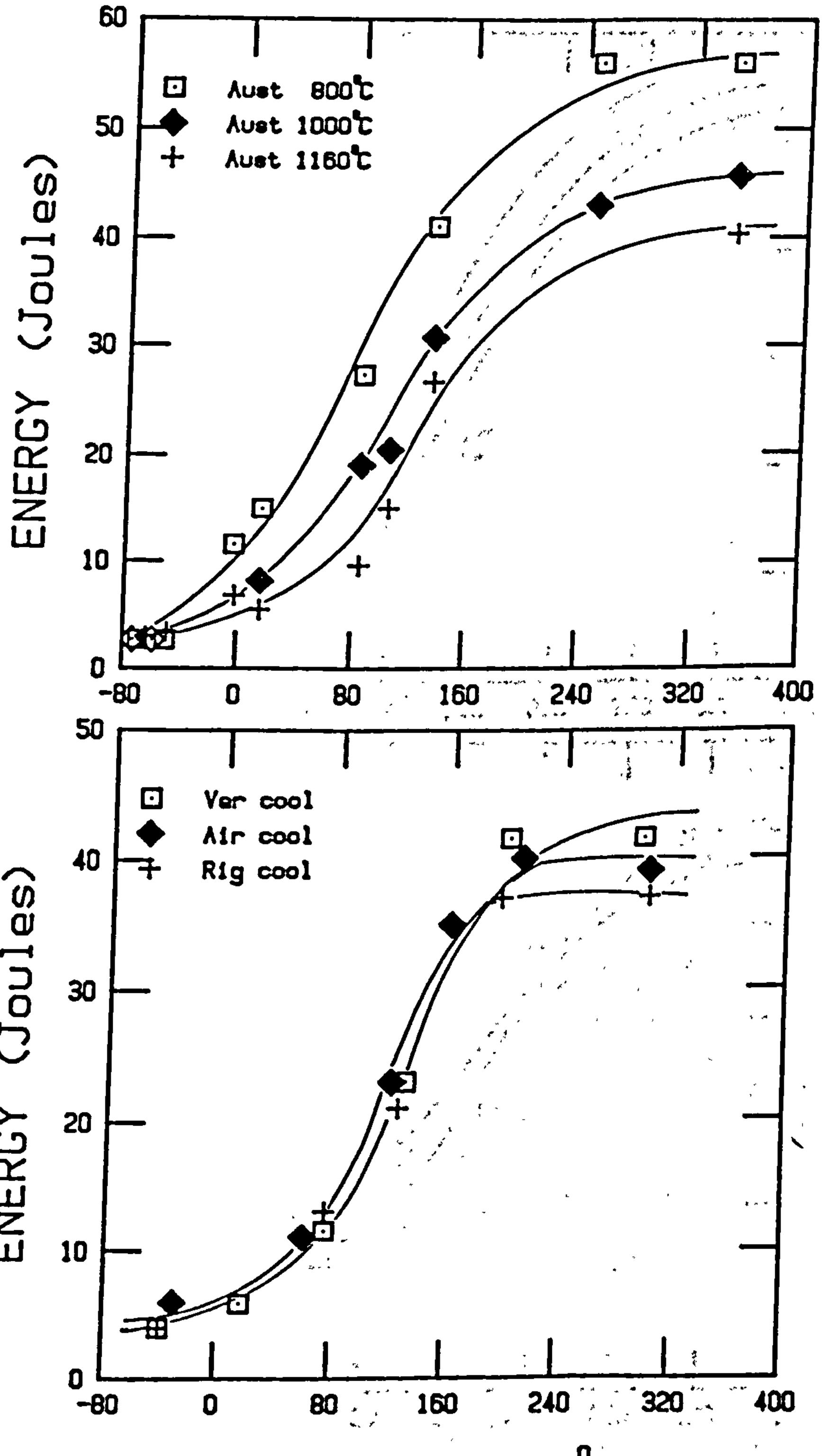

Fig 9.26 & 9.27 The effect of changes in austenitising temperature and cooling rate on the standard Charpy impact curves for the 0.59 wt%C steel.(SL175A)

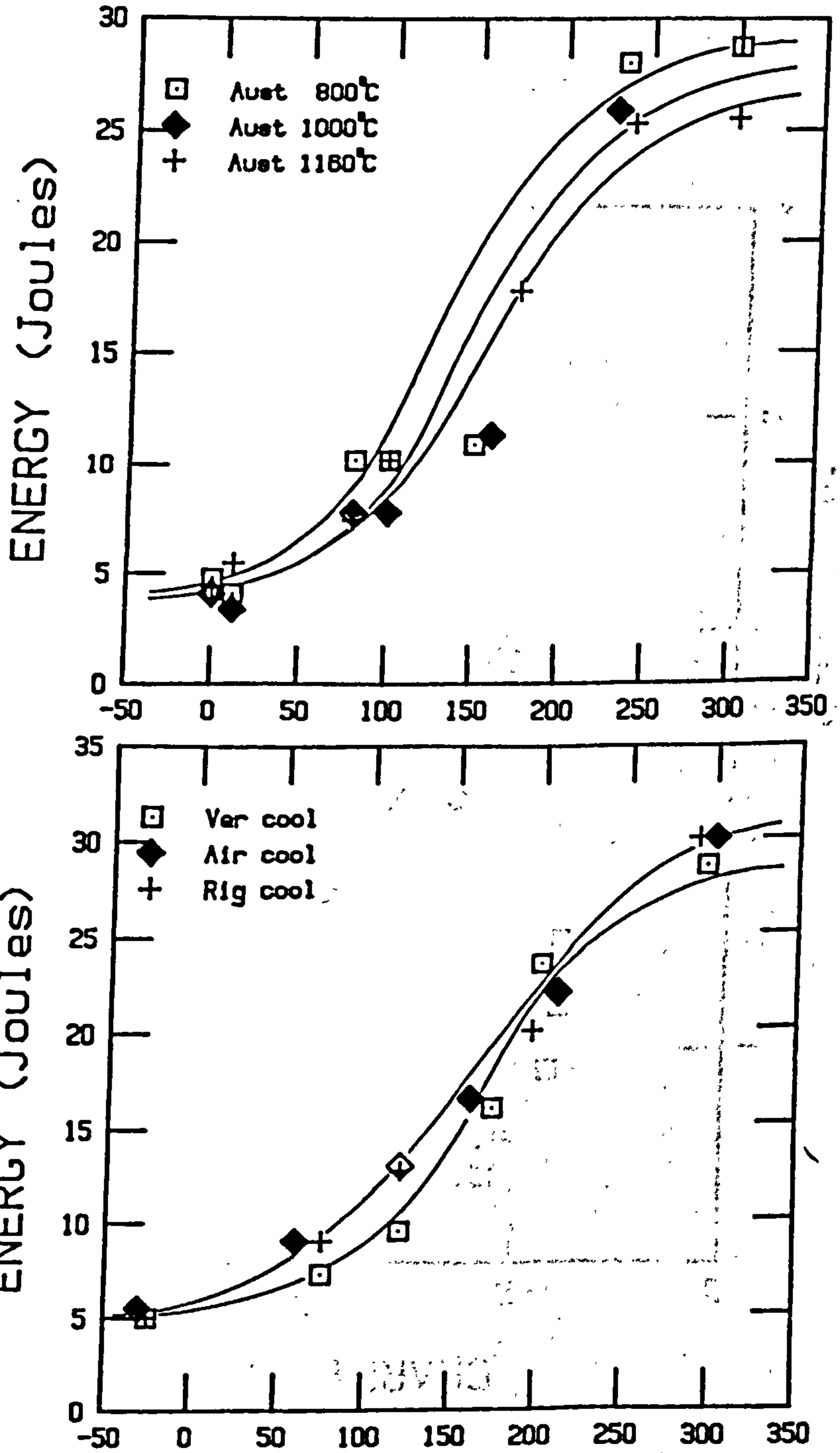

Fig 9.28 & 9.29 The effect of changes in austenitising temperature and cooling rate on the standard Charpy impact curves for the 0.82 wt%C steel.(SL175B)

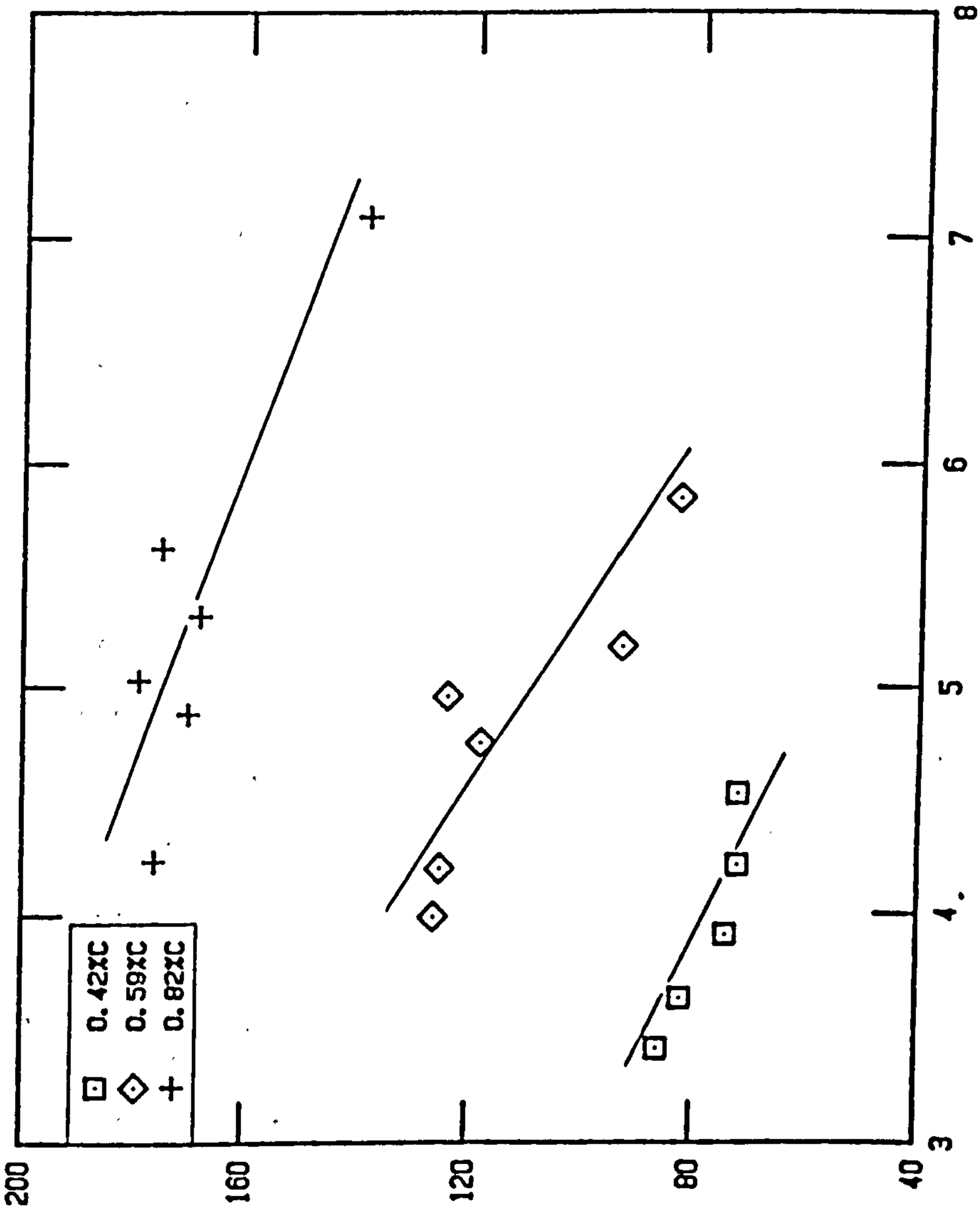

Fig 9.30 Average energy impact transition temperature as a function of the pearlite nodule size.

associated with lower austenitising temperatures. The impact transition temperatures are given in Tables 9.3 and 9.4. The effect of increased cooling rate at a constant austenitising temperature is shown in Figs. 9.25, 9.27 and 9.29. For all compositions, vermiculite cooling moved the transition curve to higher temperatures. Except in the case of the 0.42 wt.%C steel,the difference on the impact transition temperature of air and rig cooling was minimal and probably within the normal experimental variation obtained an impact testing. The lack of separation of air and rig cooled specimens may also in part be a result of attempting to cool a number of specimens in the forced cooling chamber at the same rate. As in many similar studies, the ductile-brittle transition temperature, recorded in Tables 9.3 and 9.4, were plotted as a function of the relevant grain size. Fig. 9.30 shows the relationship between the pearlite nodule size N_P (Tables 9.3 and 9.4) and the average energy transition temperature. Within the limited range of the present study a reasonable agreement is obtained for each composition, and thus the pearlite nodule size determined the ductile-brittle transition temperature. The separation of the curves in Fig. 9.30 can be explained in terms of the relative ease of brittle fracture in microstructures having a large volume fraction of pearlite.

As discussed by Knott[130], brittle fracture occurs in a Charpy test when the maximum principal (longitudinal) stress,ahead of the notch,exceeds the cleavage fracture stress,σ_f. With increasing test temperature, the uniaxial yield stress, σ_{ys},decreases and and size of the plastic zone required to elevate the notch tip tensile stress, by stress intensification, to σ_f becomes correspondingly larger. At some temperature,T_{GY}, the size of the plastic zone

is such that general yield and fracture are coincident. The fracture criterion is then[130],

$$Q_{GY}\,\sigma_{ys} = \sigma_f \qquad (9.3)$$

where Q represents the stress intensification produced by the plastic zone.

Above T_{GY}, stress intensification cannot be increased further by constraint, and cleavage fracture after general yield is a result of strain hardening in the region below the notch. This increases the flow stress by an amount $\Delta\sigma$, and the fracture criterion is then[130],

$$Q_{GY}\,(\sigma_{ys} + \Delta\sigma) = \sigma_f \qquad (9.4)$$

From equation 9.4 it can be seen that, as the strain hardening capacity increases with increasing carbon content, the temperature at which the decrease in σ_{ys} satisfies equation 9.4 increases. As a result, higher ductile-brittle transition temperatures are observed for higher carbon steels since they have a greater strain hardening capacity.

Gladman and Pickering[101] and Knott[130] have suggested that, as the lower shelf Charpy energy is associated with cleavage fracture, its value should be higher for fine grain materials. Unfortunately the energy associated with the lower shelf is so small (≃5J) that it is difficult to clearly detect an effect of microstructural changes in Figs. 9.24 to 9.29. The additional information gained from instrumented-impact testing may, however, be used to clarify the effect of heat-treatment on the resistance to brittle failure.

9.3.2 Instrumented-Impact Tests

Instrumented-impact tests were performed on specimens of 0.59 and 0.82 wt.%C steel heat treated as given in Table 9.5 and 9.6. Details of instrumented-impact test procedure are given in Section 8.2.2 and the evaluation of maximum loads and impact energies is outlined in Appendix C. These results are also presented in Tables 9.5 and 9.6.

Figs. 9.31 and 9.32 show the energy absorbed as a function of austenitising temperature and cooling rate for specimens of 0.59 and 0.82 wt.%C steel which failed entirely by cleavage fracture at room temperature. In agreement with standard Charpy transition curves the toughness is increased by using lower austenitising temperatures and faster cooling rates. Load-time curves for these specimens were typical of material which failed in a fully brittle manner[181]. The load increased steeply to a maximum where the trace fell abruptly. Figs.9.33 and 9.34 illustrate that the increase in energy absorbed as a result of lower austenitising temperatures and faster cooling rates has occurred due to a corresponding increase in the maximum load prior to unstable cleavage fracture.

As stated earlier, low temperature brittle fracture of notched specimens occurs when the maximum longitudinal stress below the notch root builds up to the critical value, σ_f. In general, a decrease in yield stress of a material will increase the toughness (at constant σ_f) because greater stress intensification is required to elevate the maximum stress below the notch to σ_f. Wilshaw et al[182] have used such an argument to explain the increase in fracture load and toughness for Charpy V-notch bars of mild steel tested between -196 and -150°C. The increase in fracture load and toughness with temperature was shown to have resulted from the fact

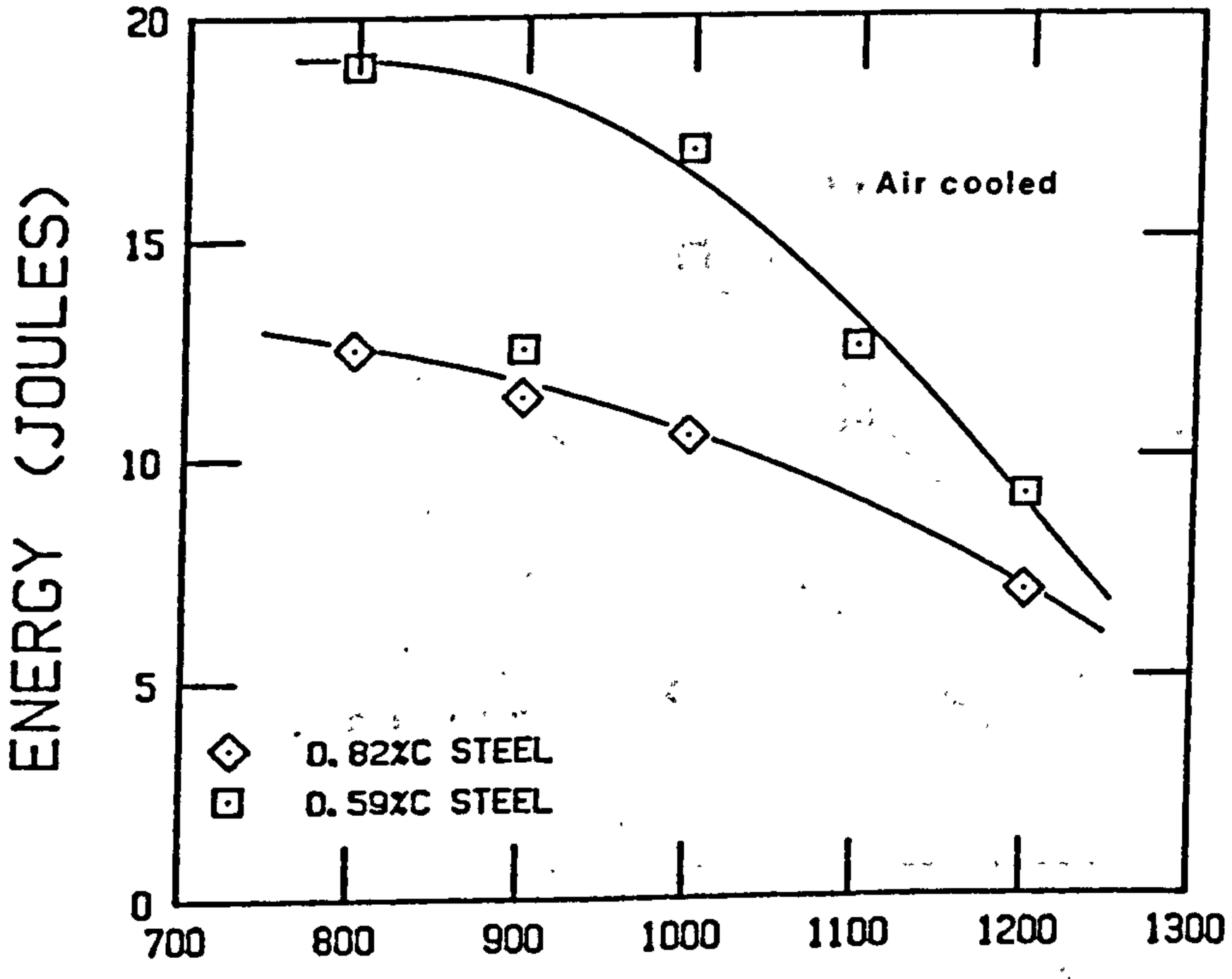

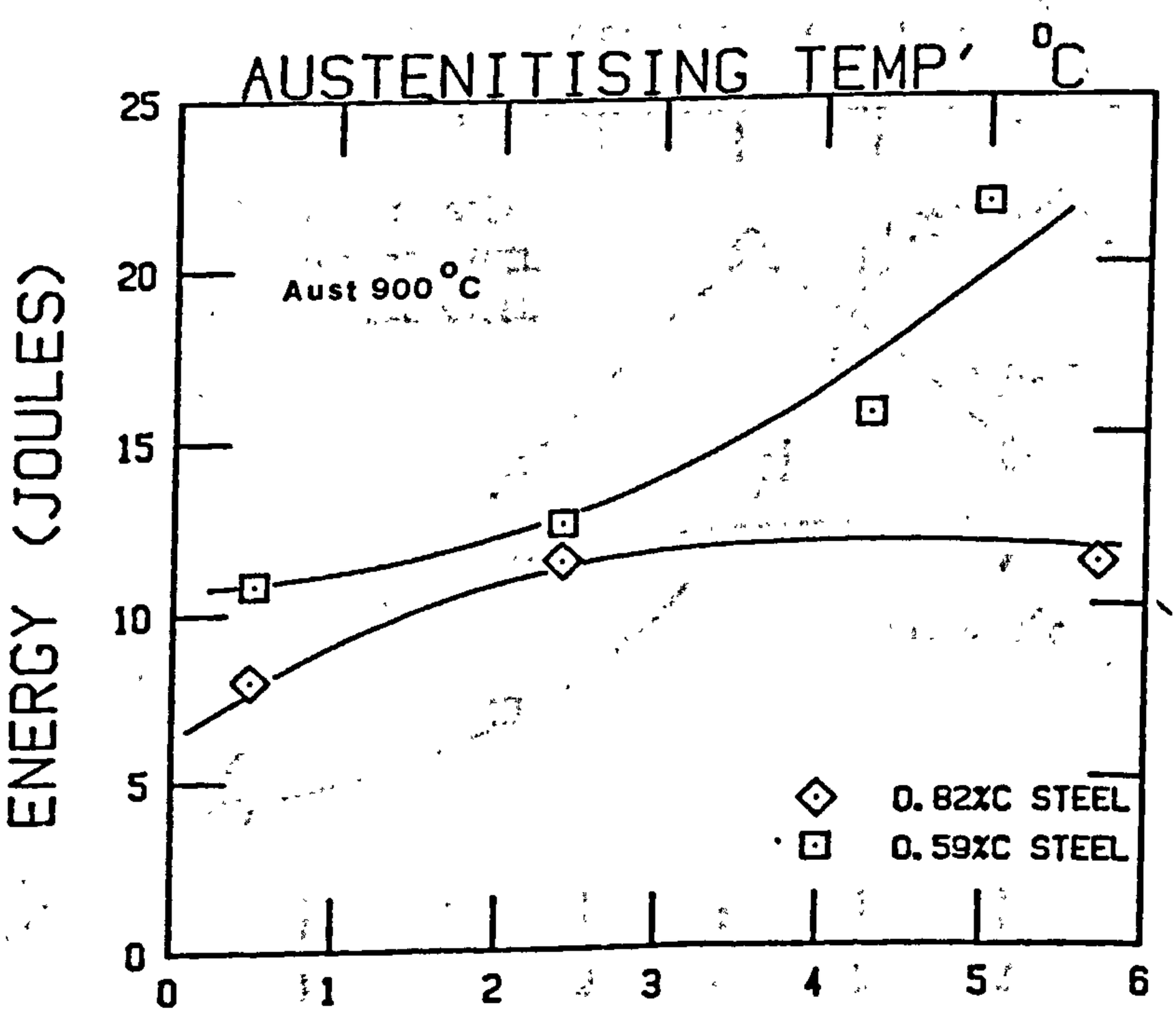

Fig 9.31 & 9.32 Energy absorbed in instrumented-tests as a function of the austenitising temperature(top) and cooling rate.(0.59 & 0.82 wt%C steel)

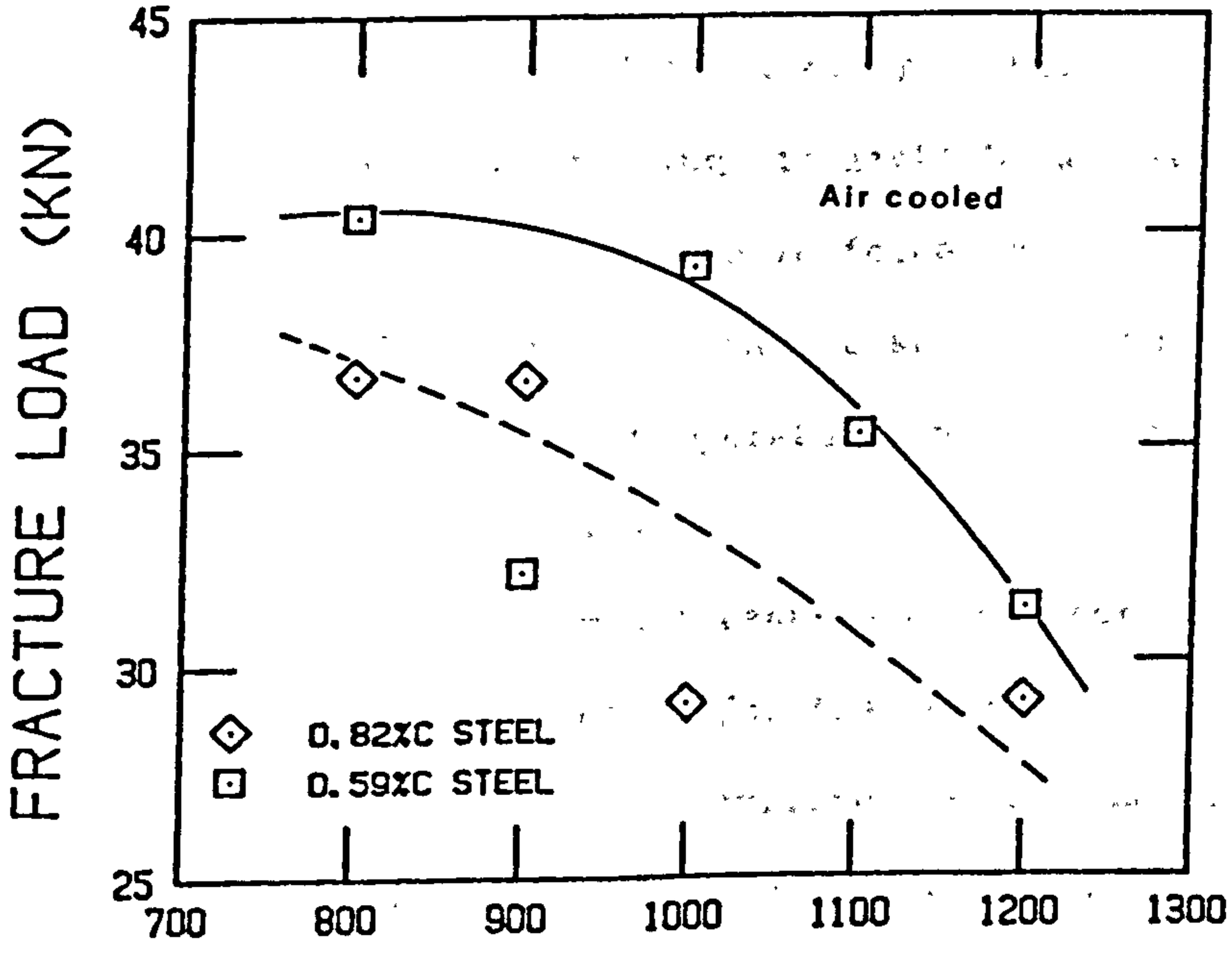

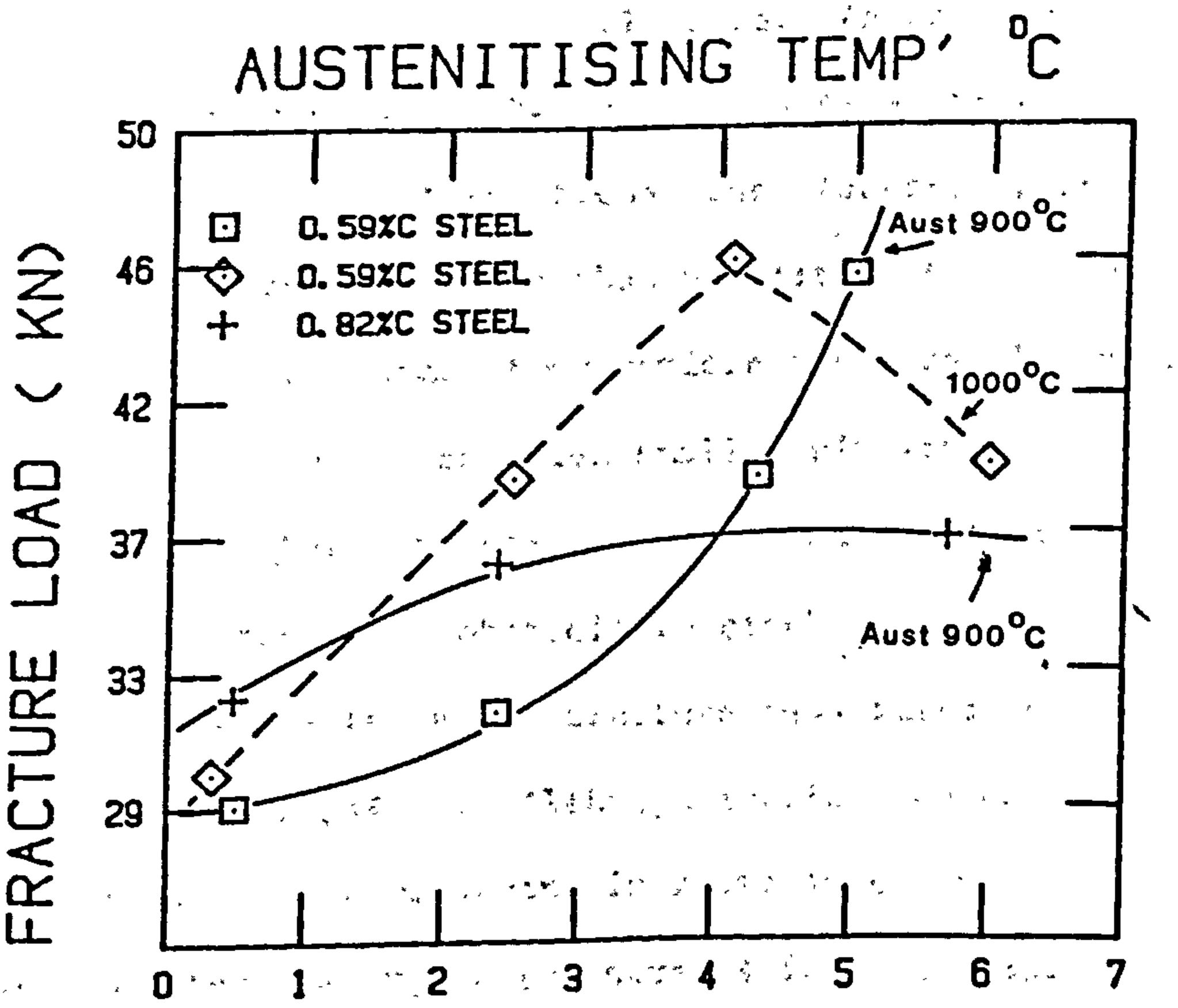

Fig 9.33 & 9.34 Fracture load obtained from instrumented-impact tests as a function of austenitising temperature(top) and cooling rate. (0.59 & 0.82 wt%C steels.)

that σ_f remained constant while the yield stress decreased with increasing temperature. A comparison of proof stress with maximum load values given in Tables 9.5, 8.9.6 indicates no clear relationship. Although the proof stress values correspond to markedly slower strain rates than is the case in impact testing, it might be argued on a purely qualitative basis, that the increase in force required to cause brittle failure in the instrumented-impact test is due to a change in σ_f with changing austenitising temperature and cooling rate rather than to any change in the flow stress.

The results of Charpy-V-notch impact tests are therefore in agreement. Low austenitising temperatures and/or fast cooling rates, within the limits of the present study, improve the toughness. This can be explained by the observation that both heat treatment variablesdecrease the pearlite grain or nodule size. As the events leading to brittle failure occur when the maximum tensile stress ahead of the notch exceeds the fracture stress, the cleavage fracture stress in notched specimens of high-carbon pearlitic steels may be assumed to be governed by the size of these microstructural features. Smaller pearlite nodule or grain sizes give smaller cleavage crack nuclei which propagate at higher stresses. In addition, as this microstructural feature is the major obstacle to crack propagation, reducing its size will increase the microstructure resistance to continuous cleavage crack propagation. Although accelerated cooling increases the flow stress, the accompanying increase in cleavage fracture stress predominates, leading to an increase in toughness.

A similar conclusion has recently been inferred by Hahn[152] in a review on the influence of microstructure on brittle fracture toughness in steels. These conclusions are also in agreement with

the work of Naylor et al[180,183] on bainitic steels. These authors showed a similar improvement in the Charpy impact toughness as a consequence of low austenitising temperatures and faster cooling rates, giving rise to smaller bainite packets. In addition the size of the bainite packet, correlated closely with measurements of cleavage facet size from broken impact specimens[180].

9.3 THE ROLE OF MICROSTRUCTURE ON DUCTILE FAILURE

Before discussing the results obtained from fracture toughness tests, some comment should be made on the obvious effect of composition and heat treatment on the Charpy upper shelf energy and the related tensile ductility of pearlitic steels.

The role of pearlite morphology on ductile fracture is not fully understood and a number of microstructural parameters have been suggested to control ductility. The pearlite nodule size[85,178], the cementite lamellae thickness[82,184] and the prior-austenite grain size[86,185] have all been correlated with the reduction in cross sectional area in tensile tests. The free nitrogen content of the steel is also important[185]. However, as the materials in the present study were manufactured by the same process route, the effect of nitrogen content may be overlooked.

The most important microstructural variable influencing the ductility of pearlitic steels is the volume fraction of pearlite. This is evident in Figs. 9.24, 9.26 and 9.28 by the substantial increase in the ductile shelf energy (DSE) with decreasing carbon content, i.e. increasing volume fraction of ferrite (c.f. 68J for the 0.42 wt.%C air cooled from 1160°C compared to 25J for a similar heat treatment in the 0.82 wt.%C steel). A similar effect is

observed with the tensile ductility figures obtained in Part 1 (see Tables 4.2, 4.4, 4.6 and 4.8). It is clear, however, from the Charpy impact curves shown in Figs. 9.24 to 9.29 that, within a given composition, the upper shelf energy is also strongly affected by the austenitising temperature and to some extent by the cooling rate. A corresponding trend is observed for the tensile test results collected in Tables 9.1 and 9.2. The effect of austenitising temperature is in complete agreement with the finding of Hyzak and Bernstein[86] on eutectoid rail steels, although these authors gave no explanation for this effect.

In the hypo-eutectoid steels of 0.42 and 0.59 wt.%C in the present study, the influence of austenitising temperature may be, in part, due to the change in volume fraction of pearlite. Higher austenitising temperatures resulted in larger prior-austenite grain sizes which gave rise to lower transformation temperatures and a slight increase in the volume fraction of pearlite. Faster cooling rates, as expected also lowered the transformation temperatures giving increased pearlite volume fractions. However, when these changes are taken into account, other microstructural variables would appear to influence both the DSE and the tensile ductility. Some authors[85,178] have suggested that the tensile ductility is related to the pearlite nodule size, with smaller nodules giving an improved ductility. Again, however, few explanations have been forwarded supporting nodule size control.

In general, deformation in pearlite leads to cracking of the cementite lamellae which link up by the shear cracking mechanism proposed by Miller and Smith[160]. Such cracks may grow across individual colonies or nodules and can then be considered as the

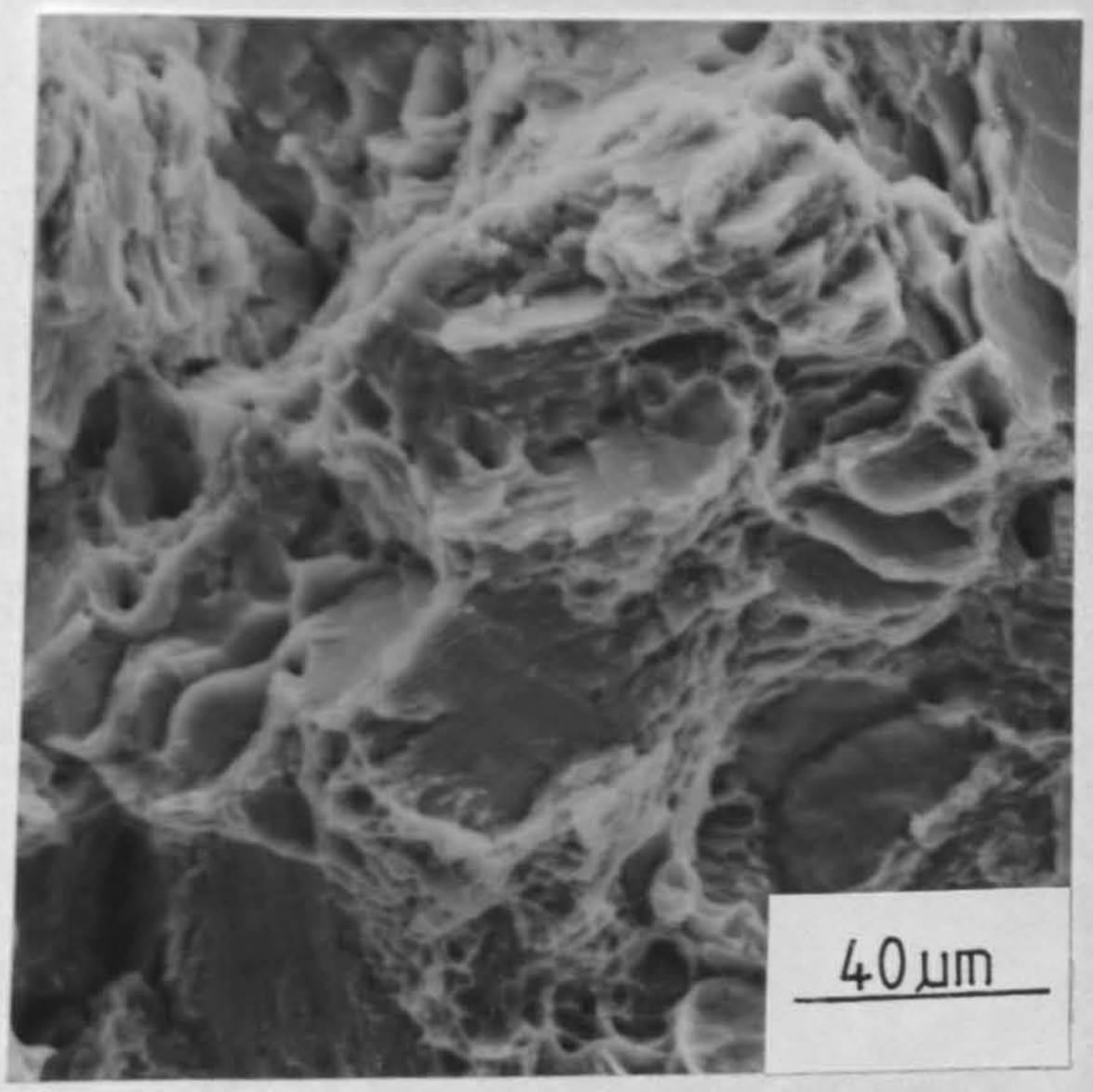

Fig 9.35 Shear cracking of pearlite in a (ductile) fracture surface of a 0.82wt%C steel.

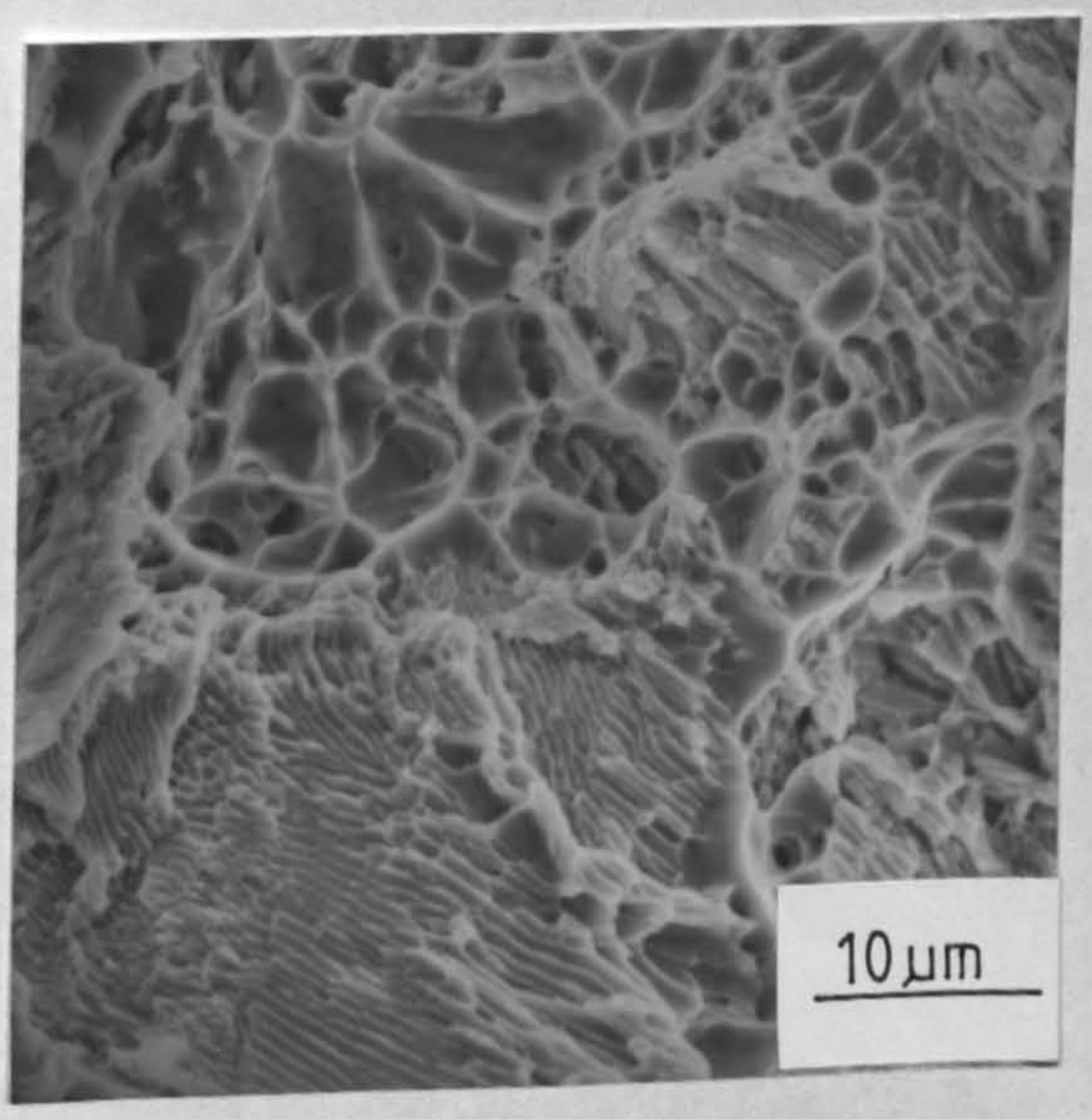

Fig 9.36 Shear cracking and dimpled regions on the fracture surface of a 0.59wt%C steel

sites of very large voids[186]. According to Inoue and Kinoshita[186] these voids link up in ferrite-pearlite steels by internal necking of the ferrite. Consequently with decreasing volume fraction of pearlite, the strain involved in void linkage increases and hence the total ductility increases. Such an argument would explain the large increase in DSE and tensile ductility in the present study (Fig. 9.24 to 9.29 and Tables 4.2, 4.4, 4.6 and 4.8) with decreasing carbon content. In fully pearlite steels the mode of void linkage changes from internal necking to a shear mechanism[186]. Shear cracking and linkage in the fully pearlitic 0.82 wt.%C steel is shown in Fig. 9.35. Similar shear cracked regions in a 0.59 wt.%C steel are shown in Fig. 9.36. The strain involved in void linkage in fully pearlitic microstructures is considerably less than that associated with the internal necking process in ferrite-pearlite steels. As a result, the total ductility of eutectoid steels is less than in ferrite-pearlite steels[186]. For pearlite nodule size to govern the ductile fracture process occurring in tensile specimens and at the upper shelf in impact tests, the process of void fromation and/or linkage, must be more difficult in materials which are heat-treated to give smaller pearlite grains or nodules. Fig. 9.37 shows the tensile reduction in cross sectional area as a function of the pearlite grain size for the case of 0.59 and 0.82 wt.%C steel from Part 1 (Tables 9.1 and 9.2).

As strain partitioning will occur between pro-eutectoid ferrite and pearlite in hypo-eutectoid steels, the pearlite grain size will be of more importance than the nodule size. Omitted from Fig. 9.37 are the results for specimens which, as indicated in Table 9.1 and 9.2, failed in a brittle manner before any appreciable

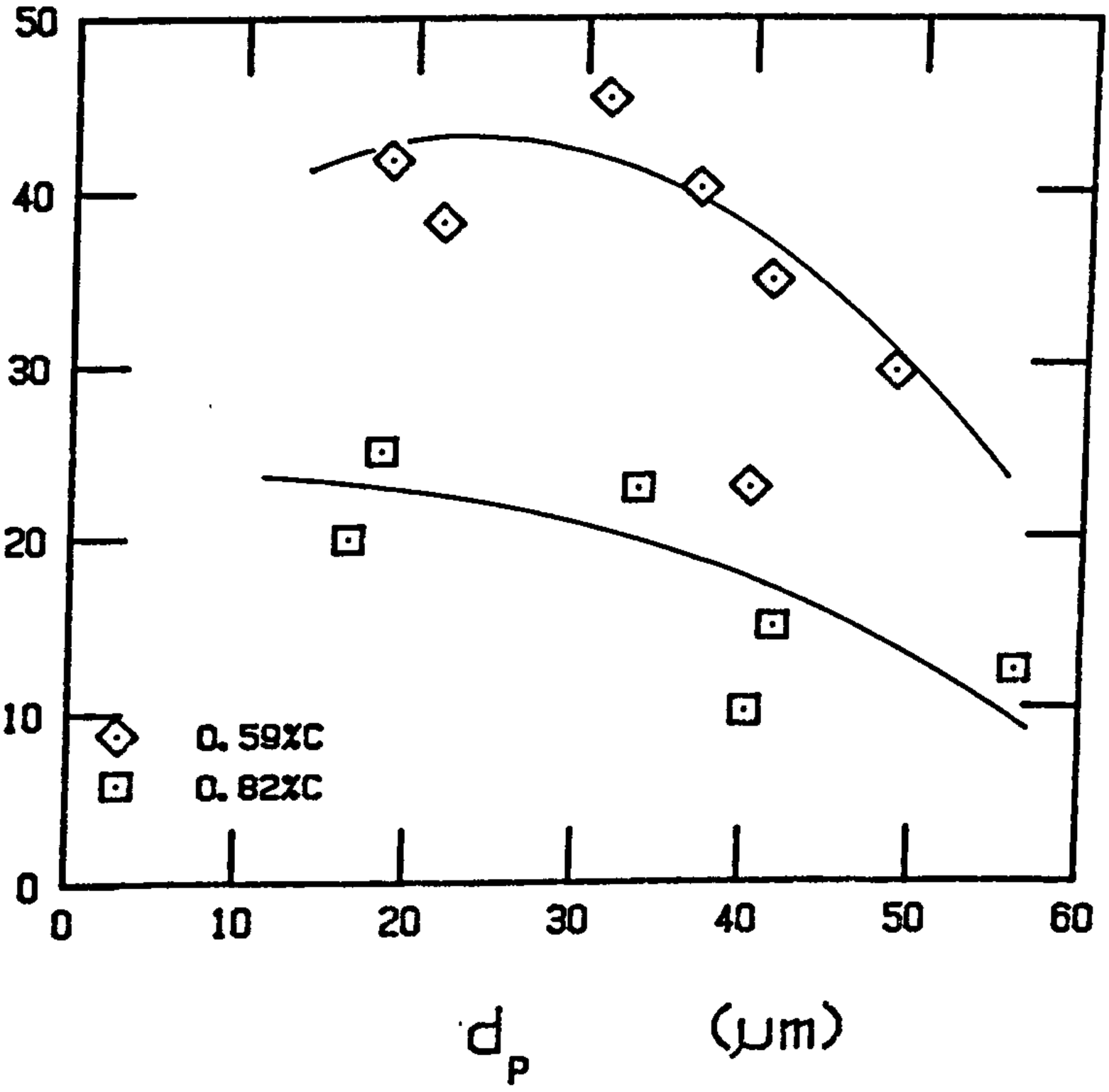

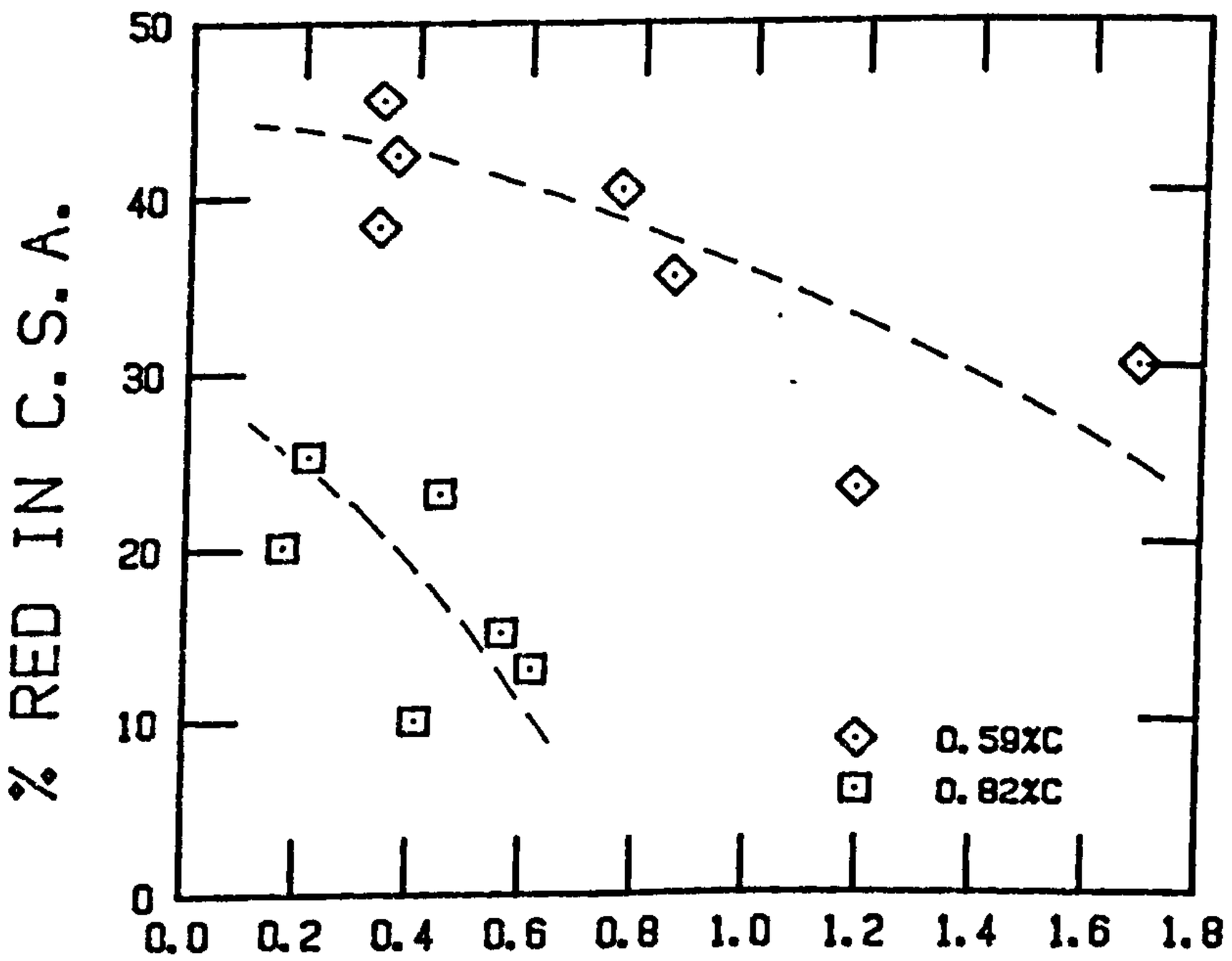

Figs. 9.37 & 9.38 Tensile reduction in cross sectional area as a function of the pearlite grain size(top) and mean free ferrite distance.

However, neither Fig. 9.37 nor Fig. 9.38 reflect the morphology of the cementite, which should also be considered in a correlation of microstructure with ductility. Spheroidised or non-lamellar pearlite has been shown to exhibit superior ductility to lamellar pearlite[24]. Thus a knowledge of the degeneracy of the pearlite may be necessary before the microstructure can be related more precisely to the ductility. Finally the concentration, size and distribution of non-metallic inclusions can also influence the ductility of pearlitic steels. Voids will form more easily around these weakly bonded inclusions than by the shear cracking of carbide lamellae.[130] Evidence of large dimpled regions were found on some of the fracture surfaces from Charpy upper shelf and tensile test specimens (Fig. 9.36).

Attempts to relate Charpy DSE and tensile ductility values with microstructural parameters were unsuccessful, and only general trends were recognised. The main factor governing both properties is the volume fraction of pearlite, lower volume fractions giving an increase in the DSE and the tensile ductility. There would nevertheless appear to be an effect of austenitising temperature and to some extent cooling rate. However, the inter-relationship between microstructural parameters requires that more work be carried out before the effect heat treatment variables on ductile fracture can be fully understood.

9.4 FRACTURE TOUGHNESS TEST RESULTS AND DISCUSSION

Heat-treatment and metallographic data for the 'valid' fracture toughness specimens of 0.59 and 0.82 wt.%C steel are given in Tables 9.7 and 9.9. Tensile test results and information relevant

to the calculation of critical stress intensity factors can be found in Tables 9.8 and 9.10.

On only two occasions did the specimen crack length a = 0.5.W satisfy the validity criteria

$$a \geq 2.5 \left[\frac{K_Q}{\sigma_{0.2}}\right]^2 \qquad (9.5)$$

where K_Q is the calculated stress intensity factor and $\sigma_{0.2}$ the 0.2% proof stress. However this lower limit of thickness cannot be specified from theoretical considerations alone but must also be established on the basis of experimental fracture tests[135,142]. As a result, specimen fracture surfaces and test records were examined for evidence of insufficient specimen thickness or ligament width (W - a). In all specimens of 0.82 wt.%C steel (SLI75B) and 0.59 wt.%C steel (RS 518) fracture surfaces showed 100% 'flat' cleavage fracture. In addition, load-displacement traces were essentially linear to failure with a 'pop-in' being recorded in only one case, that of specimen 5B10R. For this specimen the plasticity proceding 'pop-in' was within the limits set by BS 5447:1977 and the value of P_Q at the 'pop-in' was taken as the fracture load. Therefore, although equation 9.5 is not satisfied for most specimens, fracture surfaces and test records strongly support failure under plane strain conditions. In specimens 5B10V and 5B10RR the crack length marginally fell below 0.45W. However, as the purpose of the present study is to examine trends in fracture toughness with heat-treatment, specimen results which gave linear load-displacement traces and fully cleavage fracture have been regarded as 'valid'

The proof stress value obtained at $-15^{o}C$ for specimens of composition RS518 were in agreement with the results of Part 1,

for similarly heat treated specimens of composition SL175A. As the effect of lowering the test temperature on the value of both $\sigma_{0.2}$ and K_Q is therefore minimal these results may be discussed together with room temperature K_Q values for composition SL175B. In the smaller (14 x 14 mm) tests on specimens of composition SL175A (0.59 wt.%C) the test records showed evidence of stable crack growth and the majority of the results were rejected. Three of the results, however, are recorded in Table 9.8 and they will be referred to later.

It is appreciated that a limited number of tests gave satisfactory results in accordance with BS5447:1977. Nevertheless, some atte will be made to explain these results in terms of possible microstructural features which determine the fracture toughness of high-carbon steels.

Within the limited tests of the present study, lowering the austenitising temperature at a constant cooling rate increases the value of K_Q for the 0.82 wt.%C steel. This can be seen by comparing results for specimens 5B10K and 5B12K, and 5BKV and 5B10V in Tables 9.9 and 9.10. For a given austenitising temperature K_Q values also increased with increasing cooling rate. This effect is readily apparent from specimens 5B10V,5B10K, 5B10R and 5B10RR which were austenitised at 1000°C and cooled at increasing rates from 0.3 to ≈6°C s^{-1} (Table 9.9). The result of accelerated cooling was to systematically increase the toughness from 26.3 $MNm^{-3/2}$ in the slowest cooled specimen to 40.6 $MNm^{-3/2}$ in the most rapidly cooled specimen.

The effect of lower austenitising temperature is in agreement with the results of Hyzak and Bernstein[86] for a steel of similar composition. These authors argued that microstructures of smaller "nodule size" will present a larger number of barriers to crack

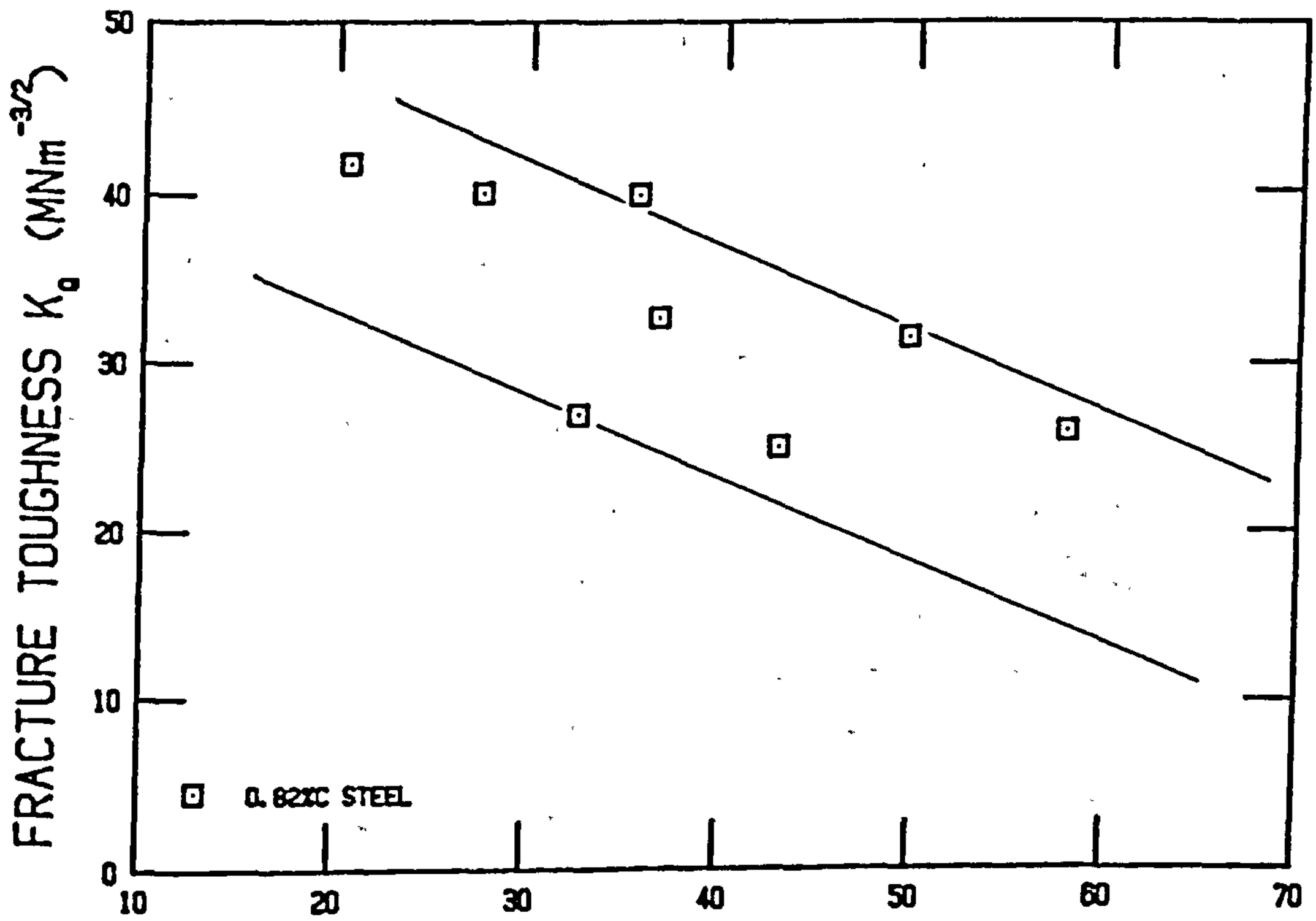

Fig 9.39 Fracture toughness as a function of the pearlite nodule size for the 0.82 wt%C steel.

propagation and therefore show improved toughness. However, according to Knott[130], this effect is more closely related to the size of the microcracks which are formed in the plastic zone ahead of the pre-crack tip. A K_{IC} test measures the amount of energy needed to create a plastic zone ahead of the crack tip which is large enough to sample a distribution of microcrack nuclei. Under the influence of the applied stress, some of the nuclei will produce microcracks. As the applied stress increases a microcrack of critical size and/or favourable orientation is produced and propagates catastrophically.

From this sequence of events it can be argued, as in the case brittle fracture in Charpy V-noth tests, that larger nodule sized microstructures should give rise to larger microcracks which would propagate at lower stresses. A plot of pearlite nodule size against K_Q values is shown in Fig. 9.39 for the data on the 0.82 wt.%C steel. Although there is some degree of scatter in Fig. 9.39, there would appear to be a trend of increasing K_Q values as the nodule size decreases. These results are therefore consistent with Charpy V-notch and instrumented-impact test results discussed previously.

Unfortunately insufficient data are available on the 0.59 wt.%C steel to draw definite conclusions on the effect of heat treatment on fracture toughness. Changing the austenitising temperature from 900 to 1200°C apparently increases the fracture toughness of this hypo-eutectoid steel, although it may be noted that the 'non-valid' results 5A8K, 5A10K and 5A12K show an opposing trend. The effect of changing the cooling rate i.e. from furnace cooling (1OF) to air cooling (1OA) at constant austenitising temperature resulted in an increase in K_Q from 41.2 to 47.3 $Mnm^{-3/2}$ and this finding is in agreement with previous conclusions.

When microstructural parameters are examined in relation to fracture toughness values it can be seen that K_Q values for the steel of composition RS518 are more closely related to variations in pearlite spacing than to changes in pearlite grain or nodule size. If the pearlite spacing is plotted against K_Q values for both this composition and the 0.82 wt.%C steel (Fig. 9.40), it becomes obvious that the improvement fracture toughness with heat treatment can equally well be explained in terms of a refinement in pearlite spacing. This is supported by the observed trend of increasing fracture toughness as the proof stress increases, as shown in Fig. 9.41. As the proof stress is closely related to the interlamellar spacing in high-carbon pearlitic steels the correlation of $\sigma_{0.2}$ with K_Q might be taken as evidence that the pearlite spacing determines the fracture toughness. A similar improvement in K_{Id} values with increasing strength was reported by Bouse et al[84] in hypo-eutectoid rail steels.

It should be noted, however, that the majority of results in Table 9.10 for the 0.82 wt.%C steel are for those heat treatments where the austenitising temperatures was held constant and the cooling rate was varied. Accelerated cooling from a constant austenitising temperature will refine both the pearlite nodule size and the pearlite spacing. Correlations of K_Q values with both N_p and $\bar{S}_r$ is then not surprising. Large changes in pearlite nodule size can, however, be produced with minor changes in pearlite spacing by keeping the cooling rate constant and varying the austenitising temperature. Comparing the results for specimens 5B10K and 5B12K it can be seen that $\bar{S}_r$ values are virtually the same whereas the value of N_p in the former specimen is smaller. This decreases in pearlite

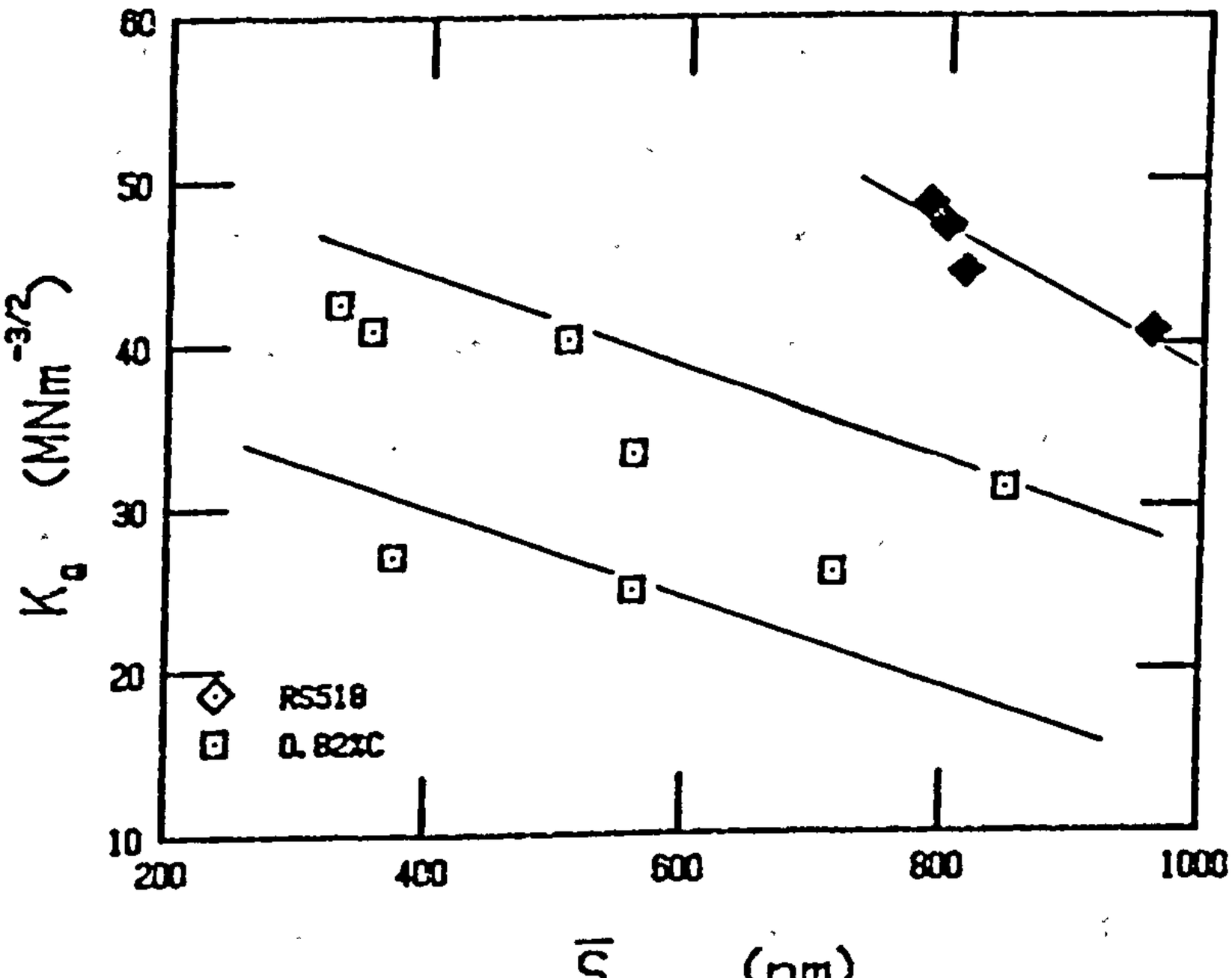

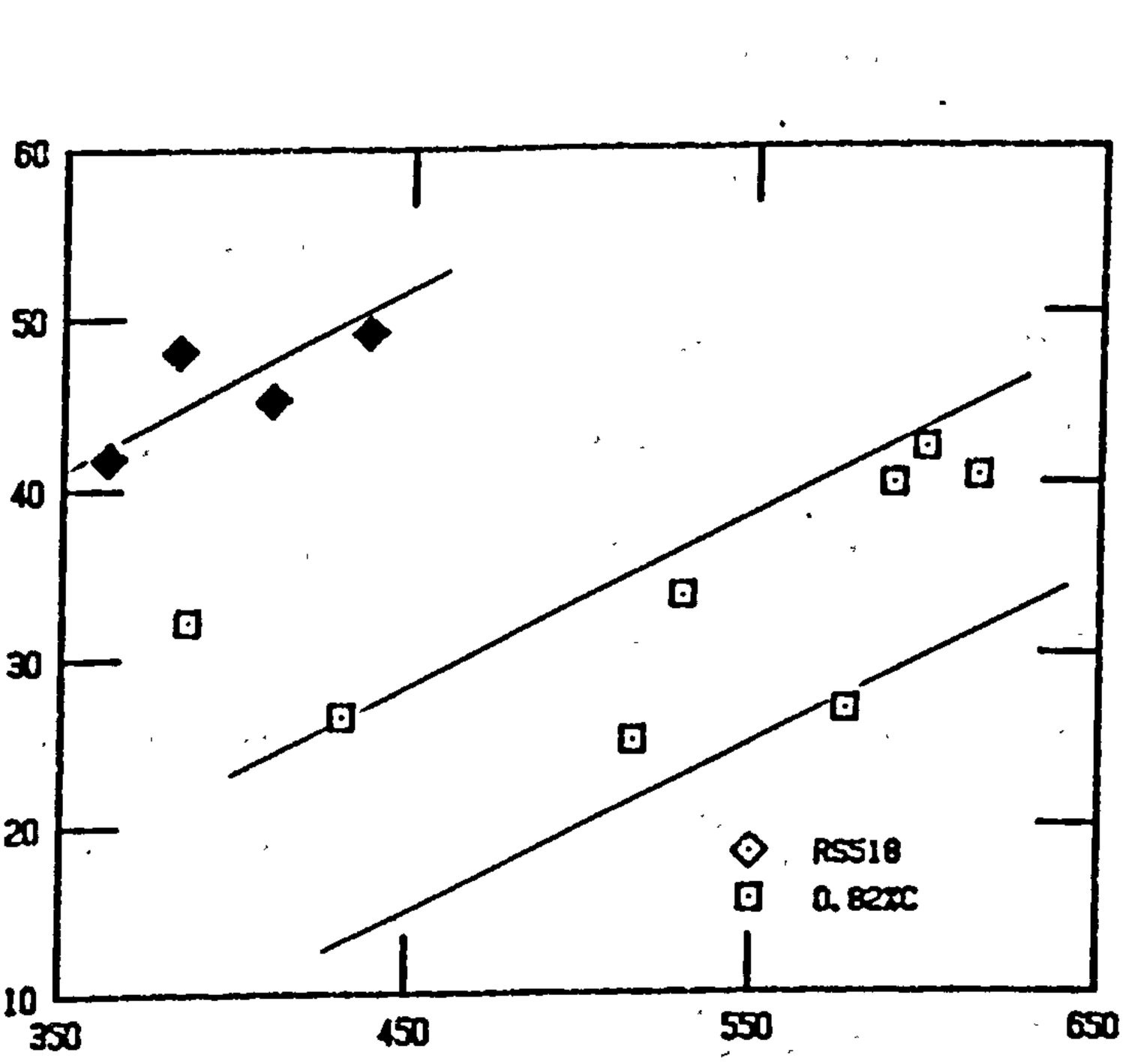

Figs. 9.40 & 9.41 Fracture toughness as a function of the mean random pearlite interlamellar spacing (top) and the 0.2% proof stress.(0.59 & 0.82 wt%C steels)

nodule size can explain the observed increase in fracture toughness from 25.0 to 33.4 $MNm^{-3/2}$ as the austenitising temperature was reduced from 1200 to 1000°C. The role of pearlite nodule size in determining the fracture toughness of the 0.82 wt.%C steel cannot therefore be ruled out on the basis of Figure 9.40 and 9.41. Nevertheless, if it is assumed for the present that the pearlite spacing does in fact determine the value of fracture toughness in plane strain K_{IC} tests, an argument for pearlite spacing control may be postulated as follows.

The concept of a characteristic distance for cleavage fracture was discussed in Section 7.1.1. In mild steel this distance is associated with the volume of material needed to assure the presence of 'eligible' carbide particles whose fracture conditions are satisfied. The magnitude for this distance depends, therefore on the size, distribution and volume fraction of carbides and on the flow stress. According to Evans[153] the most important microstructural feature in mild steel is the size distribution of carbides. When 'eligible' microcrack nuclei, i.e. cracked carbides, are located at large distances from the crack tip, a large plastic zone must be created to sample the distribution of these nuclei from which at least one is of a suitable size and orientation to propagate in a catastrophic manner. In this instance the fracture toughness, K_{IC}, will be larger than for equivalently sized but more closely spaced nuclei.

The work of Park and Bernstein[161] found no evidence of shear cracking of pearlite ahead of the fatigue precrack tip in K_{Id} specimens. The critical crack size for unstable cleavage was calculated to be of the order of the pearlite spacing ≈0.2 microns

and the authors therefore concluded that the first few dimples formed by the shear cracking mechanism of Miller and Smith[160] would propagate catastrophically. If it is assumed,as in the case of mild steel,that the propagation of these microcracks is the critical stage in the fracture process finer pearlite spacings might be expected to give rise to large values of fracture toughness. This is because the size of the microcracks will be governed by the pearlite interlamellar spacing and,although the proof stress is higher, larger plastic zone sizes would need to be created to sample 'eligible' microcracks in microstructures of fine pearlite spacings. This is further supported by the fact that at a constant carbon level finer cementite lamellae are associated with fine inter-lamellar spacings. As discussed earlier,Miller and Smith[160] predict that the combination of fine ferrite lamellae widths (giving shorter dislocation pile-up lengths) and thinner cementite lamellae would require higher applied stress levels for shear cracking. A similar trend was found by Rawal and Gurland[187] from an examination of the influence of cementite dispersions on the fracture toughness of spheroidised carbon steels. These authors found K_{IC} values to increase with decreasing.carbide spacing when this decrease was accompanied by a reduction in cementite particle size.

Pearlite spacing control in fracture toughness tests would explain the results for specimens of composition RS518. In addition, this may also account for the lack of effect of prior-austenite grain size (in the range 30 to 300 microns) found by Allery[172] for a large number of tests on medium to high carbon rail steels. This author[172] used large test specimens which were re-austenitised at different temperatures but were air cooled at a constant rate of

$\approx 1^{o}C\ s^{-1}$. As shown throughout the present study, these heat treatments can lead to minor variations in pearlite spacing and therefore should not be expected to give a significant change in fracture toughness if pearlite interlamellar spacing is the controlling microstructural feature.

However,it should be noted that the studies of Allery[172] and Bernstein et al[84,86] involved dynamic fracture toughness tests. The high strain rates involved would raise the uniaxial yield stress and increase the tendency for brittle fracture. The decrease in plastic zone size with increased strain rate may be envisaged to create a situation in which the propagation of microcracks of dimension of the order of the pearlite spacing is the critical event in the fracture process. Whether this is due to an accompanying decrease in the characteristic distance is not clear. Attempts by a parallel study[188] to relate calculated values of 'characteristic distance' to microstructural parameters in eutectoid rail steels produced no consistency of microstructural significance to this distance. Clearly more work is needed to investigate the microstructural features which determine the plane strain fracture toughness of high-carbon pearlitic steels.

To conclude, the results of the present study indicate a possible inconsistency in the effect of microstructural changes on the Charpy V-notch and plane strain fracture toughness of pearlitic steels. Test results suggest that in a Charpy test the propagation of a pearlite nodule size microcrack is the critical event leading to brittle failure. Both decreasing the austenitising temperature and increasing the cooling rate refine the size of this microstructural feature and give rise to improved toughness. In a K_{IC} test,

on the other hand, the more rapid stress gradient ahead of the sharp fatigue crack may influence the role of the microstructure in cleavage fracture. The microstructural significance of the characteristic distance ahead of the fatigue crack tip then determines the fracture toughness. If it is assumed that the cementite lamellae thickness and spacing influence this distance,then the effect of both austenitising temperature and cooling rate can be explained for the majority of the results of the present study.

PART 2: CONCLUSIONS

The relationship between heat treatment variables , microstructure and fracture toughness has been studied for high carbon pearlitic steels. The conclusions drawn from this investigation are listed below.

Microstructure:

1) The measurement of pearlite 'colony' size by optical and electron microscopy give markedly different values when the former is identified using a crystallographic dependent colour etching reagent and the latter is defined as a region of approximately parallel cementite lamellae.

2) Although lowering the austenitising temperature (i.e. smaller prior-austenite grain sizes) and faster cooling rates decrease the size of both microstructural parameters this effect is more evident for optical measurements.

3) Optically distinct regions have been termed 'pearlite grains' as they are often composed of a number of colonies of approximately parallel lamellae.

4) Pearlitic grains are easily discernible under the optical microscope by virtue of their clearly defined high angle boundaries. There is often no apparent boundary separating colonies of parallel lamellae within a given pearlite grain.

5) With reference to the work of Takahashi et al[167] the pearlite grain is regarded as indicative of a region of

pearlite in which the crystallographic orientation of the ferrite planes is constant or closely aligned. In fully pearlitic microstructures the term grain and nodule are synonomous.

Cleavage crack propagation:

6) The controversy in the literature concerning the influence of pearlite colony boundaries in obstructing cleavage crack propagation has apparently arisen from confusion in the definition of pearlite colonies and nodules.

7) The observation of a number of pearlite colonies contained within a single cleavage facet can be explained by the fact that these colonies are components of the same pearlite nodule.

8) The measurement of regions of parallel cementite lamellae is therefore of limited use in determining the microstructural feature which is the major obstacle to continuous cleavage fracture.

9) The pearlite grain or nodule in fully pearlitic microstructures was found to be directly related to the cleavage facet size.

10) The corresponding pearlite nodule size in hypo-eutectoid steels is believed to be the pearlite grain, together with the neighbouring pro-eutectoid ferrite from which this grain nucleated. When account was taken of the pro-eutectoid ferrite a satisfactory agreement was reached between the effective pearlite nodule size and the cleavage facet size in the hypo-eutectoid steels studied.

Charpy-V-notch toughness:

11) The pearlite nodule size appears to determine the size of microcracks and is the major obstacle to cleavage crack propagation. This microstructural feature therefore primarily controls the ductile-brittle transition temperature in steels having a high volume fraction of pearlite (>80% pearlite).

12) Within the composition and heat treatment limits of the present study refining the pearlite grain or nodule size by decreasing the austenitising temperature and/or accelerated cooling gives improved toughness. High strength and toughness can therefore be achieved by combining a low austenitising temperature with a fast cooling rate.

Fracture toughness:

13) The results of the present study indicate a possible inconsistency in the effect of microstructural changes on the Charpy-V-notch and plane strain fracture toughness of high-carbon pearlitic steels.

14) Although a reasonable correlation was obtained between K_Q values and the size of the pearlite nodule for the fully pearlitic steel there is some evidence that the interlamellar spacing may be a more important microstructural feature as regards this property. Some results suggest that microstructures of finer pearlite spacing may give rise to improved fracture toughness irrespective of the pearlite nodule or prior-austenite grain size.

SPECIMEN No	AUST TEMP °C	COOLING RATE $^{o}Cs^{-1}$	PEARLITE COLONY SIZE (μm) OPTICAL	SEM	mffd $\bar{\lambda}_{\alpha}$ (μm)	% RED IN C.S.A
SL175A1	900	16.7	18.1	8.4	0.363	42
" 5A2	"	13.9	21.0	10.4	0.337	38
" 5A3	"	7.0	31.3	11.0	0.331	45
" 5A4	"	3.5	35.6	20.3	0.751	40
" 5A5	"	0.9	40.9	20.8	0.858	35
" 5A8	1200	15.4	23.1	8.8	0.481	15 *
" 5A9	"	12.6	35.5	9.8	0.454	10 *
" 5A10	"	9.9	37.1	11.6	0.378	9 *
" 5A11	"	3.2	40.0	26.2	1.187	23
" 5A12	"	0.5	49.3	27.7	1.684	30
(95% confidence limits			±6-16%	± 15%		

* Fractured just after UTS.

Table 9.1 Pearlite colony size, mean free ferrite distance and tensile ductility values for specimens of 0.59%C steel.(Heat treated in Part I)

SPECIMEN No	AUST TEMP °C	COOLING RATE $^{o}Cs^{-1}$	PEARLITE COLONY SIZE (μm) OPTICAL	SEM	mffd $\bar{\lambda}_{\alpha}$ (μm)	% RED IN C.S.A
SL175B1	900	13.6	16.3	8.5	0.157	-
" 5B2	"	12.9	16.2	9.4	0.171	20
" 5B3	"	7.3	17.8	10.4	0.215	25
" 5B4	"	3.0	34.1	25.1	0.446	23
" 5B5	"	0.7	40.6	26.3	0.561	15
" 5B8	1200	13.5	33.2	9.2	0.200	5*
" 5B9	"	12.1	38.4	10.9	0.211	5*
" 5B10	"	9.4	38.9	11.0	0.216	5*
" 5B11	"	3.1	39.8	-	0.410	10
" 5B12	"	0.6	55.7	-	0.612	13
95% confidence limits			± 6%	± 15%		
* Specimen fractured at or before UTS						

Table 9.2 Pearlite colony size, mean free ferrite distance and tensile ductility values for specimens of 0.82 wt%C steel.(Heat treated in Part I)

SPECIMEN No	AUST' TEMP °C	COOLING METHOD	V_f	$\bar{L}_\gamma$ (μm)	$\bar{S}_r$ (nm)	d_p (μm)	N_p (μm)	$\bar{\lambda}_\alpha$ (μm)	FRACTURE FACET SIZE (μm)	MEAN VHN	AVERAGE ENERGY ITT °C
SL174A14	1000	AIR	0.190	95.6	788	39.6	49.0	4.040	64.5	206	72
" 4A15	1160	"	0.190	110.6	806	45.6	56.3	4.594	75.9	205	72
SL175A14	800	"	0.097	30.7	878	26.5	29.3	1.004	35.1	226	83
" 5A15	1000	"	0.060	97.0	674	35.0	37.2	0.923	35.0	249	93
" 5A16	1160	"	0.070	115.1	784	52.8	56.8	1.224	51.0	239	125
SL175B14	800	"	0.004	33.4	549	19.9	19.9	0.480	22.0	284	139
" 5B15	1000	"	0.004	95.6	369	31.6	31.6	0.324	28.0	324	175
" 5B16	1160	"	0.004	131.2	384	39.5	39.5	0.337	35.0	328	179
95% confidence limits				± 6%	± 4%	± 6% or 16%			± 13%		

Table 9.3 Heat treatment, microstructural measurements and Charpy impact test results for air cooled specimens of 0.42, 0.59 and 0.82 wt%C steels

SPECIMEN No	AUST' TEMP °C	COOLING METHOD	RATE °Cs^{-1}	TRANSFORMATION TEMPERATURES T_{min}	T_{max}	V_f	$\bar{L}_\gamma$ (μm)	$\bar{S}_r$ (nm)	d_p (μm)	N_p (μm)	$\bar{\lambda}_\alpha$ (μm)	FRACTURE FACET SIZE (μm)	MEAN VHN	AVERAGE ENERGY 1TT °C
SL174A16	1200	VERMIC	0.3	659 ± 3	668 ± 4	0.206	17.5*	825	68.2	85.9	4.212	81.3	177 ± 3	86
"4A17	"	AIR	2.1	650 " 2	663 " 1	0.138	150.0	814	65.5	76.0	3.507	70.6	199 " 6	82
"4A18	"	RIG	4.3	638 " 6	643 " 8	0.080	152.3	780	60.3	65.5	1.643	66.8	211 " 3	74
SL175A17	"	VERMIC	0.3	657 " 3	677 " 3	0.080	133.5	817	57.7	62.7	1.534	62.5	223 " 2	126
"5A18	"	AIR	2.0	639 " 3	661 " 3	0.030	127.6	717	43.0	44.3	0.747	57.2	253 " 8	118
"5A19	"	RIG	4.5	624 " 2	640 " 2	0.050	129.5	622	38.7	40.7	0.860	46.6	261 " 14	124
SL175B17	"	VERMIC	0.2	654 " 3	676 " 1	0.003	-	788	55.6	55.6	0.691	60.8	260 " 9	176
"5B18	"	AIR	2.9	635 " 1	661 " 3	0.004	-	642	42.0	42.0	0.563	45.3	290 " 7	170
"5B19	"	RIG	4.4	616 " 7	640 " 7	0.0	-	520	35.3	35.3	0.456	46.6	310 " 10	168
95% confidence limits							± 6%	± 4%	± 6 or 16%			± 13%	± Std Dev	

* Ferrite grain size

Table 9.4 Heat treatment, microstructural measurements and Charpy impact test results for specimens of 0.42, 0.59 and 0.82 wt% C steels (cooled at three different rates.)

SPECIMEN No	AUST TEMP °C	COOLING METHOD	RATE °Cs^{-1}	TRANSFORMATION TEMP °C		ENERGY ABSORBED (JOULES) ± 7% (calculated)	MAX LOAD (KN) ±5%	0.2% PROOF STRESS (Nmm^{-2})
				T_{min}	T_{max}			
5A8C	800	AIR	2.2	657	675	18.9	40.39	439
5A9C	900	"	2.4	641	654	12.5	32.14	-
5A10C	1000	"	2.5	644	668	17.0	39.16	441
5A11C	1100	"	2.5	641	665	12.5	35.34	432
5A12C	1200	"	2.3	642	663	9.1	31.28	453
5ACV	900	VERMIC	0.5	656	673	10.8	29.19	382
5ACR	"	RIG	4.3	625	665	15.6	39.16	478
5ACRR	"	"	5.0	636	660	21.9	45.32	463
5A10V	1000	VERMIC	0.3	663	685	10.4	30.17	381
5A10R	"	RIG	4.1	633	653	21.2	45.81	485
5A10RR	"	RIG	6.0	628	644	15.2	39.53	517

Table 9.5 Heat treatment data and instrumented-impact test results for specimens of 0.59 wt%C steel.

SPECIMEN No	AUST TEMP °C	COOLING METHOD	RATE °C s^{-1}	TRANSFORMATION TEMP °C		ENERGY ABSORBED (JOULES) ±7% (calculated)	MAX LOAD (KN) ± 5%	0.2% PROOF STRESS$_2$ (N mm^{-2})
				T_{min}	T_{max}			
5B8C	800	AIR	2.0	655	677	12.5	36.70	470
5B9C	900	"	2.4	632	664	11.4	36.57	527
5B10C	1000	"	2.3	640	667	10.1	29.06	518
5B12C	1200	"	2.8	634	659	6.9	29.31	452
5BCV	900	VERMIC	0.5	652	670	8.3	32.63	407
5BCRR	"	RIG	5.7	625	645	11.4	37.31	543

Table 9.6 Heat treatment data and instrumented-impact test results for specimens of 0.82 wt%C steel.

Specimen No.	Austenitising temp. °C	Cooling Data		Transformation Data			Ferrite Volume fraction V_α	Prior Austenite Grain Size L_γ (mm)	Mean Nearest Pearlite Spacing S_p (nm)	pearlite grain size d_p (μm)	Mean Free ferrite Distance λ_α (μm)
		Method	Rate $^{o}Csec^{-1}$	Time Sec.	Temperature °C Tmin.	Tmax.					
5A8K	800	AIR	2.2	-	648	666	0.120	49.6	709	19.6	1.275
5A10K	1000	"	2.5	-	641	665	0.050	111.3	818	36.5	0.725
5A12K	1200	"	1.6	-	637	659	0.032	139.8	738	59.1	0.792
RS518/9A	900	"	1.9	-	650	662	0.050	115.2	816	52.9	0.990
RS518/10A	1000	"	1.3	-	670	688	0.046	168.1	800	83.8	1.048
RS518/12A	1200	"	1.4	-	660	688	0.022	230.0	790	96.3	0.814
RS518/10F	1000	FURNACE	0.1	-	680	693	0.100	166.8	964	130.2	2.452
							95% confidence limits ± 6%		± 4%	± 6 to 16%	

Table 9.7 Heat treatment and metallographic data for fracture toughness test specimens Of 0.59 wt%C steel.

SPECIMEN No	TENSILE TEST DATA Nmm^{-2} 0.2% PROOF STRESS	UTS	FRACTURE TOUGHNESS DATA B (mm)	W (mm)	$\frac{a}{W}$	Y	P_Q (KN)	K_Q ($MNm^{-3/2}$)
5A8K	435	802	14.03	14.04	0.543	12.27	6.675	49.3
5A10K	443	837	14.03	14.04	0.482	10.07	7.125	43.1
5A12K	450	862	14.02	14.00	0.462	9.47	5.850	33.4
RS518/9A	409*	836	20.01	40.01	0.518	11.28	16.350	44.5*
" 10A	380*	819	19.02	38.03	0.535	11.94	14.700	47.3*
" 12A	437*	845	19.01	38.03	0.520	11.36	15.750	48.3*
" 10F	360*	753	19.00	38.03	0.539	12.10	12.600	41.1*

* Tested at $-15^{\circ}C$

Table 9.8 Fracture toughness and tensile test data for 0.59 wt%C steel.

Specimen No.	Austenitising Temp. °C	Cooling Data		Transformation Data			Ferrite Volume Fraction V_α	Prior Austenite Grain Size L_γ (μm)	Mean Random Pearlite Spacing S_r (nm)	pearlite grain size d_P (μm)	Mean Free Ferrite Distance $\bar{\lambda}_\alpha$ (μm)
		Method	Rate °Csec^{-1}	Time Sec.	Temperature °C Tmin.	Tmax.					
5B10K	1000	AIR	2.5	-	637	667	0.000	-	566	37.1	0.496
5B12K	1200	AIR	3.0	-	636	664	0.000	-	567	43.2	0.496
5BKV	900	VERMIC	0.4	-	655	682	0.000	-	855	49.6	0.750
5BKR	"	RIG	4.3	-	638	657	0.000	-	377	32.8	0.331
5BKRR	"	RIG	5.3	-	619	647	0.002	-	326	21.2	0.268
5B10V	1000	VERMIC	0.3	-	655	678	0.001	-	721	58.3	0.632
5B10R	"	RIG	5.7	-	627	651	0.000	-	506	35.9	0.444
5B10RR	"	RIG	6.0	-	618	638	0.000	-	350	28.0	0.286
							95% confidence limits		± 4%	± 6%	

Table 9.9 Heat treatment and metallographic data for fracture toughness test specimens of 0.82 wt%C steel.

SPECIMEN No	TENSILE TEST DATA Nmm^{-2} 0.2% PROOF STRESS	UTS	FRACTURE TOUGHNESS DATA B (mm)	W (mm)	$\frac{a}{W}$	Y	P_Q (KN)	K_Q ($MNm^{-3/2}$)
5B10K	530	1008	14.00	14.05	0.495	10.48	5.288	33.4
5B12K	517	1009	14.03	14.03	0.450	9.09	4.575	25.0
5BKV	386	899	14.03	14.03	0.476	9.88	5.325	31.7
5BKR	577	1071	14.01	14.02	0.474	9.82	4.575	27.1
5BKRR	599	1052	14.04	14.02	0.467	9.62	7.275	42.1
5B10V	431	899	14.03	14.03	0.439	8.85	5.2125	26.3
5B10R	591	1013	14.02	14.03	0.525	11.51	5.7750*	40.0
5B10RR	615	1073	14.11	14.01	0.427	3.34	8.1375	40.6

* Pop-in

Table 9.10 Fracture toughness and tensile test data for 0.82 wt%C steel.

APPENDIX C

INSTRUMENTED IMPACT TESTING

OBSERVED ENERGY ABSORBED

The conventional starting or 'armed' position of the pendulum during standard Charpy impact testing is approximately 180^{o} to the rest (vertical) position, and the initial striking energy is ≃300J, at a striking velocity of ≃5.6 ms^{-1}. As this energy was far in excess of that which would be required to break specimens, in the present study a reduced striking velocity, and therefore, initial energy was required if a meaningful force-time trace was to be obtained. The impact pendulum was held back to a preselected height, as shown in Fig. C1. When released, the pendulum swung to 54^{o} from the rest position. Assuming no energy loss, the initial height (h) of the pendulum is obtained from,

$$\text{Cos } 54^{o} = \frac{80-h}{80} \text{ cm}$$

where 80 cm was the length of the impact pendulum, as shown in Fig. C1. This gives a height, h of 33 cm.

On striking the specimen, the tup will have an initial energy given simply by,

$$\text{Energy (J)} = mgh \qquad (C.1)$$

where m = mass of impact hammer (19.5 Kg) and g the acceleration due to gravity = 9.81 ms^{-2}. The initial energy of the hammer is then 63J.

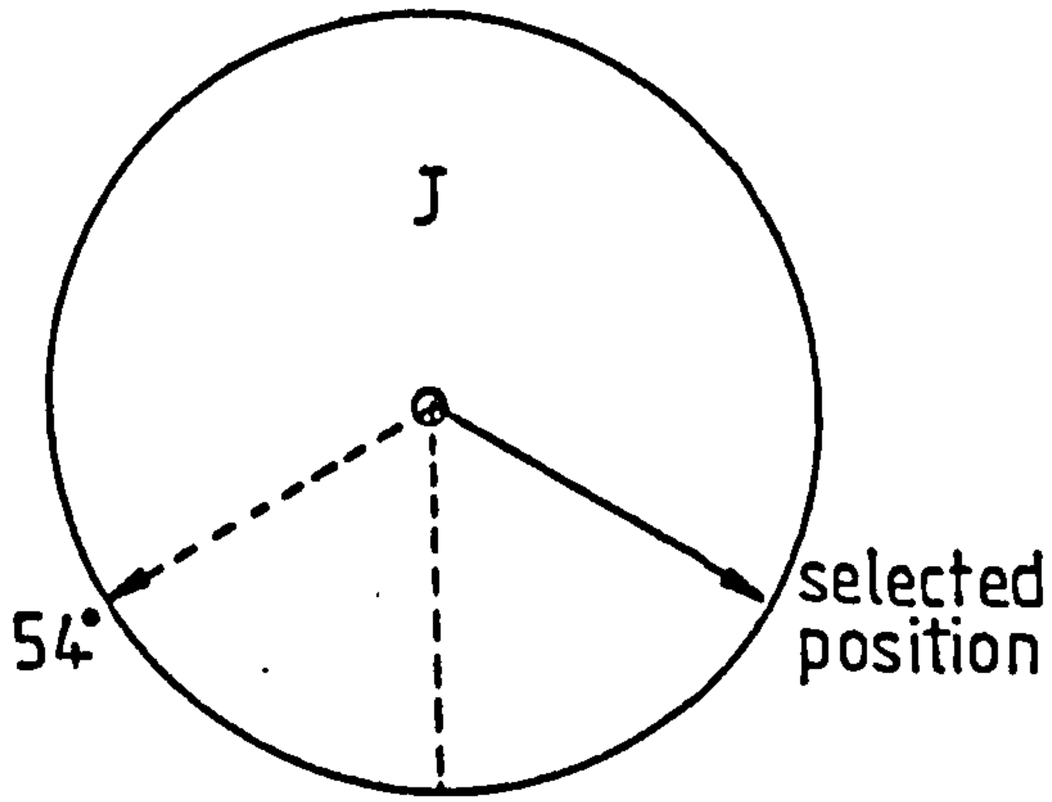

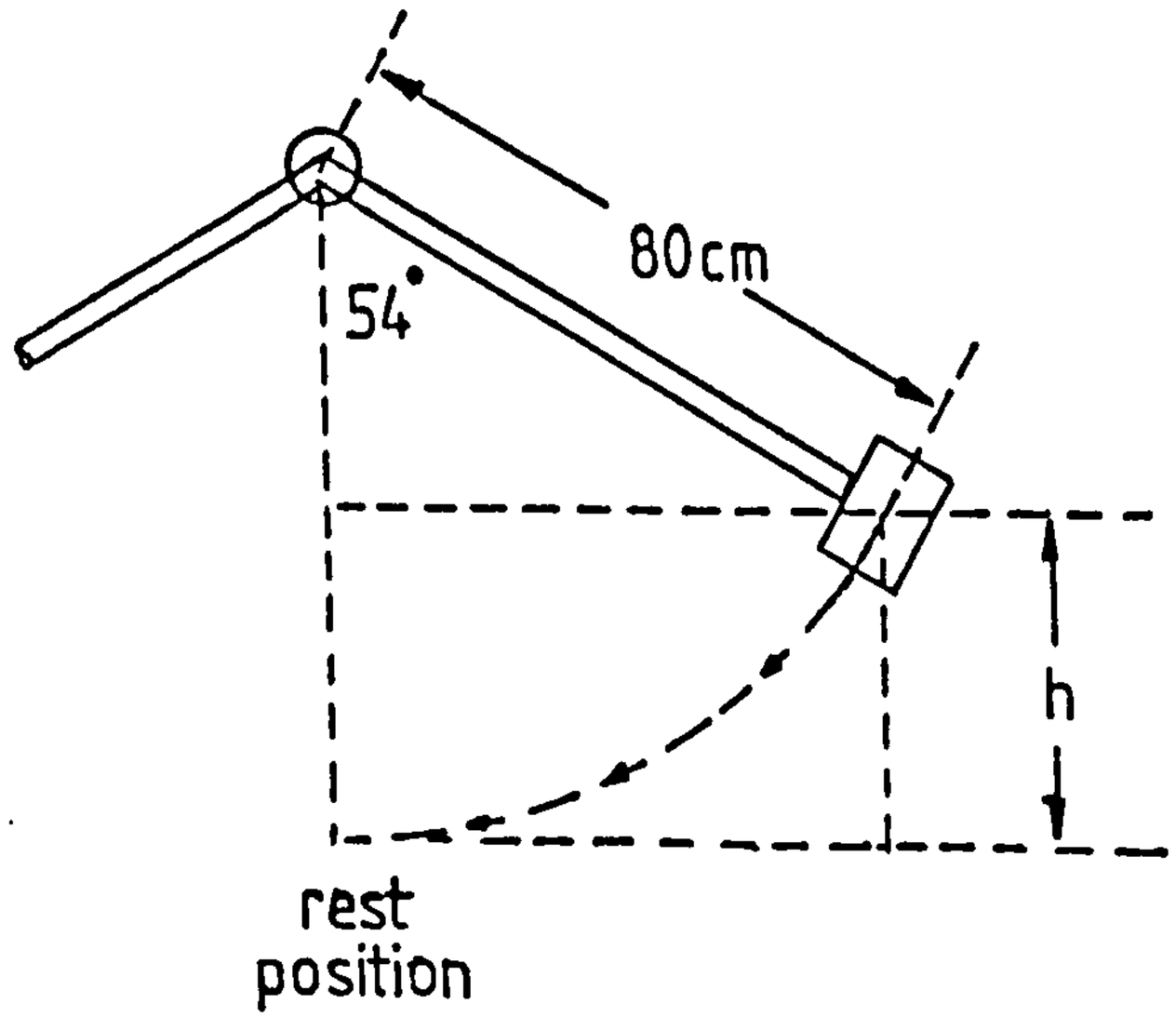

Fig.C1. Schematic diagram of Charpy impact machine showing reduced pendulum starting position.

The striking velocity, v ,of the hammer is given by

$$v = \sqrt{2gh} = 2.54 \text{ ms}^{-1} \qquad (C.2)$$

By noting the energy value corresponding to angles between 0 and 54^{o}, an approximated measure of the absorbed energy can be obtained.

CALCULATED ABSORBED ENERGY

The energy absorbed during fracture of the specimen can be calculated from the force-time curve by[141],

$$E = A \left| v - \frac{a}{2m} \right| \qquad (C.3)$$

where m is the mass of the hammer, V. the striking velocity , . A the area under the force time curve. and a, the hammer acceleration. To calculate E in Joules, the units of Kg for m and ms^{-1} for v, required that the area under the force-time curve be measured in $N\ s^{-1}$. Therefore, the mm scale on x and y axis of the fracture trace shown in Fig. C2 must be converted to the appropriate units of seconds and Newtons respectively.

Time (x) axis

From the wave function of the oscilloscope it was found that one wavelength was equal to 126 mm, which is equivalent to 1/158 seconds, at a time-base setting of 1 ms cm^{-1}. Therefore

$$126 \text{ mm} \equiv 1/158 \text{ s}$$

$$1 \text{ mm} \equiv 5.023 \times 10^{-5} \text{s}$$

As the time-base setting for the tests in the present study was

$$0.2 \text{ ms cm}^{-1}$$

$$1 \text{ mm} \equiv 1.005 \times 10^{-5} \text{ s}$$

Force (Y) axis

A signal output from the accelerometers of 2V gave a peak to peak amplitude on the oscilloscope measured to be 5 cm. 1 mm is therefore equivalent to 0.04 V. The system was arranged so that the amplifier gave an output of 3.16 mV ms^{-2} deceleration of the hammer. If V, is the peak height in volts, the maximum deceleration, a, of the hammer is given by,

$$a = \frac{V}{3.16 \times 10^{-3}} \ ms^{-1}$$

Since the force, or load L, is given by,

$$L = ma \qquad (C.4)$$

$$L = \frac{19.5\ (0.04)\ (\text{height in mm})N}{3.16 \times 10^{-3}}$$

and 1 mm ≡ 246.3N

Example:

The trace for specimen 5B12C is given in Fig. C2. The peak height is 119 mm and therefore the

Maximum load L_{max} = 119 (246.3)N

= 29310N

= 29.3(±5%)KN

The area under the trace in Fig.C2 in mm^2 measured from the Apple II computer graphics tablet was 1124(±2%)mm^2.

As 1 mm^2 = 246.3$(1.005 \times 10^{-3})Ns^{-1}$

1124 mm^2 = 1124(246.3)$(1.005 \times 10^{-5})Ns^{-1}$

= 2.78(±7%)Ns^{-1}

From equation C3, the energy in Joules

$$E = A\left|v - \frac{a}{2m}\right|$$

$$E = 2.78\left|2.54 - \frac{2.78}{2(19.5)}\right|$$

$$E = \underline{6.9(\pm 0.5)J}$$

This value compares well with the estimate of 6.6J obtained from the angle of swing of the pendulum.

REFERENCES

1. Chadwick G.A. "Metallography of Phase Transformations, Butterworths, London, 1972.

2. Hillert M. in "Decomposition of Austenite by Diffusional Processes" edited by V.F. Zackay and H.I. Aaronson, Interscience, New York, 1962, p197.

3. Mehl R.F., Trans. A.S.M. 30, 1942, 381.

4. Dippenaar R.J. and Honeycombe R.W. Proc. Roy. Soc., London, 333, 1973, 455.

5. Belaiew N.T., J.I.S.I., 124, 1931, 195.

6. Belaiew N.T., J.I.S.I., 105, 1922, 201.

7. Mehl R.F., Trans. A.S.M. 29, 1941, 813.

8. Mehl R.F., J.I.S.I., 159, 1948, 113.

9. Smallman R.E., "Modern Physical Metallurgy", Butterworths, London, 1970.

10. Joliviet H., J.I.S.I., 2, 1939, 95.

11. Smith C.S., Trans. A.S.M. 45, 1953, 533.

12. Aaronson H.I., in "Decomposition of Austenite by Diffusional Processes" edited by V.F. Zackay and H.I. Aaronson, Interscience, New York, 1962, p387.

13. Carpenter H.C.H. and Robertson J.M., J.I.S.I., 123, 1931, 345.

14. Ohmari Y., Davenport A.T. and Honeycombe R.W.K., Trans. I.S.I.J., 12, 1972, 128.

15. Samuel F.H., Trans. I.S.I.J., 23, 1983, 403.

16. Samuel F.H., Hussein A.A., Trans. I.S.I.J., 23, 1983, 65.

17. Pitsch W., Acta. Met. 10, 1962, 79.

18. Petch N.J., Acta Cryst. 6, 1953, 96.

19. Bagaryatskii, Doki Akad Nauk SSSR, 73, 1950, 1161.

20. Kurdyjumov G.C. and Sachs G., Z. Phys., 64 , 1930, 325.

21. Park Y.J., "Mechanism of Cleavage Fracture in Pearlitic Eutectoid Steels", PhD Thesis Carnegie-Mellon University, Pittsburgh, PA, 1977.

22. Andrews K.W., Acta Met. 11, 1963, 939.

23. Hultgren A and Ohlin H., Jernkontorets Ann, 144, 1960, 356.

24. Houin J.P., Simon A and Beck G., Trans. I.S.I.J., 21, 1981, 726.

25. Karlsson B and Linden G., Mat. Sci. Eng. 17, 1975, 153.

26. Smith Y.E. and Fletcher F.B., in Proc. Conf. on Rail Steels - Development Processing and Use, Denver Co., 1976, A.S.T.M. Spec.Tech.Publ., 644, American Society for Testing Materials 1978, p212.

27. Marich S. and Curico P., ibid, p167.

28. Fletcher F.B., Smith Y.E. and Biss V.A., Fast-Welding Chromium - Molybdenum-Vanadium extra-high strength rail steels, in "Vanadium in Rail Steels", Vanitec, Chicago, 1979, p41.

29. Birkbeck G., and Wells T.C., Trans. Met. Soc. A.I.M.E., 242, 1968, 2217.

30. Cheetham D. and Ridley N., Met. Sci. 9 , 1975, 411.

31. Cooksey D.J.S., Munson D., Wilkinson M.P. and Helliwell A., Phil. Mag. 10, 1964, 745.

32. Preston R.R., Private communications, 1981.

33. Puls M.P. and Kirkaldy J.S., Met. Trans A, 3, 1972, 2777.

34. Burgess D.E., MSc Thesis, University of Manchester, 1981.

35. Johnson W.A. and Mehl R.F., Trans. A.I.M.E., 416, 1939, 135.

36. Brandt W.H., J. Appl. Phys., 16 , 1945, 139.

37. Hultgren A., Trans. A.S.M., 39 , 1947, 915.

38. Hull F.C., Colton R.A. and Mehl R.F., Trans. A.I.M.E., 150, 1942, 185.

39. Zener C., Trans. A.I.M.E., 167, 1946, 550.

40. Hillert M., Inst. of Metals Monograph No.33, 1969, 231.

41. Turnbull D., Acta Met., 3, 1955, 55.

42. Cahn J.W., Acta Met., 7, 1959, 18.

43. Sundquist B.E., Acta Met. 16, 1968, 1413.

44. Shapiro J.M. and Kirkaldy J.S., Acta Met., 16, 1968, 579.

45. Cheetham D. and Ridley N., J. Inst. Met. 99, 1971, 371.

46. Marder A.R., and Bramfitt B.L., Met. Trans. A., 6A, 1975, 2009.

47. Bolling R.H. and Richman, Met. Trans. A., 1, 1970, 2095.

48. Ridley N., Met. Trans. A., 15A, 1984, 1019.

49. Hall E.O., "Yield Point Phenomena in Metals and Alloys" MacMillan and Co Ltd., London,1970.

50. Eshelby J.D., Frank F.C. and Nabarro F.R.N., Phil. Mag., 45, 1954, 1351.

51. Bilby B.A. and Bullough E., Phil. Mag. 45, 1954, 631.

52. Smith E. and Worthington P.J., Phil. Mag. 9, 1964, 211.

53. Hall E.O., Proc. Phys. Soc., B64, 1951, 747.

54. Petch N.J., J.I.S.I., 174, 1953, 25.

55. Armstrong R., Codd I., Douthwaite R.M. and Petch N.J., Phil. Mag., 7, 1962, 45.

56. Taylor G.I., J. Inst. Met., 62, 1938, 307.

57. Wilson D.V. and Chapman J.A., Phil. Mag., 8, 1963, 1543.

58. Li J.C.M. and Chou Y.T., Met. Trans. A., 1, 1970, 1145.

59. Worthington P.J., and Smith E., Acta. Met., 12, 1964, 1277.

60. Meyers M.A., and Ashworth E., Phil. Mag., A46, 1982, 737.

61. Hirth J.P., Met. Trans. A., 3, 1972, 3047.

62. Meakin J.D., and Petch N.J., ASD-TDR, 63-324 Orlando Florida, 1963, 243.

63. Li J.C.M., Trans. Met. Soc. A.I.M.E., 227, 1963, 239.

64. Conrad H., in "Ultrafine-grain Metals" edited J.J. Burke, V. Weiss Syracuse University Press., 1970, 213.

65. Johnson A.A., Phil. Mag., 7, 1962, 177.

66. Mott N.F., J. Inst. Met., 72, 1946, 367.

67. Mintz B., Cochran R.C. and Baird J.D., *Scan* J. Met., 1, 1972, 279.

68. Wilson D.V., Met. Sci. J., 1, 1967, 40.

69. Gensamer M., Pearsall E.B. and Pellini W.S., Trans. A.S.M., 30, 1942, 983.

70. Roberts C.S., Carruthers R.C., and Averbach B.L., Trans. A.S.M., 44, 1952, 1150.

71. Orowan E., Discussion in Symposium on Internal Stresses in Metals and Alloys, Inst. of Metals, London, 1948, p451-453.

72. Ashby M.F., "Oxide Dispersion Strengthening" eds. G.C. Ansell, T.D. Cooper, F.V. Lenel., Met. Soc. A.I.M.E., 143, 1958.

73. Turkalo A.M., and Low J.R., Trans. A.I.M.E., 212, 1958, 756.

74. Turkalo A.M., Trans. A.S.M., 54, 1961, 344.

75. Ansell G.S. and Lenel F.V., Acta. Met. 8, 1960, 612.

76. Tyson W.R., Acta Met., 11, 1963, 61.

77. Kossowsky R. and Brown N., Trans. Met. Soc., A.I.M.E., 233, 1965, 1389.

78. Liu C.T. and Gurland J., Trans. Met. Soc., A.I.M.E., 242, 1968, 1535.

79. Hodgson D.E., "An Experimental Investigation of Deformation and Fracture Mechanisms in Spheroidized Carbon Steels"., PhD Thesis, Stanford University ,1972.

80. Hodgson D.E., and Tetelman A.S., Proc. 2nd Int. Conf. on Fracture, edited P.L. Pratt, Chapman and Hall London ,1969, p253.

81. Embury J.D., and Fisher R.M., Acta. Met., 14, 1966, 147.

82. Brogan J. and McIvor I.D., "Quantitative relationships between the structure and tensile properties of high carbon pearlitic rod" in Steel Wire in the 80's., The British Independent Steel Producers Association, Wire Product Group Technical Conference, Stratford-upon-Avon,1980.

83. Hugo J.P., and Woodhead J.H., J.I.S.I., 186, 1957, 174.

84. Bouse G.K., Bernstein I.M. and Stone D.H., Proc. Conf. on Rail Steels - Development Processing and Use, Denver Co., 1976,in ASTM Spec. Tech. Publ., 644, American Society for Testing Materials,1978, p145.

85. Marder A.R., and Bramfitt B.L., Met. Trans. A., 7A, 1976, 365.

86. Hyzak J.M., and Bernstein I.M., Met. Trans. A., 7A, 1976, 1217.

87. Greene O.V., Trans. A.S., for Steel Treating, 16, 1929, 57.

88. Pellisier G.E., Hawkes M.F., Johnson W.A. and Mehl R.F., Trans. A.S.M., 30, 1942, 1049.

89. Gladman T., Holmes B. amd McIvor I.D., "Effect of Second Phase Particles on Strength Toughness and Ductility". I.S.I., London,1971, p68.

90. Gladman T., McIvor I.D., and Pickering F.B., J.I.S.I., 210, 1972, 916.

91. Pickering F.B., Proc. Conf. on Microalloying, Washington DC., 1975m Union CArbide Corporation, New York, 1977, p93.

92. Vander Voort G.F. and Roosz A., Metallography 17, 1984, 1.

93. Gregory B., Hall H.T., and Bullock G., Trans. A.S.M., 54, 1961, 106.

94. Brown D. and Ridley N., J.I.S.I., 204. 1966, 811.

95. Asundi M.K., and West T.C., J. Inst. Met., 94, 1966, 19.

96. Asundi M.K., and West T.C., J. Inst. Met., 94, 1966, 327.

97. Boswell P.G., and Chadwick G.A., Acta. Met., 25, 1977, 779.

98. Brown D. and Ridley N., J.I.S.I., 207, 1969, 1232.

99. Underwood E.E., "Quantitative Stereology"Reading Mass., Addison-Wesley, 1970.

100. William J., Glover S.G., data given in reference 46.

101. Gladman T. and Pickering F.B., Prof. Conf. on "Yield Flow and Fracture in Polycrystals", edited T.N. Baker, Applied Science, London, 1983, p141-199.

102. Querales A., and Byrne J.G., Met. Trans. A., 11A, 1980, 255.

103. Sevillano J.G., in Proc. 5th Inst.Conf. on the Strength of Metals and Alloys, 1979, edited by P. Haasen, V. Gerold and G. Kostorz, Pergamon, Oxford,1980, p819.

104. Flugge J., Heller W., and Schuweitzer R., Stahl U Eisen 99, 1979, 841.

105. Sunwoo H., Fine M.E., Meshii M. and Stone D.H., Met. Trans. A, 13A, 1982, 2035.

106. Karlsson B. and Sundstrom B.O., Mat. Sci. Eng., 16, 1974, 161.

107. Karlsson B. and Linden G., Mat. Sci. Eng., 17, 1975, 209.

108. Gurland J., Mat. Sci., Eng., 40, 1979, 59.

109. Gurland J., in Prof. Conf. on "Yield Flow and Fracture in Polycrystals", edited T.N. Baker, Applied Science, London, 1983, p51.

110. Reuben R.L., and Baker T.N., Mat. Sci., Eng., 62. 1984, 93.

111. Dewey M.A.P., and Briers G.W., J.I.S.I., 204, 1966, 102.

112. Takahashi T. and Nagumo M., Trans. Jap. Inst. Met., 11, 1970, 113.

113. Morton K and Cannon D.F., in Proc. Conf. on Rail Steels - Development Processing and Use Denver Co., 1976, in A.S.T.M. Spec. Tech. Publ., 644, American Society for Testing Materials, 1978, p80.

114. Knupp G.G., and Chidley; ibid p7.

115. Park Y.J., and Bernstein I.M., Proc. of 4th Int. Conf. on Fracture, edited D.M.R., Taplin, University of Waterloo Press, Waterloo, Canada, 2, 1977, 33.

116. Halliday W.I., in Metallurgical Developments in Carbon Steels, I.S.I., 1963, 65.

117. Pickering F.B., The basis of Quantitative Metallography, Inst. Met. Techns., Monograph No. 1, 1976.

118. Smith D.W., and Heheman R.F., J.I.S.I., 209, 1971, 476.

119. Kelly P.M., Scripta Met., 6, 1972, 647.

120 Bush M.E., and Kelly P.M., Acta. Met., 19, 1971, 1363.

121. Langford G., Met. Trans. A., 8A, 1977, 861.

122. Mintz B., Morrison W.B. and Jones A., Met. Tech., 6, 1979, 252.

123. Jindal P.C., and Gurland J., Met. Trans. A., 5, 1974, 1649.

124. Preston R.R., Proc. Conf. on"Yield, Flow and Fracture in Polycrystals", edited T.N. Baker, Applied Science London, 1983, p199-211.

125. Chadwick G.A., Met. Sci., 9, 1975, 300.

126. Chadwick G.A., Acta. Met., 24, 1976, 1137.

127. Armstrong R.W., in "Ultrafine-grain Metals," edited J.J. Burke, V. Weiss, Syracuse University Press 1970, p1.

128. Burns K.W. and Pickering F.B., J.I.S.I., 202, 1964, 899.

129. Puttick K.E., J.I.S.I., 185, 1956, 167.

130. Knott J.F., "Fundamentals of Fracture Mechanics" John Wiley and Sons 1972, p191-199.

131 Tetelman A.S. and McEviliy A.J., "Fracture of Structural Materials" John Wiley and Sons London, 1967.

132. Griffith A.A., Phil. Trans. A., 221, 1920, 169.

133. Irwin G.R., J. Appl. Mech., 24, 1957, 361.

134. Feldbeck D.K. and Orowan E., Weld J., (New York) 34, 1955, 570s.

135. Orowan E., Trans. Inst. Eng., Ship, Scotland 89, 1945, 165.

136. Orowan E., Weld.J. Suppl. 20, 1955, 1575.

137. Westergaard H.M., J. Appl.Mech., 61, 1939, 49.

138. Various authors: "An introduction to Fracture Mechanics", The Journal of Strain analysis, special issue, 10, No. 4, 1975.

139. Rooke D.P. and Cartwright P.J., Compendium of Stress Intensity Factors, Ministry of Defence, H.M.S.O. 1976, London.

140. Methods of test for Plane Strain Fracture Toughness (K_{IC}) of Metallic Materials, British Standards Institution BS5447:1977.

141. Ireland D.R., Prof. Conf. on"Instrumented-Impact Testing", A.S.T.M. Spec.Tech.Publ.,563, American Society for Testing Materials 1974, p3-29.

142. Walker E.F., in "Fracture Toughness", Iron and Steel Institute, B.W. Berry, I.S.I., Publication 121, 1970.

143. Kamath M.S., and Gittos M.F., Weld.Inst.Res. Bullt., 20, 1979, 114.

144. Stroh A.N., Proc.Roy.Soc., A223, 1954, 404.

145. Cottrell A.H., in "Fracture", edited B.L. Averbach et al. John Wiley, New York 1959, p20-54.

146. Petch N.J., ibid p54-67.

147. McMahon C.J., and Cohen M., Acta. Met., 13, 1965, 591.

148. Smith E., Proc.Conf. on 'Physical Basis of Yield and Fracture', ed. A.C. Stickland, Inst.Phys. and Phy.Soc., Oxford 1966, p36.

149. Lindley T.C., Oates G. and Richards C.E., Acta.Met., 18, 1970, 1127.

150. Curry D.H. and Knott J.F., Met.Sci., 10, 1976, 1.

151. Ritchie R.O., Knott J.F. and Rice J.R., J. Mech.Phy.Sol. 21, 1973, 395.

152. Hahn G.T., Met. Trans. A., 15A, 1984, 947.

153. Evens A.G., Met. Trans. A., 14A, 1983, 1349.

154. Bowan P. and Knott J.F., Met. Sci., 18, 1984, 225.

155. Danko J.C. and Stout R.D., J.Weld. 34, 1955, 113s.

156. Gross J.H. and Stout R.D., Weld.J., 34, 1955, 1175.

157. Lindborg U., Trans. A.S.M., 61, 1968, 500.

158. Porter D.A., Easterling K.E., and Smith G.D.W., Acta. Met. 26, 1978, 1405.

159. Bruckner W.H., Weld.J., 29, 1950, 467s.

160. Miller L.E. and Smith G.C., J.I.S.I., 208, 1970, 998.

161. Park Y.J. and Bernstein I.M., Met.Trans. A., 10A, 1979, 1653.

162. Ohmori Y. and Terasaki F., Trans. I.S.I.J., 16, 1976, 561.

163. Park Y.J. and Bernstein I.M., Proc. Conf. on Rail Steels - Development Processing and Use Denver Co. 1976, in A.S.T.M. Spec.Tech.Publ., 644, American Society for Testing Materials 1978, p287-302.

164. Turkalo A.M., Trans. A.I.M.E., 218, 1960, 24.

165. Terasaki F. and Ohtani H., Trans. I.S.I.J., 12, 1972, 45.

166. Alexander D.J. and Bernstein I.M., Met. Trans. A., 13A, 1982, 1865.

167. Takakashi T., Nagumo M. and Asano Y., J. Jap.Inst. Met., 42, 1978, 716.

168. Ohtani H. and Terasaki F., Tetsu-to-Hagane, 58, 1972, 67.

169. Grossman N., Weld. J., 28, 1949, 2655.

170. Rinebolt J.A., Trans. A.S.M., 46, 1954, 1527.

171. Rinebolt J.A. and Harris W.J., Trans. A.S.M., 43, 1951, 1175.

172. Allery M., "The Fracture toughness of ferrite-pearlite medium carbon-manganese steels" PhD Thesis, University of Nottingham,1977.

173. Preston R.R.. Met. and Mat. Tech., Inst.of Met. 12, No. 12, 1980, 687.

174. Cannon D.F., Walker E.F. and Barr R.R., Proc. Symp. on Rail Steel Development I.S.I., London 1972.

175. Zia-Ebrahimi F. and Krauss G., Met. Trans. A., 14A, 1983, 1109.

176. McIvor I.D., Private communications 1984.

177. Beraha E. and Shpigler B., "Color Metallography", American Society for Metals, Metals Park Ohio, 1977.

178. Takahashi T., Nagumo M. and Asano Y., J. Jap. Inst. Met., 42, 708.

179. Steele J.H.,"Correlation of fractographic and microstructural features"in"Fractograph and Material Science",edited L.N. Gilbertson and R.D. Zipp, American Society for Testing Materials 1981, p117-130.

180. Naylor J.P. and Krahe P.R., Met. Trans. A., 5, 1974, 1699.

181. Fearnebough G.D. and Hoy C.J., J.I.S.I., 202, 1964, 912.

182. Wilshaw T.R., Rau C.A. and Tetelman A.S., Eng.Fract.Mech. 1, 1968, 191.

183. Naylor J.P., Met. Trans. A., 10A, 1979, 861.

184. Heller W., Discussion in Proc. Conf. on Rail Steels - Development Processing and Use Denver Co., 1976, A.S.T.M. Spec.Tech.Publ. 644, 1978, p163-165.

185. Yamadi Y., Trans. I.S.I.J., 17, 1977, 516.

186. Inoue T. and Kinoshita S., Trans. I.S.I.J., 17, 1977, 523.

187. Rawal S.P. and Gurland J., Met. Trans. A. 8A, 1977, 691.

188. Kavishe F.P.L. and Baker T.J., "The influence of microstructural variables on the strength and fracture toughness of eutectoid rail steels", paper presented at Metals and Materials '84, Metal Science, Imperial College, London 1984.